Magnetic Resonance with *para*-Hydrogen Induced Polarisation of X-Nuclei

Jennifer Sunari Lewis

Doctor of Philosophy

University of York

Chemistry

August 2020

Abstract

Hyperpolarisation is a deviation away from the Boltzmann distribution in Nuclear Magnetic Resonance (NMR). The hyperpolarisation technique, Signal Amplification By Reversible Exchange (SABRE), is explored in this work with biologically relevant pyrimidines which reflect nucleobases and drugs including anticancer and antifungal agents. Methods to increase the ^{1}H NMR sensitivity of pyrimidine are explored and optimised by examining the various factors that influence the efficiency of polarisation transfer. This led to a ^{1}H NMR signal enhancement of −382 ± 14-fold on the H-2 of pyrimidine being recorded at 9.4 T.

Studies on 5-fluorouracil, one of the most common anticancer agents, are also described. In addition to ^{1}H hyperpolarisation, hyperpolarisation of its ^{19}F nuclei is evaluated under SABRE. Polarisation levels of −106-fold and 0.85 ± 0.53-fold for 5-fluorouracil were achieved for ^{1}H and ^{19}F, respectively. This work was expanded to include other fluorinated *N*-heterocyclic compounds including, 3-fluoropyridine which gave the greatest ^{1}H and ^{19}F signal enhancement of −1287 ± 65-fold and 62 ± 6-fold respectively. After structural characterisation, it was found that two complexes form in these experiments, $[Ir(H)_2(IMes)(sub)_3]Cl$ (**A**) and $[IrCl(H)_2(IMes)(sub)_2]$ (**B**). H_2 loss was found to proceed *via* **B** at between 0.4 and 0.2 s^{-1} which is comparable to that of **A** with 5-fluoropyridine-3-carboxylic acid in the presence of Cs_2CO_3. ^{19}F MRI images were also recorded for these molecules.

The final chapters expand the range of substrates available to the SABRE technique and considers ^{13}C, ^{15}N and ^{31}P hyperpolarisation through oxalate, adenosine triphosphate, urea, uracil and 5-fluorouracil. It was postulated that sodium oxalate could create a long-lived single spin order in its $^{13}C_2$ form. The most effective approach involved utilisation of the co-ligand, DMSO but unfortunately the dimeric species, $[Ir(H)_2(DMSO)(IMes)]_2$(μ-oxalate), forms readily (as demonstrated by NMR and X-ray diffraction) and limits SABRE performance.

List of Contents

Abstract 3

List of Contents 5

List of Tables 11

List of figures 17

Acknowledgements 33

Declaration 35

Chapter 1: Introduction 37

1.1 Nuclear magnetic resonance 37

1.2 Hyperpolarisation methods 41

1.2.1 Brute force 41

1.2.2 Spin-exchange optical pumping (SEOP) 41

1.2.3 Dynamic Nuclear Polarisation (DNP) 42

1.2.4 *Para*-hydrogen induced polarisation (PHIP) 49

1.3 The SABRE process 55

1.3.1 Role of catalyst 55

1.3.2 Quantifying the Dynamic Effects of SABRE 59

1.3.3 Relaxation effects on SABRE 60

1.3.4 Applications and developments of SABRE 63

1.4 Use of a co-ligand in SABRE 69

1.5 SABRE-Relay 72

1.6 Thesis outline 75

Chapter 2: Exploring SABRE with pyrimidine 77

2.1 Hyperpolarisation of pyrimidine and its derivatives 77

2.1.1 Initial SABRE experiments and characterisation 78

2.1.2 Formation and Characterisation of $[Ir(H)_2(IMes)(pyrimidine)_3]$ 79

2.1.3 Rate of H_2 loss from $[Ir(H)_2(IMes)(pyrimidine)_3]Cl$ 81

2.2 Optimisation of the ^1H NMR signal enhancement of pyrimidine 86

2.2.1 Concentration of substrate 86
2.2.2 Concentration of catalyst 88
2.2.3 Type of catalyst 89
2.3 T_1 relaxation values for the ^{1}H NMR resonances for pyrimidine 91
2.3.1 T_1 data for substrate and SABRE active catalyst 92
2.4 Magnetic Resonance Imaging 94
2.5 Conclusions 97
Chapter 3: ^{1}H and ^{19}F SABRE Hyperpolarisation of Fluoro *N*-Heterocycles 101
3.1 Introduction 101
3.2 Hyperpolarised ^{1}H, and ^{19}F NMR detection of *N*-heterocyclic compounds 103
3.3 Analysis of the T_1 relaxation values of the ^{1}H and ^{19}F nuclei 112
3.4 Exchange mechanism and activation of the fluorinated *N*-heterocyclic Iridium complexes 115
3.4.1 Characterisation of the fluorinated *N*-heterocyclic Iridium complexes 116
3.4.2 Ligand exchange for fluorinated *N*-heterocyclic compounds 120
3.4.3 Hydride exchange for fluorinated *N*-heterocyclic compounds 122
3.5 Examination of the ^{19}F spectra 129
3.6 Using INEPT to hyperpolarise ^{19}F 130
3.6.1 Description of the INEPT sequence 131
3.6.2 Polarisation of ^{19}F using the INEPT sequence 131
3.7 Polarisation transfer field dependence on SABRE 134
3.8 ^{19}F imaging 138
3.9 Conclusions 140
Chapter 4: Expanding the range of molecular scaffolds amenable to hyperpolarisation using SABRE 143
4.1 Perfusion agents for Magnetic Resonance Imaging (MRI) 144
4.1.1 Using hyperpolarised urea to improve MR images 145
4.1.2 Hyperpolarisation of Adenosine Triphosphate for ^{31}P imaging 148
4.1.3 Hyperpolarisation of oxalate 150

4.2 Principles and background of SABRE-Relay 151
4.2.1 Investigating the amine metal complex 153
4.3 Exploring hyperpolarisation of Urea with SABRE-Relay 154
4.3.1 Polarisation of ^{13}C and ^{15}N in urea *via* SABRE-Relay 154
4.3.2 ^{13}C-Urea imaging 156
4.4 Exploring SABRE-Relay with monosodium phosphate, ^{31}P and ^{1}H 158
4.4.1 Adenosine triphosphate 163
4.5 Exploring SABRE-Relay with Sodium oxalate, ^{13}C polarisation 165
4.5.1 Polarisation of ^{1}H and ^{13}C nuclei in sodium oxalate 165
4.5.2 SABRE Polarisation of 13C of sodium oxalate using a co-ligand 169
4.5.3 Characterisation of the complexes in 4.5.2 172
4.5.4 Rate of hydrogen and sulfoxide exchange 182
4.6 Conclusions 187
4.7 Further work 189
Chapter 5: Chapter 5 SABRE-Relay with Uracil and Fluorouracil 191
5.1 Introduction 191
5.2 Polarisation of uracil *via* SABRE 194
5.3 Polarisation uracil *via* SABRE-Relay using NH_3 195
5.3.1 Examination of SABRE-Relay with 2-^{13}C-uracil 199
5.3.2 Examination of SABRE-Relay with 2-^{13}C,^{15}N-uracil 200
5.3.3 Analysis of the T_1 relaxation values of ^{13}C and ^{15}N in ^{13}C-uracil and 2-^{13}C,$^{15}N_2$-uracil 201
5.4 Polarisation of fluorouracil with SABRE-Relay 203
5.5 Conclusions 206
Chapter 6: Conclusions and further work 209
6.1 Pyrimidine 209
6.2 ^{19}F hyperpolarisation *via* SABRE 211
6.3 Hyperpolarisation of X-nuclei *via* SABRE-Relay 214
6.4 ^{13}C hyperpolarisation using SABRE with a co-ligand 215

Chapter 7: Experimental 217

7.1 Instrumentation 217

7.1.1 NMR spectrometers and solvents 217

7.1.2 Para-hydrogen Generator 217

7.1.3 X-ray Crystallography 217

7.2 General experimental procedures 218

7.2.1 SABRE-Sample preparation 218

7.2.2 SABRE-Relay sample preparation: 218

7.2.3 Catalyst preparation 219

7.2.4 Substrates 219

7.2.5 Handheld magnet array 219

7.2.6 SABRE method 219

7.2.7 SABRE under automated flow 221

7.2.8 Enhancement calculations 223

7.2.9 Error calculations 224

7.2.10 SABRE Exchange Kinetics – EXSY 225

7.2.11 Relaxation – T_1 experiment 226

7.2.12 Imaging acquisition 231

Appendix 235

A.1 Characterisation for Chapter 2 (pyrimidine) 235

[Ir(COD)(IMes)(pyrimidine)]Cl. 235

[Ir(H)$_2$(COD)(pyrimidine)(IMes)]Cl. 236

[Ir(H)$_2$(IMes)(pyrimidine)$_3$]Cl. 237

A.2 Modelling hydride ligand exchange in [Ir(H)$_2$(IMes)(pyrimidine)$_3$]Cl 238

A.3 Effect of changing pyrimidine concentration (from chapter 2.2.1) 242

A.4 Effect of changing catalyst concentration (from chapter 2.2.2) 243

A.5 The effect of changing the SABRE pre-catalyst (from chapter 2.2.3) 244

A.6 Temperature study 245

A.7 Calculation of ^{1}H T_1 data for pyrimidine and fluorinated *N*-heterocyclic compounds 247

A.8 Calculation and plots of ^{19}F T_1 data for fluorinated *N*-heterocyclic compounds 248

A.9 Characterisation (fluorinated *N*-heterocyclic compounds) 249

Characterisation of $[Ir(H)_2(3\text{-fluoropyryridine})_3(IMes)]Cl$. 249

Characterisation of $[Ir(H)_2(3,5\text{-difluoropyridine})_3(IMes)]Cl$. 250

Characterisation of $[Ir(H)_2(fluoropyrazine)_3(IMes)]Cl$. 251

Characterisation of $[Ir(H)_2(5\text{-fluoropyridine-3-carboxylic acid})_3(IMes)]Cl$. 252

Characterisation of $[Ir(H)_2(5\text{-fluoropyridine-3-carboxylic acid})_3(IMes)]Cl$ in the presence of Cs_2CO_3. 253

Characterisation of $[IrCl(H)_2(3,5\text{-difluoropyryridine})_2(IMes)]$. 254

Characterisation of $[IrCl(H)_2(fluoropyrazine)_2(IMes)]$. 255

A.10 Exchange mechanism for substrate and hydride exchange (Chapter 3)..... 256

Modelling substrate exchange for a *tris* substituted complex, $[Ir(H)_2(IMes)(sub)_3]Cl$..... 256

Modelling substrate exchange in $[Ir(H)_2(IMes)(sub)_3]Cl$ in the presence of complex $[IrCl(H)_2(IMes)(sub)_2]$. 260

Modelling hydride exchange for $[Ir(H)_2(IMes)(sub)_3]Cl$ 260

Modelling hydride exchange for $[Ir(H)_2(IMes)(sub)_3]Cl$ *via* the intermediate $[Ir(H)_2(H_2)(IMes)(sub)_2]Cl$ 263

Rate data for hydride exchange for the interconversion of the *tris* and *bis* complexes 267

A.11 Polarisation transfer field plots for ^{19}F 268

A.12 Characterisation of $[IrCl(H)_2(DMSO)_2(IMes)]$ 270

Characterisation of $[IrCl(H)_2(DMSO)_2(IMes)]$ in methanol-d_4 270

Characterisation of $[IrCl(H)_2(DMSO)_2(IMes)]$ in dichloromethane-d_2 271

Characterisation of $[IrCl(H)_2(IMes)(PhMeSO)_2]$ in methanol-d_4 272

Characterisation of $[IrCl(H)_2(IMes)(PhMeSO)_2]$ in dichloromethane-d_2 273

Characterisation of $[Ir_2(H)_4(DMSO)_2(IMes)_2(\mu\text{-oxalate})]$ in methanol-d_4 and 50 µL of D_2O 274

X- ray diffraction of $[Ir_2(H)_4(DMSO)_2(IMes)_2(\mu\text{-oxalate})]$ 274

A.13 Ligand exchange mechanism for $[IrCl(H)_2(DMSO)_2(IMes)]$ 275

Modelling ligand exchange for sulfoxide complexes 275

Modelling hydride exchange for sulfoxide complexes 279

A.14 Plot of T_1 hyperpolarised measurements 282

Abbreviations 285

References 289

List of Tables

Table 2.1 – Rate constants obtained for the indicated exchange processes in the chemistry of $[Ir(H)_2(IMes)(pyrimidine)_3]Cl$ and $[IrCl(H)_2(IMes)(pyrimidine)_2]$, in methanol-$d_4$ solution as a function of temperature. 84

Table 2.2 – Activation parameters for the indicated processes observed whilst examining $[Ir(H)_2(IMes)(pyr)_3]Cl$ and $[IrCl(H)_2(IMes)(pyr)_2]$ in methanol-d_4 (where pyr = pyrimidine). .. 85

Table 2.3 – ^1H T_1 data for pyrimidine (25 mM) in the presence of catalyst (2.5 mM) in methanol-d_4 (0.6 mL) at 295 K. 92

Table 2.4 – ^1H T_1 and signal enhancements for pyrimidine under optimal conditions, [IrCl(COD)(1,3-bis(2,4,6-trimethylphenyl)-4,5-dimethylimidazol-2-ylidine)] (2.5 mM), pyrimidine (25 mM) in methanol-d_4 (0.6 mL). For the 4,6-d_2-pryimidine and 2,5-d_2-pyrimidine [IrCl(COD)(IMes)] (5 mM) was used with 20 mM of substrate in methanol-d_4 (0.6 mL). * = Personal communication within the group from Phil Norcott who carried out the experiments for this substrate..... 93

Table 2.5 – SNR ratios for pyrimidine (500 mM) when in the presence of different SABRE pre-catalysts (5 mM) used in Chapter 2 section 2.2.3 when using either an FISP or RARE protocol. Absolute SNR has been calculated by SNR_{Hyp} / SNR_{Th}. 95

Table 3.1 – Hyperpolarised ^1H NMR signal enhancements observed when 20 mM or 100 mM concentrations of the indicted fluorinated *N*-heterocyclic compound, undergo SABRE using 5 mM of pre-catalyst [IrCl(COD)(IMes)] in 0.6 mL MeOD-d_4 in the presence of 4 bar of *p*-H_2; measurements were carried out on a 400 MHz Bruker NMR. Pyridine reference data is as reported by Lloyd *et. al.*[111] 104

Table 3.2 – Hyperpolarised ^{19}F NMR signal enhancement when using 20 mM or 100 mM of the indicated *N*-heterocyclic fluorinated compound under SABRE with 5 mM of pre-catalyst [IrCl(COD)(IMes)] in 0.6 mL methanol-d_4 in the presence of 4 bar of *p*-H_2 as measured on a 500 MHz Bruker NMR system. 110

Table 3.3 – ^1H T_1 data for all hydrogens within each of the *N*-heterocyclic fluorinated compounds investigated at a 100 mM concentration, in the presence of 5 mM of pre-catalyst [IrCl(COD)(IMes)] in 0.6 mL of methanol-d_4 at 295 K under 4 bar of hydrogen. Pyridine data as reported by Lloyd *et. al.*[111] 113

Table 3.4 – ^{19}F T_1 measurements for the fluorinated *N*-heterocyclic compounds investigated using 100 mM of the substrate in the presence of 5 mM of pre-catalyst, [IrCl(COD)(IMes)] in 0.6 mL methanol-d_4 at 295 K under 4 bar of hydrogen. 115

Table 3.5 – Proportion of $[Ir(H)_2(IMes)(sub)_3]Cl$ to $[IrCl(H)_2(IMes)(sub)_2]$ as a function of substrate identity. Samples contained 5 mM pre-catalyst [IrCl(COD)(IMes)] and a 20 mM substrate concertation under 4 bar H_2. Where L = Cl^-. 119

Table 3.6 – Rate constants for the loss of the ligand (sub) in $[Ir(H)_2(IMes)(sub)_3]Cl$, where sub = 3-fluoropyridine or 5-fluoropyridine-3-carboxylic acid, in methanol-d_4 (mL)as a function of temperature, results *via* selective 1D-EXSY experiments at 500 MHz. 121

Table 3.7 – Activation parameters for ligand loss (sub) in $[Ir(H)_2(IMes)(sub)_3]Cl$ in methanol-d_4. 121

Table 3.8 – Rate constants for the hydride exchange processes involving $[Ir(H)_2(4)_3(IMes)]Cl$, $[IrCl(H)_2(4)_2(IMes)]$, $[IrCl(H)_2(4)_2(IMes)]$ and $[IrCl(H)_2(4)_2(IMes)]$, where 4 = 3,5-difluoropyridine, in methanol-d_4 (0.6 mL) as a function of temperature, results *via* selective 1D-EXSY experiments at 500 MHz. 125

Table 3.9 – Activation parameters for hydride loss in $[Ir(H)_2(IMes)(sub)_3]Cl$ in methanol-d_4. Sub = 3-fluoropyridine (2), 3,5-fluoropyridine (4) or fluoropyrazine (5). 126

Table 3.10 – Rate constants for the loss of hydrogen in $[Ir(H)_2$(5-fluoropyridine-3-carboxylic acid$)_3$(IMes)]Cl in the presence of Cs_2CO_3, complex in methanol-d_4 (0.6 mL) as a function of temperature. 129

Table 3.11 – Activation parameters for hydrogen loss of $[Ir(H)_2$(5-fluoropyridine-3-carboxylic acid$)_3$(IMes)]Cl in the presence of Cs_2CO_3 complex in methanol-d_4 (0.6 mL) using the experimental data from the 1D-EXSY experiments obtained using a 500 MHz Bruker NMR spectrometer. 129

Table 3.12 – Signal enhancement of hyperpolarised ^{19}F NMR when using 100 mM of the *N*-heterocyclic fluorinated compound, 5 mM of pre-catalyst [IrCl(COD)(IMes)] in 0.6 mL MeOD-d_4 in the presence of 4 bar of *p*-H_2 in conjunction with the INEPT sequence and the 'normal' single pulse sequence on a 500 MHz Bruker NMR. 132

Table 3.13 – Table comparing INEPT and direct ^{19}F and ^1H signal enhancements for all fluorinated *N*-heterocyclic compounds. 133

Table 3.14 – Comparison of the greatest ^1H T_1 in seconds and whether or not a further improved enhancement signal was obtained *via* the INEPT pulse sequence. 134

Table 4.1 – Table of sample formulations on the left. If there is a tick, then this and the volume given were used to make that sample. On the right hand side, the ^{13}C hyperpolarised signals of the solvents present, which were observed in the corresponding NMR spectra that were taken for each sample. If there is a blank, this means that the molecule was not added and therefore no signal should be seen. At G the SABRE catalyst was activated with the PEA before the substrate

was added. ^{13}C chemical shifts: *DMF = 162.60, 36.43, 31.31 ppm, $^{\#}$PEA = 139.93, 128.8, 128.4, 126.09, 43.60, 40.19 ppm, $^{\wedge}Na_2C_2O_4$ = 162.31 ppm. * = benzylamine was used, ** = NH_3 was used, $^{\#}$ = added after sample was activated, ⋆ = 1 µL was added, ⧫ = 30 µL used, $^{\sim}$ = 50:50 H_2O:D_2O. 167

Table 4.2 – Rate constants for elimination of H_2 and DMSO loss in [IrCl(H)$_2$(DMSO)$_2$(IMes)] in dichloromethane-d_2 or methanol-d_4 solution with temperature, obtained *via* selective 1D-EXSY experiments using a 500 MHz Bruker NMR spectrometer. 184

Table 4.3 – Activation parameters for ligand exchange in [IrCl(H)$_2$(DMSO)$_2$(IMes)] in dichloromethane-d_2 and methanol-d_4 solution. 185

Table 4.4 – Activation parameters for ligand exchange in [IrCl(H)$_2$(DMSO)$_2$(IMes)] in dichloromethane-d_2 after the addition of 2 x 15 µL portions of methanol. 186

Table 5.1 – Average NMR signal enhancements for ^{1}H and ^{13}C nuclei with 2-^{13}C- uracil (20 mM) dissolved in 0.3 mL DMF with [IrCl(COD)(IMes)] (5 mM) in DCM-d_2 (0.3 mL). The carrier is identified, along with its concentration. 200

Table 5.2 – ^{13}C and ^{15}N T_1 data for the carbon in the 2 position of uracil and both nitrogens using either ^{13}C-uracil (20 mM) or ^{13}C,$^{15}N_2$-uracil (20 mM) dissolved in 0.2 mL of DMF in the presence of [IrCl(COD)(IMes)] (5 mM), using NH_3 (45 mM) as the amine carrier in DCM-d_2 (0.4 mL) at 298 K with 4 bar of hydrogen. These values are determined at 9.4 T. 203

Table 7.1 – Table of optimised pulse length for ^{13}C for both 2-^{13}C-uracil and 2-^{13}C,$^{15}N_2$-uracil. 229

Table 7.2 – Table of optimised pulse length for ^{15}N for 2-^{13}C,$^{15}N_2$-uracil. 230

Table A.1 – The cell inputs used for the Excel spreadsheet to calculate the simulated rate data for the conversion of A to B, B to A and the loss of H_2 from B when the substrate used is pyrimidine. 239

Table A.2 – Least squared regression error for the experimental data obtained at 290 K for hydrogen exchange in the complex [Ir(H)$_2$(IMes)(pyrimidine)$_3$]Cl *via* the intermediate [IrCl(H)$_2$(IMes)(pyrimidine). 240

Table A.3 - Jack-knife error for the experimental data of the hydride exchange obtained at 290 K for [Ir(H)$_2$(IMes)(pyrimidine)$_3$]Cl *via* the intermediate [IrCl(H)$_2$(IMes)(pyrimidine)$_2$]. 241

Table A.4 – ^{1}H-NMR signal enhancements for the indicated resonances of pyrimidine achieved through [Ir(H)$_2$(IMes)(pyrimidine)$_3$]Cl (5 mM) in methanol-d_4 (0.6 mL) under 4 bar of *p*-H_2 as a function of substrate concentration at 298 K. 243

Table A.5 – Signal enhancements for the ^{1}H-NMR resonnces of pyrimidine as a function of [Ir(H)$_2$(IMes)(pyrimidine)$_3$]Cl concentration whilst maintaining a 1:40 catalyst :pyrimidine ratio in methanol-d_4 (0.6 mL) at 298 K.....244

Table A.6 – Average ^{1}H NMR signal enhancement factor for the indicated pyrimidine resonance as a function of catalyst. All samples contained 2.5 mM of catalyst and pyrimidine (25 mM) in methanol-d_4 (0.6 mL) with 4 bar *p*-H$_2$. Polarisation transfer was conducted at 65 G. Five experiments were conducted for statistical analysis.....244

Table A.7 – The cell inputs used for the Excel spreadsheet to calculate the simulated rate data for substrate exchange for the *tris* complex when the substrate is either 3-fluoropyridine or 5-fluoropyridine-3-carboxylic acid.....257

Table A.8 – Least squared regression error for data obtained at 280 K for the substrate exchange for the complex [Ir(H)$_2$(IMes)(sub)$_3$]Cl when the substrate is 3-fluoropyridine.....258

Table A.9 - Jack-knife error for the experimental data obtained for substrate exchange of the complex [Ir(H)$_2$(IMes)(sub)$_3$]Cl at 280 K where sub = 3-fluoropyridine.....259

Table A.10 - The cell inputs used for the Excel spreadsheet to calculate the simulated rate data for hydrogen exchange for the *tris* complex [Ir(H)$_2$(5-fluoropyridine-3-carboxylic acid)$_3$(IMes)]Cl in the presence of Cs_2CO_3. 261

Table A.11 - Least squared regression error for data obtained at 280 K for the hydride exchange for the complex [Ir(H)$_2$(IMes)(sub)$_3$]Cl when the substrate is 5-fluoropyridine-3-carboxylic acid in the presence of $CsCO_3$.....262

Table A.12 - Jack-knife error for the experimental data obtained for hydride exchange for the complex [Ir(H)$_2$(IMes)(sub)$_3$]Cl at 280 K where sub = 5-fluoropyridine-3-carboxylic acid in the presence of $CsCO_3$.....262

Table A.13 – The cell inputs used for the Excel spreadsheet to calculate the simulated rate data for hydride exchange for the *tris* complex, [Ir(H)$_2$(IMes)(sub)$_3$]Cl *via* the intermediate [Ir(H)$_2$(H$_2$)(IMes)(sub)$_2$], where the substrate is fluoropyrazine.....264

Table A.14 - The cell inputs used for the Excel spreadsheet to calculate the simulated rate data for hydride exchange for the intermediate complex [Ir(H)$_2$(H$_2$)(IMes)(sub)$_2$] to the *tris* complex, [Ir(H)$_2$(IMes)(sub)$_3$]Cl when the substrate is fluoropyrazine.....265

Table A.15 - Least squared regression error for data obtained at 265 K for the hydride exchange for the complex [Ir(H)$_2$(IMes)(sub)$_3$]Cl *via* interchange of A and B and the interchange of hydrides when the substrate is fluoropyrazine. 266

Table A.16 - Jack-knife error for the experimental data obtained for hydride exchange *via* interchange of A and B and the interchange of hydrides for the complex $[Ir(H)_2(IMes)(sub)_3]Cl$ at 265 K where sub = fluoropyrazine. 266

Table A.17 – Rate constants for the ligand exchange processes for 3-fluoropyridine (2), in methanol-d_4 as a function of temperature, results *via* selective 1D-EXSY experiments at 500 MHz. 268

Table A.18 – Rate constants for the ligand exchange processes for fluoropyrazine (5), in methanol-d_4 as a function of temperature, results *via* selective 1D-EXSY experiments at 500 MHz. 268

Table A.19 – Crystal data and structure refinement details for $[Ir_2(H)_4(DMSO)_2(IMes)_2(\mu\text{-oxalate})]$. 275

Table A.20 - The cell inputs used for the Excel spreadsheet to calculate the simulated rate data for the exchange of DMSO in complex G. 276

Table A.21 - Least squared regression error for data obtained at 268 K for the ligand exchange for the complex $[IrCl(H)_2(DMSO)_2(IMes)]$ in DCM-d_2 (0.6 mL). 278

Table A.22 - Jack-knife error for the experimental data obtained for ligand for the complex $[IrCl(H)_2(DMSO)_2(IMes)]$ in DCM-d_2 (0.6 mL) at 268 K. 278

Table A.23 - Least squared regression error for data obtained at 268 K for hydride exchange for the complex $[IrCl(H)_2(DMSO)_2(IMes)]$ in DCM-d_2 (0.6 mL). 280

Table A.24 - Jack-knife error for the experimental data obtained for hydride exchange for the complex $[IrCl(H)_2(DMSO)_2(IMes)]$ in DCM-d_2 (0.6 mL) at 268 K. 280

Table A.25 - Rate constants for elimination of H_2 and DMSO loss in $[IrCl(H)_2(DMSO)_2(IMes)]$ in dichloromethane-d_2 or methanol-d_4 solution with temperature, obtained *via* selective 1D-EXSY experiments using a 500 MHz Bruker NMR spectrometer. 281

Table A.26 - Activation parameters for ligand exchange in $[IrCl(H)_2(DMSO)_2(IMes)]$ in dichloromethane-d_2 and methanol-d_4 solution. 282

List of figures

Figure 1.1 – a) The population difference between the spin states when B_0 is zero and greater than zero, known as the Boltzmann distribution. $\boldsymbol{\alpha}$ is where the spins are aligned with the magnetic field and $\boldsymbol{\beta}$ is where they are aligned against the magnetic field. b) Population difference of the nuclear spin states of an AX spin system when both spins = ½. c) the corresponding NMR profile observed for this spin system under Boltzmann conditions.[10] 38

Figure 1.2 – Schematic showing the population distribution in the case of conventional NMR (left) and in a hyperpolarised case (right). 40

Figure 1.3 – Schematic diagram, adapted from reference 30 showing the dissolution-DNP method. [30] The sample is cooled using a liquid He bath to approximately 1-1.2 K where it is polarised using microwave irradiation. The sample is then rapidly thawed using a hot solvent to allow it to be transferred into the NMR spectrometer for detection. 43

Figure 1.4 – ^{13}C NMR spectra of urea taken from Ardenkjær-Larsen *et al*.[32] (A) ^{13}C hyperpolarised NMR spectrum using d-DNP of natural abundance urea, showing a polarisation of 20%. (B) Thermal NMR spectrum of ^{13}C for an equivalent sample of urea where the label is present at natural abundance; this multiple scan signal was averaged over 65 hours. 44

Figure 1.5 – The metabolic pathways of pyruvate in aerobic and anaerobic conditions. The formation of lactate occurs under aerobic conditions and is catalysed by lactate dehydrogenase. Under anaerobic conditions ethanol is formed instead in a process catalysed by pyruvate decarboxylase..... 45

Figure 1.6 – The four possible allowed spin states of dihydrogen.[89] 50

Figure 1.7 – a) the population diagram for an AX spin ½ system under PASADENA conditions. b) the corresponding NMR profile observed for this spin system under PASADENA conditions. 52

Figure 1.8 - a) the population diagram for an AX spin ½ system under ALTADENA conditions. b) the corresponding NMR profile observed for this spin system under ALTADENA conditions. 53

Figure 1.9 – SABRE mechanism for the exchange of *ortho*-hydrogen to *p*-H_2..... 53

Figure 1.10 – Transitions for an AX system under a) Boltzmann conditions and b) under SABRE conditions when *para*-hydrogen has been added and either chemical or magnetic inequivalence has occurred.[12, 103]..... 54

Figure 1.11 – Spectrum A-E are from figure 2 from the journal *Science*, 2009, 323, 1708-1711 from reference 13,[13] F and G are from figure 1 from the journal *J. Am. Chem. Soc.*, 2009, 131,

13362-13368 from reference 93.[93] A is the ^{1}H NMR of pyridine where the top spectrum is the thermally equilibrated NMR spectrum x128 vertical expansion to be observed here. The bottom spectrum is the corresponding 1 scan SABRE hyperpolarised spectrum, transfer carried out at 2 x 10^{-2} T. B is the ^{13}C{^{1}H} NMR of the same sample after refocusing. C is the ^{15}N SABRE polarised spectrum with refocusing. D is a hyperpolarised ^{1}H{^{13}C} NMR of nicotinamide, again after refocusing. E is the ^{1}H NMR spectrum of nicotinamide, top spectrum is the thermally equilibrated NMR spectrum x32 vertical expansion to be observed here. The bottom spectrum is the corresponding 1 scan SABRE hyperpolarised spectrum, transfer carried out at 0.5 x 10^{-4} T. F is the ^{1}H NMR of the hydride region of $[Ir(COD)(PPH_3)_2]BF_4$ with ^{15}N-pyridine, G is the corresponding ^{1}H{^{31}P} NMR spectrum. 56

Figure 1.12 – SABRE exchange pathway of hydrogen and substrate (sub) from the complex. . 59

Figure 1.13 – Molecules used to form ^{1}H long lived states. A is methyl-3-*d*-pyrazine-2-carboxylate, B is 3-d_3-methyl-6-methylpyridazine and C is 2-aminothiazole. The protons which have been highlighted and circled are the ^{1}H pair which formed the singlet state. 63

Figure 1.14 – Schematic of the flow system adapted from scheme 1 from ref. 147 with permission from The Journal of Physical Chemistry B within the supporting information (link https://pubs.acs.org/doi/abs/10.1021/jp511492q), further permissions related to the material excerpted should be directed to the ACS .[138, 147] 65

Figure 1.15 – Structure of three water soluble SABRE catalysts. A is an activated SABRE catalyst with a hydrophilic arylsulfoxanate group attached.[151] Both B and C are SABRE pre-catalysts, B is an example of a diol group added to the COD ligand[152] and C is [IrCl(COD)(IDEG)].[153] 67

Figure 1.16 – Diagram of the CASH-SABRE system, whereby the lower, organic layer is where the catalysis takes place and the top layer is the inorganic layer where the hyperpolarised substrate is and can be extracted. Adapted from figure 9 from the journal *Angew. Chem.,* 2018, 57, 6742-6753 from reference 117.[117] 68

Figure 1.17 – Graphical abstract adapted from the journal *J. Am. Chem. Soc.* 2014, 136, 7, 2695-2698 from reference 159 showing the use of the co-ligand 1-methyl-1,2,3-triazole (*mtz*) to hyperpolarise pyridine (py). [159] 70

Figure 1.18 – From figure 3 in reference 167 published by The Royal Society of Chemistry, the ^{1}H and ^{13}C hyperpolarised spectrum and corresponding spectrum taken under Boltzmann conditions for 2A are shown. The corresponding complexes when either pyridine (3A) or imidazole (4A) are added to 2A, and their ^{1}H and ^{13}C hyperpolarised and thermally equilibrated spectra are also shown.[167] 72

Figure 1.19 – Mechanism of SABRE-Relay. The hyperpolarised amine exchanges into solution. The labile proton on the amine then exchanges onto the substrate. Transfer of hyperpolarisation

into the substrate then proceeds *via* the *J*-coupling network to the amine, the labile proton then exchanges with that of the one on the substrate. 73

Figure 1.20 – Figure 1 from the journal *Sci Adv*, 2018, 4, eaao6250 *J*, reference 168. (A) ^{1}H NMR of [Ir(H)$_2$(IMes)(NH$_3$)$_3$]Cl taken under Boltzmann conditions at 298 K, a vertical expansion of x128 has been applied. (B) The corresponding ^{1}H SABRE hyperpolarised NMR spectrum.[168] 73

Figure 1.21 – Figure 4 from reference 169 published by The Royal Society of Chemistry. (a) to (c) are ^{13}C NMR spectra. (d) are the different isotopically labelled glucose molecules used along with their T_1 values. (a) –is using $_{D}$-glucose-1-^{13}C$_1$-d_1 the top is a ^{13}C{^{1}H} NMR spectrum, bottom is a ^{13}C NMR spectrum, both at 9.4 T. (b) – is the corresponding ^{13}C NMR (top) and ^{13}C{^{1}H} NMR spectrum of $_{D}$-glucose-1-^{13}C$_1$-d_1 (bottom) at 1 T and (c) – is of $_{D}$-glucose-1,2-^{13}C$_2$ top is a 1 scan SABRE-Relay hyperpolarised ^{13}C spectrum, bottom is a thermally equilibrated ^{13}C spectrum, acquired with 900 scans (x 100 for observation) at 1 T.[169] 74

Figure 2.1 - Structures of the DNA and RNA nucleobases cytosine, thymine and uracil and pyrimidine along with two commercially available drugs based upon the pyrimidine motif, Cidofovir and Trimethoprim. 77

Figure 2.2 – ^{1}H NMR spectra of pyrimidine (20 mM), [IrCl(COD)(IMes)] (5 mM). Top is a 1 scan thermally equilibrated spectrum which was left in the NMR for two minutes prior to acquisition (x32 vertical scale). Bottom is a 1 scan ^{1}H SABRE hyperpolarised spectrum of pyrimidine after polarisation transfer at 65 G. 78

Figure 2.3 – Proposed mechanism of formation of the active SABRE catalyst resulting from the reaction of [IrCl(COD)(IMes)] and pyrimidine in the presence of H$_2$. 79

Figure 2.4 – 1 scan ^{1}H NMR spectra demonstrating the change in complexes that occurs during SABRE, the vertical scale has been expanded 256 times in order to make these resonances visible. Top reflects the intermediate [Ir(COD)(IMes)(pyrimidine)]Cl, middle [Ir(H)$_2$(COD)(IMes)(pyrimidine)]Cl intermediate, and bottom the SABRE active complex, [Ir(H)$_2$(IMes)(pyrimidine)$_3$]Cl. Only pyrimidine and hydride areas have been shown here. 80

Figure 2.5 - Proposed mechanism for hydrogen exchange in the complex [Ir(H)$_2$(IMes)(pyrimidine)$_3$]Cl. 81

Figure 2.6 – ^{1}H NMR spectra of [Ir(H)$_2$(IMes)(pyrimidine)$_3$]Cl resulting from the 1D EXSY protocol when the hydride resonance of the complex at δ −22.37 is selectively excited and observed at the mixing times 0.005 (bottom spectrum) and 0.1 seconds (top spectrum). 83

Figure 2.7 – A plot of the individual signal enhancements of the ^{1}H's on the free pyrimidine as a function of pyrimidine excess with [Ir(H)$_2$(IMes)(sub)$_3$]Cl (5 mM) catalyst in methanol-d_4 (0.6 mL) exposed to 4 bar of *p*-H$_2$ as a function of substrate concentration at 298 K. A minimum of 5

experiments was undertaken and an average enhancement was calculated for each substrate concentration, see Table A.4 in the Appendix. 87

Figure 2.8 – A plot of the specified ^{1}H NMR signal enhancements for free pyrimidine as a function of catalyst concentration. The ratio of the active catalyst: pyrimidine used was 1:40 in methanol-d_4 (0.6 mL). A minimum of 5 experiments was undertaken for each data point and an average enhancement was calculated for each catalyst concentration, see Table A.5 in Appendix. 89

Figure 2.9 – Catalysts, based on the [IrCl(COD)(IMes)] motif, used for the optimisation of the pyrimidine substrate. 90

Figure 2.10 – The average ^{1}H signal enhancement of each of hydrogen resonance on pyrimidine (25 mM) with catalysts 1-6 (2.5 mM) in methanol-d_4 (0.6 mL) when exposed to 4 bar *p*-H_2 at 298 K. Polarisation transfer was conducted at 65 G (for table of results see Table A.6 in Appendix). 91

Figure 2.11 – Pyrimidine molecule with labelled hydrogen positions. 92

Figure 2.12 – A schematic diagram of the slice used to take the FISP magnetic resonance (MR) image. 94

Figure 2.13 – MR images carried out on a 9.4 T Bruker NMR system (integrated micro 2.5 gradient set) using a one-shot 2D ^{1}H hyperpolarised MRI FISP sequence with TR = 600 ms, TE = 2 ms, FOV = 1.2*1.2 cm, matrix size = 64*64, NS = 1. Images of hyperpolarised pyrimidine (500 mM) in the presence of the pre-catalyst [IrCl(COD)(1,3-bis(4-tert-butyl)-2,6-dimethylphenyl)imidazol-2-ylidine)] (catalyst 2, 5 mM). FISP 2D images acquired as a function of time from the polarisation transfer step after 0.6-6.0 s, in 600 ms intervals. 96

Figure 2.14 – Low flip angle FISP [IrCl(COD)(1,3-bis(4-*tert*-butyl)-2,6-dimethylphenyl)imidazol-2-ylidine)] 97

Figure 3.1 - Fluorinated *N*-heterocyclic molecules used here for SABRE ^{1}H and ^{19}F hyperpolarisation experiments. Compound names: (1) 2-fluoropyridine, (2) 3-fluoropyridine, (3) 4-fluoropyridine, (4) 3,5-difluoropyridine, (5) fluoropyrazine, (6) and (7) 5-fluoropyridine-3-carboxylic acid without base and with, respectively and (8) is 5-fluorouracil. 103

Figure 3.2 – ^{1}H NMR spectra of 4-fluoropyridine recorded in the presence of HCl. Bottom is a 1 scan hyperpolarised ^{1}H SABRE response after polarisation transfer at 60 G, expanded 32x vertically relative to the upper spectrum in order to visualise resonances in the substrate. The corresponding thermally equilibrated spectrum (top) which was left in the NMR for 2 minutes prior to acquisition. 105

Figure 3.3 – Zwitterionic form of 5-fluoropyridine-3-carboxylic acid. 106

Figure 3.4 – ^{1}H NMR spectra of 20 mM 5-fluorouracil with 5 mM pre-catalyst [IrCl(COD)(IMes)] in the presence of 2.5 mM Cs_2CO_3. The top spectrum is the thermally equilibrated spectrum which was left in the NMR for two minutes prior to acquisition, with the vertical expansion increased by 16x relative to the lower trace; the bottom spectrum shows the 1 scan, SABRE hyperpolarised signal, immediately after activation under 4 bar *p*-H_2. It demonstrates that a polarised ^{1}H response is observed. 107

Figure 3.5 – ^{19}F NMR signal enhancement measured for the *N*-heterocyclic fluorinated compound at 20- and 100-mM concentrations, the light grey is 20 mM and dark grey represents the 100 mM. All samples contained 5 mM of pre-catalyst [IrCl(COD)(IMes)] in 0.6 mL methanol-d_4 and were exposed to 4 bar *p*-H_2. 111

Figure 3.6 – ^{19}F NMR spectra of 100 mM of 3-fluoropyridine with 5 mM pre-catalyst [IrCl(COD)(IMes)] in 0.6 mL methanol-d_4 in the presence of 4 bar *p*-H_2. The first NMR spectrum is the thermally equilibrated spectrum which was left in the NMR for two minutes prior to acquisition polarised measurement whose vertical expansion level has been increased x32 relative to the lower trace. The bottom NMR spectrum shows the SABRE result. The peak at approximately -124 ppm is the bound ^{19}F signal, the one at approximately -127.5 ppm is the free ^{19}F signal. 112

Figure 3.7 – ^{15}N / ^{1}H HMQC with a CNST2 of 8 Hz, for the sample [IrCl(COD)(IMes)]Cl (5 mM) with 3,5-difluoropyridine (100 mM) in methanol-d_4 (0.6 mL). 117

Figure 3.8 – COSY of the hydride region for the sample [IrCl(COD)(IMes)]Cl (5 mM) with 3,5-difluoropyridine (100 mM) in methanol-d_4 (0.6 mL). 118

Figure 3.9 – Proposed mechanism for ligand exchange in the complex $[Ir(H)_2(IMes)(sub)_3]Cl$. 120

Figure 3.10 – Reaction mechanism as demonstrated by Lloyd *et. al.* (2014), showing the possible H_2 loss pathways for 3-NHC, $[Ir(H_2(Pyridine)_3(NHC)]Cl$ involving a complex with ligand L which could be chloride or methanol.[111] 123

Figure 3.11 – Proposed mechanism for hydrogen exchange in the complex $[Ir(H)_2(IMes)(sub)_3]Cl$ where sub = 5-fluoropyridine-3-carboxylic acid in the presence of base. 128

Figure 3.12 – ^{19}F NMR spectra of fluoropyrazine (100 mM) and [IrCl(COD)(IMes)] (5 mM) in methanol-d_4 (0.6 mL). Top is the Boltzmann equilibrated ^{19}F signal, when the sample was left in the spectrometer for 2 minutes to fully equilibrate, before acquisition (4 times vertical expansion applied). Top is the ^{19}F SABRE response when polarisation transfer took place at approximately 60 G (8 times vertical expansion applied). The equatorial and axial responses have been highlighted for the *bis* and *tris* complexes as well as for free fluoropyrazine. 130

Figure 3.13 – INEPT pulse sequence adapted from NMR: The toolkit by Hore *et. al*.[11] 131

Figure 3.14 – Normalised SABRE signal enhancements of the individual ^{1}H nuclei for the 3-fluoropyridine as a function of polarisation transfer field in G. 135

Figure 3.15 – Normalised SABRE signal enhancements of the individual ^{1}H nuclei for the 3,5-difluoropyridine as a function of polarisation transfer field in G. 136

Figure 3.16 – Normalised SABRE enhancements of the individual ^{1}H nuclei for the fluoropyrazine as a function of polarisation transfer field in G. 136

Figure 3.17 – Normalised SABRE signal enhancements of the individual ^{1}H nuclei for the 5-fluoropyridine-3-carboxylic acid, without base as a function of polarisation transfer field in G. 137

Figure 3.18 – Normalised SABRE signal enhancements of the individual ^{1}H nuclei for the 5-fluoropyridine-3-carboxylic acid, with base as a function of polarisation transfer field in G... 137

Figure 3.19 – MR Images carried out on a 9.4 T Bruker NMR system (integrated micro 2.5 gradient set) using a one shot, 2D centric encoded Rapid Acquisition with Relaxation Enhancement (RARE) image sequence, with TR = 600 ms, TE = 4 ms, FOV = 40*40 mm, matrix size = 64*64 using a 40 mm dual tuned ^{1}H/^{19}F volume resonator. Non-boxed images have been acquired in Boltzmann equilibrium conditions, d1 = 30s, NS = 64. Images in a dotted box are hyperpolarised, d1 = 600 ms, NS = 1. Samples were 5 mM [IrCl(COD(IMes)] with 100 mM of the fluorinated *N*- heterocycle in 3 mL methanol-d_4. 139

Figure 3.20 – 5 mM [IrCl(COD)(IMes)] and 100 mM 5-fluorouracil in 3.0 mL methanol-d_4 exposed to 4 bar *p*-H_2. CSI image taken using a Magnetom Prisma 3 T MRI scanner (Siemens Healthcare, Erlangen, Germany). Using a flex-surface coil for the *r. f.* transmission/reception. The imaging parameters used were a matrix size 8*8, 512 spectral points, across a chemical shift range of δ 172, FOV = 20*20*3 cm with TE = 2.3 ms, TR = 200 ms with a flip angle = 5 deg. A) shows the thermal signal of the sample, b) shows a 1 scan hyperpolarised image, c) shows the thermal and the hyperpolarised spectra acquired. 140

Figure 4.1 – The urea cycle. Image adapted from L. Stryer Biochemistry textbook 1975 page 697.[43] 145

Figure 4.2 – Figure 6 from the journal *J. Magn. Reson. Imaging*, 2011, 33, 692-697 from reference 256. These are axial images of hyperpolarised ^{13}C-urea, as shown in green, and ^{13}C-lactate, as shown in red. These have been overlaid on a T_2 weighted ^{1}H image (grey) of a mouse liver combining the results from the experiments. An overlap of ^{13}C-urea and ^{13}C-lactate is given in yellow. (a) normal mouse (b) and (c) liver tumour mice. The same slice shown on the left and right. [256] 146

Figure 4.3 – Figure 6 from the journal *J. Cardio. Magn. Reson.,* 2017, 19, 46-57 from reference 192. The images show a series of enhanced cardiac perfusion covering the bolus passage in the left ventricle blood pool and myocardium. (a) uses conventional excitation of ^{13}C-urea (b) uses velocity-selective excitation of ^{13}C-urea and (c) is the ^{1}H gadolinium based contrast agent. The red arrow is the left anterior descending coronary artery. The red contour shows the left ventricle blood pool.[192] 147

Figure 4.4 – Figure 8 from the journal *J. Cardio. Magn. Reson.,* 2017, 19, 46-57 from reference 192. (a) hyperpolarised ^{13}C-urea velocity-excitation and (b) ^{1}H gadolinium based contrast agent. These are both stress perfusion images with septal infarction induced by permanent ligation of the distal anterior descending coronary artery. On the left is the sum over three time frames at the myocardial bolus peak. On the right are the perfusion curves for six AHA (American Heart Association) segments. The blue arrow shows the perfusion defect.[192]..... 147

Figure 4.5 – The structures of (a) monosodium dihydrogen phosphate (MSP) and (b) adenosine triphosphate (ATP)..... 150

Figure 4.6 – from figure 1 of reference 181 from the journal *J. Am. Chem. Soc.,* 2013, 135, 42120-2123 showing the ^{13}C NMR spectra of oxalic acid recorded at 9.4 T following dissolution (a) natural-abundance and (b) 99% $^{13}C_2$-enriched [$^{16}O_4$]-oxalic acid in a 1:1 mixture (by concentration) of $D_2{}^{16}O$:$D_2{}^{18}O$ at 30 °C. The ^{18}O isotopologues formed during acid-catalysed exchange resolve as separate peaks, due to the ^{18}O isotope shift. The width of each displayed region is 0.15 ppm (15 Hz), centred at 162.02 ppm (referenced to tetramethylsilane). [181]..... 151

Figure 4.7 – Mechanism of SABRE-Relay. The hyperpolarised amine exchanges into solution. The labile proton on the amine then exchanges onto the substrate. Transfer of hyperpolarisation into the substrate then proceeds *via* the *J*-coupling network to the amine, the labile proton then exchanges with that of the one on the substrate..... 152

Figure 4.8 – Scheme 1 from *Chem. Sci.,* 2019, 10, 7709-7717 published by The Royal Society of Chemistry from reference 242 showing the catalytic cycle for the hyperpolarisation of alcohols. The metal-amine complex is the one which allows polarisation to transfer from the *p*-H_2 to the amine. The hyperpolarised proton on the amine exchanges with the one on the alcohol.[242] 153

Figure 4.9 – ^{13}C NMR hyperpolarised spectra of ^{13}C,$^{15}N_2$-urea (20 mM) dissolved in 50:50 H_2O:D_2O (10 µL) using [IrCl(COD)(IMes)] (5 mM) as the SABRE pre-catalyst in DCM-d_2 (0.6 mL), 25 mM of benzylamine-d_7 gave a 832 ± 74-fold enhancement, 35 mM NH_3 gave a 5117 ± 536-fold enhancement..... 155

Figure 4.10 – ^{15}N NMR hyperpolarised spectra of ^{13}C,$^{15}N_2$-urea (20 mM) dissolved in 50:50 H_2O:D_2O (10 µL) using [IrCl(COD)(IMes)] (5 mM) as the SABRE pre-catalyst in DCM-d_2 (0.6 mL), (a) is when 25 mM of benzylamine-d_7 has been used as the amine carrier and produced an

SNR of 14 (b) is where 35 mM NH_3 has been used as the amine carrier and produced an SNR of 16. 156

Figure 4.11 – ^{13}C phantom MRI of the 100 mM ^{13}C-urea with 5 mM [IrCl(COD)(IMes)] and 25 mM benzylamine-d_7 in methanol-d_4 exposed to 4 bar *p*-H_2. CSI image taken using a Magnetom Prisma 3 T MRI scanner (Siemens Healthcare, Erlangen, Germany). Using a flex-surface coil for the *r. f.* transmission/reception. The imaging parameters used were a matrix size 8*8, 512 spectral points, FOV = 20*20*25 cm with TE = 2.3 ms, TR = 200 ms with a flip angle = 5 deg. (a) shows the ^{13}C thermal and hyperpolarised spectra acquired. (b) shows a 1 scan ^{13}C hyperpolarised image. 157

Figure 4.12 – ^{13}C phantom MRI of the 100 mM ^{13}C-urea with 5 mM [IrCl(COD)(IMes)] and 25 mM benzylamine-d_7 in methanol-d_4 exposed to 4 bar *p*-H_2. CSI image taken using a Magnetom Prisma 3 T MRI scanner (Siemens Healthcare, Erlangen, Germany). Using a flex-surface coil for the *r. f.* transmission/reception. The imaging parameters used were a matrix size 8*8, 512 spectral points, FOV = 20*20*25 cm with TE = 2.3 ms, TR = 200 ms with a flip angle = 5 deg. The image on the left shows a 1 scan ^{13}C hyperpolarised image of ^{13}C-urea. The image on the right is a 1 scan thermal recorded under Boltzmann conditions of the sample. 158

Figure 4.13 – ^{31}P NMR of MSP (50 mM) dissolved in H_2O (10 µL) with [IrCl(COD)(IMes)] (5 mM) and PEA (13 mM) in DCM-d_2 (0.6 mL) with 4 bar of *p*-H_2 at 65 G. Top is a 1 scan ^{31}P SABRE-Relay spectrum after polarisation transfer at 65 G, producing a signal enhancement of 66 ± 3-fold. Bottom is a 1 scan thermally equilibrated spectrum which was left in the NMR for 2 minutes prior to acquisition. 159

Figure 4.14 – Average signal enhancement and SNR of ^{31}P for varying concentrations of MSP dissolved in 40 µL H_2O with [IrCl(COD)(IMes)] (5 mM), PEA (13 mM) in DCM-d_2 (0.6 mL). 160

Figure 4.15 – Hyperpolarised ^{31}P NMR spectra of MSP (40 mM) dissolved in H_2O (40 µL) with [IrCl(COD)(IMes)] (5 mM) in DCM-d_2 (0.6 mL) and varying concentrations of the carrier amine, PEA. All samples were exposed to 4 bar of *p*-H_2, polarisation transfer was carried out at 60 G. All spectra were taken with a 9.4 T Bruker NMR. 161

Figure 4.16 – ^{31}P spectra of MSP (40 mM) dissolved in 40 µL H_2O with [IrCl(COD)(IMes)] (5 mM) in DCM-d_2 (0.6 mL), exposed to 4 bar *p*-H_2, using different amines. Polarisation transfer occurred at 60 G. Bottom is with PEA (15 mM), producing a signal enhancement of 33 ± 2 (SNR = 14 ± 2). Top is with NH_3 (15 mM), producing a signal enhancement of 136 ± 2 (SNR = 49 ± 8). 162

Figure 4.17 – Hyperpolarised ^{31}P NMR spectrum with MSP (40 mM) dissolved in either 100% H_2O (bottom spectrum, signal enhancement = 28 ± 2-fold), 50:50 H_2O:D_2O (middle spectrum,

signal enhancement = 94 ± 2-fold) or 100 % D_2O (top spectrum, signal enhancement = 45 ± 7-fold) with [IrCl(COD)(IMes)] (5 mM) and PEA (15 mM) in DCM-d_2 (0.6 mL). All experiments were conducted in the presence of 4 bar of *p*-H_2 at 65 G and observed with a 9.4 T Bruker NMR. 163

Figure 4.18 – ^{31}P NMR of ATP (20 mM) dissolved in H_2O (30 µL) with PEA (15 mM) and [IrCl(COD)(IMes)] (5 mM) in DCM-d_2 (0.6 mL). Top is a SABRE-Relay spectrum after polarisation transfer at 65 G. Bottom is a 1 scan thermally equilibrated spectrum which was left in the NMR for 2 minutes prior to acquisition. 164

Figure 4.19 – SABRE-Relay hyperpolarised ^{31}P spectra of ATP (20 mM), [IrCl(COD)(IMes)] (5 mM), PEA (15 mM) in DCM-d_2, polarisation transfer occurred at 60 G. Top is using 30 µL H_2O to dissolve ATP, bottom is using 10 µL H_2O to dissolve ATP. 165

Figure 4.20 – The chemical structures of pyruvic acid, oxalic acid and sodium oxalate..... 165

Figure 4.21 – Thermally equilibrated 1 scan, ^{1}H NMR spectrum which was left in the NMR for two minutes prior to acquisition, of the hydride region of sample C which contained [IrCl(COD)(IMes)] (5 mM), sodium oxalate (20 mM) dissolved in DMF (100 µL), PEA (45 mM), with an addition of 10 µL of H_2O in DCM-d_2 (0.5 mL) after sample activation. 168

Figure 4.22 – ^{13}C NMR spectrum of sample C containing [IrCl(COD)(IMes)] (5 mM), sodium oxalate (20 mM) dissolved in DMF (100 µL), PEA (45 mM) in DCM-d_2 (0.5 mL), with an addition of H_2O (10 µL) after sample activation. Bottom is a thermally equilibrated spectrum which was left in the NMR for two minutes prior to acquisition, both DMF and DCM-d_2 are observed. Top is a 1 scan hyperpolarised spectrum after polarisation transfer at 60 G, only the PEA is observed. The smaller two peaks within this spectrum are also from the PEA. 169

Figure 4.23 – ^{13}C NMR spectrum of hyperpolarised sodium oxalate (20 mM) using DMSO (20 mM) as a co-ligand with [IrCl(COD)(IMes)] (5 mM) in 0.6 mL methanol-d_4. Polarisation transfer was carried out in a mu metal shield and the spectrum was acquired using a 9.4 T Bruker NMR. 170

Figure 4.24 – A diagram of the splitting observed in an AB coupling system, this pattern is described as a 'roofing effect' 171

Figure 4.25 – ^{1}H-^{1}H COSY NMR spectrum used to aid hydride peak assignments for the products formed when [IrCl(COD)(IMes)], DMSO and pyruvate react with H_2. 173

Figure 4.26 – Adapted from figure 3 from *Chem. Sci.*, 2019, 10, 7709-7717 published by The Royal Society of Chemistry showing a single scan hyperpolarised SABRE ^{13}C NMR spectrum of $^{13}C_2$-labelled sodium pyruvate taken from reference 165.[165] 173

Figure 4.27 – Scheme 1 from *Chem. Sci.,* 2019, 10, 7709-7717 published by The Royal Society of Chemistry schematic drawings from reference 283 of a) metal oxalate complexes $M^{II}(C_2O_4).2H_2O$, b) oxalate ligands with Mn(II) in $[MnC_2O_4(H_2O)_2].H_2O$ and c) $Na_2Cu(C_2O_4)_2.2H_2O$ d) is $Na_2Cu(C_2O_4)_2.2H_2O$ with the respective K, Rb, Cs and NH_4 salts. 174

Figure 4.28 – Possible complexes of sodium oxalate bound into the iridium catalyst based upon the observations from pyruvate. 175

Figure 4.29 – Hyperpolarised ^1H NMR spectra of the hydride region of a sample of sodium oxalate (25 mM), DMSO (20 mM), [IrCl(COD)(IMes)] (5 mM) both NMR spectra were taken as a 1 scan. Top (a) was taken at 245 K, bottom (b) was taken at 298 K. 176

Figure 4.30 – ^{13}C hyperpolarised NMR of sodium oxalate (25 mM), DMSO (20 mM) and [IrCl(COD)(IMes)] (5 mM) exposed to 4 bar *p*-H_2 at 245 K. Polarisation transfer occurred in a mu metal shield..... 176

Figure 4.31 – ^1H NMR hyperpolarised spectra of the hydride region of a sample containing sodium oxalate (25 mM), DMSO and [IrCl(COD)(IMes)] (5 mM) in methanol-d_4 (0.6 mL) with 4 bar *p*-H_2 at 245 K. Top is with 10 mM DMSO and bottom is with 20 mM DMSO..... 177

Figure 4.32 – ^1H NMR spectrum of the hydride region of the dominant complex formed with $^{13}C_2$-sodium oxalate (20 mM), [IrCl(COD)(IMes)] (5 mM) and DMSO-d_6 (20 mM) exposed to 4 bar of H_2. The spectrum was taken after the sample was left in the spectrometer for two minutes prior to acquisition. Inset is the structure of this complex. 178

Figure 4.33 – ^{13}C NMR spectra of $^{13}C_2$-sodium oxalate (20 mM), [IrCl(COD)(IMes)] (5 mM) and DMSO (20 mM) in methanol-d_4 (0.6 mL). Top is from Figure 4.23, recorded at 298 K with a signal enhancement of 4012 ± 484-fold. Bottom was recorded after the sample had been at 245 K and then warmed to 298 K, this gave a signal enhancement of 750 ± 235-fold, the spectrum has been expanded x16. 178

Figure 4.34 – ^1H NMR spectra of the hydride region of samples of [IrCl(COD)(IMes)] (5 mM), $^{13}C_2$-sodium oxalate (25 mM) and DMSO under H_2 in DCM-d_2 (0.6 mL). Top shows the hydride region when the sample contained 10 mM DMSO. Bottom shows the hydride region when the concentration of DMSO was increased to 20 mM..... 180

Figure 4.35 – ^1H NMR of the sample of [IrCl(COD)(IMes)] (5 mM), DMSO (30 mM) and $^{13}C_2$-sodium oxalate (35 mM) dissolved in D_2O (0.4 mL) and of MeOD-d_4 (0.2 mL). The hydride region has been expanded x8 to be seen here. 181

Figure 4.36 – Structure of $[Ir_2(H)_4(DMSO)_2(IMes)_2(\mu\text{-oxalate})]$ determined by X-ray crystallography. For clarity any non-hydride hydrogens and any solvents have been omitted (see Appendix A.12). 182

Figure 4.37 – The reaction of Complex D with [Ir(H)$_2$(DMSO)(IMes)] to form the dimer illustrated in Figure 4.36, [Ir(H)$_2$(DMSO)(IMes)]$_2$(μ-oxalate). 182

Figure 4.38 – The mechanism of both DMSO and *p*-H$_2$ exchange for the complex [IrCl(H)$_2$(DMSO)$_2$(IMes)] follow a common first step. 183

Figure 4.39 – Rates of ligand loss in [IrCl(H)$_2$(DMSO)$_2$(IMes)] in dichloromethane-d_2 when the volume of DMSO is increased from 1.0 - 3.0 μL. The grey squares represent the rate of loss of DMSO and the red circles represent the rate of loss of hydrogen. 186

Figure 4.40 – Rate of ligand loss in [IrCl(H)$_2$(DMSO)$_2$(IMes)] in dichloromethane-d_2 as a function of pressure of hydrogen. The grey squares represent the rate of loss of DMSO while the red circles represent the rate of loss of hydrogen. 187

Figure 4.41 – SABRE-Relay hyperpolarised ^{1}H NMR of [IrCl(COD)(IMes)] (5 mM) with PEA (15 mM) in DCM-d_2 (0.6 mL). Top is of MSP (20 mM) dissolved in 40 μL H$_2$O. Bottom is of ATP dissolved in 40 μL H$_2$O. Expansion of both spectra between 0 - 2.5 ppm is of hyperpolarised H$_2$O. 188

Figure 5.1 – The nucleobases guanine, adenine, uracil, and cytosine alongside an RNA nucleotide containing ribose sugar, phosphate ester and uracil. 191

Figure 5.2 – Formation of thymidylate (TMP) and dihydrofolate from deoxyuridylate, (dUMP) and N^5-N^{10} methylenetetrahydrofolate *via* the enzyme thymidylate synthase (TS). 192

Figure 5.3 – The mechanism to blocking the methylation of TMP (thymidylate) with the incorporation of fluorouracil into the dUMP, to form F-dUMP (fluorodeoxyuridylate, suicide inhibitor). 193

Figure 5.4 – ^{1}H NMR spectra of unlabelled uracil (20 mM) with [IrCl(COD)(IMes)] (5 mM) and Cs$_2$CO$_3$ (10 mM) in methanol-d_4 (0.6 mL). Bottom, 1 scan SABRE hyperpolarised spectrum after polarisation transfer at 60 G. The corresponding thermally equilibrated spectrum which was left in the NMR for two minutes prior to acquisition is shown above. No hydride ligand signals were observed in either NMR spectrum, consequently this region is omitted. 195

Figure 5.5 – ^{1}H spectra of uracil (20 mM) in 0.2 mL DMF with [IrCl(COD)(IMes)] (5 mM) pre-catalyst and NH$_3$ (25 mM) in 0.4 mL DCM-d_2. Top, a 1 scan ^{13}C thermally equilibrated NMR spectrum which was left in the NMR spectrometer for two minutes prior to acquisition. Bottom, 1 scan SABRE-Relay hyperpolarised NMR spectrum after polarisation transfer at 60 G. The hyperpolarised spectrum has been increased (vertically) by 8 times relative to the thermal spectrum. 197

Figure 5.6 – ^{13}C NMR spectra of uracil (20 mM) in 0.2 mL DMF with [IrCl(COD)(IMes)] (5 mM) and NH$_3$ (25 mM) in 0.4 mL DCM-d_2. Top, 1 scan ^{13}C thermally equilibrated NMR

spectrum which was left in the NMR for two minutes prior to acquisition. Bottom, 1 scan SABRE-Relay hyperpolarised NMR spectrum after polarisation transfer at 60 G. Signal assignments are as shown in the inset structures. 198

Figure 5.7 – ^{15}N NMR spectra of uracil (20 mM) in 0.2 mL DMF with [IrCl(COD)(IMes)] (5mM) and NH_3 (25 mM) in 0.4 mL DCM-d_2. Top, 1 scan ^{15}N thermally equilibrated NMR spectrum which was left in the NMR for two minutes prior to acquisition. Bottom, 1 scan SABRE-Relay hyperpolarised NMR spectrum after polarisation transfer at 60 G. Inset is the structure of uracil and corresponding peak assignments. 199

Figure 5.8 – ^{15}N NMR spectra of the signal response when 2-^{13}C,^{15} N_2-uracil (20 mM) in 0.2 mL of DMF with benzylamine-d_7 (25 mM) and [IrCl(COD)(IMes)] (5 mM) in 0.4 mL of DCM-d_2 is examined. Top, the thermally equilibrated ^{15}N NMR spectrum. Bottom, the SABRE-Relay hyperpolarised ^{15}N NMR spectrum after polarisation transfer at 60 G. 201

Figure 5.9 – Hyperpolarised ^{13}C-nicotinamide CSI of the abdomen of a mouse with a PDX breast cell line tumour. A 32*32 interpolated 128*128 overlaid on a ^{1}H MRI scan. White/yellow colour shows the areas with the greatest hyperpolarised signal. 203

Figure 5.10 – ^{13}C NMR spectrum of the signal response when 5-fluorouracil (20 mM) in 0.2 mL of DMF with benzylamine-d_7 (25 mM) and [IrCl(COD)(IMes)] (5 mM) in 0.4 mL DCM-d_2. Top, thermally equilibrated (which was left in the NMR for two minutes prior to acquisition) ^{13}C NMR spectrum. Bottom, SABRE-Relay hyperpolarised ^{13}C NMR spectrum after polarisation transfer at 60 G. 204

Figure 5.11 – ^{19}F NMR spectra 5-fluorouracil (20 mM) in 0.3 mL DMF-d_7 with [IrCl(COD)(IMes)] (5 mM) and benzylamine-d_7 (25 mM) in 0.4 mL DCM-d_2. Top, 1 scan thermally equilibrated spectrum which was left in the NMR for two minutes prior to acquisition. Bottom, 1 scan SABRE-Relay hyperpolarised spectrum after polarisation transfer at 60 G. Inset structure of 5-fluorouracil..... 205

Figure 7.1 – Schematic of the activation mechanism of the SABRE pre-catalyst [IrCl(COD)(IMes)] with a substrate and excess hydrogen to form the SABRE active catalyst [Ir(H)$_2$(IMes)(Sub)$_3$)]Cl. 220

Figure 7.2 – Schematic of the flow system adapted from scheme 1 in reference 138. [138] 222

Figure 7.3 – Pulse sequence for the selective 1D NOESY experiment, otherwise known as an EXSY experiment..... 226

Figure 7.4 – (Top) A graphical description of the inversion recovery experiment to measure the spin-lattice relaxation times, T_1. Adapted from Nuclear magnetic resonance by P. J. Hore.[8] Bottom

the pulse sequence for the inversion recovery NMR experiment to determine T_1 adapted from M. Levitt's Spin Dynamics: Basics of nuclear magnetic resonance.[9] 227

Figure 7.5 – Pulse sequence for the saturation recovery NMR experiment to determine T_1 adapted from Bruker pulse sequence files where τ is the time delay. 228

Figure 7.6 – Pulse sequence for the hyperpolarised single shot T_1 experiment, using a variable flip angle where t_1 is the SABRE polarisation transfer time, t_2 is the NMR transfer time and Δt_n is the variable time delay. 230

Figure 7.7 – Mapping the changes which occur in nuclear spins during a spin echo sequence.231

Figure 7.8 – Spin-echo and RARE pulse sequences, where R.F. is the radio frequency, TE = echo time and TR = repetition time, demonstrating the multiple echoes which can be recorded with RARE. 232

Figure 7.9 – 2D CSI pulse sequence using step gradients to allow encoding of positional information..... 234

Figure A.1 – Structure of [Ir(COD)(IMes)(pyrimidine)]Cl. 235

Figure A.2 – Structure of $[Ir(H)_2(COD)(IMes)(pyrimidine)]Cl$. 236

Figure A.3 – Structure of $[Ir(H)_2(IMes)(pyrimidine)_3]Cl$. 237

Figure A.4 – Exchange pathway for hydrogen loss during the SABRE process with pyrimidine. 238

Figure A.5 – Simplified mechanism of hydrogen exchange within the SABRE process. 239

Figure A.6 – Experimental and simulated hydrogen exchange data for $[Ir(H)_2(IMes)(pyrimidine)_3]Cl$ at 290 K..... 241

Figure A.7 – Eyring plot of the conversion of complex A to B, the conversion of B to free hydrogen and the conversion of B back to A. The results of a linear regression analysis on each set of data is given in the plot in the same presentation colour..... 242

Figure A.8 – A plot of the individual signal enhancement of the ^1H resonances of the free substrate pyrimidine as a function of temperature. 245

Figure A.9 – ^1H NMR signal enhancement for H-2 of pyrimidine from as a function of temperature. 246

Figure A.10 – ^1H NMR signal enhancement for H-4, 6 of pyrimidine as a function of temperature. 246

Figure A.11 – ^1H NMR signal enhancement for H-5 of pyrimidine as a function of temperature. 247

Figure A.12 – Plot of magnetisation intensity at different delay times ($\boldsymbol{\tau}$) during an inversion recovery experiment in which the T_1 relaxation has been calculated for free pyrimidine (25 mM) in the presence of pre-catalyst [IrCl(COD)(1,3-bis(2,4,6-trimethylphenyl)-4,5-dichloroimidazol-2-ylidine)] (2.5 mM) and H_2 (4 bar) in methanol-d_4 (0.6 mL). From this the T_1 relaxation time was calculated using equation A.3. 248

Figure A.13 – A plot of the magnetisation decay at varying time delays, τ for ^{19}F of free 5-fluoropyridine-3-carboxylic acid in the presence of Cs_2CO_3 and the SABRE pre-catalyst [IrCl(COD)(IMes)]. From this the T_1 relaxation time was calculated using equation A.3. 249

Figure A.14 – Structure of $[Ir(H)_2(IMes)(3\text{-fluoropyridine})_3]Cl$ complex. 249

Figure A.15 – Structure of $[Ir(H)_2(3,5\text{-difluoropyridine})_3(IMes)]Cl$ complex. 250

Figure A.16 – Structure of $[Ir(H)_2(fluoropyrazine)_3(IMes)]Cl$ complex. 251

Figure A.17 – Structure of $[Ir(H)_2(5\text{-fluoro-3-carboxylic acid})_3(IMes)]Cl$ complex. 252

Figure A.18 – Structure of $[Ir(H)_2(5\text{-fluoro-3-carboxylic acid})_3(IMes)]Cl$, in the presence of Cs_2CO_3. 253

Figure A.19 – Structure of $[IrCl(H)_2(3,5\text{-difluoropyridine})_2(IMes)]$ complex. 254

Figure A.20 – Structure of $[IrCl(H)_2(fluoropyrazine)_3(IMes)]$ complex. 255

Figure A.21 – Exchange pathway for substrate loss for $[Ir(H)_2(sub)(IMes)]Cl$ during the SABRE process where the substrate is 3-fluoropyridine or 5-fluoropyridine-3-carboxylic acid in the presence of base. 256

Figure A.22 – Showing the experimental and simulated change in percentage abundance of the free and bound substrate 3-fluoropyridine at 280 K. Simulated data was achieved using the formula given in equations A.4 to A.10. 258

Figure A.23 – Eyring plots for the loss of 3-fluoropyridine or 5-fluoropyridine-3-carboxylic acid in the presence of base, from $[Ir(H)_2(IMes)(sub)_3]Cl$. These data were then used to calculate the activation parameters for ligand exchange. The linear regression analysis results are also presented. 259

Figure A.24 - Hydride ligand exchange mechanism for $[Ir(H)_2(DMSO)_3(IMes)]$. To examine this mechanism, the loss of both hydride and DMSO was investigated *via* the 1D EXSY protocol. 260

Figure A.25 – The experimental and simulated change in percentage abundance of free hydrogen and bound hydride in the complex $[Ir(H)_2(5\text{-fluoropyridine-3-carboxylic acid})_3(IMes)]$ in the presence of Cs_2CO_3 in methanol-d_4 (0.6 mL) at 280 K. Simulated data was achieved using the formula given in equations A.11 to A.13. 261

Figure A.26 – Eyring plot for the loss of H_2 from[$Ir(H)_2$(5-fluoropyridine-3-carboxylic acid)$_3$(IMes)]Cl in the presence of Cs_2CO_3. These data were used to calculate the activation parameters for H_2 loss. 263

Figure A.27 – Proposed hydride exchange mechanism of the SABRE experiment with substrates 2 to 6, including the complex [$IrCl(H)_2$(IMes)$(sub)_2$]..... 264

Figure A.28 – Showing the experimental and simulated change in percentage abundance of the free and bound hydride resonances of fluoropyrazine at 265 K. Simulated data was achieved using the formula given in equations A.1 and A.2. 265

Figure A.29 – Eyring plot of the conversion of complex A to B, the conversion of B to free hydrogen and the conversion of B back to A for the substrate 3,5-difluoropyridine. This plot was then used to calculate the activation parameters for each of these pathways. The linear regression analysis for each process is given in the same colour as that shown in the plot. 267

Figure A.30 – PTF plots of 3-fluorpyridine (500 mM) and [IrCl(COD)(IMes)] (25 mM) in methanol-d_4. A) is examining magnetic fields 1-14 mT (0-140 G) and B) is examining magnetic fields 0-1 mT (0-1 G). 269

Figure A.31 – PTF plots of 3,5-difluorpyridine (500 mM) and [IrCl(COD)(IMes)] (25 mM) in methanol-d_4. A) is examining magnetic fields 1-14 mT (0-140 G) and B) is examining magnetic fields 0-1 mT (0-1 G). 269

Figure A.32 – PTF plots of fluoropyrazine (500 mM) and [IrCl(COD)(IMes)] (25 mM) in methanol-d_4 examining magnetic fields 1-14 mT (0-140 G). 270

Figure A.33 – Structure of [$IrCl(H)_2(DMSO)_2$(IMes)] complex. 270

Figure A.34 – Structure of [$IrCl(H)_2(DMSO)_2$(IMes)]. 271

Figure A.35 – Structure of [$IrCl(H)_2$(IMes)$(PhMeSO)_2$)] complex. 272

Figure A.36 – Structure of [$IrCl(H)_2$(IMes)$(PhMeSO)_2$] complex. 273

Figure A.37 – Structure of [$Ir_2(H)_4(DMSO)_2(IMes)_2$(μ-oxalate)]..... 274

Figure A.38 – Loss and gain of DMSO from [$IrCl(H)_2(DMSO)_2$(IMes)] (G). 276

Figure A.39 – Showing the experimental and simulated change in percentage abundance of free and bound DMSO in complex G at 268 K in DCM-d_2. Simulated data was achieved using the formula given in equations A.14 and A.15. 277

Figure A. 40 - Showing the experimental and simulated change in percentage abundance of free and bound DMSO in complex G at 258 K in DCM-d_2. Simulated data was achieved using the formula given in equations A.14 and A.15, without T_1. 277

Figure A.41 – Showing the experimental and simulated change in percentage abundance of free and bound hydrogen in complex G at 268 K in DCM-d_2. Simulated data was achieved using the formula given in equations A.11 to A.13. 279

Figure A.42 – Eyring plot for the loss of either DMSO or hydride in complex [IrCl(H)$_2$(DMSO)$_2$(IMes)]. This plot was then used to calculate the activation parameters for each of these ligands. The linear regression analysis for each ligand is given in the same colour as that shown in the plot. 281

Figure A.43 – A plot of the magnetisation decay at varying time delays, τ based on the variable flip angles calculated, for ^{13}C of free ^{13}C-uracil when in the presence of the SABRE pre-catalyst [IrCl(COD)(IMes)]. From this the T_1 relaxation time was calculated using equation A.16..... 283

Figure A.44 - A plot of the magnetisation decay at varying time delays, τ based on the variable flip angles calculated, for ^{15}N of free ^{13}C,^{15}N$_2$-uracil when in the presence of the SABRE pre-catalyst [IrCl(COD)(IMes)]. From this the T_1 relaxation time was calculated using equation A.16. 283

Acknowledgements

This journey would not have started had it not been for the people who encouraged me to apply for this PhD, thank you Nichola Robertshaw, Jamie Purdie and Mark Dawson. Without you I would not be where I am today.

I would like to thank my supervisor, Prof. Simon Duckett for giving me the opportunity to carry out this PhD and the chance to be part of the Marie Curie Horizon 2020 Europol ITN Hyperpolarisation network.

To the CHyM group and friends, I am indebted to you all for getting me through every aspect of the last four years, the cups of tea, quiz nights, walks around campus, the Yorkshire countryside, pub quizzes and nights out and of course the laughter. Without these I would not have made it through, thank you, Emma, Rhianna, Robin, Olga, Liz, Kate, Amy, Will, Chris, Ben, Alastair, Phil, Barby and Aminata. I must also thank those who have rung me when I have been fed up and despondent with everything and kept me going; thank you Liz and Emma.

I would also like to extend a huge thanks to the Postdocs in the group. Dr. Alexandra Olaru for taking me under her wing, showing me the ropes and pushing me to get work published. Dr Pete Rayner for all the synthesis of compounds and catalysts, I can't thank you enough, we know how good my synthesis skills are! Also, for reading my work, far above the call of duty, thank you.

Dr. Aneurin Kennerley, thank you for all your time and patience with my written work and for your help in collecting, analysing and preparing the MRI figures.

Without the support of the technical staff within the Chemistry Department and CHyM this research would have been very hard to collect. Thank you to Vicky and Rich for all your technical support and help and Adrian Whitwood for solving my crystal structure.

The biggest of thank yous goes to my boyfriend and partner in crime, Dr Pete Richardson, without your encouragement and constant belief in me, this would have been a lot harder than it was. Thank you too for reading chapters and quizzing me, even when I just wanted to give up! Finally, my family, thank you. For giving me distractions when I needed them and a push when necessary!

Declaration

I declare that this thesis is a presentation of original work and I am the sole author. This work has not previously been presented for an award at this, or any other, University. All sources are acknowledged as References.

Some work presented in this thesis has been previously published in peer-reviewed articles of which I am an author:

A. M. Olaru, T. B. R. Robertson, J. S. Lewis, A. Antony, W. Iali, R. E. Mewis and S. B. Duckett, ChemistryOpen., 2018, **7**, 97-105

B. J. Tickner, J. S. Lewis, R. O. John, A. C. Whitwood and S. B. Duckett, *Dalton Transactions*, 2019, **48**, 15198-15206.

Chapter 1: Introduction

1.1 Nuclear magnetic resonance

Nuclear Magnetic Resonance (NMR) is an information rich spectroscopic method used to analyse chemical compounds. NMR has a vast array of applications that can give detailed information on parameters such as structural information,[1] chemical exchange[2] or conformation[3, 4] and can help to understand reaction dynamics.[5, 6] Additionally, NMR can be used to image, under the aptly named magnetic resonance imaging (MRI), and is routinely used in medicine as a powerful non-invasive diagnostic tool.[7]

NMR and MRI rely on the fact that all protons and neutrons have a quantum mechanical intrinsic property; often termed 'spin'.[8] Each nucleus has a spin quantum number that is dependent on the makeup of the nucleus in question, with the simplest of these being a hydrogen nucleus. For a nucleus to be NMR active, the presence of a non-zero spin order is required.[9] Typically, if a nucleus has an even mass number then the spin parameter will be an integer and an odd mass number leads to a half-integer value of spin. However, the spin number is readily known and easily obtained for all elements. If the number of protons and neutrons are both even, then the nucleus will display a spin of zero and will be NMR silent.[10] This is the case for ^{12}C, which has a zero spin value however, its isotope, ^{13}C, has a spin value of ½ and is widely used for NMR and MRI despite its low natural abundance.

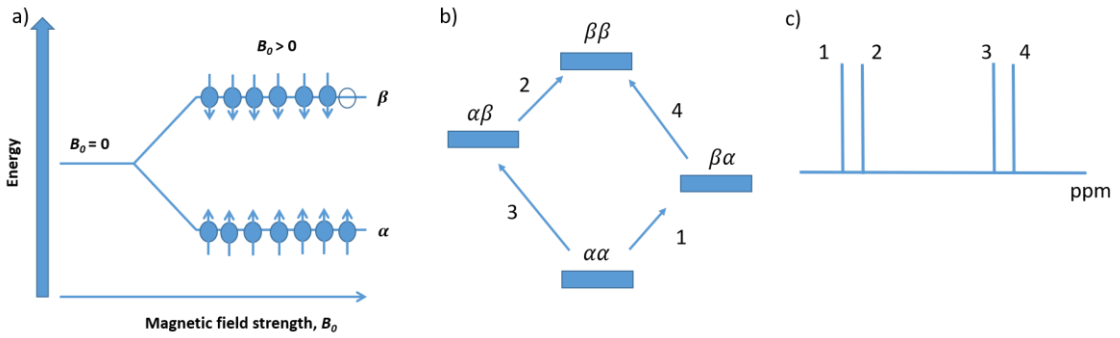

Figure 1.1 – a) The population difference between the spin states when B_0 is zero and greater than zero, known as the Boltzmann distribution. α is where the spins are aligned with the magnetic field and β is where they are aligned against the magnetic field. b) Population difference of the nuclear spin states of an AX spin system when both spins = ½. c) the corresponding NMR profile observed for this spin system under Boltzmann conditions.[10]

The spin value dictates the number of quantum mechanical states that the spins can occupy, which is defined as $2I + 1$, where I is the spin quantum number. Therefore, a spin ½ nucleus has two possible spin states which it can occupy.[10]

The two spin states for a spin-½ system are usually denoted α and β to represent spins aligned with and against the magnetic field respectively. In the absence of a static magnetic field, the two spin states are degenerate. The application of a magnetic field (B_0) causes Zeeman splitting resulting in the two states having different energy levels, as shown in Figure 1.1a), with the lower energy level belonging to the spins aligned with the magnetic field. The states are occupied according to the Boltzmann distribution, therefore there is a slight excess of spins in the lower energy state (α). The discrete energy values (E_M) for the states can be expressed in terms of the dot product of magnetic moment ($\overrightarrow{\mu}$) and magnetic field ($\overrightarrow{B_0}$), as in equation 1.1.[9]

$$E_M = -\overrightarrow{\mu}.\overrightarrow{B_0} \qquad (1.1)$$

Equation 1.1 states that the direction of the magnetic moment is dependent on the external magnetic field. The static magnetic field of an NMR spectrometer is produced by a superconducting solenoid, which generates a highly directional magnetic field along the z-axis.

The magnetic moment in the z-direction is defined in terms of the gyromagnetic ratio (γ), which is the constant of proportionality between the resonant frequency and static magnetic field, a spin quantum number (m) and reduced Planck's constant (ħ) as shown in equation 1.2.[9]

$$\mu_z = \gamma \hbar m \qquad (1.2)$$

The possible values that m can take is defined by the spin number and are integers in the form $m = -I, -I + 1 \ldots, I$. Therefore, for the spin ½ nucleus there are only two possible values of m; −½ and ½. It is therefore possible to determine the energy equations for each state (E_α and E_β) and for the energy difference between the two levels (ΔE) by combining equations 1.1 and 1.2 as shown in equations 1.3-1.5.[9-11]

$$E_\alpha = -\frac{1}{2}\gamma \hbar B_z \qquad (1.3)$$

$$E_\beta = +\frac{1}{2}\gamma \hbar B_z \qquad (1.4)$$

$$\Delta E = E_\beta - E_\alpha = \gamma \hbar B_z \qquad (1.5)$$

Now that the energy difference is known between these discrete energy levels, this can be related to the frequency (f) using the classical equation expressed in equation 1.6, where h is Planck's constant.[9-11]

$$E = hf = \frac{h\omega_0}{2\pi} = \hbar\omega_0 \qquad (1.6)$$

Since the angular frequency (ω_0) is defined as the frequency divided by 2π and subsequently h divided by 2π is reduced Planck's constant. Therefore, by combining equations 1.5 and 1.6 and rearranging for the angular frequency can be defined (equation 1.7).[9-11]

$$\omega_0 = -\gamma B_0 \qquad (1.7)$$

This equation defines the Larmor frequency, which is the fundamental equation of NMR and links the static magnetic field strength with the resonant frequency of the nucleus of interest. The gyromagnetic ratio is unique for each NMR active nucleus. This adds to the power of NMR as a

technique, as the use of specific radio frequency pulses (*r. f.*) only selective elements will be excited at any one time.[9-11]

Since the two spin states are in direct opposition with each other they mostly cancel out, however, the spins aligned with the magnetic field have a lower energy and thus a slight population imbalance occurs. The ratio of the populations in the α (n_α) and β (n_β) states can be defined by the Boltzmann distribution in the form of equation (1.8).[9, 11]

$$\frac{n_\beta}{n_\alpha} = exp\left[\frac{-\Delta E}{k_B T}\right] = exp\left[\frac{-\gamma \hbar B_0}{k_B T}\right] \qquad (1.8)$$

Equation 1.8 can be rewritten, using the Taylor expansion, to express the percentage of excess spins between the states as shown in equation 1.9.[9, 11]

$$P_0 = \frac{\gamma B_0 \hbar}{2 k_B T} \qquad (1.9)$$

Where P_0 is polarisation and k_B is the Boltzmann constant.

Both NMR and MRI, are considered insensitive due to the very small population difference within their energy levels, based on the Boltzmann distribution.[8] If the polarisation is calculated for a ^{1}H nucleus at 295 K in a 9.4 T (400 MHz) field, then there is an excess of only 33 nuclei in every million in the ground state which demonstrates the insensitivity of NMR.

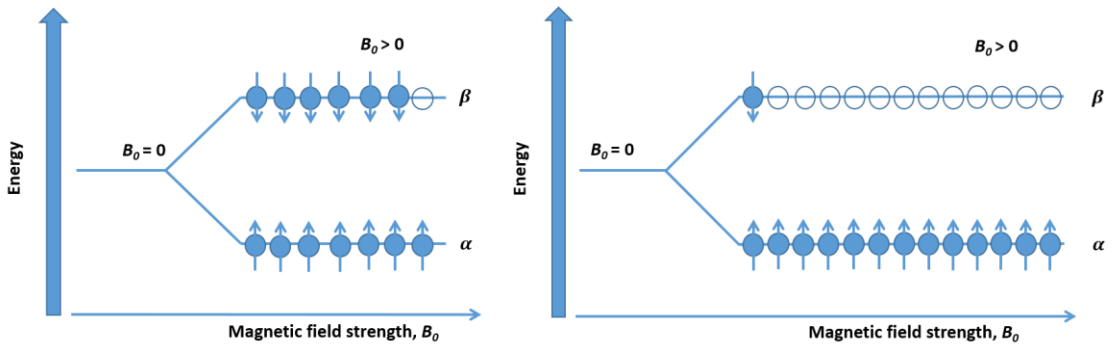

Figure 1.2 – Schematic showing the population distribution in the case of conventional NMR (left) and in a hyperpolarised case (right).

Many scientists are trying to improve this sensitivity issue by using hyperpolarisation, which is defined as any significant deviation from the Boltzmann distribution that greatly increases signal

intensity. There are several ways in which hyperpolarisation can be achieved, including; brute force, optical pumping, dynamic nuclear polarisation (DNP) and *para*-hydrogen induced polarisation (PHIP).[12-16]

1.2 Hyperpolarisation methods

1.2.1 Brute force

First described by Gorter in 1934,[17] brute force is perhaps the simplest hyperpolarisation method, however, several years of development were required before brute-force hyperpolarisation became a more well-known technique.[18, 19] In this method of hyperpolarisation, the sample is initially placed in a higher magnetic field than that in which it will be detected.[20] The initial high magnetic field increases the energy difference between states and therefore increases the population difference which results in a higher NMR signal being obtained. In some brute-force experiments, the substrate is polarised not only at higher magnetic fields but also at low temperatures, which also increases the signal due to less movement between states at lower temperatures.[20] This method therefore exploits the polarisation through either magnetic field or temperature, or a combination of both. The drawback is that the polarisation is linearly dependent on the magnetic field strength and inversely proportional to temperature. Therefore, in order to double the polarisation, the temperature would have to be halved or the magnetic field doubled. Consequently, this form of hyperpolarisation is limited, as increasing the magnetic field and decreasing temperature are both finite changes and subsequently can only offer minor gain in signal through the manipulation of the polarisation. Recently Hirsch *et. al.* (2015) used this method to hyperpolarise 1-^{13}C-pyruvate, 1-^{13}C-sodium lactate and 1-^{13}C-acetic acid, where ^{13}C signal enhancements of over 1500 were reported.[21] Although less than that obtained using other hyperpolarisation methods, this signal gain is noteworthy due to the simplicity of this method and that these signals could be used in applications such as the analysis of compounds and mixtures.[21]

1.2.2 Spin-exchange optical pumping (SEOP)

Optical pumping was first theorised and developed during the 1950s by Kastler and uses polarised light to move electrons from a lower energy state to a higher one.[22, 23] One of the most effective

uses of optical pumping is within helium and xenon to produce enhanced magnetic resonance images (MRI) in lungs after inhalation of the gas. The first hyperpolarised images using this technique with hyperpolarised helium, were published by two groups: Albert *et. al.* (imaging mouse lungs)[24] and Middleton *et. al.* (imaging guinea pig lungs).[25] Helium nuclei were initially utilised due to its higher gyromagnetic ratio compared to xenon but, more recently, an increase in cost has led to xenon imaging becoming more favourable.[26] Xenon based SEOP has now been developed for use by medical professionals in hospitals around the world, particularly with patients suffering from asthma or chronic obstructive pulmonary disease (COPD).[27]

1.2.3 Dynamic Nuclear Polarisation (DNP)

Dynamic Nuclear Polarisation (DNP) was first theorised in metal nuclei by Overhauser in 1953.[28] It was proposed that if a metallic sample was placed into a magnetic field and subsequently irradiated with a microwave frequency that meets the electron spin resonance condition in the presence of a radical then the electron spin magnetic moment and the nuclear spin magnetic moment would interact. This results in a transfer of spin population between them. The populations within the energy levels are now in a non-equilibrium state, as described by equation 1.10.[29]

$$\epsilon = \frac{\langle I_z \rangle}{I_0} = 1 - \xi \cdot f \cdot s \frac{|\gamma_e|}{\gamma_n} \qquad (1.10)$$

Where ε is the enhancement factor, I_z is the nuclear polarisation, I_0 is Boltzmann equilibrium value for the nuclear spin system, ξ is the coupling factor, f is the leakage factor and s the saturation factor. This corresponds to creating magnetic polarisation in the sample, which can produce a hyperpolarised signal when examined.[30] This hypothesis was proven by Carver and Slichter in the same year,[31] and the process is now known as Overhauser-DNP (O-DNP). There are challenges with O-DNP associated with sample heating due to the microwave irradiation step and hence performing this experiment on biologically relevant molecules can be problematic.

In 2003, Ardenkjær-Larsen *et. al.* reported a new method known as dissolution-DNP (d-DNP) whereby a substrate is dissolved with a free radical prior to polarisation in a magnetic field by

microwave irradiation at a frequency which excites the electron in the radical at low temperature (~1.2 K). Subsequently, the frozen sample is rapidly melted using hot water and transferred to the NMR for detection. Figure 1.3 shows a typical schematic of the experiment.

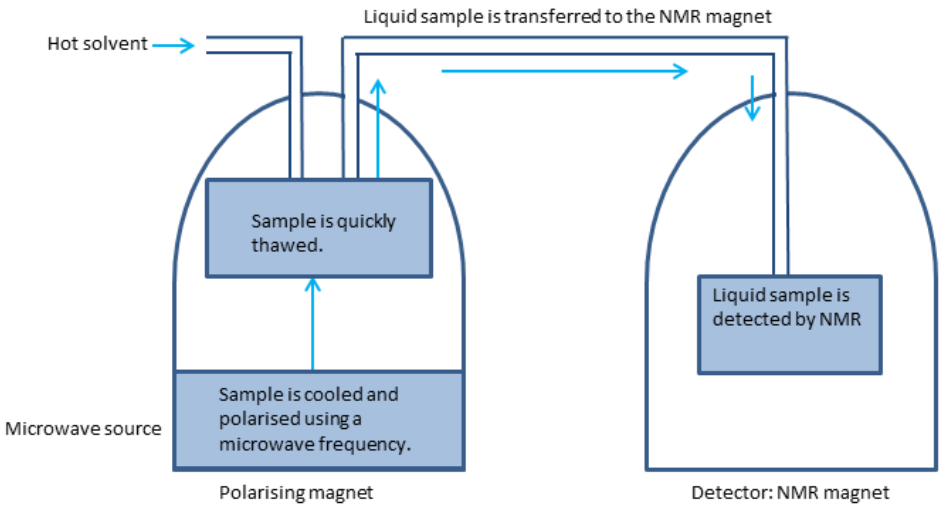

Figure 1.3 – Schematic diagram, adapted from reference 30 showing the dissolution-DNP method. [30] The sample is cooled using a liquid He bath to approximately 1-1.2 K where it is polarised using microwave irradiation. The sample is then rapidly thawed using a hot solvent to allow it to be transferred into the NMR spectrometer for detection.

In the early report, ^{13}C-urea was dissolved in glycerol and OXO63 was the trityl radical used which resulted in a 42% ^{13}C polarisation level after a build-up time of approximately 82 minutes within the polarising magnet. Due to relaxation effects within the sample, they observed 37% polarisation of the ^{13}C nuclei within the NMR spectrum.[32] Therefore, the transfer of the sample between polarisation and detection needs to be carried out quickly to reduce this effect. Nonetheless, this represents a significant enhancement which is a result of the low temperature associated with DNP, as described by equation 1.11.[29]

$$\varepsilon' = \varepsilon . \frac{B_{\mathrm{DNP}}}{B_{\mathrm{NMR}}} . \frac{T_{\mathrm{NMR}}}{T_{DNP}} \qquad (1.11)$$

Where ε' is the overall enhancement, ε is the actual DNP enhancement, *B* is the Boltzmann distribution for ^{13}C in the NMR and the electron in DNP as stated in the equation and *T* is the temperature at which the DNP or NMR process was performed. An example of this large

polarisation is shown in Figure 1.4 where a hyperpolarised ^{13}C NMR of natural abundance urea is compared to that of its thermally equilibrated NMR signal, acquired over 65 hours.

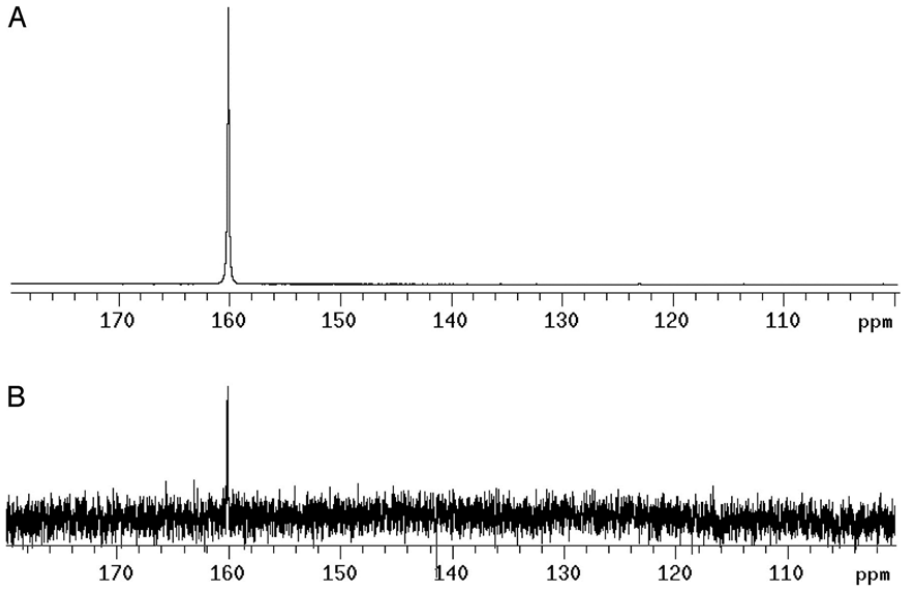

Figure 1.4 – ^{13}C NMR spectra of urea taken from Ardenkjær-Larsen *et al.*[32] (A) ^{13}C hyperpolarised NMR spectrum using d-DNP of natural abundance urea, showing a polarisation of 20%. (B) Thermal NMR spectrum of ^{13}C for an equivalent sample of urea where the label is present at natural abundance; this multiple scan signal was averaged over 65 hours.

Over the last 15 years, d-DNP has been developed for medical use and many compounds have been hyperpolarised using this method.[33, 34] The most successful molecules contain carbonyl groups which include; pyruvic acid, pyruvate, urea, glutamine and ascorbic acid due to the quaternary carbon of the carbonyl group having typically long longitudinal relaxation times. Longitudinal relaxation (T_1) is the energy exchange between the spins of the molecule(s) present in solution to return to their thermal equilibrium. This is discussed in further detail in section 1.3.3 of this chapter. T_1 values are important in the d-DNP experiment, as this time dictates both the rate of magnetisation build up and the rate of relaxation of the created magnetisation. Therefore, long T_1 values allow polarisation to remain whilst the molecule is transferred to the detection field.[34, 35]

The carboxyl functionality of many of these molecules also makes them easy to enrich in ^{13}C. This is very beneficial as it is the weak interactions of ^{13}C with the associated protons that results in a long relaxation time.[34] Therefore, d-DNP has proved successful with *in-vivo* studies of

metabolites.[36-41] The detection of these hyperpolarised ^{13}C labelled molecules have provided remarkable insights into their metabolism. The most widely known success story is based on the role of pyruvic acid in the Krebs or citric acid cycle.[38, 42]

The formation of pyruvate is very similar in most cells and this is key in the metabolism of glucose to provide energy in the form of adenosine triphosphate (ATP) *via* the Krebs cycle. However, once pyruvate is formed, it can be broken down in many different ways, three of which are shown in Figure 1.5.

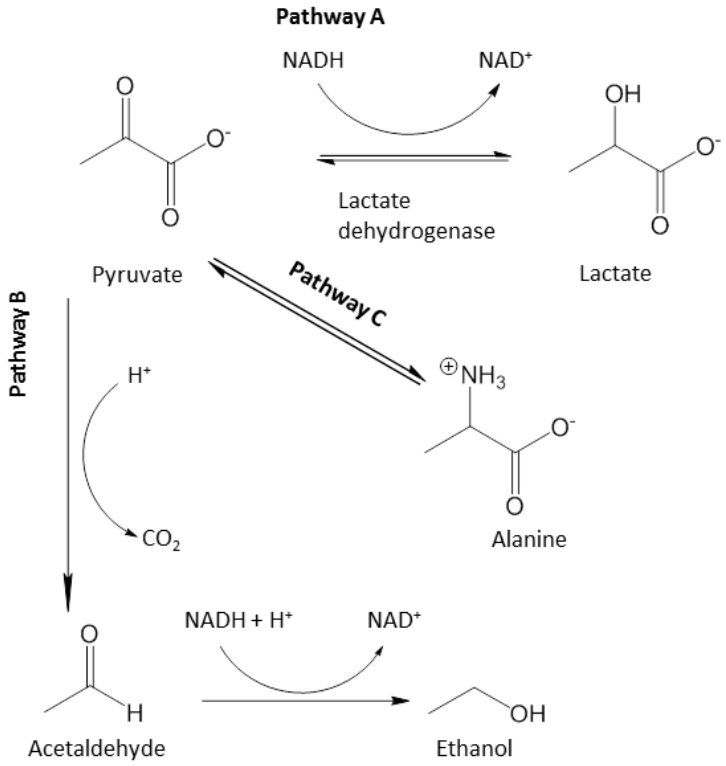

Figure 1.5 – The metabolic pathways of pyruvate in aerobic and anaerobic conditions. The formation of lactate occurs under aerobic conditions and is catalysed by lactate dehydrogenase. Under anaerobic conditions ethanol is formed instead in a process catalysed by pyruvate decarboxylase.

Pathway A is often favoured when the cell is in hypoxia and anaerobic respiration is the predominant pathway to gain energy. In this pathway, pyruvate is reduced to lactate by NADH by the enzyme lactate dehydrogenase to produce 2 lactate molecules, 2 ATPs and 2 molecules of H_2O.[43] Pathway B is usually observed in microorganisms also undergoing anaerobic respiration. As shown in Figure 1.5, the decarboxylation of pyruvate occurs first, followed by the reduction of the newly formed acetaldehyde to produce ethanol. This pathway is not observed in

multicellular organisms.[43] Finally, pathway C shows the transamination of pyruvate to form the amino acid alanine. This occurs as alanine can be transported into the liver where it is reconverted to glucose.[44]

Of these three pathways, pathway A has become key in monitoring tumours. In 1927, Otto Warburg[45] described the metabolism of tumours, noting that there was an increase in glucose uptake (aerobic glycolysis) into tumour cells, where there is then an increase in lactate production. This effect has continued to be studied and although it is not a feature of all types of cancer cells it is considered to be an important feature of rapidly growing cells.[36] Therefore, the metabolic study of pyruvate and its conversion to lactate is a very important diagnostic tool to differentiate between normal cells and cancer cells.

The first report of d-DNP being used to study cancer metabolism was made in 2006.[36] In order to do this, 1-^{13}C-pyruvate was injected into rats with P22 tumours and the production of lactate was monitored. As previously mentioned, the increase in this metabolic activity is considered to be a characteristic of many cancer cells. This study highlighted the viability of using a hyperpolarised biomarker to study metabolic pathways and subsequently image them using MRI.

The initial success of 1-^{13}C-pyruvate as a metabolic probe led to analogous studies being undertaken. For example, both carbons of pyruvate can be ^{13}C labelled and when the molecule is hyperpolarised and injected into a biological system, the ^{13}C labelled pyruvic acid is converted to ^{13}C-citrate and ^{13}C-glutamate.[34, 46-50]

Furthermore, the study of hyperpolarised ^{13}C labelled pyruvate has developed even further and has been used to track its reduction to ^{13}C-lactate which has also been linked to the abnormal metabolism of cancer cells.[48-51] The hyperpolarised lactate is transported out of the cell *via* the monocarboxylate transporter 4 (MCT4) which increases in efficiency within cancer cells.[49, 52-54] This method has been successfully demonstrated using transgenic adenocarcinoma mouse prostate (TRAMP) models and also with dog prostates.[48, 55] These works led to the development of ^{13}C labelled pyruvate metabolic imaging of humans.[38]

Other biochemical reactions to be studied through d-DNP include using hyperpolarised vitamin C or ^{13}C-dehydroascorbic acid to examine the NADPH oxidases.[56-58] This approach could be used as a method to probe cell populations in the brain as a target surrogate for looking at the role of glutathione in cancer. [34, 59-63] The metabolic route of ^{13}C-pyruvate has also been studied in normal brains and those with implanted glial tumours, again showing an increase in ^{13}C-lactate when tumours are present.[64, 65]

Hyperpolarised $H^{13}CO_3^-$ and $^{13}CO_2$ have been used to study the pH in tumours.[66, 67] These are derived from hyperpolarised ^{13}C-pyruvate and have been used to measure the pH of cells *in vivo*. As pH differences have been linked to diseased tissues this method could be developed as a vital diagnostic tool.[66, 67]

1.2.3.1 Critical Evaluation of DNP

Since the first reports of d-DNP, it has become one of the most developed methods for hyperpolarisation of biologically relevant molecules and has shown enormous potential for medical imaging.[33, 34, 37, 55, 56, 68-71] It provides the best signal enhancement of all the DNP methods. d-DNP hyperpolarised ^{13}C-pyruvate is now being used within clinical studies both in the US and the UK.[38, 72, 73] This demonstrates the viability of this method for medical imaging and metabolite monitoring. However, there are several challenges that still remain to be addressed.

Whilst d-DNP has been very successful with pyruvate, when it is applied to other contrast agents, none have shared the success of pyruvate. One reason this is the case is that pyruvate forms glassy beads when frozen, which gives it a homogenous surface. Other molecules that are polarised by d-DNP do not exhibit this phenomenon and therefore they are dissolved in glycerol to achieve this effect.[32, 74] Although glycerol allows for a glassy bead to form, if the volume is too high solvent polymorphism can occur[74] which prevents effective polarisation as the sample is no longer homogenous.[75, 76]

Another drawback of the DNP method is that polarisation of the sample can take a significant amount of time; anywhere between an hour to 4 hours is typical.[77, 78] There has been some effort to alleviate these long build-up times through the addition of *para*-magnetic materials, such as

gadolinium, in order to reduce the T_1 values. This has had the effect of improving the polarisation level and reducing the polarisation time,[79-81] however, this can be costly and have other associated issues.

DNP also requires the addition of a free radical to supply unpaired electrons to the sample, which then allows the DNP process to occur.[28, 32] To try and reduce the polarisation time of the sample, it is possible to use different radicals.[76, 82] However, after the substrate has been polarised, the radical needs to be separated from the substrate of interest along with the removal of gadolinium.[70] This needs to occur quickly to prevent the T_1 from shortening further. A number of methods have been implemented to get rid of the free radical; these include filtration, radical quenching and precipitation.[32, 83, 84] This step is not only important to prevent a reduction in the T_1 value but also needed for *in vivo* study due to biocompatibility problems. To decrease polarisation loss, a deuterated solvent can be added, which acts to reduce the relaxation within the sample mixture.[85]

Then there is the transfer time, the time taken to get the hyperpolarised sample to the place where it is needed. This is known as 'voyage time' and can also be problematic. During transfer, the sample is exposed to low magnetic fields when it is transported from the polariser to the NMR or MRI for detection, which shortens the T_1.[29] Therefore, the substrate needs to have a long T_1, so the polarisation can last long enough for a hyperpolarised signal to be observed. Pyruvate has a T_1 of 67 seconds at 3 T, (a standard magnetic field strength of the MRI used within clinics).[34] This has been proven to be long enough for a metabolic map to be seen and an MRS image to be taken.[34, 68] Reducing the voyage time has been achieved by Köckenberger *et. al*, by placing the polariser on top of the NMR. This system has a transfer time of 2.9 seconds[86] but is not easily translated into an imaging environment.

Finally, d-DNP is a one-shot method. If the injection site is wrong, or if the scanner is not scanning in the right region, the hyperpolarised signal will not be seen.[30] If a sample requires iteration, for example reaction monitoring, the sample and radical need to be separated or made up again for the same sample to be repeated. This can lead to irreproducibility of results.

Overall d-DNP is a viable method but if a cheap, less time-consuming method were developed then it may not only compete with d-DNP but could be the preferred method in the clinic.

1.2.4 *Para*-hydrogen induced polarisation (PHIP)

Para-hydrogen is one of four spin isomers of hydrogen gas (H_2), which can be easily and inexpensively created in almost unity, thus yielding very high levels of latent polarisation. To subsequently use this latent polarisation the symmetry must be broken by a chemical transformation. *Para*-hydrogen induced polarisation (PHIP) is the general term used to describe hyperpolarisation that involves any use of *para*-hydrogen, however, there are three main methods within the PHIP classification. These include, Adiabatic Longitudinal Transport After Dissociation Engenders Net Alignment (ALTADENA)[87], *Para*-hydrogen And Synthesis Allow Dramatically Enhanced Nuclear Alignment (PASADENA)[88] and Signal Amplification By Reversible Exchange (SABRE).[13] The differences between these three methods will be discussed in this section and subsequently critically evaluated.

1.2.4.1 *Para*-hydrogen

Hydrogen gas is diatomic and therefore contains two hydrogen nuclei. Each proton is spin ½ and there are two orientations they can occupy. Thus, the pair of spins yields four possible combinations of these spin states. Three of these have very similar energies and comprise the *ortho* triplet spin-state whilst the other is significantly lower in energy, the singlet spin state, termed *para*-hydrogen (p-H_2). A schematic of these is shown in Figure 1.6.

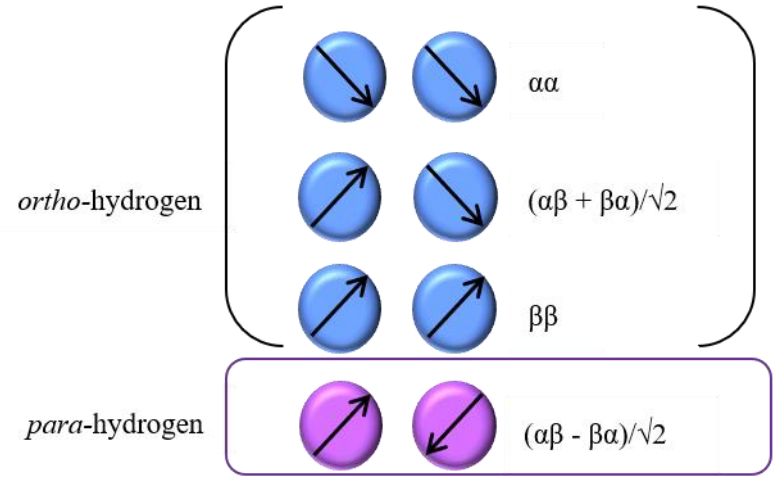

Figure 1.6 – The four possible allowed spin states of dihydrogen.[89]

The difference in energy between the spin states is far less than the thermal energy of the gas at room temperature and, as such, the spin states are equally populated at room temperature, resulting in the *p*-H_2 spin state being 25% abundant. However, if hydrogen gas is cooled to 28 K and passed over a suitable catalyst, then over 99% of the hydrogen can be converted to the *para*-spin state.[90] Since a paramagnetic catalyst is required for the conversion from *ortho* to *p*-H_2, after the removal of the catalyst *p*-H_2 is stable for a long time (many months), as the spin flip transition is forbidden. This state is considered to be anti-symmetric (or antiparallel) in quantum mechanical terms, whereas the *ortho* states are symmetric (or parallel). These definitions can be confirmed by permutation of the relative equations for each spin state given in Figure 1.6, and observing that when doing this operation the *ortho* states remain equal, however, the *p*-H_2 state undergoes a sign change. The total spin number of *p*-H_2 is therefore zero, while the *ortho* states are one. Since the spin isomer is equal to zero, *p*-H_2 is consequently NMR silent.

p-H_2 can be converted to be exclusively in one state, thus creating a pure state which can be described by a single wavefunction. The aforementioned symmetries of *p*-H_2 must be broken in order to transfer this spin order and release this latent polarisation. The symmetry of *p*-H_2 can be broken by creating either chemical (e.g. using the *p*-H_2 within a chemical reaction[87, 91, 92]) or magnetic inequivalence (e.g. using a catalytic framework to transfer polarisation to the substrate[13, 93, 94]). In these situations, the latent polarisation of *p*-H_2 is converted into observable nuclear

magnetisation and subsequently transferred to a molecule of interest, resulting in a dramatic increase of the observed signals in NMR and MRI.[13, 95, 96] Due to the inexpensive and relatively easy method of converting high purity *p*-H_2, it is becoming an increasingly popular technique used for hyperpolarisation, to be further used in a wide array of applications.

1.2.4.2 PASADENA

Para-hydrogen And Synthesis Allow Dramatically Enhanced Nuclear Alignment (PASADENA)[87] was first described in 1986 by Bowers and Weitekamp. In 1987, they carried out an experiment incorporating *p*-H_2 into acrylonitrile *via* Wilkinson's catalyst to produce ethyl cyanide. The ethyl cyanide product, contained chemically inequivalent protons and so an enhanced ^{1}H NMR spectrum was obtained.[91] This was also experimentally realised by another group in the same year, again incorporating *p*-H_2 *via* hydrogenation across a double or triple bond.[88] Although in both of these examples the increase in NMR signal was due to the incorporation of *p*-H_2 across a bond which made them chemically inequivalent, this increase in signal can also be observed if the protons are magnetically inequivalent. For this type of polarisation to take place the molecule in question must contain either a double or triple bond which can undergo hydrogenation.[91]

In PASADENA, the symmetry of the *p*-H_2 is broken due to its incorporation into the product molecule when within a strong magnetic field. This is achieved because the $(\alpha\beta - \beta\alpha)/\sqrt{2}$ state of *p*-H_2 is split in the presence of a strong magnetic field which then populates the $\alpha\beta$ and $\beta\alpha$ spin states of the product exclusively and hence gives rise to the required population difference. Observing an AX spin system with *p*-H_2 incorporated, the chemical shift difference is much larger than the *J*-coupling between the two protons. Thus, the weak coupling eigenstates of the $\alpha\beta$ and $\beta\alpha$ being formed and exclusively being populated as shown in Figure 1.7a. The occupation of these energy states gives the NMR profile, shown in Figure 1.7b where two antiphase doublets, relative to the J_{HH}-coupling are observed.[97] As two of the transitions are absorption and two are emission, the observed NMR spectrum shows two peaks pointing up and two pointing down. Both the experiment and the detection of the signal are carried out at one, strong magnetic field.

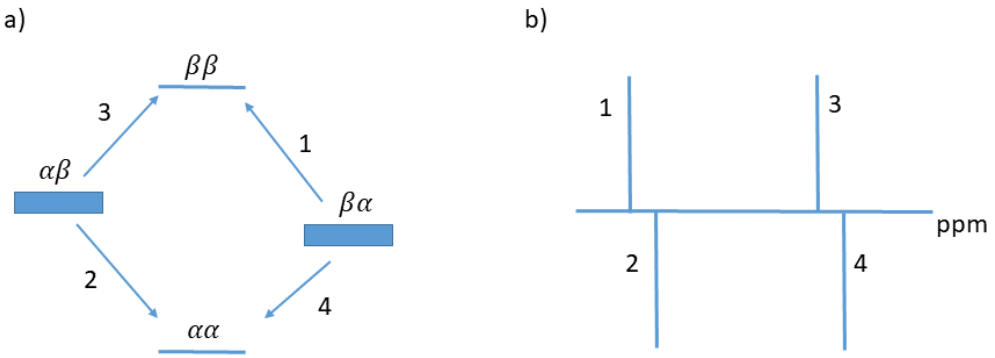

Figure 1.7 – a) the population diagram for an AX spin ½ system under PASADENA conditions. b) the corresponding NMR profile observed for this spin system under PASADENA conditions.

1.2.4.3 ALTADENA

In 1988, Pravica and Weitekamp discovered another form of PHIP, Adiabatic Longitudinal Transport After Dissociation Engenders Net Alignment (ALTADENA).[92] This method conducts the hydrogenation reaction at low magnetic fields, normally provided by the Earth's field, prior to the sample being transferred to a high field NMR spectrometer for detection. Due to the reaction taking place at low magnetic fields, the spin system is now strongly coupled and results in a population of a lower energy state relative to *p*-H_2 that is still coupled approximately $(\alpha\beta - \beta\alpha)/\sqrt{2}$. Once placed into a high magnetic field, the same splitting that is observed under PASADENA conditions occurs but, as the coupled system is lower in energy, it transfers to the $\beta\alpha$ state exclusively. Figure 1.8 shows both the energy diagram and NMR profile of ALTADENA magnetisation, where the NMR signal is now antiphase relative to the chemical shift system.[97] The adiabatic term in ALTADENA refers to the fact that the *p*-H_2 state and the strongly coupled state are so close in energy that the system can easily transition into the latter.

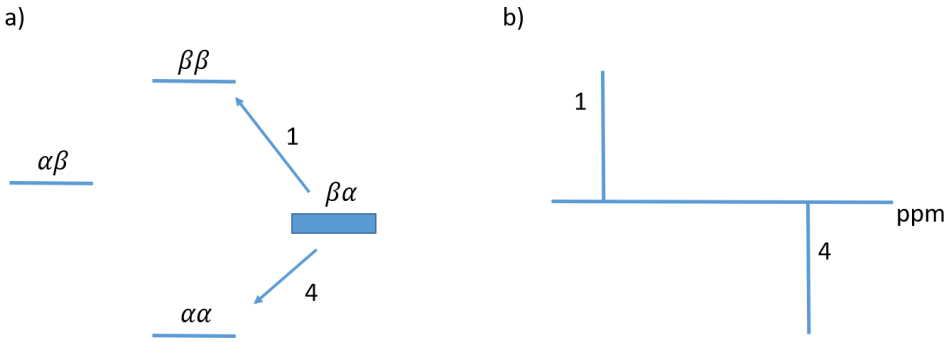

Figure 1.8 - a) the population diagram for an AX spin ½ system under ALTADENA conditions. b) the corresponding NMR profile observed for this spin system under ALTADENA conditions.

1.2.4.4 Signal amplification by reversible exchange (SABRE)

The ALTADENA and PASADENA techniques require a substrate that can be hydrogenated with *p*-H_2, which chemically alters the initial molecule. Unlike ALTADENA and PASADENA, the substrate in Signal Amplification by Reversible Exchange (SABRE) does not need to undergo a hydrogenation reaction with *p*-H_2. This method was first described and demonstrated by Duckett *et. al.* in 2009.[13] Instead, an organometallic catalyst is used to form a complex between the substrate and *p*-H_2 derived hydride ligands. As a consequence of the reversible exchange of *p*-H_2 and of the substrate into the complex, hyperpolarisation of the substrate can be built up into the surrounding solution, as shown in Figure 1.9.

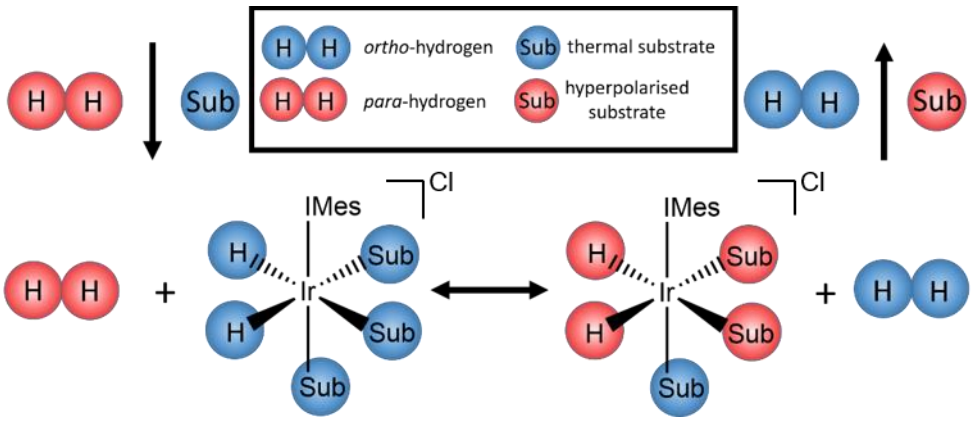

Figure 1.9 – SABRE mechanism for the exchange of *ortho*-hydrogen to *p*-H_2.

The spin order from the *p*-H_2 derived hydride ligands is transferred to the bound substrate *via* their *J*-couplings.[93, 98-100] This allows the spin states in the free substrate to be populated in the αβ and βα energy levels as shown in Figure 1.10.[12] The *J*-coupling requirements for the transfer of spin between *p*-H_2 and the substrate are met by using a low magnetic field.[13, 101, 102]

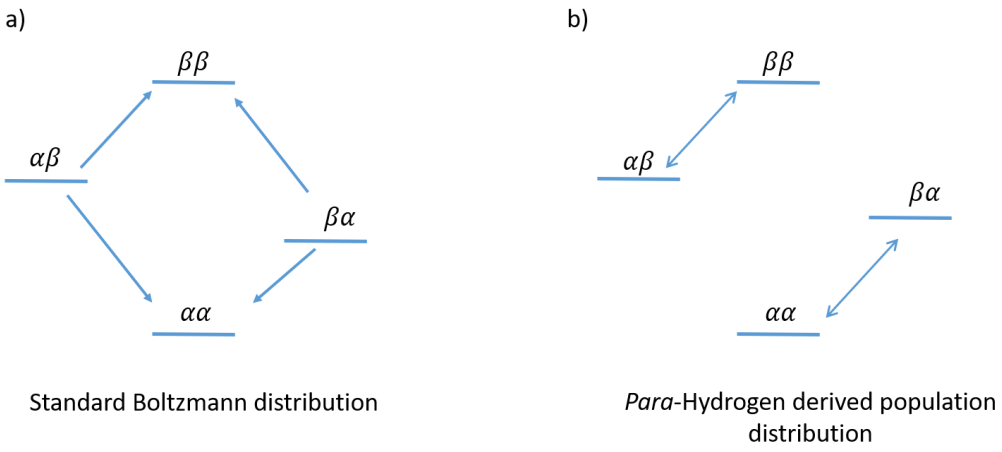

Figure 1.10 – Transitions for an AX system under a) Boltzmann conditions and b) under SABRE conditions when *para*-hydrogen has been added and either chemical or magnetic inequivalence has occurred.[12, 103]

To spontaneously transfer the polarisation from the hydrides through the *J*-coupling network to the nuclei of interest on the substrate, the *J*-coupling constant between the two groups needs to be equal to the chemical shift difference of the hydrides and the substrate nuclei.[101] Commonly within the chemical systems explored, the *J*-coupling between a substrate and the hydride is around 1.2 Hz and the *J*-coupling between the hydrides (J_{HH}), is usually around 8 Hz.[101, 104] Equation 1.12 can be used to calculate the theoretical, optimal polarisation transfer field

$$B_{PTF} = \frac{J_{HH}}{\Delta\delta_{Hx}} . B_0 \qquad (1.12)$$

where B_{PTF} is the optimal polarisation transfer field, J_{HH} is the *J* coupling between the *p*-H_2 derived hydrides (approximately 8 Hz), $\Delta\delta_{Hx}$ is the chemical shift difference between the hydrides and the nucleus of interest, x.[105] For example, for transfer from *p*-H_2 hydrides (at δ −22 ppm) to an aromatic resonance (around δ 8 ppm) there is a 30 ppm chemical shift difference, which for a 9.4 T magnet, equates to a chemical shift of 12 kHz. Therefore, taking the coupling between hydrides as 8 Hz, the aromatic proton resonance the optimal polarisation transfer field (PTF) can be calculated to be 62.7 G. To achieve the desired magnetic field, the sample can be either shaken in the stray field of the NMR spectrometer or a hand held magnet array.[106]

For heteronuclei, such as ^{13}C, there is a difference between the Larmor frequency of this nuclei and ^{1}H. Therefore, the PTF for heteronuclei will not only be different in each case but also of a lower magnetic field.[107] For example, when ^{13}C nuclei are examined under SABRE conditions the PTF for ^{13}C is calculated to be 2.5 mG using equation 1.12, where J_{HH} is 8 KHz and $\Delta\delta_{Hx}$ is 299.499200×10^6 at 400 MHz (9.4 T). Therefore to transfer polarisation to ^{13}C nuclei a mu metal shield is used.[108]

1.3 The SABRE process

In order to gain a significant build-up of hyperpolarisation, the substrate-catalyst interactions have to be fine-tuned, as the substrate needs to bind for long enough to allow polarisation to be transferred from *p*-H_2 but not too long so that the iridium centre of the metal complex relaxes the established polarisation.[109] The substrate when bound to the complex has a significantly increased relaxation rate due to several factors. Therefore an optimum exchange rate between the substrate and the catalyst results.[110] The efficiency of the hyperpolarisation transfer also needs to be contemplated and is dependent on several considerations; the polarisation transfer field (PTF), temperature, substrate concentration, optimum rate of exchange (type of catalyst and catalyst concentration) and longitudinal relaxation (T_1).[111-118] All of these factors have been shown to affect the level of hyperpolarisation and are discussed within this thesis.

1.3.1 Role of catalyst

The transfer of polarisation from *p*-H_2 to the substrate occurs when both are ligated to the metal complex. For substrate and hydrogen exchange to occur on a suitable timescale, both the steric and electronic contributions of the SABRE-active species must be considered.[102, 116] The binding of the substrate to the metal complex occurs through the nitrogen lone pair forming a weak σ-bond. This means that the substrate is a labile ligand on the complex and is therefore exchanged with the excess substrate molecules present in the solution. As the bound and free substrates exchange, as well as fresh *p*-H_2, the polarisation of the free substrate builds up.[13, 93]

Initial experiments with SABRE were performed using Crabtree's catalyst, $[Ir(COD)(PCy_3)(py)][BF_4]$, where COD is cycloocta-1,5-diene, Cy is cyclohexyl and py is

pyridine.[13, 94] The total ^{1}H NMR signal enhancement for pyridine was 550-fold and hyperpolarised signals were also reported for ^{13}C and ^{15}N as shown in Figure 1.11, spectrum **B** and **C** respectively. Alongside pyridine, other substrates were also examined including 3-fluoropyridine and nicotinamide, however, specific signal enhancements were not reported at the time, but enhanced signals were observed.

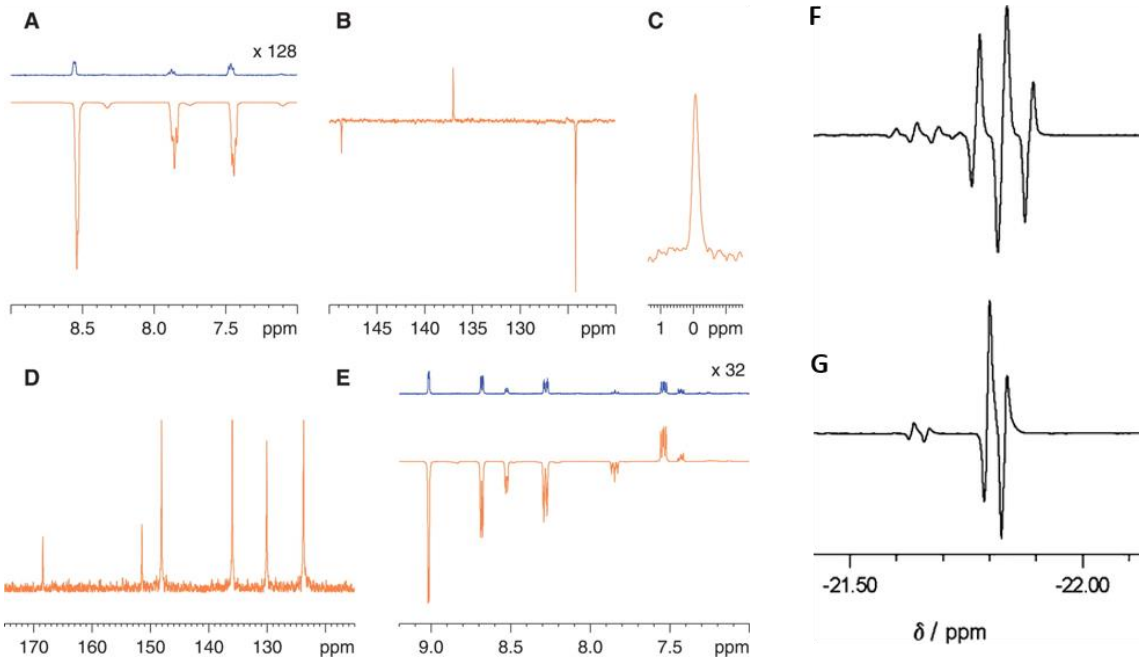

Figure 1.11 – Spectrum A-E are from figure 2 from the journal *Science*, 2009, 323, 1708-1711 from reference 13,[13] F and G are from figure 1 from the journal *J. Am. Chem. Soc.*, 2009, 131, 13362-13368 from reference 93.[93] A is the ^{1}H NMR of pyridine where the top spectrum is the thermally equilibrated NMR spectrum x128 vertical expansion to be observed here. The bottom spectrum is the corresponding 1 scan SABRE hyperpolarised spectrum, transfer carried out at 2 x 10^{-2} T. B is the ^{13}C{^{1}H} NMR of the same sample after refocusing. C is the ^{15}N SABRE polarised spectrum with refocusing. D is a hyperpolarised ^{1}H{^{13}C} NMR of nicotinamide, again after refocusing. E is the ^{1}H NMR spectrum of nicotinamide, top spectrum is the thermally equilibrated NMR spectrum x32 vertical expansion to be observed here. The bottom spectrum is the corresponding 1 scan SABRE hyperpolarised spectrum, transfer carried out at 0.5 x 10^{-4} T. F is the ^{1}H NMR of the hydride region of [Ir(COD)(PPH$_3$)$_2$]BF$_4$ with ^{15}N-pyridine, G is the corresponding ^{1}H{^{31}P} NMR spectrum.

To improve the SABRE derived signal enhancements, the identity of the polarisation transfer catalyst was examined. At first different phosphine ligands were changed on the current pre-catalyst.[93] From this investigation it was found that using PCy$_2$Ph (dicyclohexylphenylphosphine) phosphine produced the greatest ^{1}H signal enhancement across all three proton sites on pyridine.

Therefore, it was concluded that the phosphine ligand affected the rate of substrate and hydride exchange which led to an increase in signal enhancements. This change in exchange rate was probably achieved due to the increase in steric bulk and the electron donating ability of the phosphine ligand.[93]

A dramatic improvement in SABRE efficacy was achieved by changing the phosphine ligand to an *N*-heterocyclic carbene (NHC) ligand.[119] It was found that 1,3-bis(2,4,6-trimethyl-phenyl)imidazole-2-ylidene] (IMes) gave enhancements of pyridine of 6000-fold. This is an increase of 10.9 times when compared to the phosphine-derived system. The rate of exchange of pyridine in the NHC catalyst at 300 K was found to be 11.7 s^{-1}compared to 1.8 s^{-1} when using $[Ir(COD)(PCy_3)(py)][BF_4]$.[119] This increase in rate of ligand loss could be due to an increase in steric and electronic effects and highlights how the spectator ligand can affect the rate of substrate exchange within the SABRE active complex.

To date, [IrCl(COD)(IMes)] remains the most commonly used SABRE pre-catalyst as this has routinely exhibited high levels of hyperpolarisation on *N*-heterocycles.[111, 119] However, other catalysts have also been examined in order to observe and optimise their hyperpolarisation enhancement levels by comparison.[111, 114, 118] The most recent study included over 20 variants of [IrCl(COD)(NHC)], by changing the groups on the imidazole and on the *ortho*, *meta* and *para* positions of the aryl arms on the NHC ligand.[118] These changes were made to allow for both steric (measuring the $\%V_{bur}$) and electronic properties (measuring the Tolman Electronic Parameter, TEP) to be varied. It was found that increasing the TEP values could be achieved by changing the substituent in the *para* position on the aryl arm, for example adding a phenyl group.[118] However, to increase this value further, electron withdrawing groups were substituted onto the imidazole backbone. Adding chlorine into this position increased the TEP value to 2052.8 cm^{-1}.[118] Adding electron withdrawing groups to these positions decreased the TEP value and increased the electron donating capabilities of the NHC.[118] The greatest change in the steric bulk of the catalyst was achieved when changing the substituent in the *ortho* position on the aryl arm. For example, when this was changed from a methyl group to hydrogen, the $\%V_{bur}$ decreased from 31.6% to 30.5%.[118]

The greatest $\%V_{bur}$ recorded was 32.6%, this occurred when the *ortho* substituent was isopropyl.[118] From this study an optimal catalyst was found for the methyl 4,6-d_2-nicotinate and polarisation levels of up to 63% resulted. Whilst, this study showed the overall improvement of the SABRE signal enhancement when using NHC ligands it could not confirm a correlation between steric bulk and electronic properties and signal enhancement.[117, 118] Therefore, due to the complexity of the SABRE mechanism a range of catalysts should be screened for each individual substrate. [120]

Other catalysts have been screened with SABRE these include using the pre-catalyst $[IrCl(COE)_2]$. This was undertaken as this catalyst may allow more sterically bulky substrates to bind and be hyperpolarised. It was found that using this catalyst with 3,5-lutidine, a 539-fold ^1H signal enhancement was observed at 313 K.[121] When examining this catalyst with pyridine a 500-fold ^1H enhancement was recorded.[121]

An asymmetric NHC catalyst has also been developed.[122] Again, to allow more sterically bulky substrates to bind to the SABRE catalyst. Here the ligands on the NHC were changed. When using the SABRE pre-catalyst, [Ir(IMesBn)(COD)Cl] (where IMesBn = 1-mesityl-3-benzylimidazole) and the substrate 3,4-lutidine a ^1H signal enhancement of 1615-fold was recorded.[122]

A neutral iridum catalyst has also been examined. Here $[Ir(\kappa C,O\text{-}L_1)(COD)]$ was prepared, where L_1 = 3-(2-methylene-4-nitrophenolate)-1-(2,4,6-trimethylphenyl)imidazolylidene.[123] As this catalyst is neutral, it was found that it could be used in a range of different solvents.[123, 124] For example, when examining pyridine in tetrahydrofuran, a 600-fold ^1H signal enhancement was observed on the hydrogen in the *para* position.[123]

A range of iridium catalysts have also been developed with a wide bite-angle using the ligand xantphos.[125] When examining the hydroformylation reaction with p-H_2, an intermediate was fully characterised and hyperpolarised ^1H signals were observed in the aldehyde generated in this reaction.[125]

1.3.2 Quantifying the Dynamic Effects of SABRE

The SABRE process has previously been shown to be dissociative in nature[119] and therefore, the dynamic nature of the ligand exchange process can be readily determined (Figure 1.12).[118] The first step in the SABRE process is ligand dissociation from the active SABRE 18-electron complex to become the 16-electron trigonal bipyramidal intermediate which can undergo associative addition.[119] On binding of *p*-H_2, the formation of a hydrogen-dihydride complex is proposed, which allows for the refreshing of magnetisation within the system.[111, 119]

This process can be studied using Exchange Spectroscopy (EXSY)[8-11] and is described experimentally in Chapter 7 section 7.2.10.

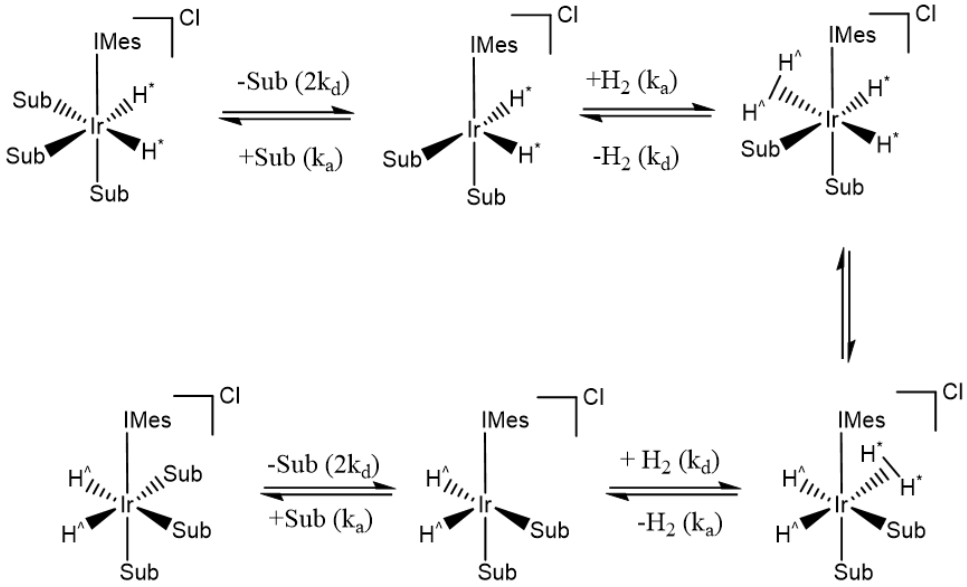

Figure 1.12 – SABRE exchange pathway of hydrogen and substrate (sub) from the complex.

In the study of the effect of changing the NHC in the SABRE pre-catalyst, Rayner *et. al.* examined the exchange rates.[118] They found that increasing the steric size of the catalyst increased the rate of ligand exchange and that it increased when NHCs included electron donating groups. It was concluded that an increase in electron density stabilised the 16-electron intermediate and therefore this allows for faster association of the substrate onto the catalyst.

In 2016 Barskiy *et. al.* produced an analytical model for the SABRE process.[110] They concluded that the k_d for the substrate is equal to the ω_{LAC} (the angular level anti-crossing frequency) which,

when $J_{AB} - J_{A'B} = 1$ Hz, should be approximately 4.5 s^{-1}.[110] Therefore to obtain the maximum signal enhancement, the optimal catalyst lifetime is required and this will change when the difference in *J*-coupling changes between the hydride and the nuclei under observation in the substrate.[110]

1.3.3 Relaxation effects on SABRE

For NMR to be observed, the spins are perturbed away from equilibrium usually using a 90° radio frequency (*r. f.*) pulse at the resonant frequency of the selected nuclei. This perturbs the spins into the xy plane, where the detectors are present. After this excitement, the spins will undergo relaxation back to their equilibrium positions. There are two routes to returning to thermal equilibrium. The characteristic time taken for the spins to return to equilibrium (z-axis) is denoted by the spin lattice relaxation time (T_1). T_1 is defined as the time it takes for 63% of the magnetisation to return to the z-axis, of the value at thermal equilibrium.[9, 126] The other, spin-spin relaxation time, T_2, is the time taken for 63% of the spins to decay away from the xy plane back to the z-axis.[9, 127]

For small molecules in liquids, in the tumbling regime, the values of T_1 and T_2 are very similar. This is due to the spin-spin interaction that dictates the T_2 relaxation being quite inefficient due to the correlation function, in liquid NMR this is defined as a function of time. If the T_2 is inefficient then it will be ultimately controlled by the T_1, and thus they are the same value in the fast tumbling regime. The T_1 relaxation will be most efficient when the motion of the molecules is on the same timescale as the resonant frequency of the given nuclei. Either side of this timescale the T_1 relaxation is less efficient and the value increases, therefore creating a T_1 minimum. The T_2 behaviour is somewhat different, as the material becomes less mobile, with either viscous solutions or solids the T_2 value will continue to decrease and approach zero. Since the spins are closer in proximity the spin-spin interactions affecting T_2 are much more efficient and the energy can be dissipated quickly. Therefore, for more immobile systems the T_1 and T_2 values start to deviate. In this study the T_1 relaxation has been measured as this parameter controls the polarisation build-up and decay, the T_2 for these systems are likely to be similar and therefore are superfluous.

Within the SABRE mechanism relaxation is problematic as the hyperpolarised signal needs to be used within the time limit of T_1.[128] As soon as hyperpolarisation has been created *via* this mechanism, the substrate is already relaxing back to its thermal equilibrium. Alongside this, once you have used an *r. f.* pulse, particularly a 90°, the signal is detected but then most of the hyperpolarised signal will have been 'destroyed'. Therefore, in SABRE it is important to have a substrate with a long T_1 to gain a large signal enhancement for as long as possible. If molecules are hyperpolarised and then required elsewhere, for example to an injection site, this relaxation time needs to be long so the signal will remain enhanced during the experiments. For example, in relation to MRI, this would allow the signal to last whilst it reached the area of the body that needed to be imaged. When using SABRE as the hyperpolarisation method the catalyst present to aid the transfer of polarisation causes the substrate to relax back to its thermal equilibrium faster than when it is free in solution.[111, 129]

It is the interaction between molecules which causes T_1 relaxation and therefore it can be determined that having different molecules within an NMR sample will change the T_1 of the substrate.[11, 130, 131] Therefore, relaxation times have been investigated for free and bound substrates when in the presence of the SABRE catalyst. For the substrate methyl 4,6-d_2-nicotinate the T_1 is over 60 s, however when bound to the catalyst this decreases to 0.5-2 s.[129] This not only demonstrates the reduction in T_1 when in the presence of the catalyst but that also when a T_1 experiment is undertaken, it is the average of the free and bound substrate which is observed.

To overcome this effect the concentration of the substrate can be increased but the signal enhancement will suffer due to an increase in the number of molecules binding to the catalyst and becoming polarised.[111] For example when using 100 mM of pyridine a ^{1}H signal enhancement of less than 1000-fold was recorded. However, when using 20 mM of pyridine the total ^{1}H signal enhancement is over 5000-fold.[111] What is also noted is the lifetime of the substrate when in the presence of the pre-catalyst against when the catalyst has been fully activated. When observing ^{1}H in the *para* position of pyridine, the T_1 decreases from 30.1 s to 18.9 s, for [IrCl(COD)(IMes)].[111] Another point to note is the lifetime of the catalyst and the effect on the T_1

relaxation. The catalysts with a small lifetime, for example when using [IrCl(COD)(SiPr)] (where SiPr = 1,3-bis(2,6-diisopropyl)-4,5-dihyroimidazol-2-ylidene), the lifetime of this catalyst is 0.0019 s and the T_1 of the ^{1}H in the *para* position was 18.8 s.[111] Examining a catalyst with a longer lifetime, [IrCl(COD)(IMe)] (where IMe = 1,3-bis(methyl)-imidazol-2-ylidene), the catalyst lifetime was reported as 0.83 s and the observed T_1 was 26.6 s.[111]

Another way to overcome the reduction in T_1 is to deuterate the NHC ligand within the catalyst, this has proved to increase the T_1 without the loss of signal enhancement.[112, 129, 132, 133] When methyl-4,6-d_2-nicotinate was hyperpolarised using [IrCl(COD)(d_{22}-IMes)], the T_1 for H-5 was reported to be 26.6 s, with a ^{1}H signal enhancement of 19.9%.[129] When using [IrCl(COD)(IMes)] the T_1 was 20.9 s and the ^{1}H signal enhancement is 9.5%.[129] Adding electron withdrawing groups to the NHC ligand was also found to improve the relaxation times but this may be a combination effect as there is also a reduction in rate of ligand loss.[118]

An interesting development of ^{13}C SABRE hyperpolarised species, is the use of long-lived states (LLS). This was first demonstrated by Levitt *et. al.* in 2004 in which a pair of isolated protons could have their nuclear spin order stored on them.[128, 134] This can be achieved by placing the sample, which contains a pair of inequivalent protons, into a low magnetic field.[128] As their spin exchange is anti-symmetric, they are not affected by T_1 relaxation. When the sample is then placed in a high field, their signals can be 'unlocked'.[128] Another way to create an LLS, is to use a series of *r. f.* pulses. A 90° pulse is applied, followed by a time delay and a 180° pulse, followed by a further time delay and 90° pulse and another time delay.[134] These prepare zero coherence within the sample, which prevents the singlet state from mixing with the triplet state.[134] A long time delay precedes a 90° readout pulse, allowing for the signal to be detected[134] (see Chapter 4 section 4.5 for more detail).

This mechanism has also been extended to the ^{1}H nuclei within SABRE. To achieve this, the substrates had to be selectively deuterated to isolate this pair.[135] A range of deuterated nicotinamides and methyl-3-*d*-pyrazine-2-carboxylate, were examined and SABRE induced polarisation was stored on the ^{1}H nuclei.[135] Here, a singlet lifetime of over 50 s was reported

alongside a total ^{1}H single enhancement of 4%.[135] This method was also used to examine a range of deuterated pyridazines.[136] Here for they found that for 3-d_3-methyl-6-methylpyridazine a T_{LLS} of 255 ± 23 s when in the presence of the catalyst was observed. In the absence of catalyst this increased to 262 s, with a ^{1}H signal enhancement of 950-fold.[136]

The creation of a ^{1}H long lived state, without deuteration has also been implemented with 2-aminothiazole.[137] When using the SABRE pre-catalyst, [IrCl(COD)(SIMes)], where SIMes = 1,3-bis(2,4,6-trimethylphenyl)-4,5-dihydroimidazolium a T_{LLS} of 26.8 ± 3.9 s was observed, with a ^{1}H signal enhancement of −356 and −425 for H-4 and H-5, respectively.[137] With this success, the lifetime and signal enhancements could be developed further for use as a probe into disease.

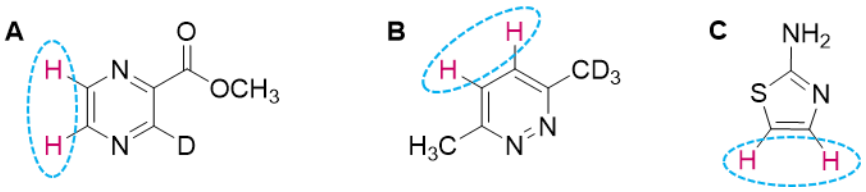

Figure 1.13 – Molecules used to form ^{1}H long lived states. A is methyl-3-*d*-pyrazine-2-carboxylate, B is 3-d_3-methyl-6-methylpyridazine and C is 2-aminothiazole. The protons which have been highlighted and circled are the ^{1}H pair which formed the singlet state.

1.3.4 Applications and developments of SABRE

SABRE is one of youngest methods for hyperpolarisation but offers some significant cost and time benefits. Given its comparatively new discovery, there are a number of applications of the SABRE method. Firstly, it has not only been used to enhance the signal of ^{1}H, but it has also been used to hyperpolarise other x-nuclei, including ^{13}C, ^{15}N, ^{19}F, ^{31}P, ^{29}Si and ^{119}Sn.[13, 107, 138, 139] Since the first experiments of SABRE in 2009 examining ^{13}C, ^{15}N and ^{19}F, these signal enhancements have been dramatically increased.[13] For example, total signal enhancements with ^{13}C in pyridine were first reported as 0.06%,[13] since then these have been increased to over 4% when using 50% *p*-H_2.[140]

Since the first reported enhanced ^{15}N signals,[13] huge advancements have been made with the direct polarisation of ^{15}N *via* SABRE-SHEATH (in SHield Enables Alignment Transfer to Heteronuclei).[107] This method has allowed low magnetic fields (μT) to be utilised, exploiting the

strong *J*-coupling between the hydrides on the SABRE catalyst to the ^{15}N of the substrate and producing 10% ^{15}N polarisation.[107, 141] This has been extended to a $^{15}N_2$-diazirine containing molecule to demonstrate the potential use of this molecule and nuclei as a tag for biomolecular imaging.[142] More recently over 50% ^{15}N polarisation has been reported, again using an ultra-low magnetic field but also with a co-ligand to stabilise the SABRE catalyst (see Chapter 1 section 1.5 for more detail).[143]

Two other nuclei of interest, which are shown to hyperpolarise *via* SABRE are ^{19}F, on 3-fluoropyridine and ^{31}P.[13] A ^{19}F signal enhancement of 93-fold (0.28%) was reported on fluoropyridine in 2017.[144] Although this nuclei maybe of interest as a molecular imaging probe, particularly as there's no background signal, the signal enhancement would need to be increased further.[144] Also, the reported T_1 of ^{19}F was 1.3 ± 0.3 s, which is a very short relaxation time, particularly if the desire is to be used as a probe for imaging.[144] SABRE polarisation of ^{31}P was observed by Fekete *et. al.* (2013).[132] They reported a 30-fold signal enhancement on the bound triphenylphosphine ligand within the SABRE active catalyst.[132]

In 2015 Zhivonitko *et. al.* improved this signal to 260-fold with triphenylphosphine.[145] They examined the change in kinetics when changing the temperature and found that at 80 °C the greatest signal enhancement and rate constants were produced.[145] The rate constant for hydride exchange was 5.3 ± 0.6 s^{-1} at 80 °C, and 8.7 ± 1.5 s^{-1} for ligand exchange.[145] Whereas at 60 °C, the rate constants were 1.5 ± 0.7 s^{-1} and 1.2 ± 0.5 s^{-1}, respectively.[145] To obtain these results they carried out their experiment by bubbling *p*-H_2 directly into the sample whilst it was in a mu-metal shield.[145] Alongside Zhivonitko, Burns *et. al.* produced even more impressive ^{31}P signal enhancements of 3588-fold using a partially deuterated pyridyl substituted phosphonate ester.[146] Unlike Zhivonitko's experiments, these were conducted at room temperature and rather than the use of a mu-metal shield, they found that the optimal PTF was 45 G.[146]

Two other nuclei which have been of interest are ^{119}Sn and ^{29}Si, to run a standard NMR experiment for these nuclei can take days as their gyromagnetic ratios (-9.579×10^7 rad T^{-1} s^{-1} and -5.315×10^7 rad T^{-1} s^{-1} respectively) are very small and their natural abundance is less than 10%.[139]

They were examined as potential reaction probes for the examination of intermediates in synthetic pathways and were first hyperpolarised *via* SABRE in 2016 by Olaru *et. al.*[139] Examining 5-(tributylstannyl)pyrimidine they found that when transfer of polarisation from the *p*-H_2 derived hydrides occurred at 25 G a 772-fold ^{119}Sn signal gain. For 5-(trimethylsilyl)pyrimidine there was a 200-fold ^{19}Si signal enhancement .[139]

The signal enhancement achieved through the shake and drop method varies due to many different parameters, such as, variations when shaking the sample, particularly if using the stray magnetic field, shaking time and the shake intensity of the user. A development of the SABRE method was that of a flow system which omits the variation of all of these factors to generate more reproducible results.[138]

The automated flow system was developed in collaboration with Bruker, it includes a polariser and a sample delivery system. The flow system is accurately controlled, and the triggers are incorporated into the pulse sequence directly so human error is completely removed. This allows the process to be easily repeated, a schematic of the flow system is shown in Figure 1.14.[138]

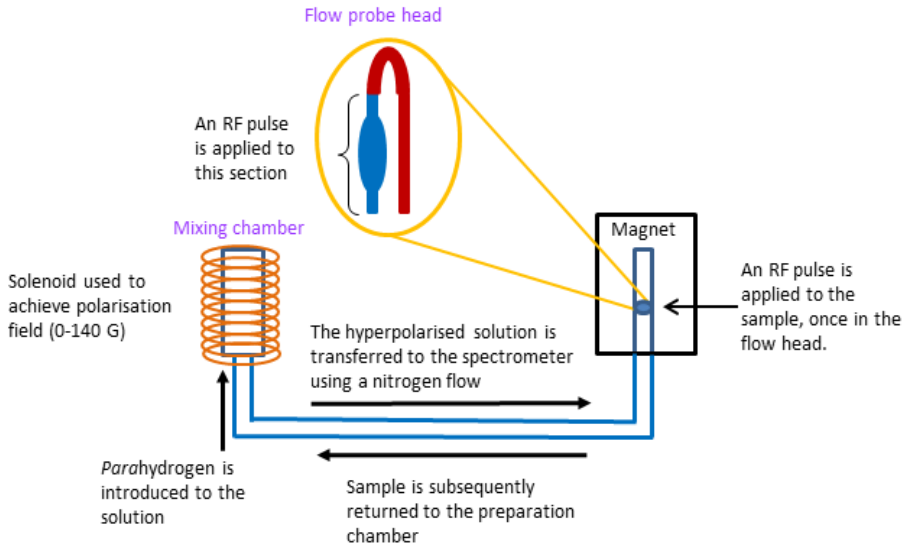

Figure 1.14 – Schematic of the flow system adapted from scheme 1 from ref. 147 with permission from The Journal of Physical Chemistry B within the supporting information (link https://pubs.acs.org/doi/abs/10.1021/jp511492q), further permissions related to the material excerpted should be directed to the ACS .[138, 147]

Although the results obtained from the flow system are more reproducible, the enhancements are routinely lower than that achieved by the shake and drop method. For example total ^{1}H signal enhancement for the flow system with nicotinamide is 720-fold,[138] with the manual method this increases to 2167-fold,[129] over 3 times that of the flow system. This effect is most likely due to a combined effect of the mixing of *p*-H_2 being less effective and longer transfer times on the flow system, allowing relaxation of the substrate before detection. However, the increased control of the flow system allows accurate measurement of the magnetic field dependency of the SABRE approach. This provides a route to ascertain the optimal polarisation transfer field to perform SABRE for any given substrate and therefore gaining the best enhancement when shaken, manually at this field. The sample chamber is placed inside a solenoid, which is used to deliver the small magnetic field required for SABRE, with a range of fields from 0 to 140 G.

Another area of development is using SABRE as a hyperpolarised magnetic resonance imaging (MRI) method. For this to be viable the iridium catalyst must be removed along with a change in the solvent system used. Most SABRE samples are made up in non-biocompatible solvents such as methanol-d_4, ethanol-d_6 or dichloromethane-d_2. The use of a biocompatible solvent mixture of ethanol-d_6 and D_2O has been used, where 6.6-fold ^{1}H signal enhancement was observed.[148] Unfortunately however, the T_1 decreases in samples prepared in a mixture of solvents.[129] Another advancement in the solvent system was achieved by Zeng *et. al.* they found that activating the catalyst in an organic solvent and then adding a biocompatible solvent, for example water to the sample gave large ^{1}H polarisation (1% for 3-amino-1,2,4-triazine).[149] Truong *et. al.* (2014) reported a similar experiment whereby the SABRE catalyst was activated with *p*-H_2 and nicotinamide in ethanol-d_6.[150] Once fully activated this sample was then dried and re-dissolved in D_2O where ^{1}H signal enhancements of 30-fold were reported.[150]

Water soluble catalysts have also been developed these include adding a ligand which is hydrophilic,[151] another was to add diol groups to the COD ligand within the SABRE pre-catalyst.[152] However, the method which proved to give the greatest signal enhancement was one where PEG (polyethylene glycol) groups were added to the NHC.[152, 153] The catalyst with the

greatest success, producing a ^{1}H signal enhancement of 42-fold on nicotinamide in D_2O, was when using the pre-catalyst, [IrCl(COD)(IDEG)], where IDEG = 1,3-bis(3,4,5-tri(diethyleneglycol)benzyl)imidazole-2-ylidene).[153] Examples of these catalysts are shown in Figure 1.15.

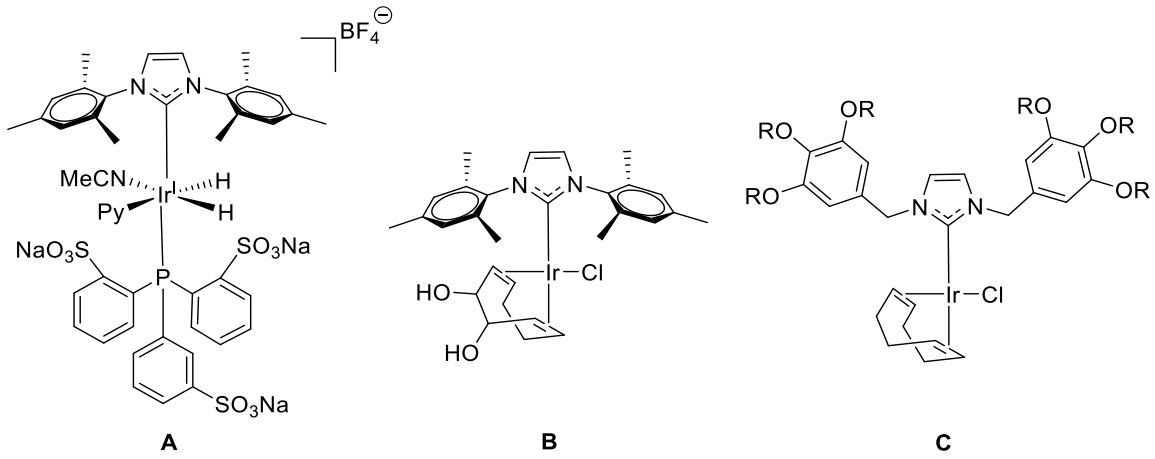

Figure 1.15 – Structure of three water soluble SABRE catalysts. A is an activated SABRE catalyst with a hydrophilic arylsulfoxanate group attached.[151] Both B and C are SABRE pre-catalysts, B is an example of a diol group added to the COD ligand[152] and C is [IrCl(COD)(IDEG)].[153]

Although dissolving the catalyst in a biocompatible solvent with the substrate of interest is required, removal of the iridium catalyst is also needed. Advancements have been made into the removal of this. There are currently a few areas of development, one is to use a heterogenous catalyst,[154, 155] another is to chelate and filter the catalyst out.[156] Also a biphasic system is being developed in the hope of removing the catalyst and allow the hyperpolarised substrate to remain in a separate, biological solvent.[157]

The heterogeneous catalyst immobilises the SABRE catalyst on polymer microbeads delivering a ^{1}H signal enhancement on pyridine, of 5-fold.[154] Kovtunov *et. al.* reported using silica particles to immobilise the catalyst and found that when doing this with ^{15}N-pyridine, ^{15}N signal enhancements of 100-fold were observed.[155] The signal enhancements reported when using heterogeneous catalysts are not enough for imaging purposes and the samples are still dissolved in non-biocompatible solvent.

Kidd *et. al.* (2018) reported the use of functionalised SiO_2 to deactivate the iridium catalyst, the sample is then purified, to remove the catalyst *via* filtration.[156] The hyperpolarised substrate was then detected in a 9.4 T NMR. The hyperpolarised signals were reported for ^{15}N on metronidazole and upon removal of the catalyst, which took approximately 20 s, these were 34%.[156] Another deactivation of the catalyst was also published in 2018, here Manoharan *et. al.* used bathophenanthrolinedisulfonic acid disodium salt (BPS).[158] The substrate was then removed from the sample *via* ion-exchange chromatography. This process was reported to take 12 s with a ^{1}H signal enhancement of 74 ± 21-fold for methyl-4,6-d_2-nicotinate.[158] Most importantly, however, there was less than 2% of catalyst remaining, after removal which is within the cytotoxicity limits for a bolus injection.[158]

A possible way to overcome these low signal enhancements and use a biocompatible solvent could be to use a biphasic system. This system is known as CAatalyst-Separated Hyperpolarisation *via* Signal Amplification by Reversible Exchange (CASH-SABRE).[157] The SABRE catalyst is dissolved in chloroform-*d* and the substrate of interest is dissolved in D_2O with 0.16 w/v% NaCl, as shown in Figure 1.16.[157]

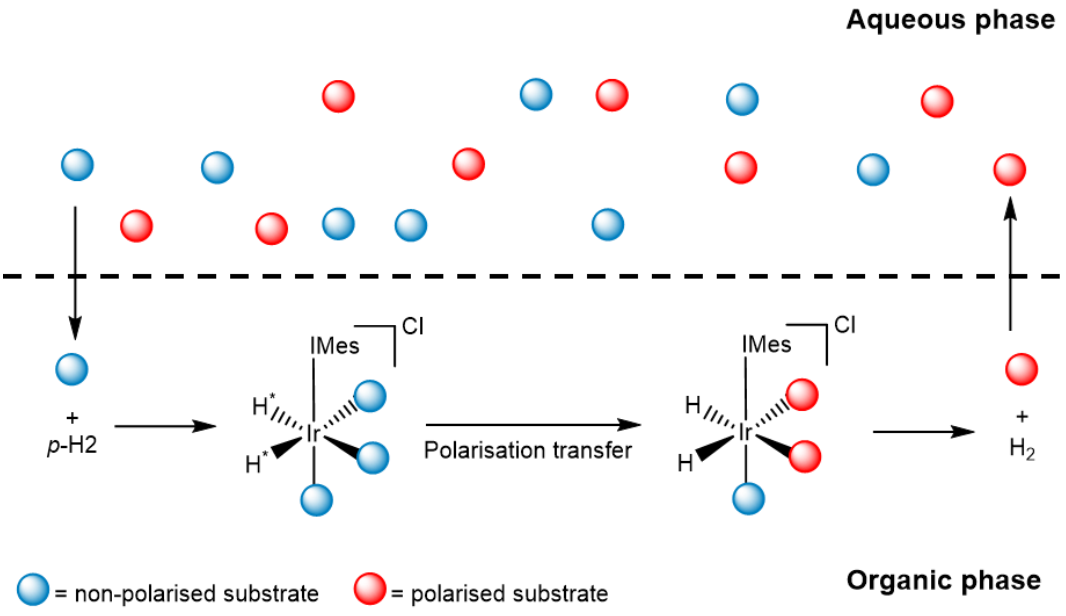

Figure 1.16 – Diagram of the CASH-SABRE system, whereby the lower, organic layer is where the catalysis takes place and the top layer is the inorganic layer where the hyperpolarised substrate is and can be extracted. Adapted from figure 9 from the journal *Angew. Chem.*, 2018, 57, 6742-6753 from reference 117.[117]

When this sample system was used with methyl 4,6-d_2-nicotinate a ^{1}H signal enhancement of 3000-fold was observed with a residual catalyst concentration of 1.5×10^{-6} M and 0.06% chloroform-*d* present in the aqueous layer.[157]

With the large signal enhancements observed with ^{1}H and the range of nuclei that can be polarised using SABRE, there are a large range of applications which can be applied to this. These include the analysis of low concentration analytes within solution.[159, 160] This has included the development of hyperpolarised NMR experiments such as the examination of 2D DOSY,[161] COSY,[162] HMBC[162] and ultrafast EXSY measurements[163] With the development of analysis of low concentration analytes this has progressed into the study of metabolomics with *p*-H_2 at nanomolar concentrations.[164]

1.4 Use of a co-ligand in SABRE

A key requirement for successful SABRE is the formation of an iridium hydride complex that can reversibly bind both a substrate and *p*-H_2. However, in some cases this is not possible and therefore a co-ligand can be employed to drive the formation of an active SABRE complex. For example, if the concentration of substrate is too low to observe the use of a co-ligand is required. Tessari *et. al.* (2014) reported the use of a co-ligand to observe hyperpolarised signals at µM concentrations.[159] This was required to allow the SABRE pre-catalyst to become activated and to stabilise the active catalyst to allow the substrate to bind. As well as this, they found that the addition of the co-ligand prevented the formation of the complexes $[IrCl(H)_2(IMes)(pyridine)_2]$ and $[Ir(H)_2(IMes)(methanol)(pyridine)_2]Cl$.[159] They stated that a successful co-ligand must bind to the metal centre of the catalyst with the same or lower affinity to that of the substrate of interest but be able to bind to the catalyst more effectively than the solvent used. The co-ligand should be present within the sample so that it is in excess with respect to the SABRE pre-catalyst, the SABRE complex formed must also, like in all SABRE experiments, have an exchange rate favourable to allow the maximum polarisation build up on the substrate. Alongside all of this it is important that the co-ligand used does not have ^{1}H signals which overlap with that of the substrate.[159] The co-ligand used was 1-methyl-1,2,3-triazole (*mtz*) and concentrations between

5 µM and 0.5 µM of pyridine were added to the sample which led to enhanced ^{1}H signals at all of these concentrations.[159]

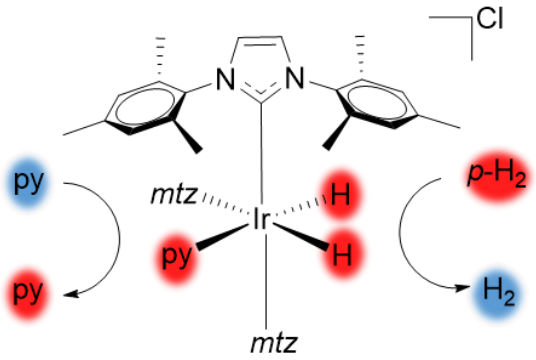

Figure 1.17 – Graphical abstract adapted from the journal *J. Am. Chem. Soc.* 2014, 136, 7, 2695-2698 from reference 159 showing the use of the co-ligand 1-methyl-1,2,3-triazole (*mtz*) to hyperpolarise pyridine (py). [159]

In 2015, Mewis *et. al.* reported the addition of pyridine to aid in the polarisation of ligands which bind weakly to the catalyst. They demonstrated this with the hyperpolarisation of acetonitrile.[147] Here they confirmed, through density functional theory (DFT) calculations, that the formation of the *cis,cis*-$[Ir(H)_2(IMes)(MeCN)(py)_2]Cl$ (where MeCN = acetonitrile and py = pyridine) was more thermodynamically stable than that of the $[Ir(H)_2(IMes)(MeCN)_3]Cl$ complex. Therefore, the SABRE active catalyst is not only more likely to form, it is also now more stable, allowing the acetonitrile to bind to it and become hyperpolarised. This was shown by the 2.5 × increase in ^{1}H signal enhancement which was 8-fold without the presence of pyridine and 20-fold with it. This signal enhancement was further improved, to 80-fold, by using pyridine-d_5.[147] With the success of the ^{1}H signal enhancement, the ^{13}C SABRE hyperpolarisation of acetonitrile was investigated. In unlabelled acetonitrile, a ^{13}C signal was observed at a chemical shift of δ 116.7, producing a signal to noise ratio (SNR) of 11.[147] When the carbon on the nitrile group was labelled a signal was observed at δ 116.7 and produced an SNR of 105.[147]

The use of a co-ligand to increase ^{1}H signal enhancements was further developed by Rayner *et. al.* (2017) to study a range of nicotinamides and nicotinates.[129] This was utilised to try and minimise the number of times each substrate molecule was bound to the catalyst, therefore, reducing the amount of spin dilution in the active catalyst. Here, they used methyl-2,4,5,6-d_4-

nicotinate as the co-ligand, the ^{1}H signal enhancement exhibited on 3-methyl-4,6-d_2-nicotinate was 16415-fold (50% polarisation) on the H-2 site.[129] However the deuterated pre-catalyst [IrCl(COD)(d_{22}-IMes)] was used and the *p*-H_2 pressure was 5.5 bar (absolute).[129] Fekete *et. al.* also reported the use of a co-ligand, here they used acetonitrile.[112] When using the SABRE pre-catalyst [IrCl(COD)(IMes)] they reported a ^{1}H signal enhancement of 515-fold, this signal increased to 830-fold when in the presence of the co-ligand, acetonitrile.[112]

The use of sulfoxides as co-ligands has been recently developed to increase the binding potential of pyruvate and also to optimise the polarisation transfer of this substrate.[165, 166] The formation of two isomers were identified, [$Ir(H)_2$(κ_2-pyruvate)(DMSO)(IMes)] and a ^{13}C signal enhancement of 1070-fold was recorded.[165] Upon optimisation, however, these signals have increased to over 2000-fold for each ^{13}C site on pyruvate.[166] This was accomplished by using [IrCl(COD)(IMes)] with phenylmethylsulfoxide as the co-ligand.[166]

In 2019 Tickner *et. al.* found using a co-ligand produced [$Ir(H)_2$(IMes)(α-$^{13}C_2$-carboxyimine)(**L**)] complexes, where **L** is the co-ligand.[167] In this investigation various co-ligands were used, including benzylamine, phenethylamine, pyridine and imidazole. When an amine, pyridine or imidazole were used both ^{1}H hydride $^{13}C_2$ imine signal enhancements were observed.[167] Using a thiol produced a thiol oxidative addition product which led to 870-fold ^{13}C signal enhancement on pyridine.[167] This occurred due to the α-carboxyimines blocking the active coordination sites, allowing only one site in which pyridine could bind and polarisation could be transferred to it, as shown in Figure 1.18.[167]

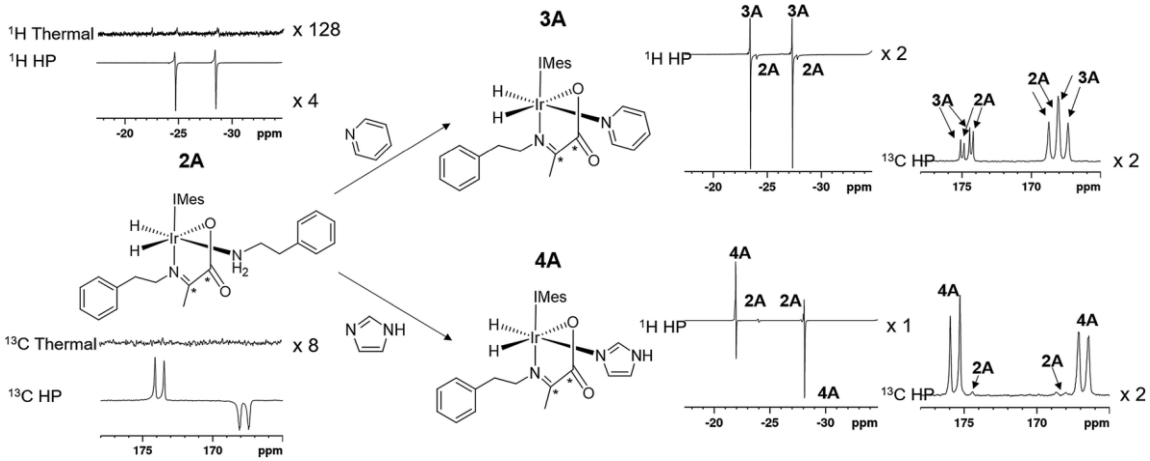

Figure 1.18 – From figure 3 in reference 167 published by The Royal Society of Chemistry, the ^{1}H and ^{13}C hyperpolarised spectrum and corresponding spectrum taken under Boltzmann conditions for 2A are shown. The corresponding complexes when either pyridine (3A) or imidazole (4A) are added to 2A, and their ^{1}H and ^{13}C hyperpolarised and thermally equilibrated spectra are also shown.[167]

1.5 SABRE-Relay

The SABRE method requires the substrate of interest to bind to the iridium catalyst. For this to occur, there needs to be a lone pair that can be donated to the iridium centre, which has often come from either, nitrogen, sulphur or oxygen. However, if the molecule is sterically hindered it is unable to bind to the catalyst even if they contain one or more of these atoms. Therefore, SABRE is somewhat limited to the range of target molecules that are amenable to hyperpolarise.

In 2017, a new technique was discovered whereby ammonia, or a primary amine is first polarised *via* SABRE and upon dissociation from the catalyst the amine NH protons can undergo proton exchange with another target molecule. Hence, the amine can act as a carrier to transfer a polarised proton into the target molecule, in the case shown in Figure 1.19, a primary alcohol. This technique is known as SABRE-Relay.[168]

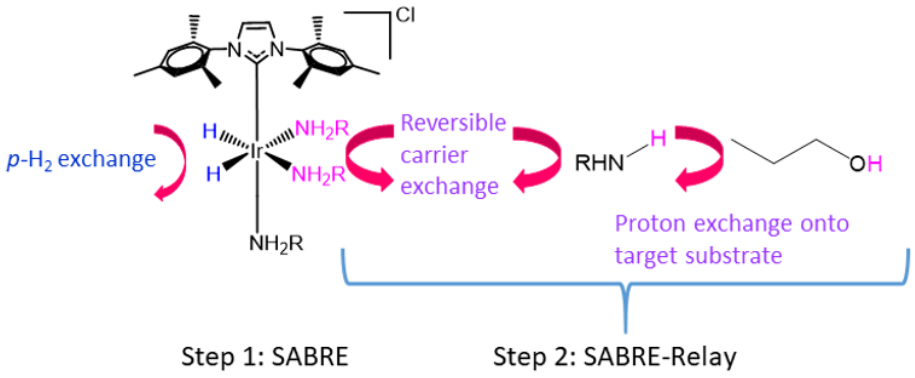

Figure 1.19 – Mechanism of SABRE-Relay. The hyperpolarised amine exchanges into solution. The labile proton on the amine then exchanges onto the substrate. Transfer of hyperpolarisation into the substrate then proceeds *via* the *J*-coupling network to the amine, the labile proton then exchanges with that of the one on the substrate.

When first reported, ^{1}H signal gains of 10-fold were observed for ammonia.[168] This signal enhancement was found to improve to 40-fold upon the addition of water.[168] This was believed to be due to the formation of several isotopologues of the SABRE active catalyst, $[Ir(H)_2(IMes)(NH_3)_3]$, due to H-D exchange.[168]

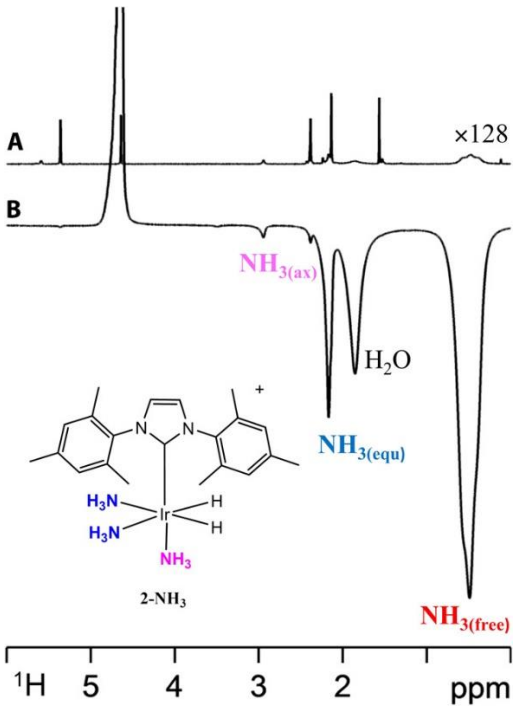

Figure 1.20 – Figure 1 from the journal *Sci Adv*, 2018, 4, eaao6250 *J*, reference 168. (A) ^{1}H NMR of $[Ir(H)_2(IMes)(NH_3)_3]Cl$ taken under Boltzmann conditions at 298 K, a vertical expansion of x128 has been applied. (B) The corresponding ^{1}H SABRE hyperpolarised NMR spectrum.[168]

The first experiments were conducted using a range of alcohols as the target molecule. Examining 1-propanol, a ^{1}H signal enhancement of 265-fold was observed.[168] However, when reducing the concentration of 1-propanol to 1.5 mM (from 15 mM), this increased to over 500-fold.[168] Other molecules were examined, for example propionic acid, where not only were ^{1}H polarised signals observed but also a 109-fold ^{13}C signal enhancement.[168]

Glucose ^{13}C polarisation has also been successfully examined under SABRE-Relay conditions.[168, 169] Hyperpolarised ^{13}C signal enhancements of 250-fold were obtained at high field (9.4 T) and 3100-fold at low field (1 T).[169] This also allowed for the different tautomeric forms to be identified as shown in Figure 1.21. Also, with ^{13}C and ^{2}H labelled glucose, the T_1 lifetime was extended from 1.99 ± 0.1 s to 11.6 ± 0.5 s and a singlet state formed.[169]

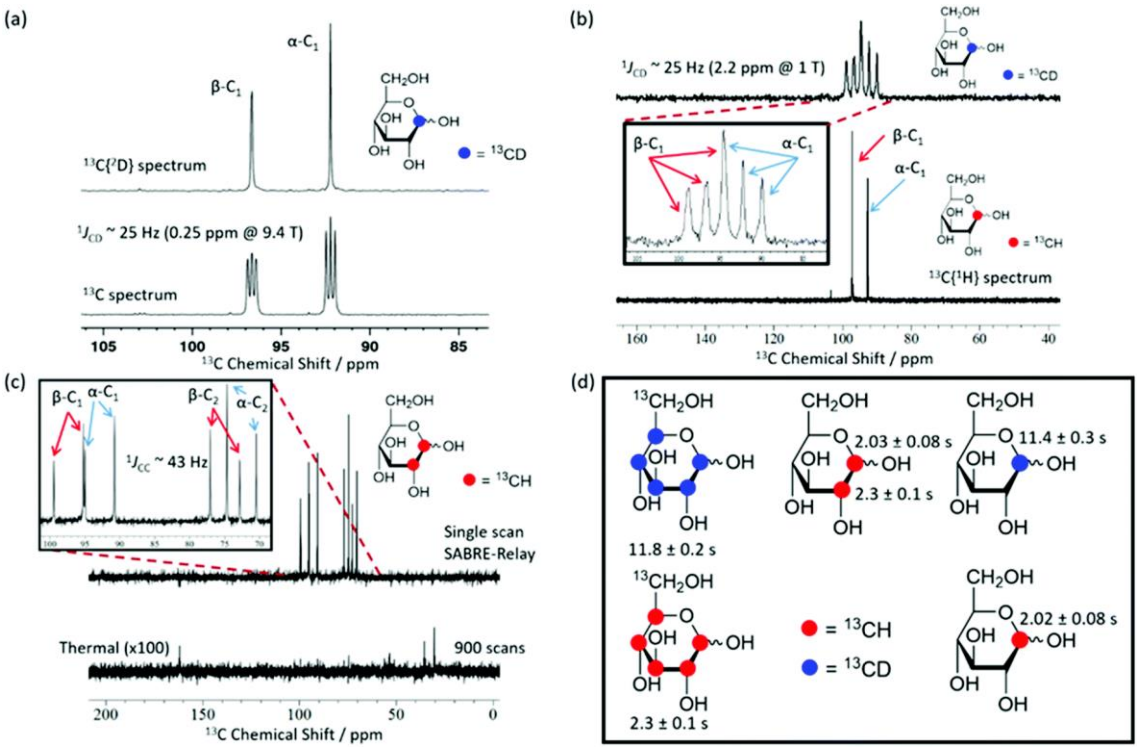

Figure 1.21 – Figure 4 from reference 169 published by The Royal Society of Chemistry. (a) to (c) are ^{13}C NMR spectra. (d) are the different isotopically labelled glucose molecules used along with their T_1 values. (a) –is using D-glucose-1-$^{13}C_1$-d_1 the top is a $^{13}C\{^{1}H\}$ NMR spectrum, bottom is a ^{13}C NMR spectrum, both at 9.4 T. (b) – is the corresponding ^{13}C NMR (top) and $^{13}C\{^{1}H\}$ NMR spectrum of D-glucose-1-$^{13}C_1$-d_1 (bottom) at 1 T and (c) – is of D-glucose-1,2-$^{13}C_2$ top is a 1 scan SABRE-Relay hyperpolarised ^{13}C spectrum, bottom is a thermally equilibrated ^{13}C spectrum, acquired with 900 scans (x 100 for observation) at 1 T.[169]

Another nuclei that has been examined under SABRE-relay conditions is ^{29}Si. As mentioned in Chapter 1 section 1.3.4, signal enhancements of over 700-fold were observed for ^{29}Si using SABRE.[139] When using benzylamine as the relay amine, Rayner *et. al.* observed over 3000-fold signal enhancements on tris(tert-butoxy)silanol, over 4 times that observed with standard SABRE conditions.[170]

As shown here, this technique has not only expanded the range of target analytes and nuclei. It has also increased their signal enhancements, including the improved signal enhancements for ^{13}C and ^{29}Si.[168-170]

1.6 Thesis outline

The focus of this research is the application of PHIP based hyperpolarisation, in particular SABRE, as it has been shown to exhibit great potential to produce large enhancements quickly and cheaply.[171] The aims of this thesis are to investigate the hyperpolarisation of ^{1}H and a range of X-nuclei including ^{19}F, ^{13}C and ^{31}P within simple *N*-heterocyclic molecules and biological molecules such as urea, adenosine triphosphate, uracil and fluorouracil.

^{1}H is the most exploited nuclei in NMR and MRI detection, it has a high abundance and sensitivity due to its high gyromagnetic ratio. However, the use of X-nuclei has become popular due to their large chemical shift range, low or negligible background signal and reduction in line-broadening.[172] Unfortunately some of these X-nuclei for example, ^{13}C have a low natural abundance and therefore using hyperpolarisation techniques to increase their signal is advantageous for MRI[173, 174] and reaction monitoring.[6]

The substrates urea, adenosine triphosphate, uracil and fluorouracil are to be explored within this thesis, picked for their various X-nuclei and their biological relevance. For example urea is already used as a perfusion agent.[175] Using ^{31}P MRI in adenosine triphosphate would be advantageous for cell metabolomics, as this would take a long time to achieve using conventional methods,[176] hyperpolarising this nuclei would make this examination easier. 5-fluorouracil is one of the commonest anti-cancer agents[177] and using the ^{19}F of this molecule could be beneficial to examine the efficacy of this drug when used to treat a specific tumour/cancer within a patient.

Pyrimidine will be examined first as it is a biological motif to many simple molecules, including DNA and RNA nucleobases such as thymine, cytosine and uracil.[43] The aim is to optimise the hyperpolarised ^{1}H NMR signal by examining the NHC of the catalyst based on the SABRE pre-catalyst, [IrCl(COD)(IMes)] (IMes = 1,3-bis(2,4,6-trimethylphenyl)imidazole, COD = 1,5-cyclooctadiene). Investigations into the polarisation transfer field (PTF) of pyrimidine and examining the effects of changing the concentration of the substrate and catalyst will also be undertaken. An examination into the exchange mechanism will also be carried out.

The pyrimidine motif is also contained in one of the longest standing anti-cancer drugs, 5-fluorouracil.[177, 178] Therefore, if pyrimidine is successful the ^{1}H and ^{19}F nuclei will be examined under SABRE conditions for this molecule. ^{19}F has no background signal and therefore could be used as a way of tracking treatment of a tumour. Therefore, if ^{19}F polarisation is successful, an examination into the exchange mechanism will be undertaken along with possible ^{19}F phantom MR images. As well as fluorouracil, other simple, fluorinated *N*-heterocycles will be examined as their motifs are found in other drug scaffolds.[179, 180] An examination into the exchange mechanism will also be undertaken along with an investigation into the optimal polarisation field transfer of both ^{1}H and ^{19}F.

With the development of SABRE-Relay, ^{19}F will also be examined under these conditions with the potential to produce higher signal enhancements than those with SABRE. If this is successful, again possible phantom MR images will be obtained to demonstrate the ease of which this could be used as a possible diagnostic tool. Alongside ^{19}F this thesis will also examine the X-nuclei ^{13}C, ^{15}N and ^{31}P under SABRE-Relay conditions. The molecules under investigation with SABRE-Relay will be biologically relevant molecules including urea and adenosine triphosphate.[43]

As proof of concept, the oxalate motif will also be examined under SABRE-Relay conditions as it may offer access to long ^{13}C magnetic lifetimes and large signal enhancements. Due to the symmetry of sodium oxalate a study will be undertaken to ascertain whether a possible singlet state could be formed between the two carbons within the molecule. This has previously been achieved by Levitt *et. al.* (2014) using labelled ^{18}O within the molecule.[181, 182]

Chapter 2: Exploring SABRE with pyrimidine

2.1 Hyperpolarisation of pyrimidine and its derivatives

The pyrimidine motif is found within the DNA and RNA nucleobases, cytosine, thymine and uracil, whose structures are shown in Figure 2.1. Pyrimidine derivatives are known to exhibit a range of biological and pharmaceutical applications which include acting as anti-viral (Cidofovir[183] and Idoxuridine[184]), anti-cancer (5-fluorouracil[185]), anti-fungal (Flucytosine[183]) and anti-bacterial drugs (Trimethaprim[184]). Additionally, this motif is found within vitamin B, vitamin B1, folic acid and riboflavin.[186]

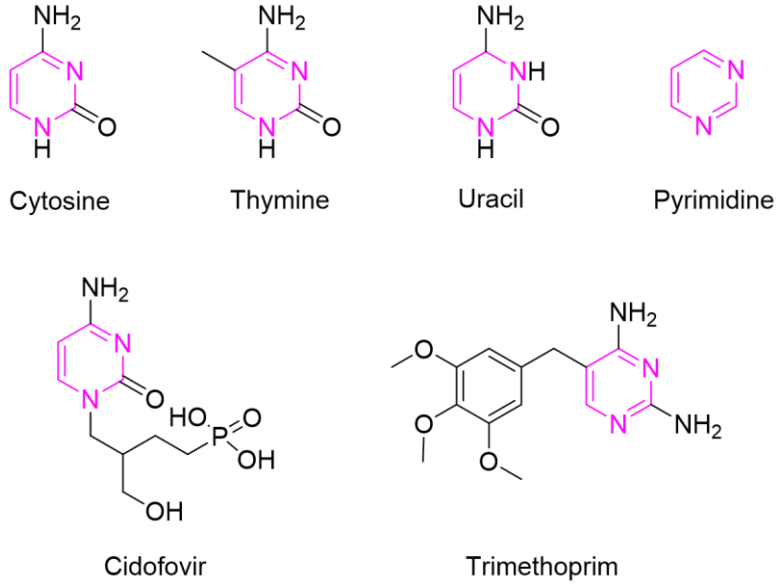

Figure 2.1 - Structures of the DNA and RNA nucleobases cytosine, thymine and uracil and pyrimidine along with two commercially available drugs based upon the pyrimidine motif, Cidofovir and Trimethoprim.

The hyperpolarisation of nucleic acids, from bone samples, has been carried out by DNP.[71] Pyrimidine, purine, ribose and deoxyribose motifs were detected and distinguished in this work by solid state NMR. Pyrimidine and its derivates have also been shown to be readily amenable to the SABRE process.[121, 129, 135, 139] As this process requires the simultaneous and reversible binding of the substrate and *p*-H_2 to the iridium centre of the catalyst,[13] it is not surprising that pyrimidine (and other *N*-heterocyclic substrates) are effective substrates due to the presence of nitrogen lone pairs that are suitable for ligation. In this chapter, the SABRE hyperpolarisation of pyrimidine is

developed, and several key parameters needed for high signal enhancement defined. These include optimal substrate concentration, catalyst concentration and catalyst structure.

2.1.1 Initial SABRE experiments and characterisation

In order to complete this work an NMR tube containing [IrCl(COD)(IMes)] (5 mM) and pyrimidine (20 mM) dissolved in methanol-d_4 (0.6 mL) was exposed to 4 bar H_2 to form an active SABRE system. Subsequently, the H_2 gas was removed and replaced with *para*-hydrogen (p-H_2) at the same pressure. The sample was then shaken at 65 G in the stray field of the magnet for 10 seconds, before being rapidly placed into an NMR spectrometer. At this point, a ^{1}H NMR spectrum was immediately acquired for which Figure 2.2 displays a typical result.

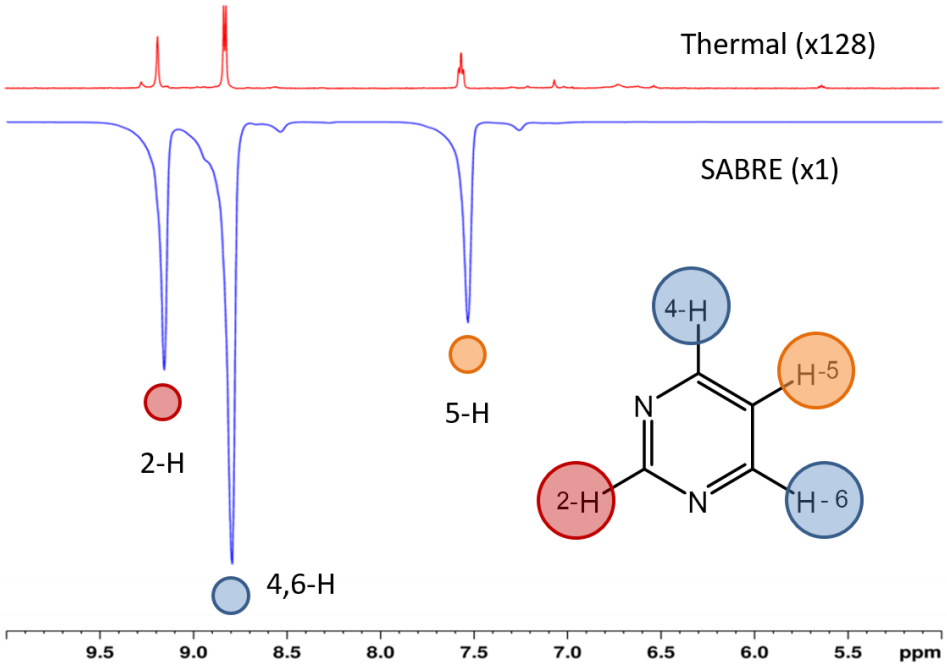

Figure 2.2 – ^{1}H NMR spectra of pyrimidine (20 mM), [IrCl(COD)(IMes)] (5 mM). Top is a 1 scan thermally equilibrated spectrum which was left in the NMR for two minutes prior to acquisition (x32 vertical scale). Bottom is a 1 scan ^{1}H SABRE hyperpolarised spectrum of pyrimidine after polarisation transfer at 65 G.

It should be clear from the two NMR spectra in this figure that the signals for pyrimidine are much stronger than those seen in a spectrum collected under Boltzmann conditions. The corresponding signal enhancements were calculated using standard literature methods[13, 119, 162] which, in brief, comprise dividing the integral of the enhanced peak by that of the corresponding

peak in the thermal NMR spectrum collected after equilibration in the magnet for > 1 minute. Using this method, the average signal enhancements for each of the pyrimidine proton resonances were −489 (2-H), −439 (4- and 6-H) and −381 (5-H). It is therefore clear that SABRE offers a route to dramatically improve the detectability of materials possessing such functionality.

2.1.2 Formation and Characterisation of [Ir(H)$_2$(IMes)(pyrimidine)$_3$]

It is well established in the literature that the reaction of [IrCl(COD)(IMes)] begins with the displacement of its chloride ligand by the substrate, before oxidative addition of H_2 takes place.[94, 119] Subsequently, hydrogenation of the COD ligand and binding of additional substrate molecules occurs and this ultimately leads to a SABRE active complex of type [Ir(H)$_2$(IMes)(substrate)$_3$]Cl. This result has been shown experimentally for pyridine, pyridazine and phthalazine and is also supported by DFT calculations.[119, 187] We sought here to examine the mechanism of the reaction between [IrCl(COD)(IMes)] and pyrimidine in the presence of H_2. The proposed mechanism, based on this literature precedent, is shown in Figure 2.3.

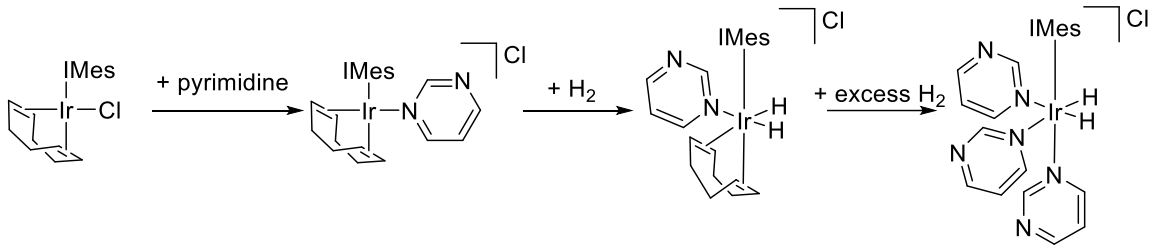

Figure 2.3 – Proposed mechanism of formation of the active SABRE catalyst resulting from the reaction of [IrCl(COD)(IMes)] and pyrimidine in the presence of H_2.

An NMR tube containing [IrCl(COD)(IMes)] (5 mM), pyrimidine (20 mM) in methanol-d_4 (0.6 mL) was prepared and examined by NMR spectroscopy. Evidence for the displacement of chloride by pyrimidine was observed due to the observation of four new resonances in the ^{1}H NMR spectrum at positions diagnostic of bound pyrimidine; at δ 8.76 (doublet, 2.85 Hz), 8.57 (singlet), 8.16 (doublet, 4.72 Hz) and 7.43 (complex multiplet). These resonances integrate in a 1 : 1 : 1 : 1 ratio and are assigned to the H-2, H-6, H-4 and H-5 protons of this ligand respectively on the basis of 2D NMR methods. Subsequently, this sample was cooled to 245 K and H_2 (4 bar) added prior to NMR interrogation at the same temperature. Two characteristic hydride ligands

were detected at δ −12.05 and −17.03 and the full low temperature 2D NMR characterisation of the associated complex confirmed it to be $[Ir(H)_2(COD)(IMes)(pyrimidine)]Cl$. The hydride resonance for this species that appears at δ −12.05 is due to a ligand that lies *trans* to COD while the resonance at δ −17.03 arises from a ligand that is *trans* to pyrimidine. See Appendix section A.1 for full NMR assignments.

Upon warming the NMR spectrometer to 295 K, and adding more hydrogen, conversion of this complex to $[Ir(H)_2(IMes)(pyrimidine)_3]Cl$ occurs. A single hydride resonance is seen for this species at δ −22.37 while resonances for equatorially (δ 8.99, 8.81, 8.62 and 7.32) and axially (δ 9.06, 8.34, 8.72 and 7.17) bound pyrimidine are also readily apparent. Free pyrimidine ^1H peaks are also observed at δ 9.23, 8.87, and 7.62. The hydride spectrum of this sample is complicated by the presence of a second product. This product is characterised by its inequivalent hydride ligands which appear at δ −23.20 and −24.69, the latter being a clear doublet with a hydride-hydride coupling constant 6.58 Hz. This species is $[IrCl(H)_2(IMes)(pyrimidine)_2]$ on the basis of literature precedent.[111]

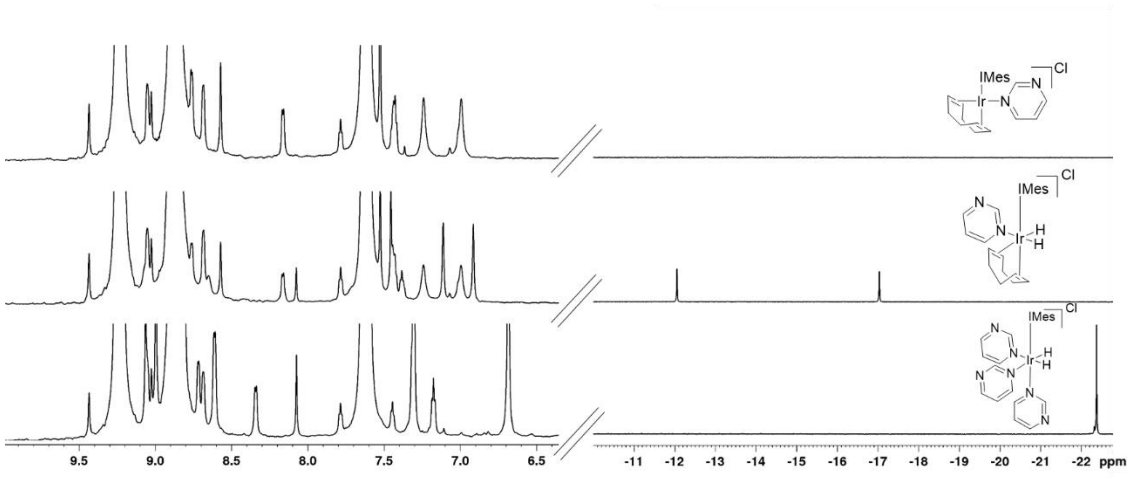

Figure 2.4 – 1 scan ^1H NMR spectra demonstrating the change in complexes that occurs during SABRE, the vertical scale has been expanded 256 times in order to make these resonances visible. Top reflects the intermediate [Ir(COD)(IMes)(pyrimidine)]Cl, middle $[Ir(H)_2(COD)(IMes)(pyrimidine)]Cl$ intermediate, and bottom the SABRE active complex, $[Ir(H)_2(IMes)(pyrimidine)_3]Cl$. Only pyrimidine and hydride areas have been shown here.

2.1.3 Rate of H_2 loss from $[Ir(H)_2(IMes)(pyrimidine)_3]Cl$

The rates of ligand exchange in the active catalyst are a key factor in determining the efficiency of polarisation transfer.[188, 189] This is due to the rate of polarisation transfer being proportional to the hydride-hydride and hydride-substrate scalar couplings in a process which is terminated by ligand loss. Thus, complex lifetime is crucial. This phenomenon has been proven experimentally on a number of occasions[111, 118, 139] and data supports the predicted optimal substrate exchange rate of *ca*. 4.5 s^{-1}.[110]

On the basis of the work of Cowley *et. al.*, this reaction is dissociative[119] and as described by them and others[94, 111, 187] the SABRE process starts with the loss of a substrate molecule from, for example, $[Ir(H)_2(IMes)(pyrimidine)_3]Cl$ which creates a 16 electron intermediate. Subsequently, dihydrogen can ligate to the metal at the vacant site that is created by ligand loss. This product indicates an unusual dihydrogen-dihydride complex and ultimately the elimination of H_2 from it allows for the refreshing of *p*-H_2 within the catalyst system. Rebinding of a substrate molecule then completes the catalytic cycle as shown in Figure 2.5.[94, 111, 187]

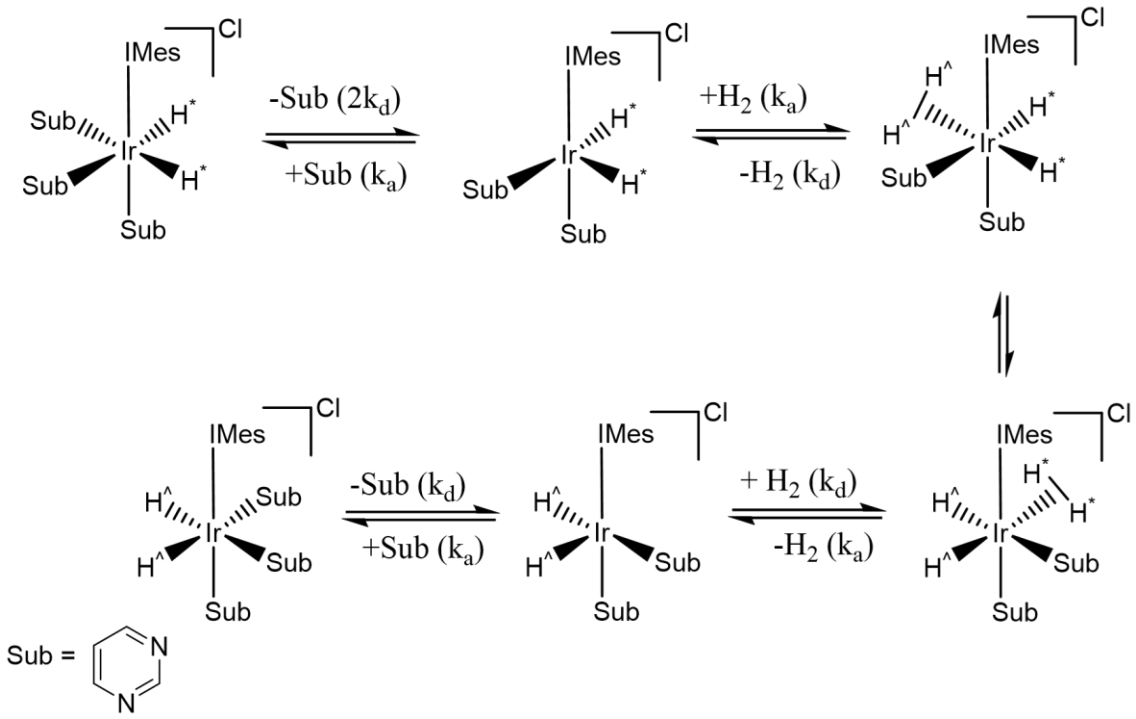

Figure 2.5 - Proposed mechanism for hydrogen exchange in the complex $[Ir(H)_2(IMes)(pyrimidine)_3]Cl$.

This process has been well studied for analogous systems by 1D EXSY methods.[111] The EXSY NMR experiment involves the excitation of a selected bound signal, a delay to allow for ligand or hydrogen exchange and a subsequent acquisition step. By incrementally increasing the time between the excitation and acquisition steps, a series of such measurements can be used to map the exchange process in a quantitative fashion. Thus, comparison of the integral for the free and bound peaks and fitting to a kinetic model can give rate constants for substrate and hydride ligand dissociation.

By varying the time between the excitation and acquisition steps (mixing times), usually from 0.005 to 1.0 seconds to span the reaction. This allows the nuclei which gives the selected signal time to move to a different position, a trace builds up which encodes the exchange process. The ratio of the integral of the bound and free peaks is then defined (normalised to 100) and the results analysed. A plot of signal intensity against mixing times, alongside the simulated data, is used to assess the quality of the result. Precise rate constants are calculated by fitting these data to a suitable differential rate equation using a least mean squares approach. The errors in the resulting rate data were calculated using the Jack-knife method which takes into account the number of observations.[190]

A series of 1D EXSY spectra were therefore recorded on a sample that initially contained [IrCl(COD)(IMes)] (5 mM), pyrimidine (20 mM) in methanol-d_4 (0.6 mL) which was exposed to 4 bar H_2 to form $[Ir(H)_2(IMes)(pyrimidine)_3]Cl$ at 280 K. The loss of its hydride ligands to form H_2 was successfully probed using this method. Figure 2.6 shows a typical 1D EXSY spectra for delay times of 0.005 and 1.0 seconds after the initial excitation of the hydride ligand signal (δ −22.63) of the *tris* complex, $[Ir(H)_2(IMes)(pyrimidine)_3]Cl$. The presence of a signal at δ 4.57 in the result is indicative of the formation of hydrogen during the experiment.

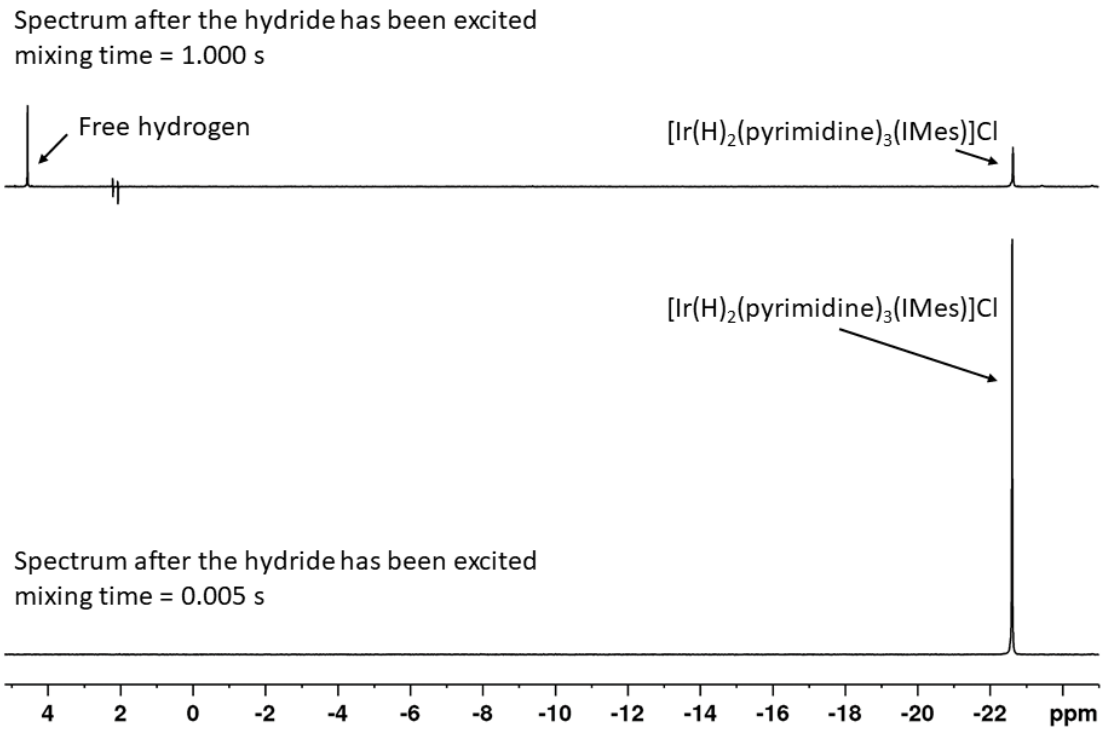

Figure 2.6 – ^{1}H NMR spectra of [Ir(H)$_2$(IMes)(pyrimidine)$_3$]Cl resulting from the 1D EXSY protocol when the hydride resonance of the complex at δ −22.37 is selectively excited and observed at the mixing times 0.005 (bottom spectrum) and 0.1 seconds (top spectrum).

The spectrum is however complicated by exchange into the minor species and free H$_2$. Simulation revealed that H$_2$ loss from [Ir(H)$_2$(IMes)(pyrimidine)$_3$]Cl actually proceeds *via* the minor species. This was proven using the Excel SOLVER package (see experimanetal chapter 7, section 7.2.10). The data was plotted and solved using the established SABRE exchange mechanism. The data did not fit this simulation. However, when the mechanism was changed to allow for the minor species and that the loss of H$_2$ was *via* this species, the data fitted and a rate constant could be found. There are therefore three rates of reaction that are well defined in this mixture. They are the rate of conversion of [Ir(H)$_2$(IMes)(pyrimidine)$_3$]Cl (A**) into [IrCl(H)$_2$(IMes)(pyrimidine)$_2$] (**B**), the reverse of this and the rate the second complex, B, liberates H$_2$. These rate constants are presented in**

Table 2.1 as a function of temperature. The associated errors were calculated from the data during fitting to the kinetic model according to the Jack-knife method.[190] A description of the Jack-knife

error calculation is presented in Chapter 7 section 7.2.9 and an example of this error in relation to the rate constants given here are in the Appendix section A.2, Table A.3.

Table 2.1 – Rate constants obtained for the indicated exchange processes in the chemistry of [Ir(H)$_2$(IMes)(pyrimidine)$_3$]Cl and [IrCl(H)$_2$(IMes)(pyrimidine)$_2$], in methanol-d_4 solution as a function of temperature.

Temperature, (K)	Rate **A** goes to **B** / s^{-1}	Rate H_2 loss from **B** / s^{-1}	Rate **B** goes to **A** / s^{-1}
285	0.613 ± 0.006	1.329 ± 0.010	3.637 ± 0.170
290	1.346 ± 0.004	0.829 ± 0.012	10.366 ± 0.047
295	2.501 ± 0.006	1.982 ± 0.019	17.055 ± 0.063
300	3.978 ± 0.033	4.448 ± 0.080	23.999 ± 0.238
305	7.046 ± 0.155	9.269 ± 0.053	41.576 ± 1.199

From these rate data collected at varying temperatures, activation parameters for hydride loss were determined using the Eyring equation shown in equation 2.1.

$$\ln\frac{k}{T} = \frac{-\Delta H^{\ddagger}}{R}\frac{1}{T} + \log\frac{k_B}{h} + \frac{\Delta S^{\ddagger}}{R} \qquad (2.1)$$

Where k is the rate constant for the loss ofthe hydride ligands from [Ir(H)$_2$(IMes)(pyrimidine)$_3$]Cl, R is the gas constant (8.314 J K^{-1} mol^{-1}), T is temperature in K, k_B is the Boltzmann constant and h is Planck's constant. $\Delta H^{\ddagger}$ is the change in enthalpy and $\Delta S^{\ddagger}$ is the change in entropy associated with this. However, in this mechanism hydrogen can approach the transition state from either direction. Therefore $\ln\frac{2k}{T}$ is used instead of $\ln\frac{k}{T}$ in obtaining these values. A plot of $\frac{1}{T}$ vs $ln\frac{2k}{T}$ enables $\Delta H^{\ddagger}$ to be calculated from the gradient and $\Delta S^{\ddagger}$ from the intercept using a linear regression method. The error for these was calculated by averaging the lower and upper 95%

values and calculating the maximum and minimum $\Delta H^{\ddagger}$ or $\Delta S^{\ddagger}$ values. These parameters are presented in Table 2.2 alongside $\Delta G^{\ddagger 300}$.

Table 2.2 – Activation parameters for the indicated processes observed whilst examining $[Ir(H)_2(IMes)(pyr)_3]Cl$ and $[IrCl(H)_2(IMes)(pyr)_2]$ in methanol-d_4 (where pyr = pyrimidine).

	$\Delta H^{\ddagger}$ kJ mol^{-1}	$\Delta S^{\ddagger}$ J mol^{-1} K^{-1}	$\Delta G^{\ddagger}_{300\ K}$ kJ mol^{-1}
Conversion of $[Ir(H)_2(IMes)(pyr)_3]Cl$ (**A**) to (**B**)	83.3 ± 12.6	50.1 ± 42.8	68.2 ± 1
Loss of H_2 from $[IrCl(H)(IMes)_2(pyr)_2]$ (**B**)	99.8 ± 30.7	105.5 ± 104.2	68.1 ± 1
Conversion of $[IrCl(H)_2(IMes)(pyr)_2]$ (**B**) to (**A**)	73.7 ± 21.4	33.6 ± 72.7	63.7 ± 1

The value of the Gibb's free energy ($\Delta G^{\ddagger 300}$) was calculated using equation 2.2. The error was determined using the average of the upper and lower limits of $\Delta H^{\ddagger}$ and $\Delta S^{\ddagger}$ at 300 K.

$$\Delta G^{\ddagger} = \Delta H^{\ddagger} - T\Delta S^{\ddagger} \qquad (2.2)$$

The rate of conversion of complex **A** to complex **B**, at 295 K is 2.5 s^{-1} and from **B** to **A** it is 17.1 s^{-1}. These values are similar to those presented by Lloyd *et. al* (2014).[111] When examining the ^1H signal enhancement with temperature (see Appendix A.6), the greatest enhancement was observed at 300 K. The rate constant for the conversion of **A** into **B** at this temperature is 4.6 s^{-1} which is close to that of the reported optimal for ligand loss of 4.5 s^{-1}.[110] The rate of H_2 loss is 1.982 s^{-1} at 295 K and proceeds *via* **B**.

The activation data shows that the $\Delta G^{\ddagger 300}$ is very similar for both the conversion of **A** to **B** (68.2 ± 1 kJ mol^{-1}) and that of loss of hydrogen from complex **B** (68.1 ± 1 kJ mol^{-1}). This reflects their

common first step, substrate loss, which dominates the reaction coordinate. The $\Delta G^{\ddagger 300}$ for the conversion of complex **B** back to **A** is lower at 63.7 ± 1 kJ mol^{-1} in accordance with **A** being the dominant species. When examining $\Delta S^{\ddagger}$ it is clear that the temperature range is too small to make any significant deductions as the errors are high.

2.2 Optimisation of the ^{1}H NMR signal enhancement of pyrimidine

The net rate of ligand loss from [Ir(H)$_2$(IMes)(pyrimidine)$_3$]Cl is therefore close to the predicted optimum of 4.5 s^{-1} at 295 K and good SABRE behaviour should result.[110] There are a number of reported routes for improving the size of signal enhancements achieved in the SABRE process. These include the identity of the ancillary ligand in the catalyst, the polarisation transfer field (PTF), the temperature, the pressure of *p*-H$_2$ and the concentration of the catalyst and substrate. Each of these factors will be examined in detail to determine an optimal SABRE enhancement for pyrimidine.

2.2.1 Concentration of substrate

The concentration of substrate has previously been shown to have a dramatic effect on the observed polarisation level across a number of substrates.[139, 187, 191] For example, when 4 equivalents of pyridine (20 mM) and [IrCl(COD)(IMes)] (5 mM) are utilised a 5500-fold total ^{1}H NMR signal enhancement was achieved.[111] This decreases to just *ca*. 1000-fold when 20 equivalents (100 mM) of pyridine is present. As the SABRE process is dissociative, the rate of substrate loss is independent of the concentration of substrate present. However, when there are fewer molecules of substrate available to bind to the metal centre, there is a higher probability that a partially polarised substrate will rebind. Thus, the observed polarisation level will increase due to reduced spin dilution when a fixed amount of catalyst and *p*-H$_2$ are present. Conversely, as the rate of magnetic state relaxation is increased whilst the substrate is bound to the catalyst,[129] higher substrate concentrations can lead to increased observed T_1 values due to changing the equilibrium position which can help offset this effect. For the case of 5-(tributylstannyl)pyrimidine, a 4-fold excess of substrate was found to give the highest level of ^{1}H signal gain, however, an 18-fold excess was found give the higher level of ^{119}Sn polarisation.[139]

For this investigation 13 samples were prepared using [IrCl(COD)(IMes)] (5 mM) with varying concentrations of pyrimidine (20-500 mM, 4-100 equivalents) in methanol-d_4 (0.6 mL). Each sample was activated with H_2 as previously described. Once activation was completed, 4 bar *p*-H_2 was added and the SABRE experiment was performed at 65 G at 298 K. The resulting ^{1}H signal gains for each proton resonance are shown in Figure 2.7 (see Table A.4 in Appendix for data).

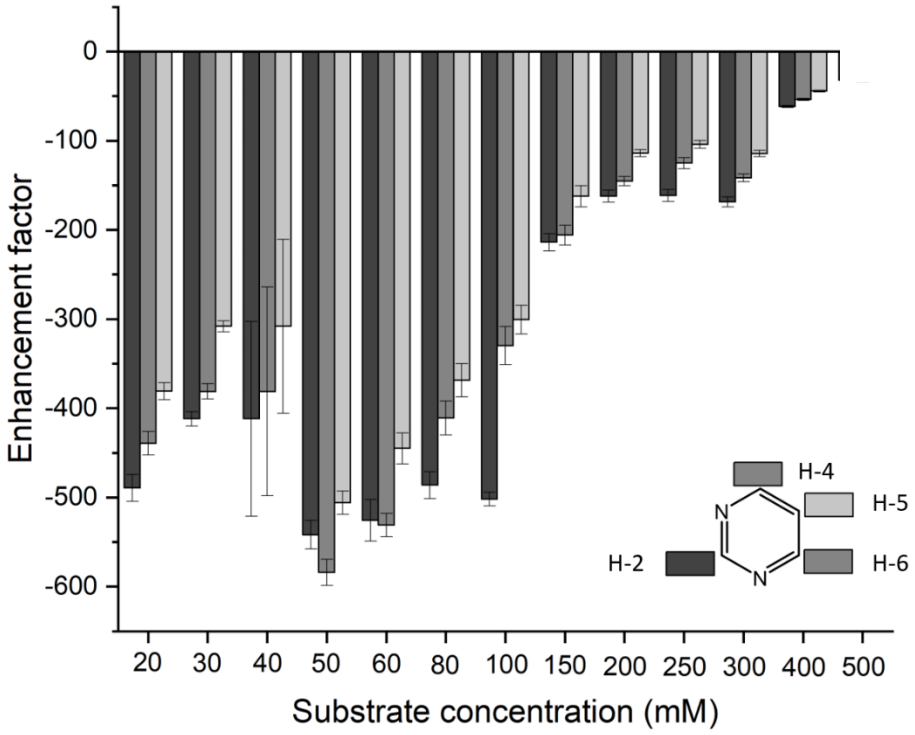

Figure 2.7 – A plot of the individual signal enhancements of the ^{1}H's on the free pyrimidine as a function of pyrimidine excess with [Ir(H)$_2$(IMes)(sub)$_3$]Cl (5 mM) catalyst in methanol-d_4 (0.6 mL) exposed to 4 bar of *p*-H_2 as a function of substrate concentration at 298 K. A minimum of 5 experiments was undertaken and an average enhancement was calculated for each substrate concentration, see Table A.4 in the Appendix.

Figure 2.7 shows that the signal enhancement is dependent upon substrate concentration. Surprisingly, the highest enhancement is found at 50 mM concentration (10 equivalents) of pyrimidine which differs from the optimal ^{1}H signal gains for other substrates.[111, 129, 187]

In previous work carried out by Olaru *et. al.* (2016) where both ^{119}Sn and ^{29}Si were hyperpolarised *via* SABRE using the substrates, 5-(tributylstannyl)pyrimidine and 5-(trimethylsilyl)pyrimidine respectively, they found that at 50 mM concentrations the greatest polarisation was gained.[139]

These substrates are multivalent and when the reaction times of these experiments were extended a series of iridium trimers formed; these were confirmed by X-ray crystallography. It is hypothesised that these trimers form more readily at low substrate concentration and this change in catalyst speciation could explain the lower ^{1}H NMR signal enhancements seen here at reduced loadings of pyrimidine. Crystals suitable for X-ray diffraction could not be obtained from the experiments reported here.

2.2.2 Concentration of catalyst

Whilst the catalyst is required to allow the transfer of polarisation from the *p*-H_2 to the substrate *via* the *J*-coupling network, it also contributes to the relaxation of the substrate back to its thermal equilibrium during a SABRE experiment when the *p*-H_2 is consumed. The presence of the catalyst in solution also decreases the apparent spin-lattice relaxation (T_1) of the free substrate through exchange (for experimental details and table of results see Appendix section A.4.). This decrease in T_1 will result in a decrease in the enhanced signal seen after a SABRE experiment has been performed due to the time required to transfer the sample to the detection field.[116] Therefore, the effect of the concentration of catalyst was investigated. For these experiments, the ratio between the catalyst and the substrate was kept the same whilst the concentration of the polarisation catalyst was increased. A 1:40 ratio of catalyst: substrate was used to minimise any change in speciation effects. Figure 2.8 shows the signals enhancements seen in the 2-H, 4, 6-H and 5-H positions of pyrimidine that result.

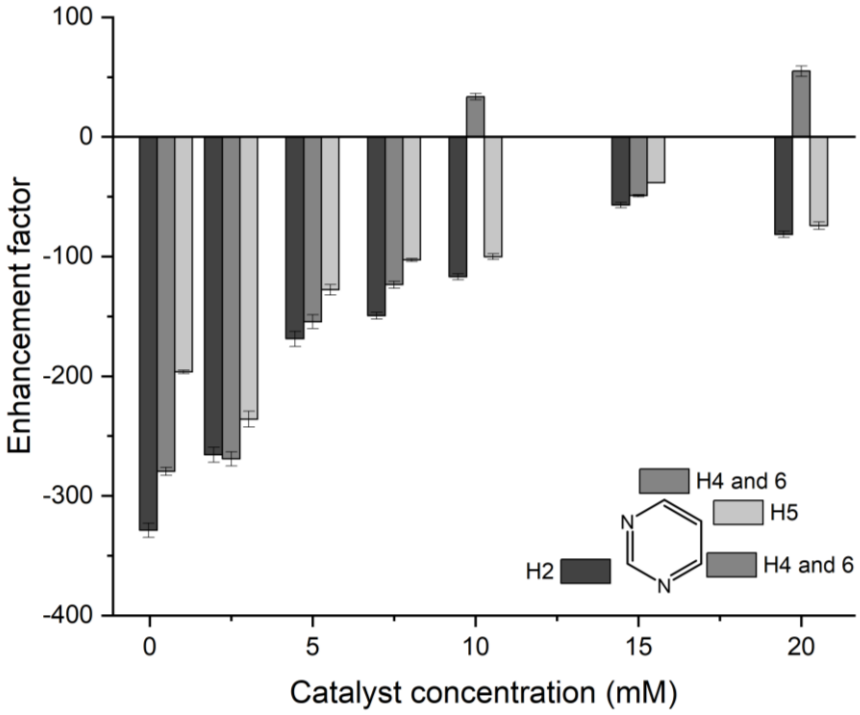

Figure 2.8 – A plot of the specified ^{1}H NMR signal enhancements for free pyrimidine as a function of catalyst concentration. The ratio of the active catalyst: pyrimidine used was 1:40 in methanol-d_4 (0.6 mL). A minimum of 5 experiments was undertaken for each data point and an average enhancement was calculated for each catalyst concentration, see Table A.5 in Appendix.

The optimum catalyst concentration was found to be 0.5 mM which gave enhanced signals of −329 ± 6-fold for H-2, −280 ± 4-fold for H-4 and H-6 and −197 ± 1-fold for H-5. However, when examining the signal to noise ratio (SNR) of this sample it was found to be low (SNR = 825). The catalyst concentration at 2.5 mM gave the second highest signal enhancements and yielded a higher SNR value of 15206. Therefore, the balance between signal enhancement and SNR is shown. For the proceeding experiments a 2.5 mM concentration of catalyst was employed as the signal size is more important for potential applications than the signal enhancements.

2.2.3 Type of catalyst

In 2009, SABRE was initially achieved with Crabtree's catalyst which bears a phosphine ligand.[93] Two years later it was reported that more efficient SABRE catalysis can be achieved by using an iridium *N*-heterocyclic carbene (NHC) catalyst, such as [IrCl(COD)(IMes)]. The development of the SABRE catalyst has continued to draw attention in an attempt to improve the observed signal gains.[111, 114, 122, 132 118] An extensive study of the carbene catalyst was undertaken in 2018 by Rayner

et. al. by examining the Tolman Electronic Parameter (TEP) and the buried volume (% V_{bur}) of a range of NHC catalysts.[118] From this study, it was established that changing these parameters can tune the observed signal enhancement for a given substrate. If a substrates exchange rate is slow with the IMes derived system, then a sterically bulky carbene ligand could be beneficial to speed up dissociation. Conversely, if the substrates exchange rate is fast, then an electron deficient catalyst can improve the observed signal gains. This effect was seen for ^{1}H, ^{13}C and ^{15}N SABRE hyperpolarisation. Additionally, selective deuteration of the carbene ligand has been shown to be an effective method for extending the magnetic relaxation times for substrates bound to the catalyst.[112, 118, 132, 133, 147] This has resulted in higher polarisation levels being achieved through a combination of reducing spin dilution and increasing effective T_1 relaxation times.

For pyrimidine, a range of catalysts of the type [IrCl(COD)(NHC)] (where NHC = *N*-heterocyclic carbene) were selected for investigation as shown in Figure 2.9. These encompass a range of steric and electronic properties; increased TEP and %V_{bur} (catalysts **4** and **5**) or decreased parameters (catalysts **1**-**3** and **6**). Catalyst **5** is the standard pre-catalyst [IrCl(COD)(IMes)] and catalyst **7** is the most electron deficient used, with chlorine groups on the backbone of the imidazole group.

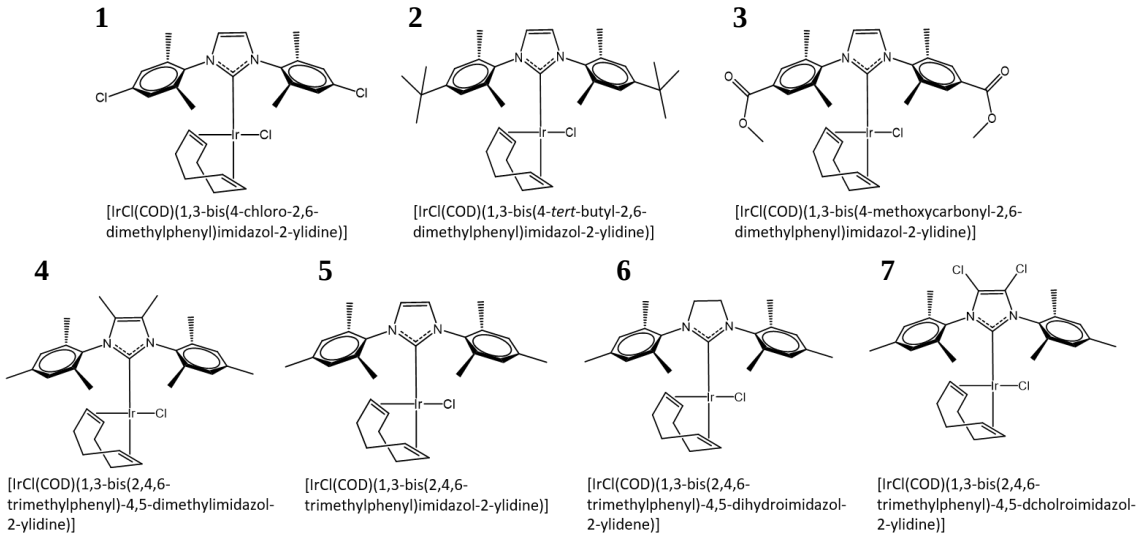

Figure 2.9 – Catalysts, based on the [IrCl(COD)(IMes)] motif, used for the optimisation of the pyrimidine substrate.

Each catalyst was present at a 2.5 mM concentration with an initial substrate concentration of 25 mM (10 equivalents) as previously discussed. Figure 2.10 shows the ^{1}H signal enhancement

for each ^{1}H resonance of pyrimidine achieved with each of the catalysts listed. From these results it is clear that catalyst **4**, [IrCl(COD)(1,3-bis(2,4,6-trimethylphenyl)-4,5-dimethylimidazol-2-ylidine)] gives the best NMR signal enhancement followed by the standard catalyst [IrCl(COD)(IMes)] (catalyst **5**).

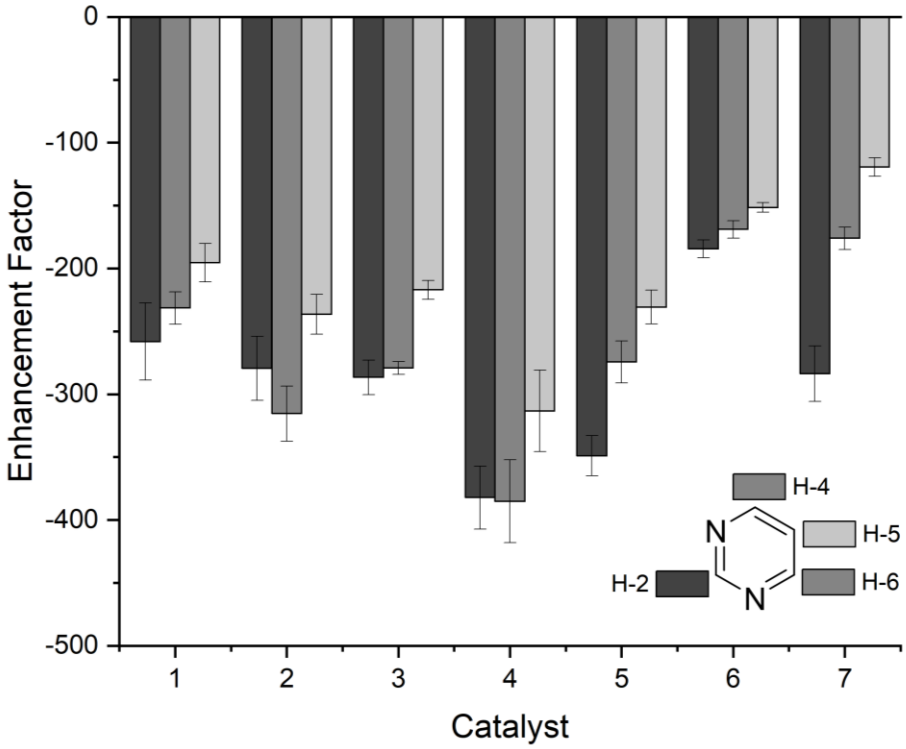

Figure 2.10 – The average ^{1}H signal enhancement of each of hydrogen resonance on pyrimidine (25 mM) with catalysts 1-6 (2.5 mM) in methanol-d$_4$ (0.6 mL) when exposed to 4 bar *p*-H$_2$ at 298 K. Polarisation transfer was conducted at 65 G (for table of results see Table A.6 in Appendix).

Catalyst 4 must therefore have optimal T_1 and exchange rates to give the greatest enhancement for pyrimidine. With this in mind, T_1 data for pyrimidine was determined in the presence of the catalyst (2.5 mM) in methanol-d_4 (0.6 mL) when exposed to 4 bar hydrogen.

2.3 T_1 relaxation values for the ^{1}H NMR resonances for pyrimidine

It is beneficial if the hyperpolarised magnetic states that are created during the SABRE process are able to last until the point of measurement. Therefore, long T_1 values are essential. For example, if SABRE is to realise its *in vivo* potential, the hyperpolarised probe would need to survive until it reached the targeted area of the body. As discussed in Chapter 1 (section 1.3.3), it

is the interaction between molecules which causes T_1 relaxation. Therefore, it can be determined that different molecules within an NMR sample will change the T_1 of the substrate.[8, 130, 131]

2.3.1 T_1 data for substrate and SABRE active catalyst

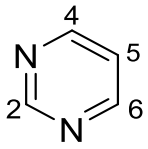

Figure 2.11 – Pyrimidine molecule with labelled hydrogen positions.

It is reported in the literature that the T_1 relaxation times for pyrimidine in a degassed solution of methanol-d_4 are 77.4, 38.8 and 29.2 seconds for the H-2, H-4/6 and H-5 resonances respectively.[129] For comparison, the effective T_1 values of the free pyrimidine resonances measured in the presence of catalysts **1-7** (2.5 mM) in methanol-d_4 (0.6 mL) and 4 bar H_2 are shown in Table 2.3.

Table 2.3 – ^{1}H T_1 data for pyrimidine (25 mM) in the presence of catalyst (2.5 mM) in methanol-d_4 (0.6 mL) at 295 K.

Catalyst	T_1 inversion recovery on each hydrogen on pyrimidine (s)		
	H-2	H-4 and 6	H-5
None	77.4	38.8	29.2[129]
1	42.5 ± 0.6	28.1 ± 0.3	19.7 ± 0.2
2	30.1 ± 0.4	23.1 ± 0.2	17.5 ± 0.1
3	29.9 ± 0.7	21.7 ± 0.2	14.9 ± 0.1
4	32.3 ± 0.7	23.3 ± 0.2	17.6 ± 0.1
5	36.6 ± 0.4	24.8 ± 0.2	18.9 ± 0.1
6	27.8 ± 0.3	20.5 ± 0.2	16.9 ± 0.1
7	48.2 ± 0.4	35.2 ± 0.4	26.6 ± 0.4

The data presented in Table 2.3 shows that the presence of the iridium catalyst reduces the measured T_1 relaxation value in all cases when compared to that of pyrimidine alone. This is as expected as the catalyst reduces the effective T_1 of the substrate.[129]

Catalyst **7** has the smallest influence on the T_1 relaxation values for free pyrimidine in solution. It bears Cl groups on the imidazole ring of the *N*-heterocyclic carbene backbone of the catalyst which has been shown previously to slow the rate of ligand dissociation in a number of analogous studies.[118] The presence of Cl on the imidazole backbone also appears to remove a dominant spin-spin coupling route to relaxation of the bound substrate.

However, the greatest ^{1}H signal enhancements were produced with catalyst **4** despite it not having the longest T_1 values. Catalyst **4** must therefore exhibit the optimal rate of ligand dissociation for the SABRE process and this should be investigated in the future.

Further extension of the T_1 relaxation times can be obtained by selectively deuterating the catalyst. In 2017, Rayner *et. al* deuterated pyrimidine in two positions to give 4,6-d_2-pyrimidine and 2,5-d_2-pyrimidine.[129] The data from their findings, along with the optimal enhancement gathered from pyrimidine, is shown in Table 2.4. The literature describes the polarisation levels for the deuterated pyrimidines as a percentage, however, for ease of comparison these values have been converted to signal enhancement at 9.4 T.

Table 2.4 – ^{1}H T_1 and signal enhancements for pyrimidine under optimal conditions, [IrCl(COD)(1,3-bis(2,4,6-trimethylphenyl)-4,5-dimethylimidazol-2-ylidine)] (2.5 mM), pyrimidine (25 mM) in methanol-d_4 (0.6 mL). For the 4,6-d_2-pryimidine and 2,5-d_2-pyrimidine [IrCl(COD)(IMes)] (5 mM) was used with 20 mM of substrate in methanol-d_4 (0.6 mL). * = Personal communication within the group from Phil Norcott who carried out the experiments for this substrate.

Substrate	T_1 (s)			Signal enhancement		
	H-2	H-4,6	H-5	H-2	H-4,6	H-5
pyrimidine	32.3	23.3	17.6	394 ± 15	385 ± 19	313 ± 19
4,6-d_2-pyrimidine*	30.1	n/a	72.2	558	n/a	525
2,5-d_2-pyrimidine	n/a	34.6	n/a	n/a	1182	n/a[129]

From Table 2.4 the deuterated pyrimidines produce a slightly greater ^{1}H NMR signal enhancement when compared to undeuterated pyrimidine. These effects are particularly clear when the protons in the 2 and 5 position of pyrimidine are deuterated. The ^{1}H NMR signal enhancement for the H-4, 6 position increases from 385 ± 19-fold to 1182-fold ± 53 assuming the same percent error as observed with optimised pyrimidine. It may therefore be advantageous in the future to examine these substrates further.

2.4 Magnetic Resonance Imaging

Phantom based SABRE hyperpolarised ^{1}H MR images have previously been presented for a range of substrates, including nicotinamide, phthalazine and vitamins B3.[129, 187, 191] With the success of the ^{1}H NMR signal enhancements for pyrimidine, an investigation into their applicability for ^{1}H MRI detection in phantoms was conducted. A 10 mm NMR tube, containing pyrimidine (500 mM) with a SABRE pre-catalyst either **1-6** (5 mM) and methanol-d_4 (3 mL), was exposed to 4 bar p-H_2 for subsequent hyperpolarisation using the SABRE (shake & drop) method. Following a single hyperpolarisation step, either Free Induction with Steady State Free Precession (FISP) or Rapid Acquisition with Relaxation Enhancement (RARE) single slice images (see Figure 2.12) at 9.4 T were obtained (see experimental 7.2.12).

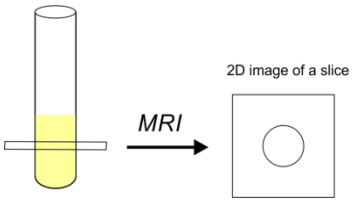

Figure 2.12 – A schematic diagram of the slice used to take the FISP magnetic resonance (MR) image.

Resultant image SNRs (thermal and hyperpolarised) for both FISP and RARE experiments are shown in Table 2.5 and their absolute SNRs calculated (following normalisation to the equivalent thermal image). The thermal and hyperpolarised SNR for FISP is generally lower than that observed with a RARE sequence. This is due to a smaller excitation flip angle being used in FISP (in this case 5°) compared to the RARE sequence which utilised a 90° excitation pulse. Therefore, using the absolute SNR gain, means that SNR is independent of flip angle.

Examining the absolute SNRs, catalyst **4** gives the greatest gain when examined under the RARE sequence. It is noted that absolute SNR is within standard error of that found for catalyst **1** and **2**. This is slightly unexpected as catalysts **1** and **2** have increased TEP and $\%V_{bur}$ compared to **4**. This could be a due to the increased substrate concentration (500 mM vs 25 mM) which may alter the exchange rate dynamics.

Examining the FISP data the pattern of absolute SNR is the same as that observed for RARE, apart from catalyst **4**, which seems to be an outlier. It is noted that FISP measurements are single point measurements (see below) and it could be that polarisation transfer conditions were hampered by the manual 'shake and drop' approach used for polarisation transfer. Therefore, it would be advantageous in the future to repeat the FISP data acquisition not only to check this but also to establish the standard error across such experiments.

Table 2.5 – SNR ratios for pyrimidine (500 mM) when in the presence of different SABRE pre-catalysts (5 mM) used in Chapter 2 section 2.2.3 when using either an FISP or RARE protocol. Absolute SNR has been calculated by SNR_{Hyp} / SNR_{Th}.

Catalyst number	FISP			RARE		
	SNR_{Th}	SNR_{Hyp}	Absolute SNR	SNR_{Th}	Mean SNR_{Hyp}	Absolute SNR
1	1.1	61.0	55.5	9.1	398.6	43.7 ± 1.5
2	1.1	63.1	57.4	9.5	382.1	47.9 ± 5.9
3	1.2	34.6	28.8	13.5	278.8	20.7 ± 2.5
4	1.1	40.1	36.5	9.5	459.2	48.2 ± 6.4
5	1.1	27.1	25.0	17.3	259.8	21.9 ± 1.0
6	1.1	16.9	15.4	9.6	144.6	15.1 ± 2.8

The FISP sequence was primarily used to produce a series of images over time to investigate signal decay under constant probing with 5° flip angle radio frequency (*r. f.*) (to maintain the steady state for readout). The image repetition time (TR) for this sequence was 600 ms meaning several images could be taken over the T_1 lifetime of the substrate (between 15 and 48 s) before

hyperpolarised signal is 'lost' due to natural decay to thermal equilibrium. Decay experiments were carried out for all catalysts tested. Figure 2.13, shows representative time resolved data for catalyst **2** (exhibiting the greatest SNR gain, see Table 2.5) and demonstrates a clear decay in hyperpolarised signal over 36 s. The signal decay curve from a region of interest (ROI) within the phantom is plotted in Figure 2.14.

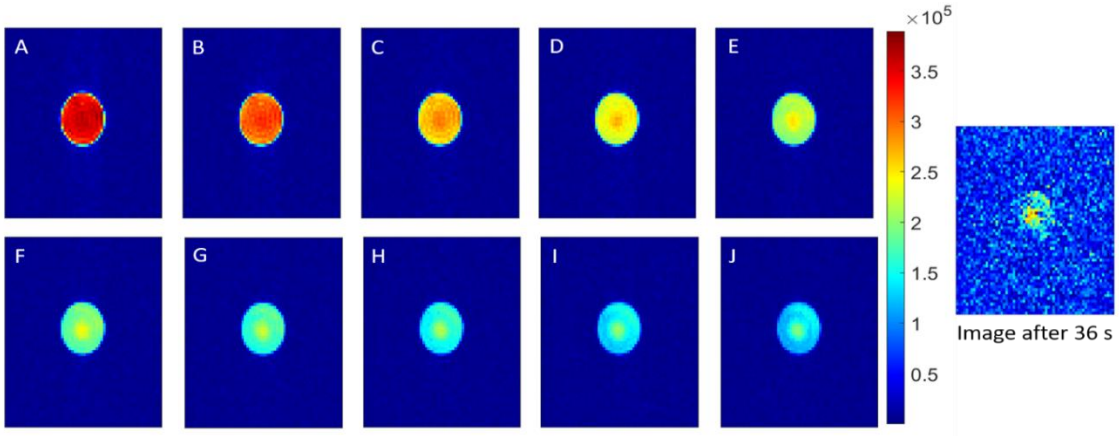

Figure 2.13 – MR images carried out on a 9.4 T Bruker NMR system (integrated micro 2.5 gradient set) using a one-shot 2D ^{1}H hyperpolarised MRI FISP sequence with TR = 600 ms, TE = 2 ms, FOV = 1.2*1.2 cm, matrix size = 64*64, NS = 1. Images of hyperpolarised pyrimidine (500 mM) in the presence of the pre-catalyst [IrCl(COD)(1,3-bis(4-tert-butyl)-2,6-dimethylphenyl)imidazol-2-ylidine)] (catalyst 2, 5 mM). FISP 2D images acquired as a function of time from the polarisation transfer step after 0.6-6.0 s, in 600 ms intervals.

The decay profile was fitted to a mono-exponential and the time constant of decay was calculated to be 5.9 s. This time constant of decay is much shorter than the measured T_1 of pyrimidine (between 15 and 48 s). This is expected as the system is exposed to multiple *r. f.* pulses to maintain the steady state magnetisation required for FISP acquisition. Such excitation pulses will somewhat attenuate the magnetisation remaining in the longitudinal plane for subsequent measurement. This is demonstrated through the poor fit observed to the mono-exponential (see figure 2.14 insert which displays the residual between the mono-exponential model and the data). The residual has a time-based dependence/function and is not simply a reflection of random noise (random fluctuation around 0).

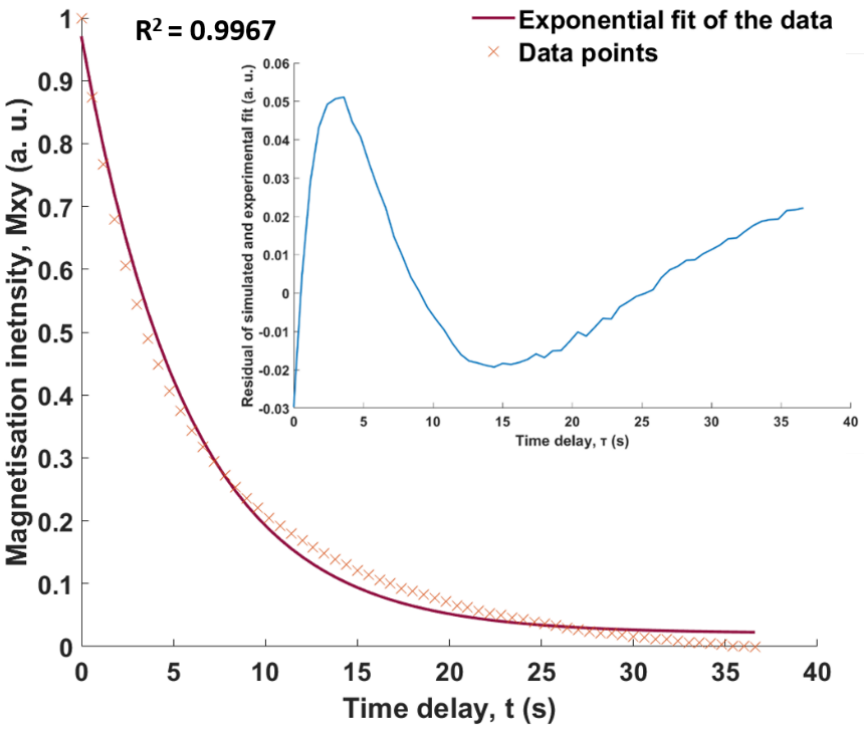

Figure 2.14 – Low flip angle FISP [IrCl(COD)(1,3-bis(4-*tert*-butyl)-2,6-dimethylphenyl)imidazol-2-ylidine)]

It is noted that the measured signal will be a complex interplay of signal undergoing *r. f.* attenuation, which is required to maintain steady state acquisition along with T_1 decay which is under exchange with fresh signal. Fresh 'unlabelled' signal (yet to be excited and only undergoing thermal decay) could be diffusing in from above/below the imaging plane between subsequent excitations. Together these effects are difficult to model and make it difficult to predict the actual T_1 from the FISP data. Nevertheless, this data demonstrates that pyrimidine, can not only be polarised *via* SABRE but that a ^{1}H MRI trace can be obtained with it.

2.5 Conclusions

Pyrimidine has been shown to successfully undergo ^{1}H SABRE hyperpolarisation. The active SABRE catalyst and intermediates have been fully characterised as $[Ir(H)_2(IMes)(pyrimidine)_3]Cl$ (**A**) and $[IrCl(H)_2(IMes)(pyrimidine)_2]$ (**B**). These complexes proved to interconvert on the NMR timescale and the associated hydride ligand exchange rates were obtained to map the conversion of complex **A** into **B**, alongside the hydride loss rate from complex **B** to form H_2 and the conversion of **B** back into **A**.

During the SABRE exchange pathway, it is understood that ligand loss (in this case pyrimidine) occurs before H_2 loss. This leads to a dihydrogen dihydride complex which through site interchange allows fresh *p*-H_2 to enter the coordination sphere. Once the H_2 is lost, a substrate molecule binds to the catalyst centre to reform the active catalyst (**A**).[110, 111, 119] During the investigation into hydrogen exchange with $[Ir(H)_2(IMes)(pyrimidine)_3]Cl$, it was discovered that loss of H_2 from **A** involved **B**, $[IrCl(H)_2(IMes)(pyrimidine)_2]$. It has been noted that for pyridine while **A** forms predominantly, about 1% of $[Ir(H)_2(IMes)(MeOH)(pyridine)_2]$ (**C**, where MeOH = methanol) can be seen at low temperatures with form **B** being detected in dichloromethane-d_2.[111]

The rate of conversion of complex **A** into **B** at 300 K proved to be $3.93 \pm 0.03\ s^{-1}$.[111] The competing rate of exchange from **B** to form H_2 at 300 K is $4.62 \pm 0.08\ s^{-1}$. Both steps proceed by 2-electron donor loss and hence the net rate of ligand loss from **A** must exceed $3.93\ s^{-1}$. Unfortunately, due to peak overlap we were unable to probe the ligand loss process directly and the reversibility of these processes makes extracting a precise rate from the hydride ligand data impossible. However, for $[Ir(H)_2(IMes)(pyridine)_3]Cl$, this is not the case as the process is much simpler and the loss rate of pyridine is $23\ s^{-1}$ per mole of metal complex.[111] This rate is dramatically larger than that for pyrimidine and may account for its poor SABRE performance. For pyridine the gains are −2397, −1472 and −1629 fold for the hydrogens in the *ortho*, *meta* and *para* positions, respectively[111] while those obtained here for pyrimidine are -542 ± 16, -584 ± 15 and -506 ± 13 fold for H-2, H-4 and 6 and H-5 respectively.

In this chapter, the SABRE hyperpolarisation of pyrimidine has been optimised to create a large ^1H NMR signal enhancement. This was achieved by examining substrate concentration, catalyst concentration and type of catalyst. The optimal conditions were 50 mM concentration of pyrimidine (10 equivalents of substrate loading), using 2.5 mM concentration of pre-catalyst and using [IrCl(COD)(1,3-bis(2,4,6-trimethylphenyl)-4,5-dimethylimidazol-2-ylidine)] as the SABRE pre-catalyst. It should be noted however, that the optimal concentration of pyrimidine and catalyst were carried out with the pre-catalyst [IrCl(COD)(IMes)]. When these optimal

conditions were applied to the different catalysts it was realised that the ^{1}H signal enhancements achieved were not as good as those originally gained. Therefore, each catalyst needs to be optimised with the substrate under investigation to achieve the highest signal enhancement. The temperature at which the experiments were carried out was also examined but no discernible trend could be achieved. For the results of these experiments see Appendix A.6.

Using these optimal conditions, ^{1}H MR images were successfully obtained for pyrimidine. The hyperpolarised image was still present 6 seconds after beginning a series of imaging sequences, demonstrating that the enhanced ^{1}H signal lasts long enough to take repeat images. To improve this, deuterated forms of pyrimidine could be examined under the optimal conditions investigated here. From the literature[129] and without optimisation, 4,6-d_2-pyrimidine produces a long T_1 on H-5, 72.2 s and a ^{1}H signal enhancement of 558 and 525-fold, for H-2 and H-5 respectively.[129] 2,5-d_2-pyrimidine, however, gives a shorter T_1, 34.6 s but a larger ^{1}H. Therefore, this molecule and particularly its motif, would warrant further investigation as use as a possible MR contrast agent. This is explored in Chapter 3 and 5 with 5-fluorouracil.

Chapter 3: ^{1}H and ^{19}F SABRE Hyperpolarisation of Fluoro *N*-Heterocycles

3.1 Introduction

The hyperpolarisation of heteronuclei has shown promise in ^{13}C-pyruvate,[36, 40, 73, 174] ^{13}C-urea,[174, 192] ^{13}C-glucose[35, 41, 169, 193] and the ^{19}F in fluorinated styrene,[194, 195] amongst many others.[63, 196] The success of these agents is due to their high polarisation levels and long lifetimes.[13, 36, 94, 107, 141, 195, 197] Hyperpolarised ^{13}C detection has already been successfully used in magnetic resonance spectroscopy (MRS) *via* PHIP and DNP methods, where *in vivo* images were produced of the heart and cardiovascular system, using maleic acid and ^{13}C-urea, respectively.[198-201] Additionally, hyperpolarised ^{15}N-pyridine derivatives have been shown to be suitable as an MRI probe for *in vitro* pH changes in phantoms, due to wide chemical shift dispersion.[202] It was suggested that these probes might also find use in detecting changes within tissues[202] such as brain tumours through the imaging of the ratio of hyperpolarised ^{13}C-bicarbonate to CO_2 signals.[66, 67] Hyperpolarised ^{15}N, ^{13}C and ^{19}F nuclei delivered *via* SABRE have also been successfully detected using MRI methods.[141, 144, 202-204] Other heteronuclei have also been exploited with SABRE, including ^{31}P, ^{29}Si and ^{119}Sn.[139, 145]

More recently, the hyperpolarisation of ^{19}F nuclei has gained interest due to the use of fluorinated compounds in biomedicine.[205, 206] Additionally, the MRI detection of ^{19}F nuclei under Boltzmann conditions has previously been used to investigate catabolic and anabolic drug conversions of anticancer drugs, particularly 5-fluorouracil.[207-212] Whilst ^{19}F nuclei are abundant in skeletal tissue, predominantly as calcium fluoride, they are not present at any significant concentration within other tissues or cells. Therefore, the detection of exogenous ^{19}F contrast agents could be appealing due to low residual background signal. Fluorine is already used as a tracer in the form of ^{18}F-fluorodeoxyglucose (^{18}F-FDG) in positron emission tomography (PET).[213, 214] Such studies involve the injection of ^{18}F-FDG into the patient, and the resulting uptake of glucose can be monitored in conjunction with the half-life of the ^{18}F response.[213, 214] Images of the radiotracer

result from analysis of the gamma radiation emitted by this tracer.[214] Hence, there is a knowledge base that could make such studies feasible.

Not surprisingly, ^{19}F NMR has been well utilised since the first 1950 report by Dickinson.[215] It represents an NMR active nucleus, with 99.8% natural isotopic abundance and has a gyromagnetic ratio that is very similar to that of ^{1}H. Using the equation for receptivity (*R*), given in equation 3.1, the relative signal strength of fluorine is 84% of that of ^{1}H.

$$R = N.(\gamma^2.\big(I(I+1)\big)) \qquad (3.1)$$

Where *N* is the isotope natural abundance, γ is the gyromagnetic ratio and *I* is the spin quantum number (½ for both ^{1}H and ^{19}F nuclei). Therefore, such signals should be of relatively high intensity when compared to those of other heteronuclei. ^{19}F nuclei have been successfully hyperpolarised by DNP[216-218] and hydrogenative PHIP methods, ALTADENA and PASADENA, and detected by NMR.[195, 217] As previously mentioned, ^{19}F has also been successfully polarised *via* SABRE.[13] Recently, the ^{19}F hyperpolarisation of 3-fluoropyridine was re-examined with promising data presented, including an image of the ^{19}F hyperpolarised signal.[144, 219] A potential drawback of using ^{19}F nuclei as hyperpolarised contrast agents is that the T_1 relaxation times of the created magnetisation are typically short. Bober *et. al.*in 2017, reported ^{19}F T_1 times of between 0.149 to 0.386 s for the drug fluoxetine *in vivo* in the brain.[220] Mattes *et. al.* (2016) measured a ^{19}F T_1 of 1.1 s for the drugs fluconazole and flumethasone.[221] The dominant pathway to relaxation for ^{19}F is chemical shift anisotropy, therefore a short T_1 is to be expected.[222]

This chapter investigates a variety of fluorinated *N*-heterocyclic compounds as potential MR contrast agents and discusses the SABRE hyperpolarisation of their ^{1}H and ^{19}F nuclei. Additionally, T_1 relaxation times and ligand exchange rates are defined in order to determine their suitability for further *in vivo* study. The molecules used for screening ^{19}F hyperpolarisation are shown in Figure 3.1 and all contain a pyridine, pyrazine or pyrimidine motif. Pyridine and pyrazine based molecules have been widely studied using SABRE and therefore provide a robust starting point for this study. Pyrimidine based molecules have also been shown to be SABRE active. These include, pyrimidine itself,[129, 223] pyrimidine based phosphates,[146] 5-

tributylstannylprimidine and 5-trimethylsilylprimidine.[139] Pyrimidine based molecules are also prevalent in a number of biologically useful molecules including one of the most common anti-cancer drugs, 5-fluorouracil.[224] Fluorinated compounds are also widely found in pharmaceuticals, including antidepressants (Prozac), anticancer (fluorouracil), antibacterial (fluoroquiolones) and antiviral drugs (Maraviroc).[179, 225] They are also contained in the anti-fungal drug Vorincazole, (2S,3R)-3-(2,4-difluorophenyl)-2-(5-fluoropyrimidin-4-yl)pentan-3-ol and fluoxetine.[219]

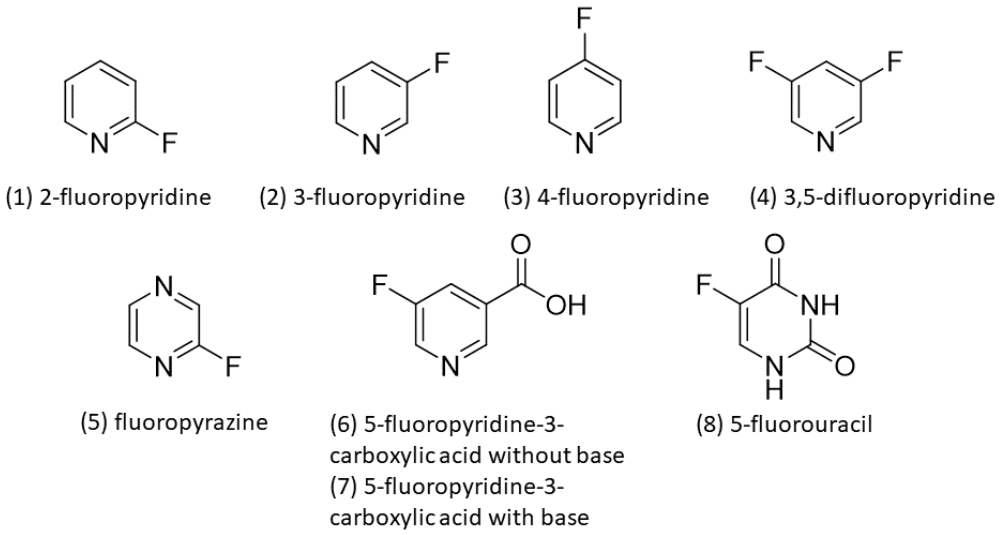

Figure 3.1 - Fluorinated *N*-heterocyclic molecules used here for SABRE ^{1}H and ^{19}F hyperpolarisation experiments. Compound names: (1) 2-fluoropyridine, (2) 3-fluoropyridine, (3) 4-fluoropyridine, (4) 3,5-difluoropyridine, (5) fluoropyrazine, (6) and (7) 5-fluoropyridine-3-carboxylic acid without base and with, respectively and (8) is 5-fluorouracil.

3.2 Hyperpolarised ^{1}H, and ^{19}F NMR detection of *N*-heterocyclic compounds

For each of the fluorine containing molecules investigated (Figure 3.1), two NMR samples were initially prepared for the related SABRE experiments. These samples contained 5 mM solutions of [IrCl(COD)(IMes)] and either 20 mM or 100 mM of the substrate in 0.6 mL of methanol-d_4. After degassing using a freeze-pump-thaw method, the samples were placed under a 4 bar atmosphere of *para*-hydrogen (p-H_2). Subsequently, seven distinct SABRE experiments were performed on each sample and the average ^{1}H NMR signal enhancement, associated with each substrate was calculated as described previously. The results of this process are presented in Table 3.1.

Table 3.1 – Hyperpolarised ^{1}H NMR signal enhancements observed when 20 mM or 100 mM concentrations of the indicted fluorinated *N*-heterocyclic compound, undergo SABRE using 5 mM of pre-catalyst [IrCl(COD)(IMes)] in 0.6 mL MeOD-d_4 in the presence of 4 bar of *p*-H_2; measurements were carried out on a 400 MHz Bruker NMR. Pyridine reference data is as reported by Lloyd *et. al.*[111]

N-heterocyclic fluorinated compound	Hydrogen position	Average enhancement at 20 mM concentration of substrate	Average enhancement at 100 mM concentration of substrate
2-fluoropyridine (**1**)	3	−0.448 ± 0.1	−0.282 ± 0.1
	4	−0.454 ± 0.1	−0.282 ± 0.1
	5	−0.285 ± 0.1	−0.214 ± 0.1
	6	−0.664 ± 0.1	−0.364 ± 0.1
3-fluoropyridine (**2**)	2	−1287 ± 65	−861 ± 73
	4	−535 ± 18	−364 ± 12
	5	−924 ± 38	−1207 ± 35
	6	−817 ± 26	−435 ± 48
4-fluoropyridine (**3**)	-	-	-
3,5-difluorpyridine (**4**)	2, 6	−591 ± 10	−454 ± 12
	4	−501 ± 11	−341 ± 11
Fluoropyrazine (**5**)	3, 6	−716 ± 42	−618 ± 20
	5	−461 ± 19	−469 ± 13
5 –fluoropyridine-3-carboxylic acid without base (**6**)	2	−272 ± 20	−60 ± 1
	4	−181 ± 11	−50 ± 1
	6	−112 ± 7	−55 ± 1
5 –fluoropyridine-3-carboxylic acid with base (**7**)	2	−635 ± 98	−254 ± 10
	4	−191 ± 31	−222 ± 7
	6	−278 ± 42	−247 ± 7
5-fluorouracil (**8**)	2	−106	-
Pyridine[111]	2	−2397	392
	3	−1472	−192
	4	−1629	−323

Of these simple fluorinated *N*-heterocyclic compounds, only 4-fluoropyridine (**3**) failed to hyperpolarise as shown in Figure 3.2. This is a result of **3** being unstable and only available as a salt, in this case of hydrochloric acid. It is hypothesised that the presence of the acid hinders

binding of the *N*-heterocycle to the catalyst and as such SABRE is not able to occur. This is due to the nitrogen lone pair no longer being free to bind to the metal centre.

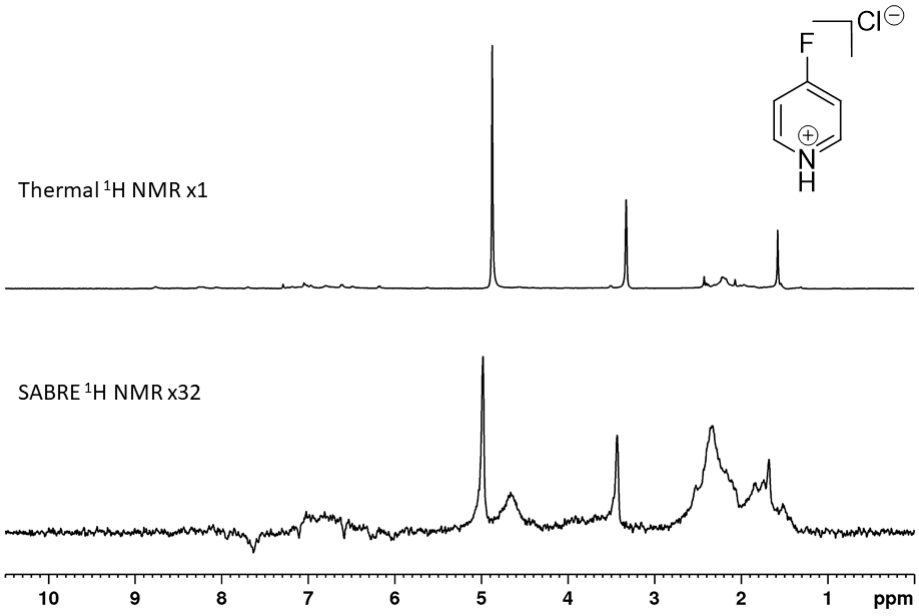

Figure 3.2 – ^{1}H NMR spectra of 4-fluoropyridine recorded in the presence of HCl. Bottom is a 1 scan hyperpolarised ^{1}H SABRE response after polarisation transfer at 60 G, expanded 32x vertically relative to the upper spectrum in order to visualise resonances in the substrate. The corresponding thermally equilibrated spectrum (top) which was left in the NMR for 2 minutes prior to acquisition.

To investigate whether this hypothesis was the case, the HCl was removed *via* two different methods. The first method involved filtering a 20 mM solution of 4-fluoropyridine hydrochloride in methanol-d_4 through basic alumina and then adding 5 mM of [IrCl(COD)(IMes)] to the filtrate. The second method was to add 20 mM of Cs_2CO_3 to 20 mM of the 4-fluoropyridine hydrochloride and 5 mM of [IrCl(COD)(IMes)] in 0.6 mL methanol-d_4. The two samples were examined under SABRE conditions. Unfortunately, no NMR signal enhancements were observed from either sample. No further SABRE experiments were conducted on this substrate.

5-Fluoropyridine-3-carboxylic acid is zwitterionic because it has a base and an acid within itself as shown in Figure 3.3. This means that it has a protonated nitrogen, and a deprotonated carboxylic group, and consequently binding to the catalyst could again be inhibited.

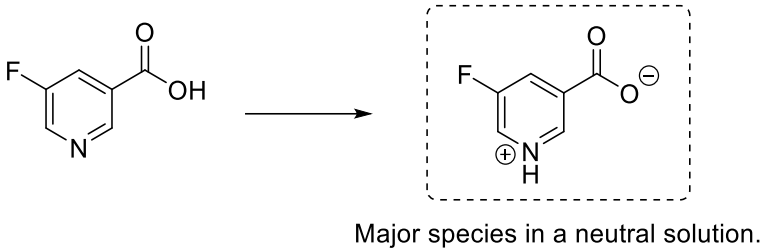

Major species in a neutral solution.

Figure 3.3 – Zwitterionic form of 5-fluoropyridine-3-carboxylic acid.

Therefore, to remove the proton from the nitrogen binding site, a base was added again with the hope that this would aid binding to the catalyst as shown previously.[191] This was achieved by preparing two samples with Cs_2CO_3 (1 equivalent) for each 20 mM and 100 mM concentration of substrate, in a similar vain to the 4-fluoropyridine in the presence of HCl. This seemed to be successful as the ^{1}H NMR signal enhancement observed for the proton in the 2-position increased from 272 ± 20-fold to 635 ± 98-fold in the presence of base. This proton gave the highest signal gain of all the protons in this molecule. It is concluded that the presence of base has aided binding to the catalyst and thus a higher signal gain is observed.

The lone pair on both the nitrogen atoms in 5-fluorouracil will be involved in the π system of the ring, and therefore binding to the SABRE catalyst is again likely to be inhibited. However, in this case conjugation will stabilise the corresponding conjugate base. Therefore, Cs_2CO_3 was also added to this compound and the resulting ^{1}H NMR signal enhancement was quantified to be 30-fold after transfer from a 65 G field. As this signal gain was quite small, the concentration of base was reduced to 10 mM, the enhancement increased to 106-fold. Figure 3.4 shows both a thermally equilibrated spectrum, where the sample was left in the NMR for two minutes prior to acquisition, and a hyperpolarised ^{1}H NMR spectrum for 5-fluorouracil. The enhanced signal rapidly decreased when subsequent SABRE experiments were repeated, possibly due to cyclometallation[226-228] of the catalyst. Cyclometallation of similar substrates, such as 6-methyl-2-thiouracil, has been previously reported in the literature to occur with related iridium complexes. Such catalyst deactivation must be prevented if SABRE is to work.[229]

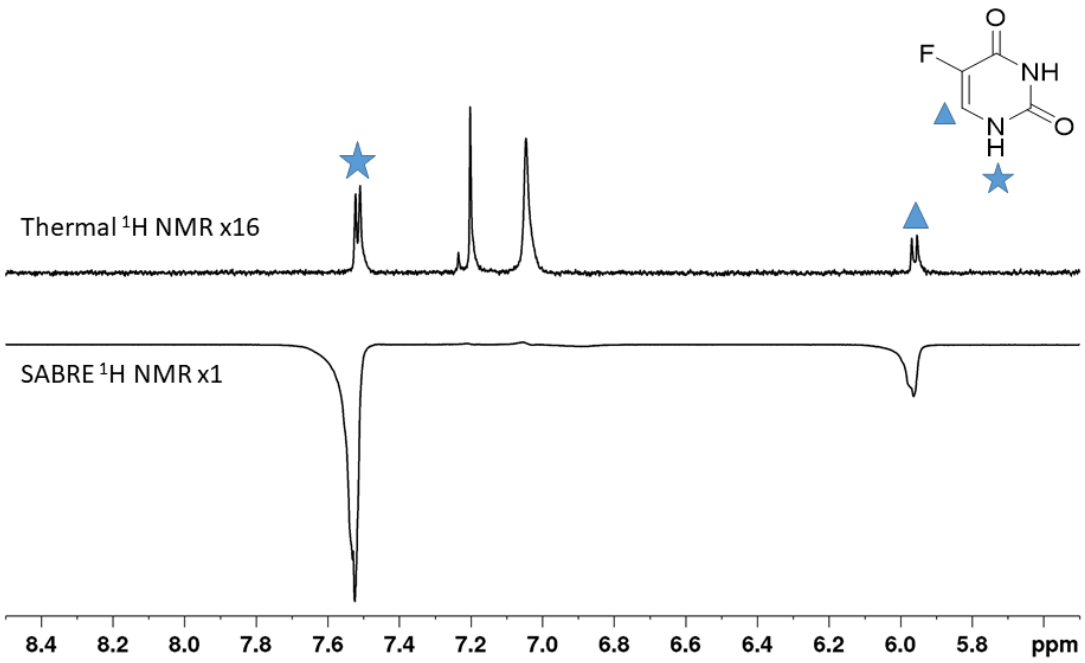

Figure 3.4 – ^{1}H NMR spectra of 20 mM 5-fluorouracil with 5 mM pre-catalyst [IrCl(COD)(IMes)] in the presence of 2.5 mM Cs_2CO_3. The top spectrum is the thermally equilibrated spectrum which was left in the NMR for two minutes prior to acquisition, with the vertical expansion increased by 16x relative to the lower trace; the bottom spectrum shows the 1 scan, SABRE hyperpolarised signal, immediately after activation under 4 bar *p*-H_2. It demonstrates that a polarised ^{1}H response is observed.

Apart from 4-fluoropyridine, all the other fluorinated *N*-heterocyclic compounds gave an enhanced signal for each of their protons. Table 3.1 shows the enhancement factor for all of the protons for each fluorinated *N*-heterocyclic compound at both 20 mM and 100 mM concentrations.

3-Fluoropyridine produced the greatest ^{1}H signal improvement of all the fluorinated *N*-heterocyclic compounds investigated, with a signal enhancement of −1287 ± 65-fold being seen for the proton in the second position. Fluoropyrazine produced an enhanced signal of −761 ± 42-fold on the protons in position 2 and 6 respectively. 5-Fluoropyrididine-3-carboxylic acid in the presence of Cs_2CO_3 produced an enhancement factor of −635 ± 98-fold for the proton in the second position. This was almost twice that of the measurement made without base which was −272 ± 20 for the same proton. 3,5-Difluoropyridine yielded an enhancement factor of −591 ± 10-fold for the overlaying protons in positions 2 and 6. 5-Fluorouracil produced an enhanced

signal of −106-fold on the proton in the second position. This sample deactivates rapidly, and the data is presented for the first SABRE experiment where any errors will be minimised.

Of the *N*-heterocyclic substituted fluorinated compounds, 3-fluoropyridine therefore gave the best enhancement factor at both concentrations. At 20 mM the enhancements were, −1287 ± 65 for H2, −817 ± 26 for H4, −924 ± 38 for H5 and −535 ± 18 for H6. For 100 mM the enhancements were, −861 ± 73 for H2, −364 ± 12 for H4, −1207 ± 35 for H5 and −435 ± 48 for H6. Comparing the best ^{1}H signal enhancement for each substrate there is an average improvement of 2.69 times at 20 mM concentration for 3-fluoropyridine when compared to that achieved with the other substrates and this increases to 7.37 times for the 100 mM concentration.

SABRE hyperpolarisation of 2-fluoropyridine was observed but it gave poor NMR signal enhancements that ranged between 0.664 to 0.285 times the size of the thermally equilibrated signal. As the steric difference between fluorine and hydrogen is minimal[230] the reason behind the low signal enhancement must be due to electronic effects.[231] Fluorine is highly electron withdrawing and causes electron density to be withdrawn from the nitrogen binding site, therefore, influencing the rate of exchange between the substrate and the catalyst. Consequently, the exchange rate is no longer optimal for polarisation transfer. This may also be the case with 3,5-difluoropyridine compared to 3-fluoropyridine. The latter has a very high enhancement factor ranging between 1287 to 535, whereas 3,5-difluoropyridine has a lower one, between 591 to 501. This could be due to 3,5-difluoropyridine having an extra electron withdrawing group. This would allow further electron density to be withdrawn from the nitrogen binding site, again influencing the rate of exchange between the substrate and the catalyst.

For 2- and 3-fluoropyridine, 3,5-difluorpyridine and fluoropyazine the enhancement factor increased 1.8, 1.1, 1.3 and 1.2 times respectively, when the concentration of the substrate reduced from 100 mM to 20 mM. 5-Fluoropyridine-3-carboxylic acid without base exhibited an increase of 4.5x at 20 mM compared to 100 mM. However, without base, the increase was only 2.5x between the two concentrations, though the enhancement factor is still larger when the substrate was analysed in the presence of base. Such increases in enhancement factor at 20 mM

concentrations was reported in 2014 by Lloyd *et. al.* though notably this large change in enhancement was only observed by them when using [IrCl(COD)(IMes)] as the pre-catalyst.[111] When a different catalyst was employed the effect was less varied between the different concentrations of substrate.[111] This demonstrates the variability between substrates and catalysts, and perhaps a different catalyst may provide a greater enhancement for some of the substrates investigated here and could be investigated in the future. Nonetheless these results validate the hypothesis that SABRE can be used to successfully hyperpolarise a range of fluorinated heteroaromatics.

Comparing this data to pyridine though, as reported by Lloyd *et. al.*,[111] at 20 mM concentrations, the *N*-heterocyclic fluorinated compounds do not hyperpolarise as well. For example, the enhancement of 3-fluoropyridine is approximately half that of pyridine. However, at higher concentrations 3-fluoropyridine and fluoropyrazine hyperpolarise better than pyridine. The ^{1}H signal enhancements for 3,5-difluoropyridine and 5-fluoropyridine-3-carboxylic acid with base are comparable to pyridine under these conditions.

It is well established in the literature that both the T_1 relaxation of the substrate and the rate of ligand exchange have an effect on the signal enhancement.[102] These factors could therefore explain the difference between the enhancement factors obtained.

As 2-fluoropyridine gave such a weak ^{1}H signal enhancement, it was excluded from all remaining studies. The main purpose of this work though was to explore ^{19}F detection, and the remaining *N*-heterocyclic fluorinated compounds of Table 3.1 were re-examined using SABRE to test this. All of the substrates produced a hyperpolarised ^{19}F signal (see Table 3.2 and Figure 3.5).

Table 3.2 – Hyperpolarised ^{19}F NMR signal enhancement when using 20 mM or 100 mM of the indicated *N*-heterocyclic fluorinated compound under SABRE with 5 mM of pre-catalyst [IrCl(COD)(IMes)] in 0.6 mL methanol-d_4 in the presence of 4 bar of *p*-H_2 as measured on a 500 MHz Bruker NMR system.

Fluorinated N-heterocyclic compound	^{19}F enhancement factor for 20 mM concentration of substrate	^{19}F enhancement factor for 100 mM concentration of substrate
2-fluoropyridine **(1)**	-	-
3-fluoropyridine **(2)**	62 ± 6	63 ± 4
4-fluoropyridine **(3)**	-	-
3,5-difluoropyridine **(4)**	14 ± 1	12 ± 2
fluoropyrazine **(5)**	20 ± 1	12 ± 1
5-fluoropyridine-3-carboxylic acid (without base) **(6)**	14 ± 1	9 ± 1
5-fluoropyridine-3-carboxylic acid (with base) **(7)**	3 ± 1	43 ± 2

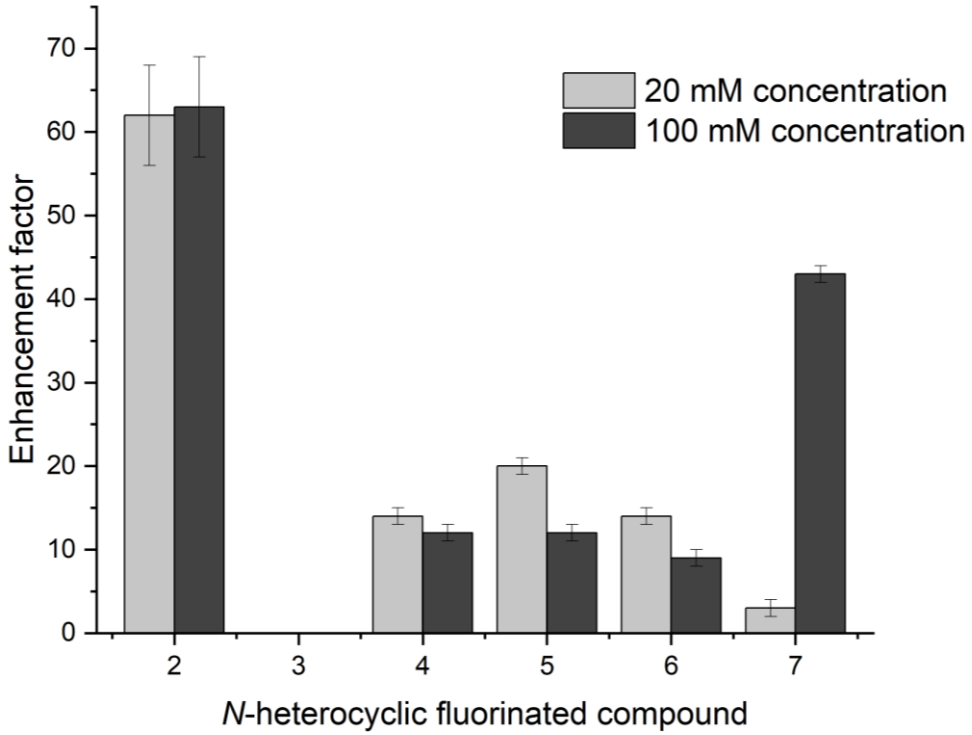

Figure 3.5 – ^{19}F NMR signal enhancement measured for the *N*-heterocyclic fluorinated compound at 20- and 100-mM concentrations, the light grey is 20 mM and dark grey represents the 100 mM. All samples contained 5 mM of pre-catalyst [IrCl(COD)(IMes)] in 0.6 mL methanol-d_4 and were exposed to 4 bar *p*-H_2.

Figure 3.6 shows two typical ^{19}F NMR spectra, under thermal and SABRE conditions, for 3-fluoropyridine (**2**) which gave the best ^{1}H and ^{19}F NMR signal enhancements; it gave a ^{19}F signal enhancement of 62 ± 6-fold and 63 ± 4-fold, within error, at the two concentrations respectively. The difference in signal level seen for the other samples are also far less than those of the ^{1}H NMR results. In contrast, 5-fluorouracil gave an enhanced ^{19}F signal, but this decreased in size very quickly after the first shake, signal enhancement calculations on the ^{19}F were therefore confounded. This decrease in signal enhancement was due to a reduction in the rate of catalyst activation.

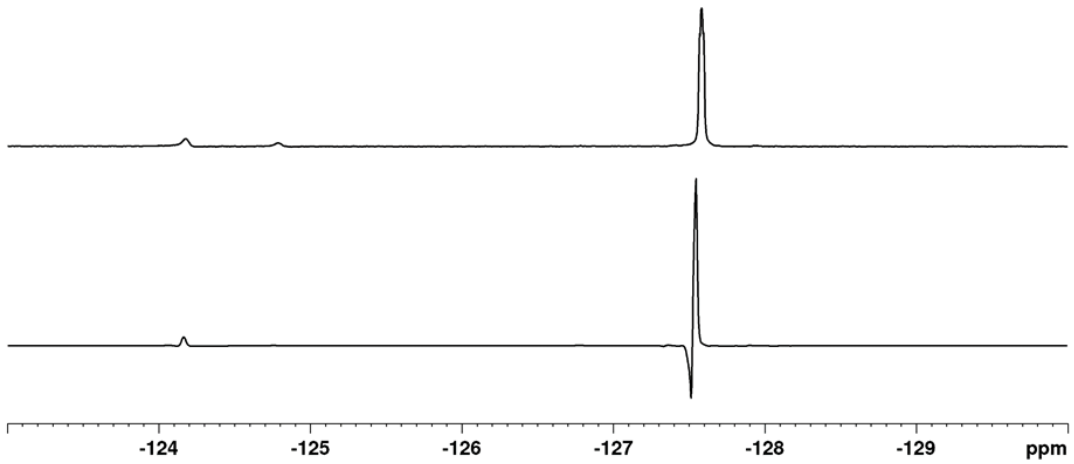

Figure 3.6 – ^{19}F NMR spectra of 100 mM of 3-fluoropyridine with 5 mM pre-catalyst [IrCl(COD)(IMes)] in 0.6 mL methanol-d_4 in the presence of 4 bar p-H_2. The first NMR spectrum is the thermally equilibrated spectrum which was left in the NMR for two minutes prior to acquisition polarised measurement whose vertical expansion level has been increased x32 relative to the lower trace. The bottom NMR spectrum shows the SABRE result. The peak at approximately -124 ppm is the bound ^{19}F signal, the one at approximately -127.5 ppm is the free ^{19}F signal.

3.3 Analysis of the T_1 relaxation values of the ^{1}H and ^{19}F nuclei

The longitudinal relaxation time, T_1 was determined for these *N*-heterocyclic fluorinated compounds. The inversion recovery method was used as described in the experimental chapter (see section 7.2.11.1). The measurements were made using 100 mM substrate, in the presence of 5 mM pre-catalyst [IrCl(COD)(IMes)] under 4 bar of hydrogen gas. Although the 20 mM concentration of substrate gave the best signal enhancement, 100 mM concentration of substrate was used to collect the T_1 data. As the catalyst aids in the relaxation of the substrate working at the higher concentration will provide a longer value.[94, 102]

As with the previous experiments performed on 5-fluoropyridine-3-carboxylic acid, two samples were prepared; one without base and one in the presence of base, in which the sample was prepared with a 1:1 ratio of Cs_2CO_3 to substrate, therefore 100 mM concentration of base was used. As previously mentioned, this was to aid nitrogen binding into the metal centre of the catalyst.

Table 3.3 – ^{1}H T_1 data for all hydrogens within each of the *N*-heterocyclic fluorinated compounds investigated at a 100 mM concentration, in the presence of 5 mM of pre-catalyst [IrCl(COD)(IMes)] in 0.6 mL of methanol-d_4 at 295 K under 4 bar of hydrogen. Pyridine data as reported by Lloyd *et. al.*[111]

Fluorinated *N*-heterocyclic compound	T_1 (s)				
	H2	H3	H4	H5	H6
2-fluoropyridine (**1**)	-	-	-	-	-
3-fluoropyridine (**2**)	19.03	-	13.47	21.11	11.56
4-fluoropyridine (**3**)	-	-	-	-	-
3,5-difluoropyridine (**4**)	21.90	-	29.24	-	21.90
Fluoropyrazine (**5**)	-	22.59	-	26.19 (H5 and H6)	-
5-fluoropyridine-3-carboxylic acid (without base) (**6**)	14.52	-	14.54	-	12.73
5-fluoropyridine-3-carboxylic acid (with base) (**7**)	46.14	-	16.04	-	16.91
Pyridine[111]	12.60	14.70	18.90	-	-

As shown in Table 3.3, the relaxation times of all the ^{1}H resonances in the substrates extend from 11.56 to 46.14 seconds and are therefore comparable to those of pyridine which span 12.6 to 18 seconds.[111] The effect of protonation of the ring nitrogen is evident in the data from 5-fluoropyridine-3-carboxylic acid. The removal of the effect of this hydrogen atom gives a substantial improvement in the T_1 values of all three protons, particularly H-2.

Based on previous studies the H-2 signal of 5-fluoropyridine-3-carboxylic acid, with the longest T_1 might be expected to yield the largest signal enhancement. In contrast, 3-fluoropyridine with a T_1 of 21.1 seconds in the H-2 position, yields the best ^{1}H signal with gains of −1287 ± 65-fold. As the ^{19}F signal gain is delivered through in-molecule transfer *via* ^{1}H coupling it is not too surprising that this substrate also gives the best ^{19}F signal enhancement even though its T_1 at

500 MHz is lower than that of 5-fluoropyridine-3-carboxylic acid. The T_1 values for these protons ranged from 11.56 to 46.14 seconds. 5-Fluoropyridine-3-carboxylic acid in the presence of Cs_2CO_3, had the longest T_1, which was 46.14 s on H-2 within the molecule. 3-Fluoropyridine which gave the best ^{1}H and ^{19}F signal enhancements, exhibits a T_1 of 21.11 s on H-5.

The T_1 relaxation time was also obtained for the fluorine atom on the fluorinated *N*-heterocyclic compounds. As expected,[34] these proved to be dramatically shorter than the range of values seen for these molecules ^{1}H signals and they varied from one another by just 50%. The longest value was just 5.5 seconds for 3,5-difluoropyridine, while the shortest was 3.2 seconds. These were shorter than the corresponding ^{1}H resonances. These ^{19}F T_1 values are summarised in Table 3.4.

Table 3.4 – ^{19}F T_1 measurements for the fluorinated *N*-heterocyclic compounds investigated using 100 mM of the substrate in the presence of 5 mM of pre-catalyst, [IrCl(COD)(IMes)] in 0.6 mL methanol-d_4 at 295 K under 4 bar of hydrogen.

Fluorinated N-heterocyclic compound	T_1 for ^{19}F (s)
2-fluoropyridine	-
3-fluoropyridine	4.46
4-fluoropyridine	-
3,5-difluoropyridine	5.51
fluoropyrazine	4.91
5-fluoropyridine-3-carboxylic acid (without base)	3.16
5-fluoropyridine-3-carboxylic acid (with base)	3.28

3.4 Exchange mechanism and activation of the fluorinated *N*-heterocyclic Iridium complexes

As mentioned in Chapter 2 section 2.1.3, the rate of ligand exchange within the active SABRE catalyst is very important when determining the efficiency of the catalyst. This, alongside a long T_1 can provide a large enhancement but also one that can last a long time. Therefore, for each fluorinated *N*-heterocyclic compound, the rate of ligand and hydride exchange was examined.

Utilization of the 1D-EXSY[232] protocol was used to assess the impact of the catalyst and the ligand exchange processes exhibited by the SABRE active complexes formed by the *N*-heterocyclic fluorinated compounds. Data was recorded for the substrates 3-fluoropyridine, 2–fluoropyrazine, 3,5-difluoropyridine and 5-fluoropyridine-3-carboxylic acid with and without base. To investigate the role of the catalyst for each substrate, the hydride region of the associated NMR spectra was considered first. Most commonly, in SABRE active complexes, a single hydride resonance is observed at between δ −20 and −30.[111] This is due to the formation of a *tris*

substituted complex, where the substrate is bound either through a nitrogen or oxygen lone pair of electrons.[111]

Upon examination of this region with the fluorinated *N*-heterocyclic compounds, three hydride resonances were typically seen instead of one, in the region δ −22 to −25. This suggests that as well as the *tris* complex, a second adduct is formed. Therefore, full characterisation of these species, using standard NMR methods, was carried out.

3.4.1 Characterisation of the fluorinated *N*-heterocyclic Iridium complexes

With the substrates 3,5-difluoropyridine and fluoropyrazine, both the *tris* and *bis* species were formed but with more equal intensities, therefore these two substrates could be used to characterise the second complex more accurately. Using 3,5-difluoropyridine as an example, it can be shown from Figure 3.7 (^{15}N / ^{1}H HMQC), that there are three hydride signals in solution. The dominant hydride signal at δ −23.94 is that of the *tris* substituted complex, the other two come from a *bis* substituted complex. Figure 3.7 presents a ^{15}N / ^{1}H cross peak at δ 269 / δ −23.94 for the hydride signal *trans* to 3,5-difluoropyridine in the *tris* substituted complex. The hydride at δ −24.69 is due to the *bis* substituted complex where the hydride ligand is *trans* to either methanol or Cl. Confirmation that the hydride signal at δ −24.69 was *trans* to Cl was done by replacing the pre-catalyst [IrCl(COD)(IMes)] with [Ir(COD)(IMes)(acetonitrile)]PF_6.

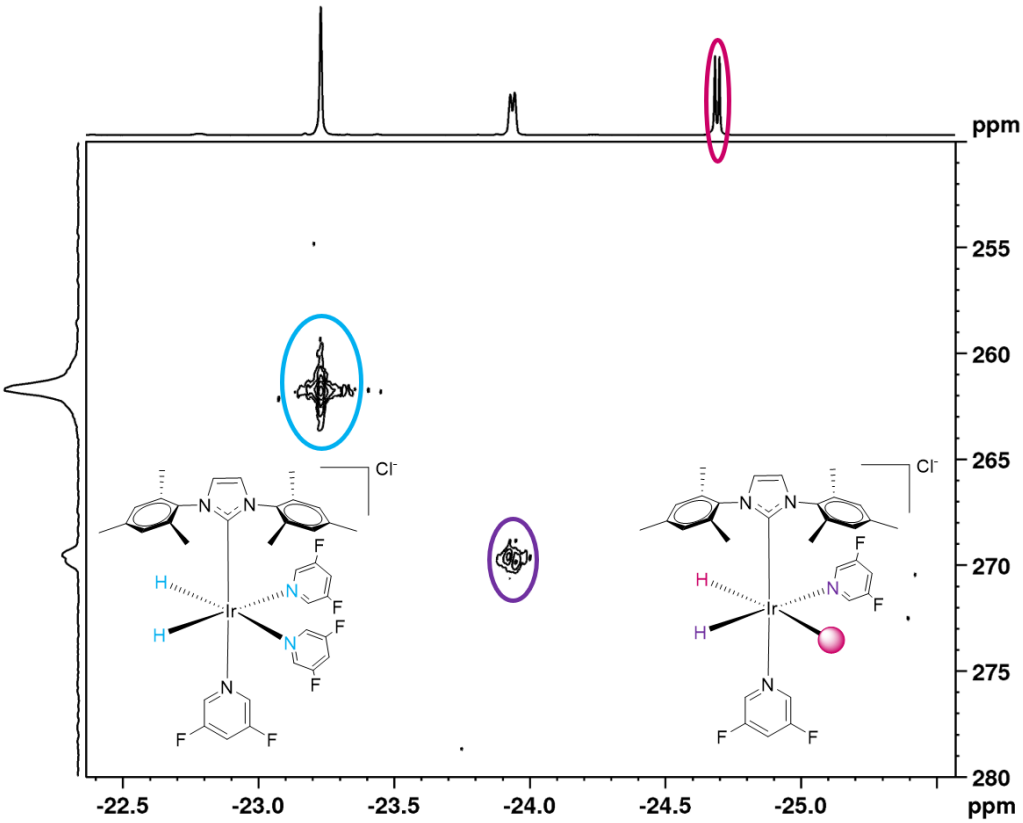

Figure 3.7 – ^{15}N / ^{1}H HMQC with a CNST2 of 8 Hz, for the sample [IrCl(COD)(IMes)]Cl (5 mM) with 3,5-difluoropyridine (100 mM) in methanol-d_4 (0.6 mL).

Examining the cross couplings in the hydride region of Figure 3.8 confirms the hydride signals at δ −23.94 and δ −24.69 which show a link between them, thereby demonstrating both ligands are within the same complex.

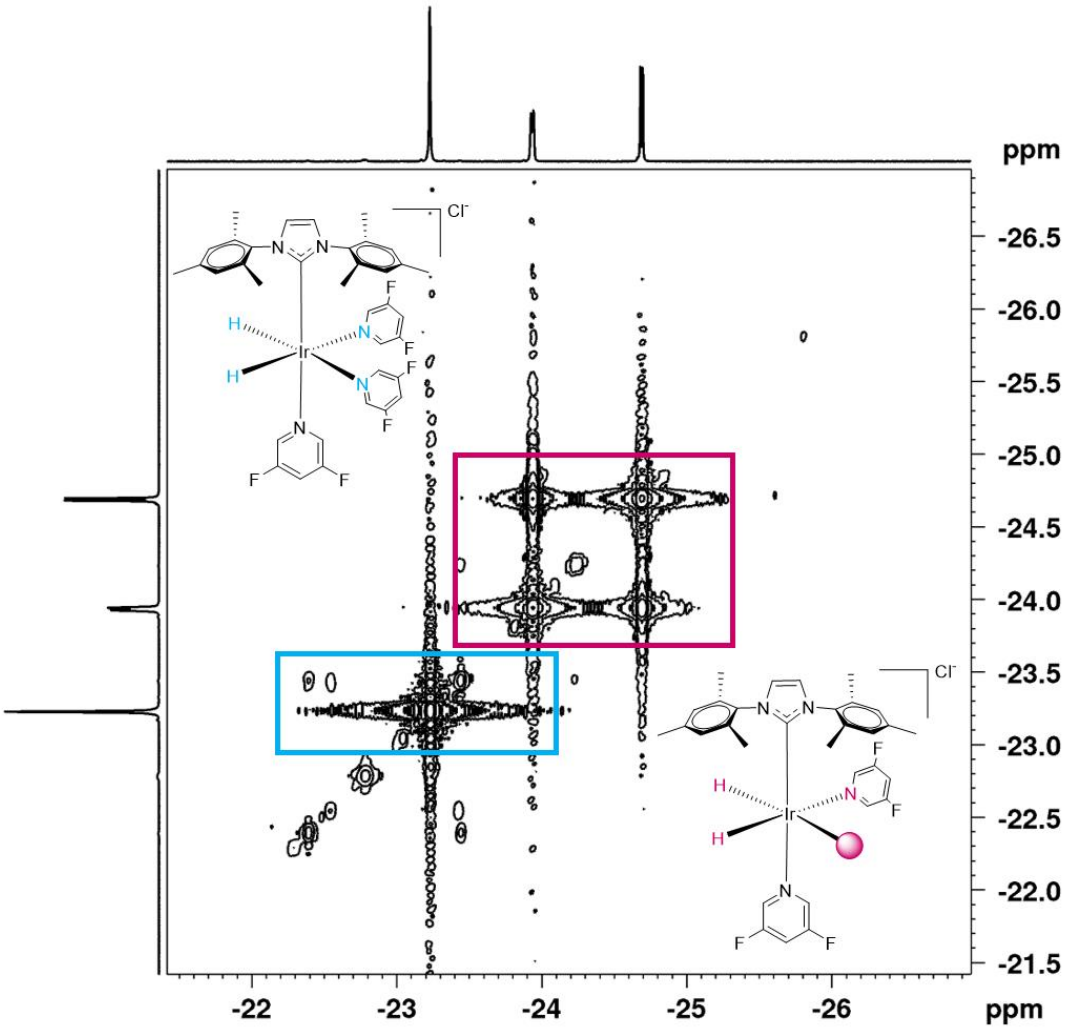

Figure 3.8 – COSY of the hydride region for the sample [IrCl(COD)(IMes)]Cl (5 mM) with 3,5-difluoropyridine (100 mM) in methanol-*d*$_4$ (0.6 mL).

For full characterisation details of all complexes see Appendix A.9.

Upon examination of all the substrates investigated, it was found that the species of the type $[Ir(H)_2(IMes)(sub)_3]Cl$ (**A**) yields a single hydride signal in the region around δ −22. Species such as $[IrCl(H)_2(IMes)(sub)_2]$ (**B**) yield two mutually coupled signals at slightly higher field.

The relative proportion of these complexes at an initial substrate concentration of 20 mM, alongside the hydride chemical shifts of the associated species, are given in Table 3.5.

Table 3.5 – Proportion of $[Ir(H)_2(IMes)(sub)_3]Cl$ to $[IrCl(H)_2(IMes)(sub)_2]$ as a function of substrate identity. Samples contained 5 mM pre-catalyst [IrCl(COD)(IMes)] and a 20 mM substrate concertation under 4 bar H_2. Where L = Cl^-.

Fluorinated *N*-heterocyclic compound	$[Ir(H)_2(IMes)(sub)_3]Cl$ (**A**)	Hydride Chemical Shift	$[Ir(H)_2(\mathbf{L})(IMes)(sub)_2]$ (**B**)	Hydride Chemical Shift
2-fluoropyridine (**1**)	-	-	-	-
3-fluoropyridine (**2**)	88	−22.98	12	−23.73, −25.09
4-fluoropyridine (**3**)	-	-	-	-
3,5-difluoropyridine (**4**)	24	−23.31	76	−24.01, −24.73
Fluoropyrazine (**5**)	15	−22.39	85	−22.82, −24.41
5-fluoropyridine-3-carboxylic acid (without base) (**6**)	80	−22.59	20	−23.77, −24.63
5-fluoropyridine-3-carboxylic acid (with base) (**7**)	100	−22.83	0	-

Examination of the ^{19}F NMR spectra was undertaken to probe the speciation of the catalysts present due to the low background signal. Unfortunately, the *bis* substituted catalyst was not observed as an enhanced response, as shown in section 3.5 of this chapter. However, when examining the hydride region of 3-fluoropyridine the ratio of **A** to **B** in the hydride region proved to be 7.3:1 and the greatest ^{19}F and ^{1}H signal enhancement was 62 ± 6 and −1287 ± 65 respectively. When comparing this to 3,5-difluoropyridine, where the ratio of **A** to **B** was 1:3.6 the ^{19}F and ^{1}H signal enhancements were now 14 ± 1 and −591 ± 10-fold respectively. These data suggest that probing the ligand exchange behaviour of these complexes is essential if we are to understand these results.

3.4.2 Ligand exchange for fluorinated *N*-heterocyclic compounds

The accepted mechanism for substrate loss in a $[Ir(H)_2(IMes)(sub)_3]Cl$ type complex is given in Figure 3.9 which details how the labelled groups (*) evolve over time and therefore how the EXSY data needs to be examined when this species is present.[119]

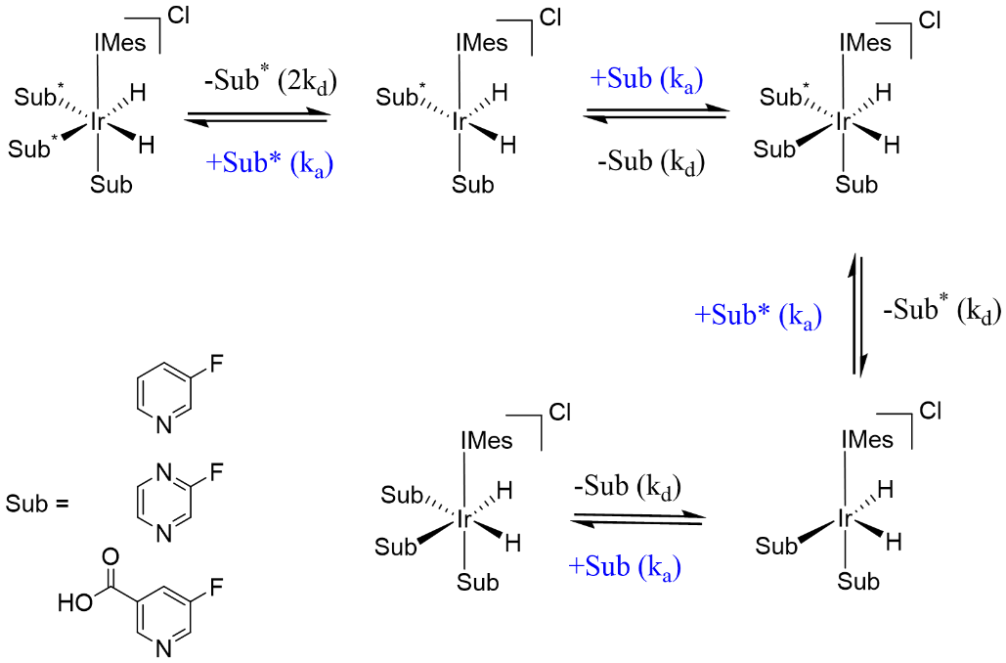

Figure 3.9 – Proposed mechanism for ligand exchange in the complex $[Ir(H)_2(IMes)(sub)_3]Cl$.

As a result of this process, when a bound ligand site is selectively excited, the detected signal will move into a signal at the free ligand peak position as described in Chapter 2.1.3 and experimental 7.2.10. For the substrates studied in this chapter, only 5-fluoropyridine-3-carboxylic acid in the presence of Cs_2CO_3 followed the simple mechanism described in Figure 3.9 as only one major complex, $[Ir(H)_2(\mathbf{7})_3(IMes)]Cl$ is formed in solution. For **2**, 88% of the *tris* adduct forms and the rate of ligand loss proved to fit with this mechanism even though a second form of the catalyst is present in solution. The resulting ligand loss rate constants are presented in Table 3.6. The rate of ligand loss could be calculated to a large degree of accuracy, as highlighted by the low errors obtained.

Table 3.6 – Rate constants for the loss of the ligand (sub) in $[Ir(H)_2(IMes)(sub)_3]Cl$, where sub = 3-fluoropyridine or 5-fluoropyridine-3-carboxylic acid, in methanol-d_4 (0.6 mL)as a function of temperature, results *via* selective 1D-EXSY experiments at 500 MHz.

Temperature, T (K)	3-fluoropyridine Rate of ligand loss / s^{-1}	5-fluoropyridine-3-carboxylic acid with base Rate of ligand loss / s^{-1}
260	0.061 ± 0.001	0.019 ± 0.001
265	0.163 ± 0.001	0.052 ± 0.001
270	0.389 ± 0.040	0.112 ± 0.001
275	0.867 ± 0.003	0.268 ± 0.001
280	2.040 ± 0.001	0.569 ± 0.002
285	4.523 ± 0.013	-
290	9.112 ± 0.023	-
295	17.189 ± 0.095	-

The resulting activation parameters are derived from an Eyring analysis as described in Chapter 2.1.3. The results of this analysis are shown in Table 3.7 and were obtained from the rate constants in Table 3.6.

Table 3.7 – Activation parameters for ligand loss (sub) in $[Ir(H)_2(IMes)(sub)_3]Cl$ in methanol-d_4.

Sub	$\Delta H^{\ddagger}$ kJ mol^{-1}	$\Delta S^{\ddagger}$ J mol^{-1} K^{-1}	$\Delta G^{\ddagger}_{300\ K}$ kJ mol^{-1}
3-fluoropyridine (**2**)	99.4 ± 2.7	121.9 ± 9.6	62.8 ± 1.0
5-fluoropyridine-3-carboxylic acid in the presence of base (**7**)	96.4 ± 6.1	100.5 ± 22.4	66.2 ± 1.0
Pyridine	95 ± 1[111]	96 ± 2[111]	66 ± 0.04[111]

The enthalpy of activation of $\Delta H^{\ddagger}_{(Ligand)}$ for loss of 5-fluoropyridine-3-carboxylic acid in the presence of base is 96 ± 6 kJ mol^{-1} and $\Delta S^{\ddagger}_{(Ligand)}$ is 101 ± 22 J mol^{-1} K^{-1}. The associated Gibbs free energy barrier to ligand loss at 300 K is 66 ± 1 kJ mol^{-1}. It is notable that the value of $\Delta S^{\ddagger}$ is large and positive in accordance with the dissociative nature of this reaction and that the barrier is similar to that reported for pyridine for the analogous complex.[111]

Unfortunately, when the substrates 3,5-difluorpyridine and 2-fluoropyrazine were examined, the data no longer fit to this simple model. Instead, the model needed to change to reflect the presence of two complexes in solution and the fact that these complexes interconvert. Upon examination of the NMR spectra however significant overlap between the ligand and free substrate resonances was revealed. Consequently, even though several attempts were made, no suitable kinetic solution could be found for ligand loss when these results were analysed. It was decided, therefore, not to pursue the rate of ligand loss for these complexes any further. For 5-fluoropyridine-3-carboxylic acid many species were formed due to it being zwitterionic. Therefore, no reliable rate data could be obtained for this substrate.

3.4.3 Hydride exchange for fluorinated *N*-heterocyclic compounds

However, the SABRE process requires both substrate and H_2 loss to occur. The latter step being important as it allows the latent source of polarisation to be refreshed within the complex. Furthermore, the rate that complex **A** goes to complex **B** can be no larger than the ligand loss rate as this precedes the formation of **B**. Thus, the role of **A** and **B** was examined for substrates **2, 4, 5** and **6** *via* their hydride sites. Lloyd *et. al.* (2014) suggested an explicit role for [Ir(H)$_2$(methanol)(sub)$_2$(IMes)]Cl in this reaction.[111] Consequently, the mechanism shown in Figure 3.10 was used in the kinetic model where **L** could be chloride or methanol.[111]

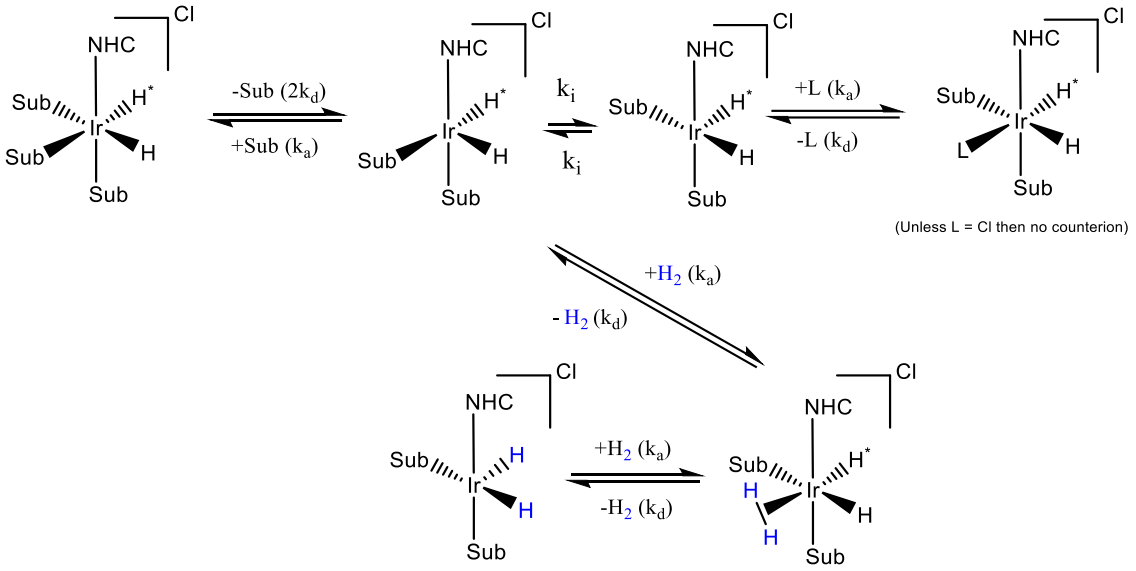

Figure 3.10 – Reaction mechanism as demonstrated by Lloyd *et. al.* (2014), showing the possible H_2 loss pathways for 3-NHC, [Ir(H_2(Pyridine)$_3$(NHC)]Cl involving a complex with ligand L which could be chloride or methanol.[111]

It can be seen from Figure 3.10 that loss of pyridine from the product [Ir(H)$_2$(NHC)(pyridine)$_3$]Cl, where NHC = *N*-heterocyclic carbene, is competitively trapped by methanol or Cl. This step has been confirmed experimentally at 265 K by investigating the kinetic fate of the hydride ligands of both the major and minor hydride species. This behaviour was established *via* a series of long-acquisition time EXSY measurements under 3 bar H_2 pressure, when the NHC was IMes. The modelling from Lloyd *et. al.* (2014) suggested that the experimentally dominant H_2 loss pathway involves [Ir(H)$_2$(**L**)(NHC)(pyridine)$_2$] of Figure 3.10 (where **L** was methanol) with an observed rate of H_2 loss of 1.72 s^{-1} at 265 K. Under these conditions, the rate of conversion of [Ir(H)$_2$(IMes)(pyridine)$_3$]Cl into [Ir(H)$_2$(**L**)(IMes)(pyridine)$_2$]Cl proved to be 0.08 s^{-1} and the rate for the return process was 4.14 s^{-1}.[111]

They proposed that the successful trapping of 16-electron [Ir(H)$_2$(NHC)(pyridine)$_2$]Cl by methanol was a consequence of the concentration of methanol being far greater than that of H_2. Further confirmation for this pathway came from the observed linear dependence of the H_2 loss rate on H_2 concentration over the H_2 pressure range 1 to 3 bar. They comment that H_2 loss is also

inhibited by adding pyridine in accordance with a shift in equilibrium towards $[Ir(H)_2(IMes)(pyridine)_3]Cl$.

The relative ratios of these species were 100:1 respectively which made these studies hard to implement. However, they found that the δ –23.45 hydride signal of $[Ir(H)_2(IMes)(methanol)(sub)_2]Cl$ exhibited a *trans* ^{15}N-hydride coupling of 15 Hz with ^{15}N-labelled pyridine and that upon adding H_2O, the other hydride signal at δ −25.49 moved to δ −25.74 due to the formation of $[Ir(H)_2(H_2O)(NHC)(pyridine)_2]Cl$. These results confirmed the identity of their minor species. The similarity in these reported chemical shifts, to those reported in Table 3.6 is highly noteworthy. As previously mentioned, confirmation of whether **L** was methanol or Cl in the studies with the fluorinated *N*-heterocycles was carried out by using the catalyst $[Ir(COD)(IMes)(Acetonitrile)]PF_6$ rather than [IrCl(COD)(IMes)]. From these experiments it was confirmed that **L** was Cl.

A series of qualitative deductions from the EXSY data were made to establish the method of analysis needed. In the first instance when the hydride signal at δ −22.96 due to $[Ir(H)_2(\mathbf{2})_3(IMes)]Cl$ was excited and exchange into free H_2 and the two hydride signals for what is proposed to be $[IrCl(H)_2(\mathbf{2})_2(IMes)]$ at δ −23.72 and δ −25.1 was seen. The latter two signals appear with equal intensity as expected for an exchange process which effectively takes a H_2 molecule and splits it into two inequivalent single protons in the product. When the mixing time is 0.6 s and the temperature 270 K, the relative signal intensities are 1: 0.5 and 0.07 for the three species respectively. In a second measurement, the hydride signal at δ −23.72 was selected. Now exchange into H_2, to $[Ir(H)_2(\mathbf{2})_3(IMes)]Cl$ and the second hydride site is seen. The ratio of these signals at a mixing time of 0.15 s is 1 (signal left on the parent):0.13:0.44:0.2 respectively. These values confirm that the species with inequivalent hydride ligands **B** is far more reactive than $[Ir(H)_2(\mathbf{2})_3(IMes)]Cl$. Consequently, the presence of **B** will have a significant impact on the SABRE results. As indicated in Table 3.5, the proportion of these complexes changes with the substrate, with **B** dominating in the other systems. It is therefore necessary to fully analyse these data if appropriate deductions are to be made on the role of these species under SABRE.

The hydride site interconversions were therefore analysed by EXSY for these systems. The experimental rate constants (k_{obs}) for four processes where sub = 3,5-difluoropyridine, are presented in Table 3.8. These processes correspond to the conversion of **A** into **B**, the loss of H_2 from **B**, the interchange of the hydride ligand positions in **B** and the conversion of **B** to **A**.

The full reaction pathway and rate constants for all substrates, **2** and **5**, is presented in the Appendix (section A.10).

Table 3.8 – Rate constants for the hydride exchange processes involving $[Ir(H)_2(4)_3(IMes)]Cl$, $[IrCl(H)_2(4)_2(IMes)]$, $[IrCl(H)_2(4)_2(IMes)]$ and $[IrCl(H)_2(4)_2(IMes)]$, where 4 = 3,5-difluoropyridine, in methanol-d_4 (0.6 mL) as a function of temperature, results *via* selective 1D-EXSY experiments at 500 MHz.

Temp, T (K)	Experimental rate constants for the indicated process (s^{-1})			
	$[Ir(H)_2(\mathbf{4})_3(IMes)]Cl$ (rate **A** goes to **B**)	$[IrCl(H)_2(\mathbf{4})_2(IMes)]$ (**B**) (rate H_2 loss)	$[IrCl(H)_2(\mathbf{4})_2(IMes)]$ (**B**) (rate interchange of hydrides)	$[IrCl(H)_2(\mathbf{4})_2(IMes)]$ rate **B** goes to **A**
255	0.0476	0.1097	0.0659	0.0076
260	0.0760	0.1863	0.2717	0.0380
265	0.2426	0.4290	0.7646	0.1029
270	0.5435	0.9076	1.9127	0.2122
275	1.2057	1.7930	4.3667	0.5383
280	2.4636	3.7989	6.8171	1.1000

3-fluoropyridine and fluoropyrazine proved to behave in a similar way to 3,5-difluoropyridine. The corresponding activation parameters, for the substrates 3-fluoropyridine, 3,5-difluoropyridine and fluoropyrazine are shown in Table 3.9 according to the rate constants collected in Table 3.8 or in Appendix A.10 Table A.17 and Table A.18.

Table 3.9 – Activation parameters for hydride loss in $[Ir(H)_2(IMes)(sub)_3]Cl$ in methanol-d_4. Sub = 3-fluoropyridine (2), 3,5-fluoropyridine (4) or fluoropyrazine (5).

		Substrate		
		2	**4**	**5**
Conversion of (**A**) to (**B**)	$\Delta H^{\ddagger}$ kJ mol^{-1}	102.4 ± 7.0	93.4 ± 4.1	102.0 ± 15.0
	$\Delta S^{\ddagger}$ J mol^{-1} K^{-1}	129.6 ± 25.6	102.5 ± 15.0	122.7 ± 56.7
	$\Delta G^{\ddagger 300\ K}$ kJ mol^{-1}	63.5 ± 1	62.6 ± 1	65.2 ± 1
Loss of H_2 from (**B**)	$\Delta H^{\ddagger}$ kJ mol^{-1}	88.9 ± 8.2	83.4 ± 7.5	87.6 ± 6.5
	$\Delta S^{\ddagger}$ J mol^{-1} K^{-1}	88.2 ± 29.9	69.9 ± 27.9	78.2 ± 24.0
	$\Delta G^{\ddagger 300\ K}$ kJ mol^{-1}	62.5 ± 1	62.5 ± 1	65.2 ± 1
Process wherein inequivalent hydride ligands in **B** swop	$\Delta H^{\ddagger}$ kJ mol^{-1}	82.4 ± 18.7	108.3 ± 20.8	101.6 ± 12.0
	$\Delta S^{\ddagger}$ J mol^{-1} K^{-1}	67.0 ± 68.0	166.7 ± 77.8	142.0 ± 43.5
	$\Delta G^{\ddagger 300\ K}$ kJ mol^{-1}	66.5 ± 1	58.3 ± 1	59.0 ± 1
Conversion of (**B**) to (**A**)	$\Delta H^{\ddagger}$ kJ mol^{-1}	93.8 ± 22.7	96.1 ± 11.9	97.2 ± 10.4
	$\Delta S^{\ddagger}$ J mol^{-1} K^{-1}	114.4 ± 82.8	104.9 ± 44.4	92.1 ± 37.3
	$\Delta G^{\ddagger 300\ K}$ kJ mol^{-1}	59.5 ± 1	64.6 ± 1	69.6 ± 1

The conversion of **A** to **B** involves the loss of substrate and coordination of chloride. It is associated with a large positive activation entropy in accordance with a process that involves the dissociative loss of substrate in the first step. If the binding of chloride were to play a major role

in this change the activation entropy would be substantially reduced. Hence $\Delta H^{\ddagger}$ will also be reflective of the barrier to substrate loss which is larger for substrates **2** and **5** than that previously reported for pyridine (95 ± 1 kJ mol^{-1}).[111] These complexes are therefore less reactive than $[Ir(H)_2(IMes)(pyridine)_3]Cl$.

It can be seen from these data that the rate of H_2 loss in this mixture is controlled by **B** as the fitting process results in the rate of H_2 loss from **A** being zero. Again, this change from **B** is reflected in a large positive entropy of activation which suggests dissociative character in agreement with previous reports.[111, 119, 187] We know from the SABRE results that substrate **2** performs the best of this series. The values of $\Delta G^{\ddagger 300\,K}$ suggest that this behaviour is a consequence of the higher reactivity of this substrate when compared to the other two in this series.

The exchange mechanisms within the SABRE process are important, this includes the ligand and hydride exchange. Although the ligand exchange is the process which is examined in more detail, the overlapping peaks of the ligand in the two complexes meant the data could not be fitted. Therefore, the hydride exchange needed to be examined more comprehensively for these systems.

The $[Ir(H)_2(methanol)(pyridine)_2(IMes)]$ complex reported by Lloyd *et. al.* (2014) has a rate of H_2 formation of 1.72 s^{-1} at 265 K. The *bis* substituted complexes formed in this study exhibit analogous rates at 265 K for **2** of 0.37 s^{-1}, for **4** of 0.43 s^{-1} and for **5** of 0.16 s^{-1}. Again, the fluorinated *N*-heterocyclic compounds yield higher barriers, and this might go a little way to explaining why they yield ^{1}H enhancements that are good (−1287 ± 65 for H-2 on 3-fluoropyridine) rather than excellent as with pyridine (−2397 for H-2 on pyridine). In contrast, at 265 K the rate of conversion of **A** to **B** for pyridine is 0.08 s^{-1}, whereas for **2** it is 0.11 s^{-1}, for **4** it is 0.24 s^{-1} and for **5** it was found to be 0.06 s^{-1}. Examining the conversion of **B** back to **A** the rate was 4.14 s^{-1} for pyridine, 1.23 s^{-1} for **2**, 0.10 s^{-1} for **4** and 0.01 s^{-1} for **5**. For all three substrates, $\Delta S^{\ddagger}$ is positive and all the exchange pathways are in accordance with the dissociative nature of these reactions.

For $[Ir(H)_2(5\text{-fluoropyridine-3-carboxylic acid})_3(IMes)]Cl$, data was collected in the presence of Cs_2CO_3 and the rate of hydrogen loss could also be analysed using a similar protocol to that of

ligand exchange because the second species was not seen. Rate data was calculated at different temperatures, see Table 3.10. Using the Eyring equation, activation parameters were also calculated.

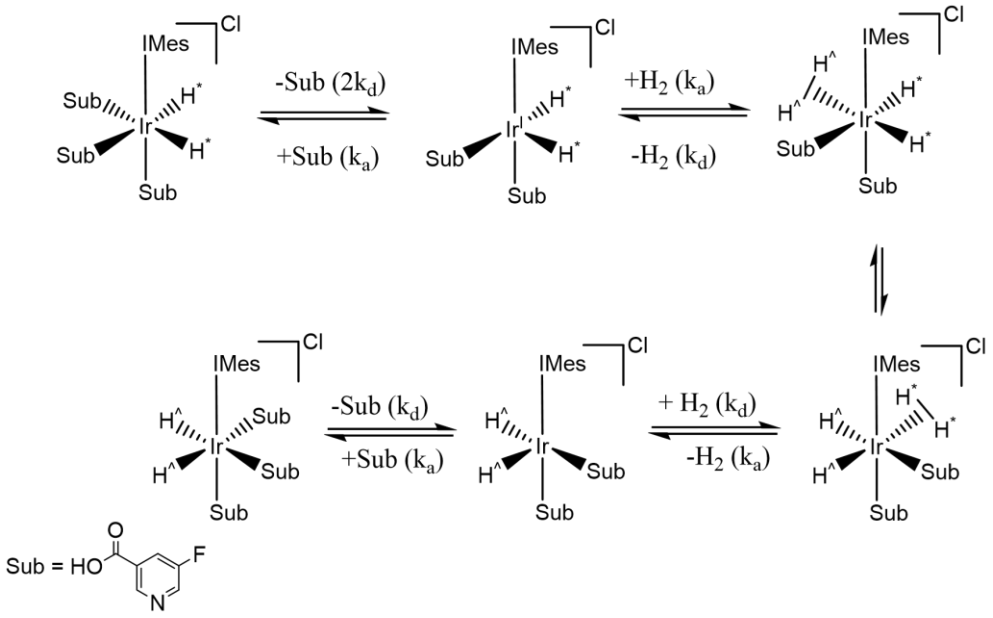

Figure 3.11 – Proposed mechanism for hydrogen exchange in the complex $[Ir(H)_2(IMes)(sub)_3]Cl$ where sub = 5-fluoropyridine-3-carboxylic acid in the presence of base.

The barrier for H_2 loss $\Delta H^{\ddagger}_{(H2)}$ is 97 ± 12 kJ mol^{-1} and $\Delta S^{\ddagger}_{(H2)}$ is 95 ± 40 J mol^{-1} K^{-1} which is the same, within error as the, $\Delta H^{\ddagger}_{(Ligand)}$ = 96.7 ± 11.5 and the $\Delta S^{\ddagger}_{(Ligand)}$ = 95.2 ± 40.4 (Table 3.11). The rate of substrate loss and hydrogen loss at 280 K is 0.56 and 0.3 s^{-1} respectively and hence as expected the rate of hydrogen loss is slower than that of substrate loss. This is reflected in a $\Delta G^{\pm 300K}$ of 68 ± 1.0 kJ mol^{-1}, compared to the $\Delta G^{\ddagger 300\ K}$ of 64 ± 1.0 kJ mol^{-1} for ligand loss. This is consistent with the H_2 loss process happening after ligand loss.

Table 3.10 – Rate constants for the loss of hydrogen in [Ir(H)$_2$(5-fluoropyridine-3-carboxylic acid)$_3$(IMes)]Cl in the presence of Cs_2CO_3, complex in methanol-d_4 (0.6 mL) as a function of temperature.

Temperature (K)	Rate of hydrogen loss (s^{-1})
270	0.04 ± 0.001
275	0.12 ± 0.003
280	0.34 ± 0.005
285	0.58 ± 0.005
290	1.13 ± 0.005
295	2.04 ± 0.009
300	3.92 ± 0.059

Table 3.11 – Activation parameters for hydrogen loss of [Ir(H)$_2$(5-fluoropyridine-3-carboxylic acid)$_3$(IMes)]Cl in the presence of Cs_2CO_3 complex in methanol-d_4 (0.6 mL) using the experimental data from the 1D-EXSY experiments obtained using a 500 MHz Bruker NMR spectrometer.

Substrate	$\Delta H^{\ddagger}$ kJ mol^{-1}	$\Delta S^{\ddagger}$ J mol^{-1} K^{-1}	$\Delta G^{\ddagger 300\ K}$ kJ mol^{-1}
5-fluoropyridine-3-carboxylic acid in the presence of Cs_2CO_3	96.7 ± 11.5	95.2 ± 40.4	68.1 ± 1.0

3.5 Examination of the ^{19}F spectra

Upon detailed examination of the SABRE ^{19}F NMR spectra for all substrates where both the *tris* and *bis* substituted complexes are formed, ^{19}F peaks are detected for both complexes as well as the free substrate. This is most clearly seen for fluoropyrazine (see Figure 3.12) where 15% of the *tris* complex is formed. In the ^{19}F SABRE response a greater signal gain is seen for the ^{19}F signals of the equatorial ligands of both complexes. It is worth noting that the ^{19}F signal in the equatorial position of the *bis* substituted complex is broad. This feature is indicative of slow ligand rotation and consequently a blurring of chemical shift. In contrast, the resonances for the axial ligands

remain sharp, but poorly enhanced due to slow exchange at best. These spectra confirm a role and importance for the second species.

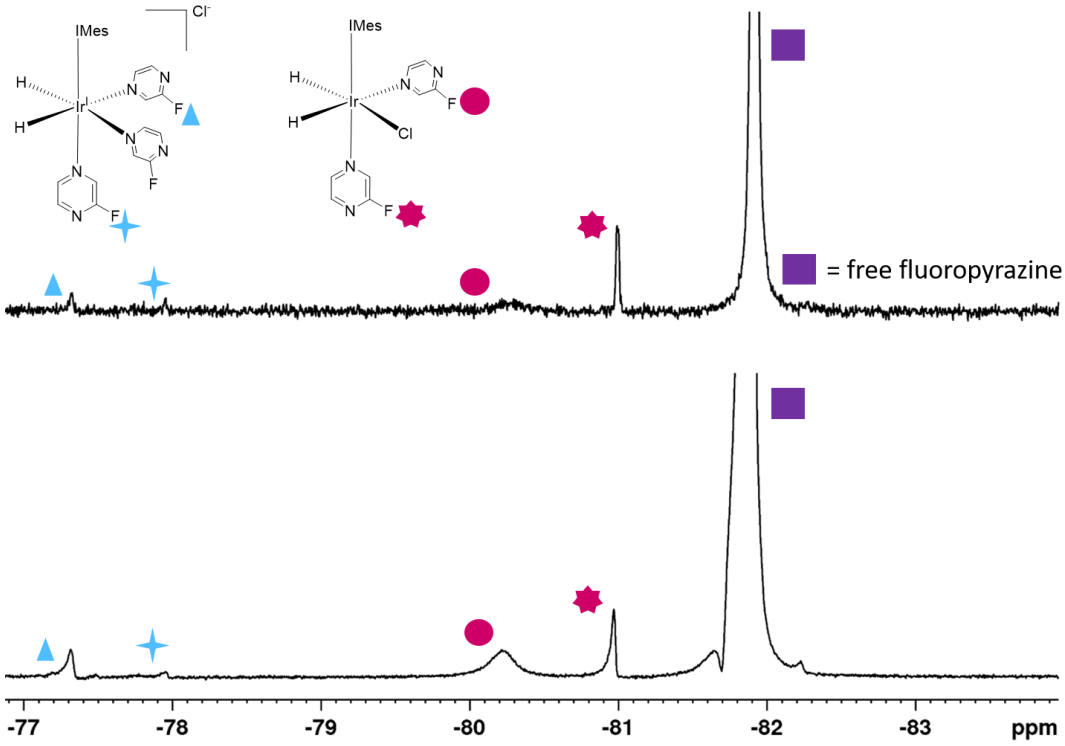

Figure 3.12 – ^{19}F NMR spectra of fluoropyrazine (100 mM) and [IrCl(COD)(IMes)] (5 mM) in methanol-d_4 (0.6 mL). Top is the Boltzmann equilibrated ^{19}F signal, when the sample was left in the spectrometer for 2 minutes to fully equilibrate, before acquisition (4 times vertical expansion applied). Top is the ^{19}F SABRE response when polarisation transfer took place at approximately 60 G (8 times vertical expansion applied). The equatorial and axial responses have been highlighted for the *bis* and *tris* complexes as well as for free fluoropyrazine.

3.6 Using INEPT to hyperpolarise ^{19}F

Due to the short T_1 values of the fluorine resonances, it was hypothesised that if hyperpolarisation was moved from the longer lived ^{1}H nuclear spin order to the ^{19}F nuclei at high field, using *r. f.* methods, an increased ^{19}F signal might result. This transfer of hyperpolarisation can be achieved using the Insensitive Nuclei Enhanced By Polarisation Transfer (INEPT) sequence.[233] It could also be carried out under Nuclear Overhauser Effect (nOe)[28] conditions or by Distortionless Enhancement by Polarisation Transfer (DEPT) sequences.[234]

3.6.1 Description of the INEPT sequence

The INsensitive Nuclei Enhanced by Polarisation Transfer (INEPT) pulse sequence was first described and named in 1979 by Morris *et. al*.[233] This sequence uses the magnetisation of a nucleus with a large γ (^{1}H) to increase the signal of a nucleus with a low γ (X). The INEPT sequence is presented in Figure 3.13. The ^{1}H is excited with a 90° *r. f.* pulse, a time interval of τ_1 is waited and then a 180° pulse is applied to both nuclei. This pulse combination refocuses any magnetisation evolution/dephasing that has occurred due field inhomogeneity effects. Another delay of τ_1 is then given and a 90° is then applied again to both nuclei. These pulses result in the transfer of polarisation from ^{1}H to X, thereby producing an enhanced signal on the X nucleus.

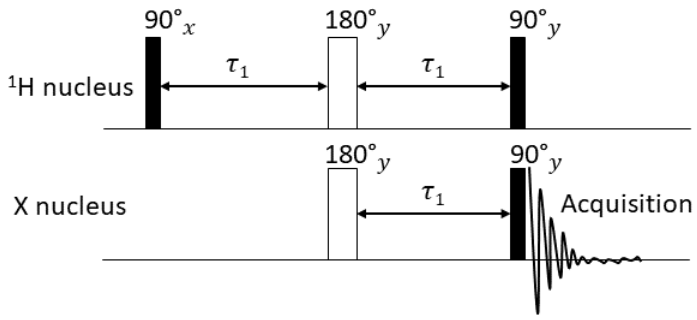

Figure 3.13 – INEPT pulse sequence adapted from NMR: The toolkit by Hore *et. al*.[11]

The time delay, τ_1 can be calculated using equation 3.2

$$\tau = \frac{1}{(4J_{HX})} \qquad (3.2)$$

where J_{HX} is the J coupling between ^{1}H and the X nucleus, for example ^{19}F. In the case of ^{19}F the $^3J_{HF}$ values range from 2-15 Hz, therefore τ should be in the range of 0.017 ms to 0.125 ms. If this time delay has been miscalculated, then poor polarisation transfer will result and if it is too long the impact of relaxation could be substantial.

3.6.2 Polarisation of ^{19}F using the INEPT sequence

The seven substrates in this study exhibited J_{HF} couplings in the range of 2.6 to 9.4 Hz, close to that expected in literature ($^3J_{HF}$ = 2-15 Hz)[235] and therefore, different time delays were needed for the INEPT experiments.

The results of INEPT transfer are presented in Table 3.12 alongside the ^{19}F signal enhancements of the SABRE experiments carried out on the ^{19}F nucleus. Comparing the enhanced INEPT signal to that of the control INEPT thermal measurement, a signal improvement of between 2 times and 32 times was observed with 3,5-difluoropyridine and 5-fluoropyridine-3-carboxylic acid in the presence of base respectively. Unfortunately, for 3-fluoropyridine and 5-fluoropyridine-3-carboxylic acid, the signal enhancement decreased by approximately 5 and 2 times respectively when compared to the indirect transfer results. For fluoropyrazine, there was no improvement when using the INEPT sequence.

Table 3.12 – Signal enhancement of hyperpolarised ^{19}F NMR when using 100 mM of the *N*-heterocyclic fluorinated compound, 5 mM of pre-catalyst [IrCl(COD)(IMes)] in 0.6 mL MeOD-d_4 in the presence of 4 bar of *p*-H_2 in conjunction with the INEPT sequence and the 'normal' single pulse sequence on a 500 MHz Bruker NMR.

Fluorinated N-heterocyclic compound	^{19}F INEPT enhancement factor	^{19}F enhancement factor, indirect transfer
2-fluoropyridine (**1**)	-	-
3-fluoropyridine (**2**)	13 ± 1	62 ± 6
4-fluoropyridine (**3**)	-	-
3,5-difluoropyridine (**4**)	27 ± 4	14 ± 1
Fluoropyrazine (**5**)	17 ± 2	20 ± 1
5-fluoropyridine-3-carboxylic acid (without base) (**6**)	7 ± 1	14 ± 1
5-fluoropyridine-3-carboxylic acid (with base) (**7**)	98 ± 6	3 ± 1
5-fluorouracil (**8**)	3 ± 1	-

It was hypothesised that INEPT efficiency could be driven by initial ^{1}H enhancement levels with greater signal enhancement on the ^{1}H leading to ^{19}F polarisation improvement when using the INEPT sequence. However, as shown in Table 3.13 there is no clear correlation between ^{1}H

signal enhancement and ^{19}F signal intensity. For example, 3-fluoropyridine had the greatest ^{1}H and ^{19}F SABRE response but a very low INEPT signal. 5-fluoropyridine-3-carboxylic acid, without base, had both a low ^{1}H and ^{19}F response and this was decreased further when using the INEPT sequence.

Table 3.13 –Comparing INEPT and direct ^{19}F and ^{1}H signal enhancements for all fluorinated *N*-heterocyclic compounds.

Fluorinated N-heterocyclic compound	^{19}F INEPT enhancement factor	^{19}F enhancement factor, indirect transfer	Greatest ^{1}H enhancement
2-fluoropyridine (**1**)	-	-	−0.664 ± 0.1
3-fluoropyridine (**2**)	13 ± 1	62 ± 6	−1287 ± 65
4-fluoropyridine (**3**)	-	-	-
3,5-difluoropyridine (**4**)	27 ± 4	14 ± 1	−591 ± 10
Fluoropyrazine (**5**)	17 ± 2	20 ± 1	−716 ± 42
5-fluoropyridine-3-carboxylic acid (without base) (**6**)	7 ± 1	14 ± 1	−272 ± 20
5-fluoropyridine-3-carboxylic acid (with base) (**7**)	98 ± 6	3 ± 1	−635 ± 98
5-fluorouracil (**8**)	3 ± 1	-	−106

Therefore, when examining the T_1 data of the ^{1}H nuclei in each of the substrates, the substrate with the longest ^{1}H T_1 of 46.14 s displayed the highest increase with the INEPT sequence which was, 5-fluoropyridine-3-carboxylic acid in the presence of base. Fluoropyrazine displayed no difference between SABRE and INEPT and the T_1 was 27.09 s. Below this relaxation time, 21.11 and 14.54 s for 3-fluoropyridine and 5-fluoropyridine-3-carboxylic acid, a decrease in signal enhancement was observed. This has been tabulated in Table 3.14. However, all the substrates have similar ^{19}F T_1values and hence this is not the reason. Going forward it might be possible to

deuterate the other sites to not only increase the ^{1}H signal but also T_1. A consequence of this would be improved INEPT transfer.

Table 3.14 – Comparison of the greatest ^{1}H T_1 in seconds and whether or not a further improved enhancement signal was obtained *via* the INEPT pulse sequence.

Fluorinated *N*-heterocyclic compound	Highest T_1 within the molecule (s)	INEPT improvement
3-fluoropyridine (**2**)	21.11	×
3,5-difluoropyridine (**4**)	29.24	✓
Fluoropyrazine (**5**)	27.09	No change
5-fluoropyridine-3-carboxylic acid (**6**)	14.54	×
5-fluoropyridine-3-carboxylic acid, with base (**7**)	46.14	✓

3.7 Polarisation transfer field dependence on SABRE

As described in Chapter 1 section 1.3.4, an automated SABRE polariser can be used to create a hyperpolarised bolus and transfer the sample to the NMR spectrometer.[138] This approach was used in the following section to investigate the polarisation transfer field (PTF) dependence on the ^{1}H and ^{19}F NMR signal gains as it provides increased reproducibility when compared to manual SABRE experiments.[138] It is well known that for ^{1}H transfer a 65 G field is normally appropriate. For ^{19}F however no such data existed prior to this work. Equation 3.3 can be used to calculate the theoretical, optimal polarisation transfer field for ^{19}F,

$$B_{PTF} = \frac{J_{HH}}{\Delta\delta_{Hx}} . B_0 \qquad (3.3)$$

where B_{PTF} is the optimal polarisation transfer field, J_{HH} is the J coupling between the p-H_2 derived hydrides (approximately 8 Hz), $\Delta\delta_{Hx}$ is the chemical shift difference between the hydrides and the nucleus of interest, x.[105] The frequency difference at 500 MHz between the hydrides and ^{19}F is 29.5 MHz. Substitution into equation 3.3, results in the suggestion that the optimal PTF for ^{19}F is around 32 mG and therefore around 1/10th of the Earth's magnetic field.

Samples were prepared with 25 mM of the pre-catalyst [IrCl(COD)(IMes)] and all seven substrates at a 500 mM level in 3 mL of methanol-d_4. Figure 3.14 to Figure 3.18 show the ^{1}H NMR signal enhancement for these materials that result from use of the polariser. The optimal PTF for the compounds varied. For 3-fluoropyridine, it was found to be 50 G, 3-5-difluoropyridine was 60 G, the 5-fluoropyridine-3-carboxylic acid was between 50 – 60 G, whereas for the fluoropyrazine this was 70 G. 5-fluoropyridine-3-carboxylic acid yielded the best response at 60 G with and without base as shown in Figure 3.17 and Figure 3.18, respectively.

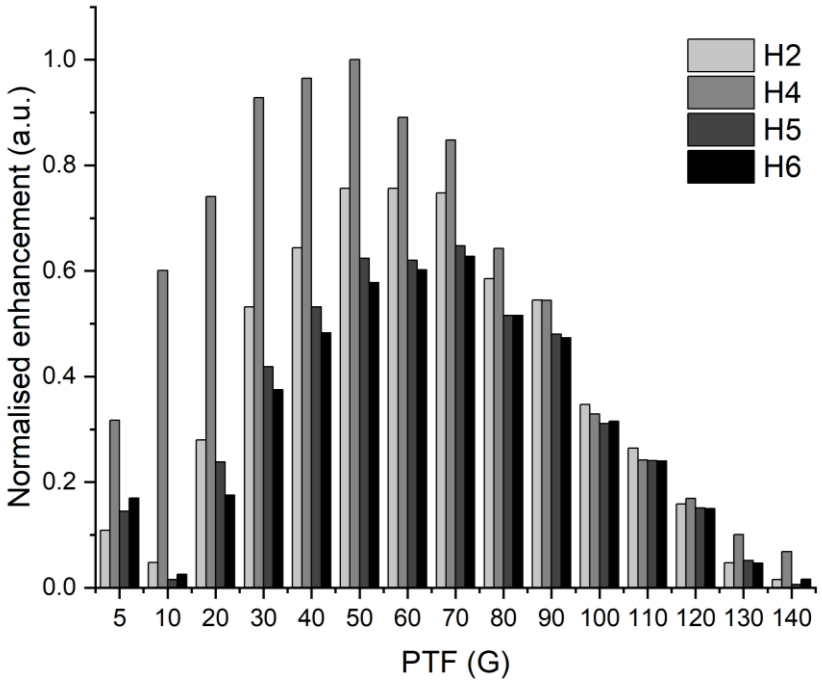

Figure 3.14 – Normalised SABRE signal enhancements of the individual ^{1}H nuclei for the 3-fluoropyridine as a function of polarisation transfer field in G.

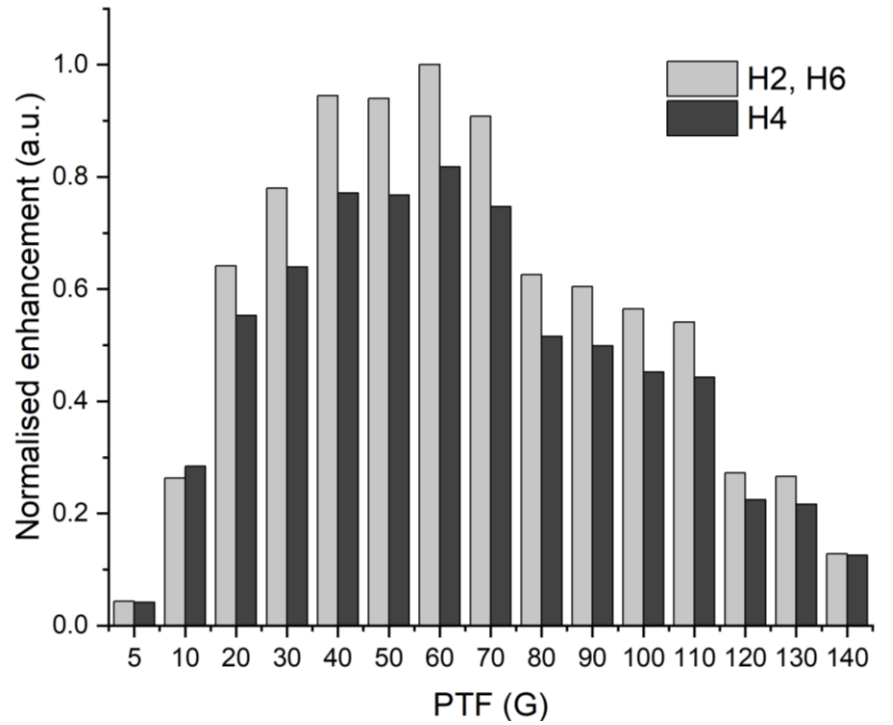

Figure 3.15 – Normalised SABRE signal enhancements of the individual ^{1}H nuclei for the 3,5-difluoropyridine as a function of polarisation transfer field in G.

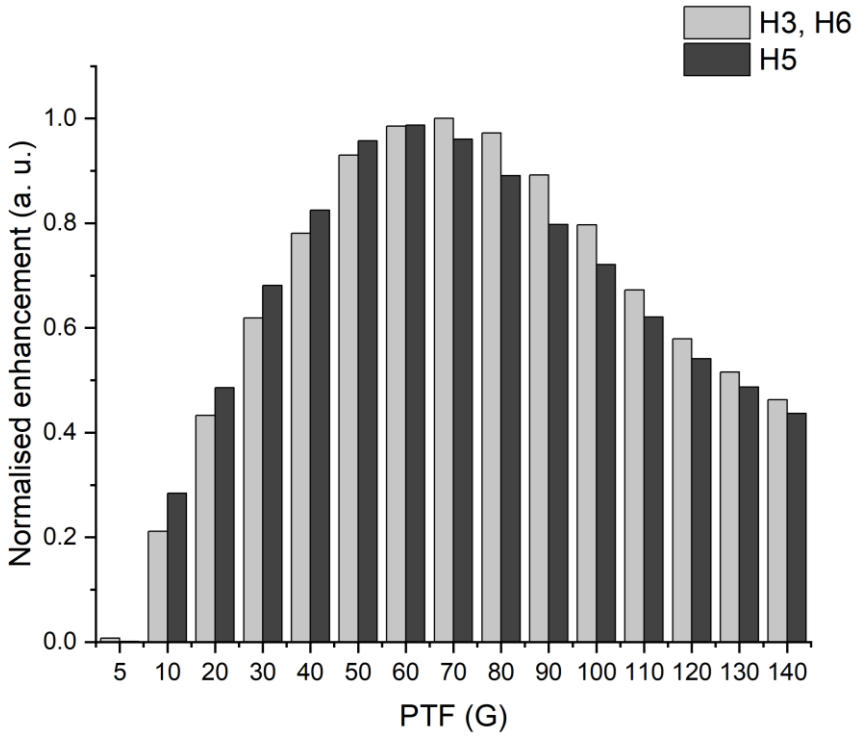

Figure 3.16 – Normalised SABRE enhancements of the individual ^{1}H nuclei for the fluoropyrazine as a function of polarisation transfer field in G.

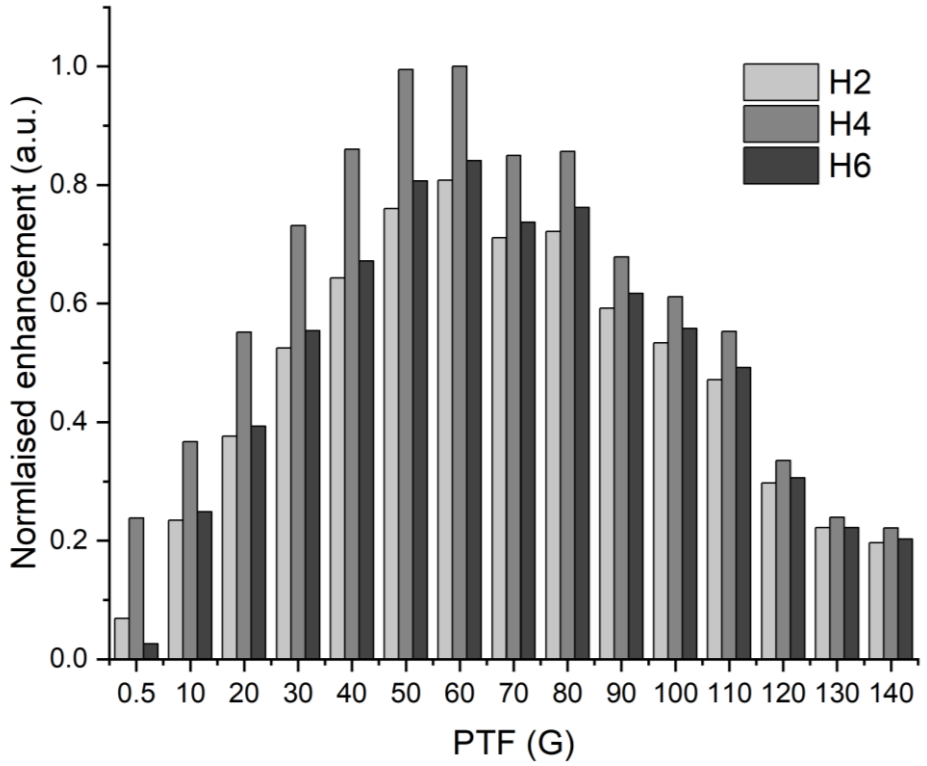

Figure 3.17 – Normalised SABRE signal enhancements of the individual ^{1}H nuclei for the 5-fluoropyridine-3-carboxylic acid, without base as a function of polarisation transfer field in G.

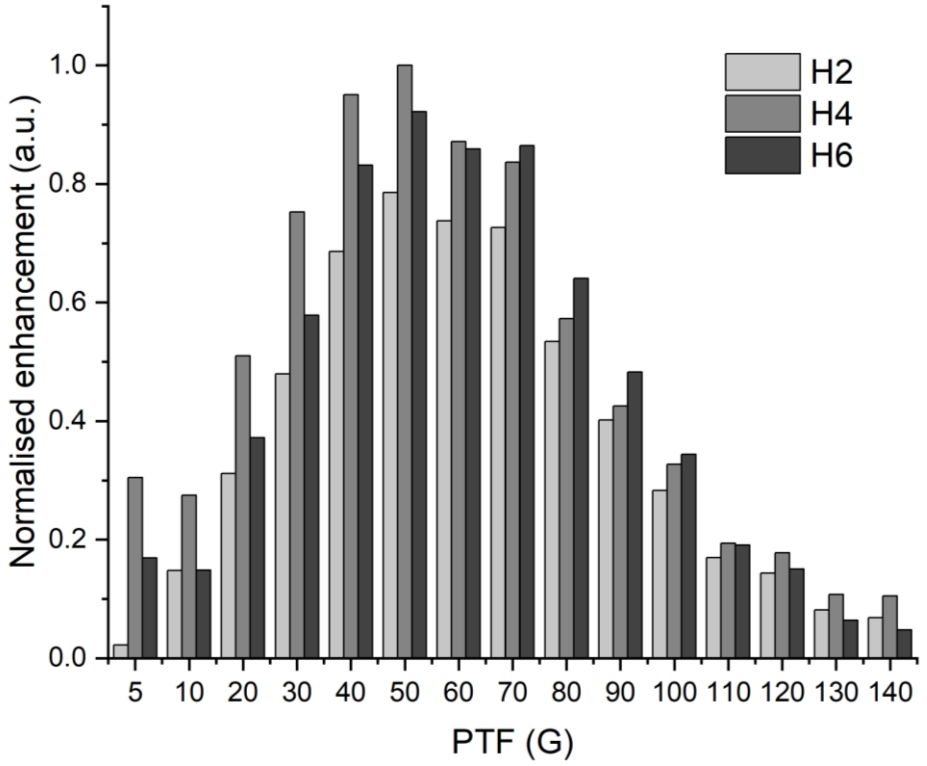

Figure 3.18 – Normalised SABRE signal enhancements of the individual ^{1}H nuclei for the 5-fluoropyridine-3-carboxylic acid, with base as a function of polarisation transfer field in G.

Hence as expected there is little variation for the efficiency of ^{1}H transfer with PTF provided a value of 60 G is used. When the corresponding ^{19}F measurements were made much lower signal gains resulted. This is likely to be linked to the short ^{19}F T_1 and 3 second transfer time. As a consequence, at least 60% of the hyperpolarised signal has vanished before the ^{19}F measurement is made (though these are in the Appendix, section A.11 for completeness). Hence the ^{19}F PTF plots suffer from low accuracy, although we can see that a PTF within the ^{1}H range is appropriate for these materials. In the future it might be possible to achieve direct transfer to ^{19}F *via* the use of a mu-metal shield and top-up solenoid.[204]

3.8 ^{19}F imaging

As previously discussed, SABRE hyperpolarised ^{1}H, ^{13}C, ^{31}P and ^{15}N nuclei have been detected using MRI methods.[176, 203, 236, 237] Hyperpolarised ^{19}F has also been exploited for imaging.[144] Here the fluorinated *N*-heterocyclic compounds which produced enhanced ^{19}F signals were examined under MR imaging conditions. Typical images from these measurements are shown in Figure 3.19. They were taken on a 9.4 T Bruker system, using a one shot, 2D centric encoded Rapid Acquisition with Relaxation Enhancement (RARE) image sequence with repetition time (TR) = 600 ms, echo time (TE) = 4 ms, field of view (FOV) = 40*40 mm, matrix size = 64*64 using a 40 mm dual tuned ^{1}H/^{19}F volume resonator.

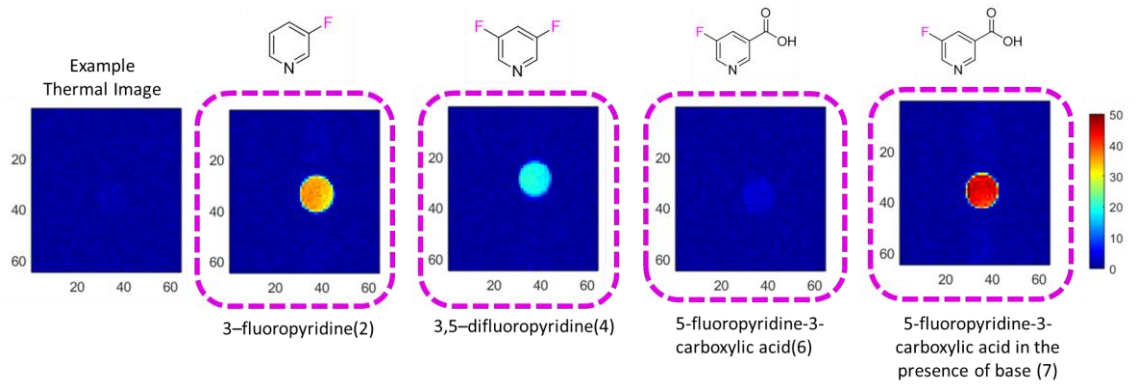

Figure 3.19 – MR Images carried out on a 9.4 T Bruker NMR system (integrated micro 2.5 gradient set) using a one shot, 2D centric encoded Rapid Acquisition with Relaxation Enhancement (RARE) image sequence, with TR = 600 ms, TE = 4 ms, FOV = 40*40 mm, matrix size = 64*64 using a 40 mm dual tuned $^{1}H/^{19}F$ volume resonator. Non-boxed images have been acquired in Boltzmann equilibrium conditions, d1 = 30s, NS = 64. Images in a dotted box are hyperpolarised, d1 = 600 ms, NS = 1. Samples were 5 mM [IrCl(COD(IMes)] with 100 mM of the fluorinated *N*- heterocycle in 3 mL methanol-d_4.

5-Fluoropyridine-3-carboxylic acid in the presence of Cs_2CO_3 resulted in the highest ^{19}F image SNR, although signal can be seen for all four tested substrates. In a later study, 5-fluorouracil was successfully imaged after SABRE using a Magnetom Prisma 3 T MRI scanner (Siemens Healthcare, Erlangen, Germany). A flex-surface coil was used for the *r. f.* transmission/reception. The imaging parameters used were a matrix size 8*8, 512 spectral points, across a ppm range of 172 ppm, FOV = 20*20*3 cm with TE = 2.3 ms, TR = 200 ms with a flip angle = 5 deg. The image acquired along with the thermal and hyperpolarised spectrum are shown in Figure 3.20. This infers that SABRE could be a good clinical route for imaging a biological response to 5-Fluorouracil.

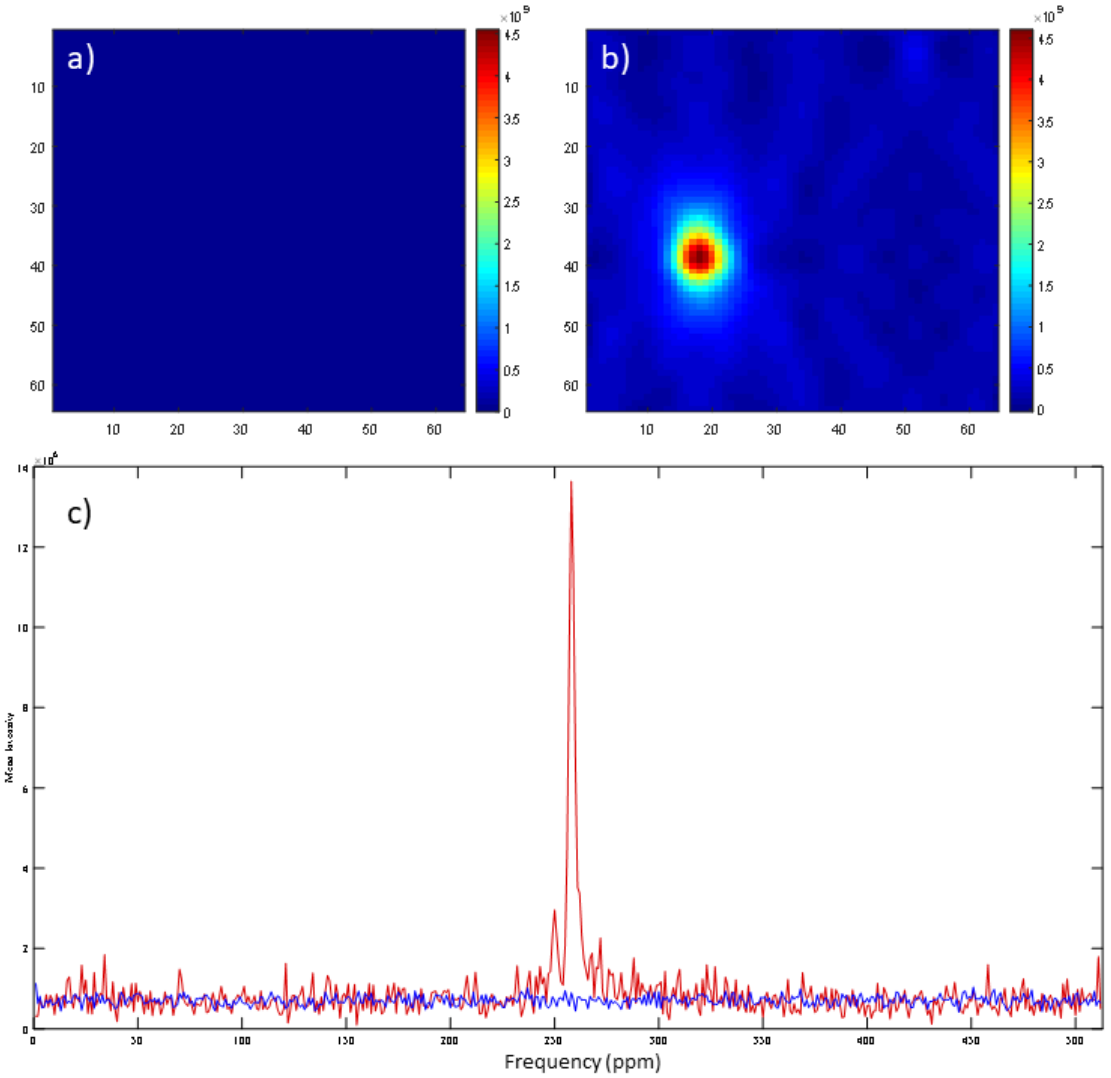

Figure 3.20 – 5 mM [IrCl(COD)(IMes)] and 100 mM 5-fluorouracil in 3.0 mL methanol-d_4 exposed to 4 bar *p*-H_2. CSI image taken using a Magnetom Prisma 3 T MRI scanner (Siemens Healthcare, Erlangen, Germany). Using a flex-surface coil for the *r. f.* transmission/reception. The imaging parameters used were a matrix size 8*8, 512 spectral points, across a chemical shift range of δ 172, FOV = 20*20*3 cm with TE = 2.3 ms, TR = 200 ms with a flip angle = 5 deg. A) shows the thermal signal of the sample, b) shows a 1 scan hyperpolarised image, c) shows the thermal and the hyperpolarised spectra acquired.

3.9 Conclusions

SABRE was successfully used to hyperpolarise a range of fluorinated *N*-heterocyclic compounds. 3-Fluoropyridine produced the highest ^{1}H and ^{19}F NMR signals, a −1286 ± 145 signal enhancement was observed for H-2 at a 20 mM concentration while a 62 ± 6 signal enhancement was seen for ^{19}F. 4-Fluoropyridine did not produce an enhanced signal in the corresponding ^{1}H NMR spectrum while 2-fluoropyridine yields low signal enhancements. Consequently, upon

shaking with *p*-H_2 weakly enhanced ^{1}H NMR signals are seen at 8.2, 8, 7.3, 7.1 for the free material but no SABRE enhanced hydride signal is seen, nor are any polarised signals seen for the bound ligand. This suggests ligand loss is slow. Other compounds, such as 3-5-difluoropyridine, 5-fluoropyridine-3-carboxylic acid and fluoropyrazine, gave good signal enhancements for both ^{1}H and ^{19}F.

Collectively, the T_1 values of the ^{1}H resonances of these materials at 9.4 T were found to be longer than those of the ^{19}F at 11.75 T, which is expected.[34]

The exchange data was collected *via* a 1D EXSY protocol for all the successful ^{1}H and ^{19}F signal enhanced substrates. However, the data for 3,5-difluoropyridine and fluoropyrazine did not prove suitable for further analysis. To provide data to examine ligand exchange, peak overlap needs to be overcome. This could be achieved by using a higher field or using a different approach. Bipyridyl has been used to study exchange rates in catalysts and might provide the answer.[238, 239] Another method could be to use UV detection (stop flow). Rate data for the zwitterionic compound, 5-fluoropyridine-3-carboxylic acid, could not be obtained due to too many different complexes forming making the signal too weak for the complexes of interest.

As described in Chapter 2 (2.1.3), two complexes were formed with pyrimidine and the SABRE pre-catalyst [IrCl(COD)(IMes)], $[Ir(H)_2(IMes)(sub)_3]$ (**A**) and $[IrCl(H)_2(IMes)(sub)_2]$ (**B**). Lloyd *et. al*. described another adduct, $[Ir(H)_2(IMes)(methanol)(pyridine)_2]$[111] (**C**), therefore there are three possible complexes that can form, and these can be distinguished by their different hydride resonances. At approximately δ −28 indicates a hydride resonance *trans* to oxygen, while those that appear at approximately δ −24 suggest hydride ligands *trans* to nitrogen. Those at approximately δ −23 seem to indicate a hydride *trans* to chlorine. The assignment of hydrides *trans* to nitrogen is relatively easy to confirm in these complexes through ^{15}N/^{1}H NMR as they possess strong trans J_{H15N} couplings of around 20 Hz. In both this chapter and in Chapter 2, it was demonstrated that the formation of catalyst **B**, particularly in large quantities, reduces the signal enhancement obtained in the substrate.

When looking at the species present in solution a single hydride is visible at between δ −22.5 and −23.3, indicative of $[Ir(H)_2(IMes)(sub)_3]Cl$. However, the situation is complicated for the exchange pathway for substrates **2**, **4**, **5** and **6** where another species is present. NMR analysis of these data is consistent with $[IrCl(H)_2(sub)_2(IMes)]$. This is further exhibited in the fact that the hydride signals *trans* to oxygen are known to appear at ca δ −28.[111] Analysis of the hydride ligand exchange processes confirmed that H_2 loss proceeds dominantly *via* **B** which yields a common intermediate from **A**, the 16 electron complex shown in the scheme in Figure 3.11.

^{19}F images were also obtained for these compounds which were successfully hyperpolarised by ^{19}F SABRE, although 3-fluoropyridine was not the substrate which produced the strongest phantom image. Instead this was taken from 5-fluoropyridine-3-carboxylic acid in the presence of Cs_2CO_3. It is hypothesised that this is due to delivery time from the SABRE experiment to the acquisition of the MR image. Therefore, the time between these should be measured in future experiments.

The image acquired on the Magnetom Prisma 3 T MRI for 5-fluorouracil was very promising, producing a large signal gain over the thermal. Although 5-fluorouracil was successfully hyperpolarised on ^{19}F and imaged, due to the cyclometallation reaction this substrate requires developing.

The work in this chapter demonstrates the success of ^{19}F polarised images obtained *via* the SABRE method. This represents the first steps in using these agents within the clinic to monitor drug metabolism and possibly drug targeting to tumour sites.

Chapter 4: Expanding the range of molecular scaffolds amenable to hyperpolarisation using SABRE

The Signal Amplification by Reversible Exchange (SABRE) process is extremely successful in polarising small *N*-heterocycles as their nitrogen donors often bind suitably to iridium.[13] Unfortunately, there are many substrates such as adenosine triphosphate (ATP), uracil and urea which do not bind to the SABRE catalyst due to their steric and electronic properties. For example, while ATP does have a suitable lone electron pair for ligation the molecule is so large ligation is poor. Conversely, uracil is sterically amenable, but it contains no free site for binding as the NH functions are highly conjugated.

The removal of the proton bound to nitrogen through the use of Cs_2CO_3 (exemplified with 5-fluorouracil; Chapter 3) or another suitable base makes such molecules more amenable to the SABRE process. However, the SABRE catalyst itself is unstable in acid solution. Researchers have functionalised such biological molecules to allow for their derivatives to be polarised *via* SABRE. For example, Diaz-Rullo *et al*, (2017) added a nitrogen ring to L-arginine, this allowed the molecule to bind to the active catalyst.[240] The drawback of this method is the requirement for pre-functionalisation of the target molecules.

To overcome this limitation, the use of sulfoxide as a co-ligand is explored. This co-ligand is used to stabilise the active catalyst and allow weak binding substrates to ligate. A new polarisation relay method, known as SABRE-relay[241, 242] is also explored. This method allows substrates with exchangeable protons to be polarised, without binding directly to the SABRE catalyst. Instead an amine, with a labile proton is bound to the SABRE catalyst and is polarised *via* SABRE.[241, 242] The labile proton can then be exchanged with a proton on the substrate. This exchange of protons allows polarisation to be relayed from the amine to the substrate of interest.[169, 241, 242] Thus the chemical structure of the substrate of interest remains unchanged, and the method expands the range of substrates which can be polarised *via* SABRE. This approach is discussed further in section 4.2.

This chapter describes experiments for SABRE-Relay polarisation of urea (section 4.3) and mono sodium phosphate (section 4.4) and the use of SABRE and a co-ligand, with sodium oxalate (section 4.5).

4.1 Perfusion agents for Magnetic Resonance Imaging (MRI)

Although injecting a contrast agent makes perfusion imaging invasive, exogenous agents like gadolinium (Gd) are already used in the clinic for enhancing MRI. Gd is one of the most widely used contrast agents in MRI.[243] It is already successfully used in MR perfusion on the cardiovascular system. In recent years, the use of Gd has come under scrutiny and the Food and Drug Administration has reclassified it with a warning and precaution label describing the increase in Gd retention in some patients.[244] Furthermore, in patients with pre-existing kidney problems there is a correlation between use of Gd and the development of nephrogenic systemic fibrosis (NSF).[245, 246] NSF presents as a hardening and thickening of tissue within the kidney. Unfortunately, the mechanism as to why the use of Gd exacerbates NSF remains unclear;[247-249] hence research into new, safer agents for perfusion imaging is needed.

Other, safer methods of performing these experiments have been investigated including using water as an endogenous contrast agent in arterial spin labelling (ASL).[250-252] Water can be magnetically labelled using inversion *r. f.* pulses. Over a particular transit time this labelled water will perfuse organs of interest, where a weighted image can be acquired. A difference image, when compared to a non-labelled control results in a quantifiable perfusion based image.[252] ASL images are confounded by both low spatial resolution and contrast to noise ratio (CNR).[250] Intra voxel incoherent motion (IVIM) measurements have also been used to assess perfusion without the use of contrast agents.[253] Just as with ASL, IVIM also gives a limited CNR and further developments are needed before this is seen in clinic.[254] Hyperpolarisation of water, albeit as an exogenous contrast agent, holds the potential to overcome the CNR limitation. Hence, the technology could be used to diagnose subtle perfusion based changes such as those in Alzheimer's disease.[251] One way to overcome the problems with ASL and IVIM would be to use hyperpolarised molecules, for example water or urea. These molecules are metabolically inactive,

Expanding the range of molecular scaffolds amenable to hyperpolarisation using SABRE

biologically safe and are already widely used as contrast agents in perfusion based imaging.[201, 255-258]

4.1.1 Using hyperpolarised urea to improve MR images

The hyperpolarisation of urea can be used as an alternative method to both Gd and ASL. Urea is a biological by-product of the urea cycle through which the body removes ammonia from the body as shown in Figure 4.1. It is therefore metabolically inactive and biologically safe.

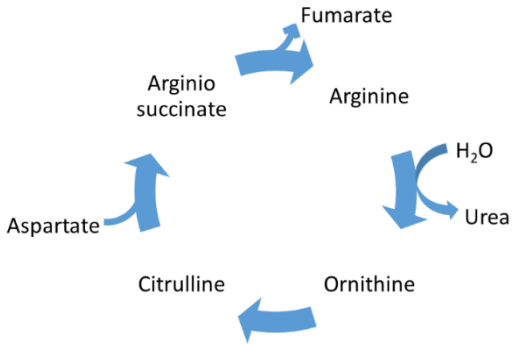

Figure 4.1 – The urea cycle. Image adapted from L. Stryer Biochemistry textbook 1975 page 697.[43]

Urea was one of the first molecules to be hyperpolarised by dissolution DNP,[32] with 37% ^{13}C polarisation and 7.8% ^{15}N polarisation being described.[32] Since then, ^{13}C-urea has been used as a perfusion agent for studies of the kidneys,[259] liver,[237] tumours[260] and as a cardiac agent to probe swine.[192]

In 2011, von Morze *et al* used hyperpolarised urea to image the blood flow in pre-clinical cancer models.[256] Using a hyperpolarised agent approach, the rate of renal to hepatic blood flow was measured to be 3.45 ± 0.80 ml min^{-1} and found to be in agreement with published measurements using radioactive microspheres.[256, 261] They also noted that there was a 19% reduction in mean blood flow in tumours when compared to healthy cells. It was therefore concluded that the low ^{13}C-urea signal observed, coupled with the high lactate (poor perfusion and high metabolic activity) presents as an indicator of tumour progression (Figure 4.2).

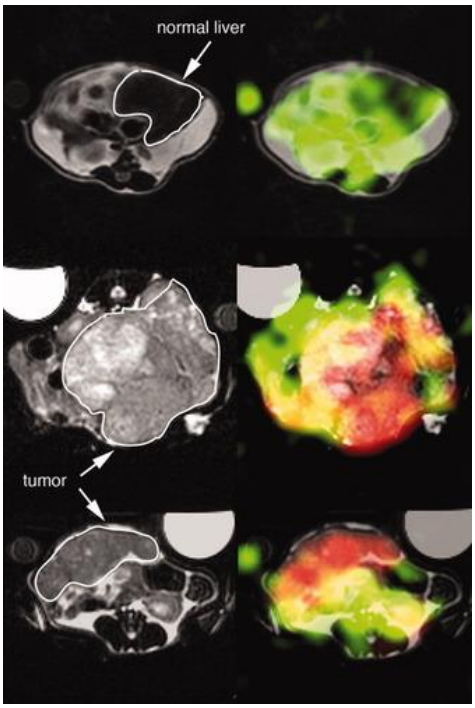

Figure 4.2 – Figure 6 from the journal *J. Magn. Reson. Imaging*, 2011, 33, 692-697 from reference 256. These are axial images of hyperpolarised ^{13}C-urea, as shown in green, and ^{13}C-lactate, as shown in red. These have been overlaid on a T_2 weighted ^{1}H image (grey) of a mouse liver combining the results from the experiments. An overlap of ^{13}C-urea and ^{13}C-lactate is given in yellow. (a) normal mouse (b) and (c) liver tumour mice. The same slice shown on the left and right. [256]

Fuetterer *et. al.* (2017) carried out a comparison of gadolinium and hyperpolarised ^{13}C-urea as myocardial first pass perfusion imaging agents *in vivo*.[192] They found that the image quality of the hyperpolarised ^{13}C-urea was comparable to that of those obtained with Gd as shown in Figure 4.3. In addition, hyperpolarised ^{13}C-urea permitted exploration of a velocity-selective excitation sequence. This allowed the improved detection of perfusion defects (Figure 4.4).

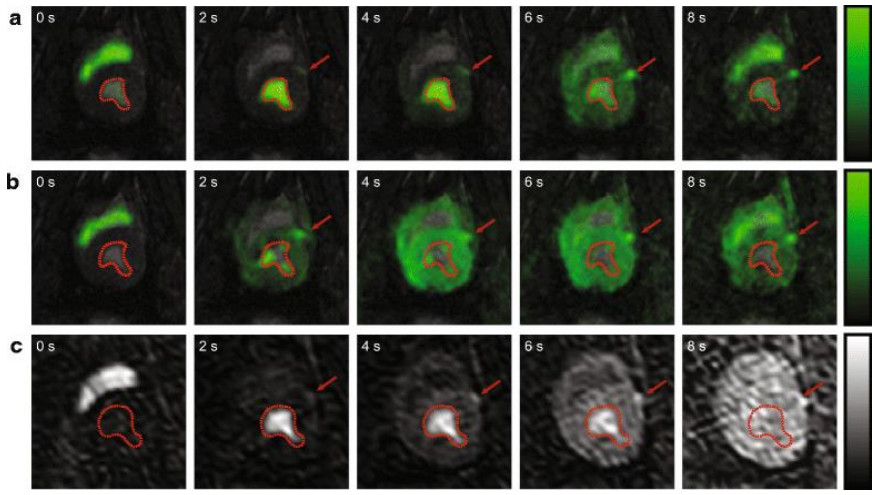

Figure 4.3 – Figure 6 from the journal *J. Cardio. Magn. Reson.*, 2017, 19, 46-57 from reference 192. The images show a series of enhanced cardiac perfusion covering the bolus passage in the left ventricle blood pool and myocardium. (a) uses conventional excitation of ^{13}C-urea (b) uses velocity-selective excitation of ^{13}C-urea and (c) is the ^{1}H gadolinium based contrast agent. The red arrow is the left anterior descending coronary artery. The red contour shows the left ventricle blood pool.[192]

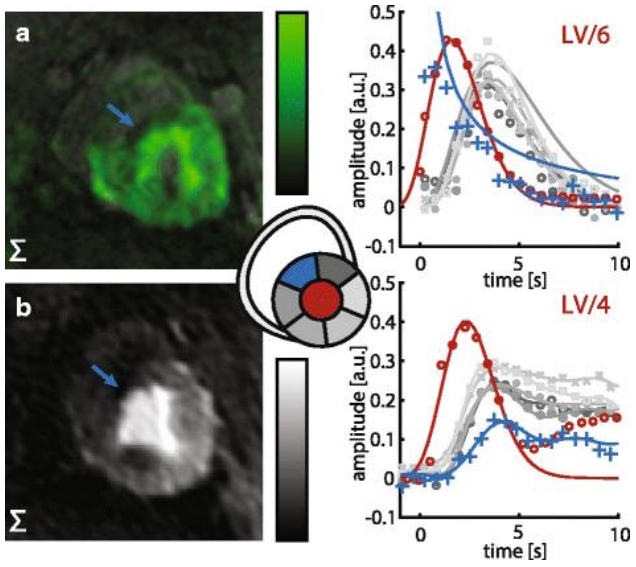

Figure 4.4 – Figure 8 from the journal *J. Cardio. Magn. Reson.*, 2017, 19, 46-57 from reference 192. (a) hyperpolarised ^{13}C-urea velocity-excitation and (b) ^{1}H gadolinium based contrast agent. These are both stress perfusion images with septal infarction induced by permanent ligation of the distal anterior descending coronary artery. On the left is the sum over three time frames at the myocardial bolus peak. On the right are the perfusion curves for six AHA (American Heart Association) segments. The blue arrow shows the perfusion defect.[192]

The research with hyperpolarised ^{13}C-urea demonstrates its potential as a perfusion agent. Alongside the development of hyperpolarised urea, DNP has also been successful in polarising

other small biomolecules of interest, such as water.[255, 262] The two main drawbacks to DNP hyperpolarisation is the time it takes to polarise a sample and the cost of running the polariser as a large amount of cryogens, including helium are required.

SABRE is a very quick way to polarise a substrate and is cheaper than DNP, using a cold head and catalyst to create the *para*-hydrogen (*p*-H_2) which can be stored for several months. However, neither water nor urea bind to the SABRE catalyst due to the lack of a lone pair of electrons, as with urea or very poorly bind to it, like water.

Oxygen from water could bind into the active SABRE catalyst, unfortunately, the SABRE pre-catalyst is not soluble in water.[117] Also, due to exchange when hyperpolarising water *via* SABRE there is an overlap between the water peak and methanol, both present at δ 1.5. If the solvent is then changed to dichloromethane (DCM), there is an issue with solubility between DCM and water. Urea is another molecule which does not polarise *via* SABRE as it doesn't bind to the catalyst, but it is of interest for *in vivo* imaging and has been identified as a possible perfusion agent.[256, 263]

4.1.2 Hyperpolarisation of Adenosine Triphosphate for ^{31}P imaging

^{31}P imaging has the potential to be used as a diagnostic probe for metabolism tracking, for example *via* adenosine triphosphate (ATP), which is used in the body to store and release energy.[43, 157] ATP synthase is vital in providing the energy for all metabolic pathways within the body, such as glycolysis and the formation of pyruvate, its role is therefore far reaching.[43, 158, 264] During aerobic respiration, two ATP molecules are generated when glucose is converted to pyruvate. Pyruvate is then stored as lactate or enters the TCA cycle (or Krebs cycle) to generate another thirty four molecules of ATP *via* oxidative phosphorylation.[43] Tracking hyperpolarised ATP or its precursors with ^{31}P MR could enable not only their observation but also which metabolic pathway, aerobic or anaerobic, is active within the population of cells.

During the 1980s and 1990s there was a huge series of developments in ^{31}P imaging by Bottomley *et. al.*,[265, 266] Ernst *et. al.*[267], Friedrich *et. al.*[268] and others, where the first brain and heart images were recorded. However, ^{31}P is not as sensitive as ^{1}H for detection due to its smaller gyromagnetic

Expanding the range of molecular scaffolds amenable to hyperpolarisation using SABRE ratio (10.9 x 107 s^{-1} T^{-1} compared to 26.8 x 107 s^{-1} T^{-1} for ^{1}H). As such greater signal averaging is required and this results in long acquisition times. With the development of fast imaging techniques, higher and stronger field strengths and better MRI systems, ^{31}P imaging has recently undergone a resurgence in popularity.[176, 269] However, at low fields there is still low spectral dispersion.[270]

Hyperpolarised phosphorous could potentially allow such images to be obtained, even at low fields. SABRE has been used to successfully hyperpolarise phosphorous within a partially deuterated pyridyl substituted phosphonate ester[146] and triphenylphosphine.[145] With the success of these hyperpolarised ^{31}P molecules, SABRE based images were also obtained.[145, 146] Monopotassium phosphate and phosphate creatine have also been hyperpolarised *via* d-DNP.[63]

Despite the success of ^{31}P and SABRE, phosphorous containing biological molecules are often sterically bulky. As previously mentioned, these cannot bind to the metal centre of the SABRE catalyst. Therefore, biologically relevant molecules have been difficult to polarise successfully with this method.[240] However, with the development of SABRE-Relay, these molecules can now be investigated.

As a proof of concept that SABRE-Relay can be optimised for ^{31}P containing molecules, section 4.4 investigates the use of monosodium dihydrogen phosphate (MSP). It presents as a simple molecular model and a motif that is contained in many biological molecules such as, adenosine triphosphate (ATP) as shown in Figure 4.5. Although MSP is not as sterically bulky as ATP, it is expected to only bind weakly to the SABRE catalyst and is the area of ATP which contains labile protons near to phosphorous. Our aim was to investigate this first and then if it was successful examine ATP.

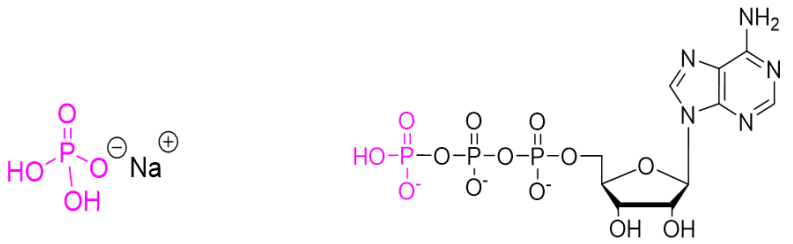

(a) Monosodium dihydrogen orthophosphate

(b) Adenosine triphosphate

Figure 4.5 – The structures of (a) monosodium dihydrogen phosphate (MSP) and (b) adenosine triphosphate (ATP).

4.1.3 Hyperpolarisation of oxalate

Oxalic acid is a metabolic product derived from the decomposition of monophosphoric acid[264] and can be used with orotic acid to produce uracil.[264] It is also found in many food and drink products (e.g. tea, rhubarb, spinach and beets).[271] Oxalic acid is known to bind to mineral ions in the body, for example calcium to form calcium oxalate, (deposits of which lead to kidney stones).[264] Sodium oxalate contains the same motif as that of oxalic acid, which is chemically symmetrical and may therefore possess near-magnetic equivalence. This symmetry is useful to extend the spin-lattice relaxation or longitudinal relaxation (T_1) times of a molecule, known as the long-lived singlet state (LLS). The LLS concept is used to store the polarisation of a substrate, Levitt *et.al.* (2013).[181] LLS states can be achieved with spin locking[272] or by use of a low magnetic field.[128] In essence both these methods convert triplet state magnetisation into the singlet form which is NMR 'silent'.[128, 134, 273-275] To subsequently record the magnetisation, the sample is often returned to high magnetic field and a suitable *r. f.* pulse applied. Enabling the symmetry to be broken and therefore providing an observable signal.[128, 134, 273, 274] In spin-locking, the sample remains in the NMR and an *r. f.* pulse train is used to initially maintain a pseudo singlet state, which can then be probed once it is removed.[272]

Levitt *et. al* (2013) have created a long lived state in oxalate by substituting some ^{16}O nuclei for the ^{18}O in conjunction with a ^{13}C pair.[182] Substitution in this way allows the ^{16}O ^{18}O mixture to deliver near magnetic equivalence within the molecule (a requirement for these LLS approaches).[181] This is often achieved by introducing chemical asymmetry but can be caused by

Expanding the range of molecular scaffolds amenable to hyperpolarisation using SABRE inequivalent long-range *J*-coupling to otherwise identical nuclei. The NMR spectrum resulting from this approach is reproduced in Figure 4.6. As the ^{13}C *J*-coupling of unlabelled ^{18}O-oxalate cannot be observed by ^{13}C NMR it was calculated from the $^{16}O_3{}^{18}O_1$ and $^{16}O_1{}^{18}O_3$-oxalate spectra as 86.9 ± 0.15 Hz.[181] In 2017 they reported creating a long-lived state between the hyperpolarised $^{13}C_2$ spins of a deuterated ester derivative of oxalate using d-DNP.[182]

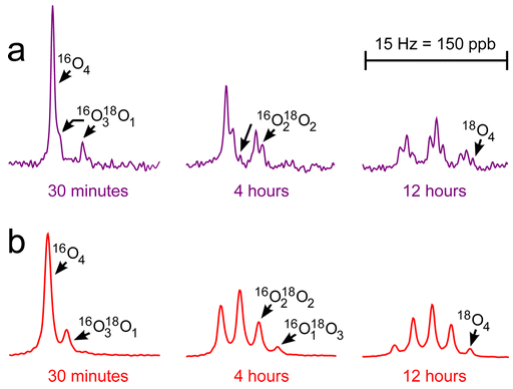

Figure 4.6 – from figure 1 of reference 181 from the journal *J. Am. Chem. Soc.*, 2013, 135, 42120-2123 showing the ^{13}C NMR spectra of oxalic acid recorded at 9.4 T following dissolution (a) natural-abundance and (b) 99% $^{13}C_2$-enriched [$^{16}O_4$]-oxalic acid in a 1:1 mixture (by concentration) of $D_2{}^{16}O$:$D_2{}^{18}O$ at 30 °C. The ^{18}O isotopologues formed during acid-catalysed exchange resolve as separate peaks, due to the ^{18}O isotope shift. The width of each displayed region is 0.15 ppm (15 Hz), centred at 162.02 ppm (referenced to tetramethylsilane). [181]

Due to oxalates structural similarities to pyruvic acid it was examined under SABRE and SABRE-Relay.

4.2 Principles and background of SABRE-Relay

The SABRE method requires the target substrate to be in reversible exchange with the active catalyst. Therefore, the substrates that are easily able to ligate to a metal catalyst, such as *N*-heterocycles, are commonly used. To hyperpolarise molecules which are not *N*-heterocycles, do not have a free lone pair of electrons or are too sterically bulky to bind to the catalyst (e.g. urea or ATP), another route to polarisation is required. One such route is SABRE-relay. This method is based upon SABRE whereby ammonia or a primary amine is polarised first.[168, 241] Upon dissociation from the catalyst the amine (NH) protons can undergo proton exchange with the labile protons of a substrate as shown in Figure 4.7. Polarisation can transfer from the

Expanding the range of molecular scaffolds amenable to hyperpolarisation using SABRE hyperpolarised proton into the substrate molecule such that a hyperpolarised response can be detected in its ^{15}N, ^{13}C, ^{19}F and ^{31}P nuclei.[242]

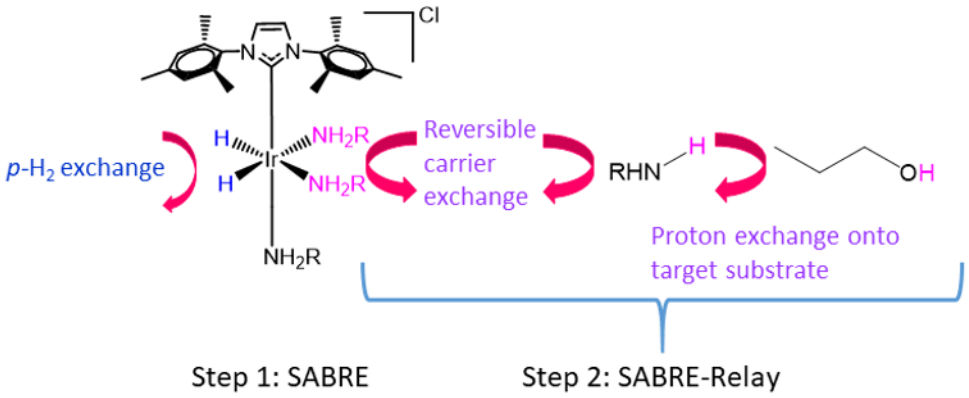

Figure 4.7 – Mechanism of SABRE-Relay. The hyperpolarised amine exchanges into solution. The labile proton on the amine then exchanges onto the substrate. Transfer of hyperpolarisation into the substrate then proceeds *via* the *J*-coupling network to the amine, the labile proton then exchanges with that of the one on the substrate.

The advancement of SABRE-Relay has opened up a plethora of new compounds that previously could not be polarised by the traditional SABRE method, including those used in the clinic by d-DNP. These include, for example, water, urea and pyruvate, which do not bind directly to the iridium centre in the catalyst but do have exchangeable protons and can therefore be polarised *via* SABRE-Relay.[204]

An in-depth study of the mechanism and optimisation of polarisation into alcohols *via* SABRE-Relay has been conducted.[242] In the SABRE-Relay mechanism it was shown that in determining substrate enhancement, the total signal enhancement of the carrier amine was important along with the exchange rate between the amine and substrate.[242] This exchange may be different for each substrate and therefore one of the key variables to test is which amine carrier provides the best signal enhancement for the substrate selected for investigation. It was noted that when polarising an alcohol, any water contamination within the system causes a reduction in signal gain,[242] therefore anhydrous conditions would be an advantage to ensure high signal enhancements. This is because water acts as a hyperpolarisation sink; it becomes hyperpolarised

Expanding the range of molecular scaffolds amenable to hyperpolarisation using SABRE rather than the target substrate. Unfortunately for some systems, water is required to dissolve the substrate. This remains a limitation of SABRE-Relay.

In an analogous fashion to SABRE, there are many variables that can be adjusted to improve the polarisation gain in the amine, for example, the polarisation transfer field (PTF). In SABRE the PTF has an effect on substrates between 0-80 G.[132] For SABRE-Relay the enhancement of the substrate is limited to that of the amine (60-80 G)[242] and the field dependence of the substrate is inherently tied to that of the carrier. Alongside this, changing the carbene backbone of the SABRE pre-catalyst and examining the rates of dissociation from the active complex of the amine and hydrogen would be advantageous to optimise the carrier enhancement.[242] The NHC not only effects the dissociation rate of the substrate but also the magnetic relaxation and the size of the J_{HH} coupling, all of which effect the SABRE transfer.[117, 118] Both the steric bulk and electronic donating or withdrawing groups attached to the NHC affect the properties previously mentioned.[118] This therefore demonstrates that for each substrate the optimal polarisation conditions must be investigated as there is not a 'one size fits all' approach.

4.2.1 Investigating the amine metal complex

The role the amine metal complex $[Ir(H)_2(IMes)(NH_2R)_3]Cl$, (Figure 4.8, where NH_2R is the amine) plays in the relay of polarisation to propanol has been investigated.[242]

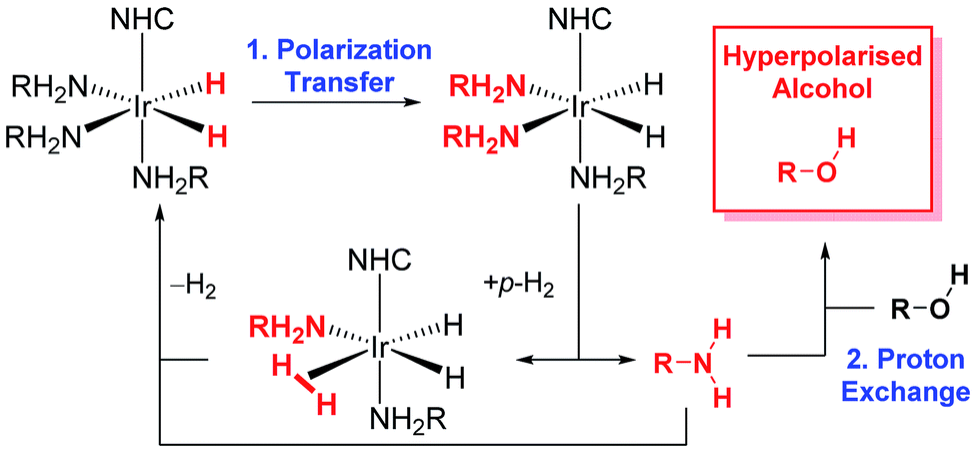

Figure 4.8 – Scheme 1 from *Chem. Sci.*, 2019, 10, 7709-7717 published by The Royal Society of Chemistry from reference 242 showing the catalytic cycle for the hyperpolarisation of alcohols. The metal-amine complex is the one which allows polarisation to transfer from the *p*-H_2 to the amine. The hyperpolarised proton on the amine exchanges with the one on the alcohol.[242]

The SABRE pre-catalyst reacts first to form a metal amine complex, which is used to transfer polarisation from *p*-H_2 derived hydrides into the amine. Upon amine dissociation, a hyperpolarised proton is then transferred to the substrate *via* the labile proton.[242] The most common amines that have been investigated are benzylamine, phenethylamine (PEA) and ammonia (NH_3). The deuterated forms of both benzylamine and PEA have also been screened.[168, 169, 241, 242] Generally, NH_3 gives the best polarisation transfer, then deuterated benzylamine, then deuterated PEA. Though, this is not always the case and all amines should be screened for each substrate being investigated.[168, 169, 241, 242] There are also challenges with using NH_3. Firstly, it is added as a gas and therefore gaining the desired concentration can be very difficult, as a consequence reproducibility between samples can be challenging. Due to this, for optimisation of SABRE-Relay, most substrates use a liquid amine.[169, 242]

The rates of exchange between the *p*-H_2 and the amine need to be optimised to help provide the best signal enhancement on the substrate of interest and therefore need thorough investigation to ascertain which amine would provide the best enhancement.[242]

4.3 Exploring hyperpolarisation of Urea with SABRE-Relay

Section 4.1.1 described how using hyperpolarised ^{13}C-urea would be advantageous to explore as a perfusion agent.[263] This has already been successfully demonstrated in various organs, in various animals using d-DNP.[175, 192, 237, 256, 259] However, trying to hyperpolarise this molecule *via* SABRE was not feasible, urea does not bind to the SABRE catalyst. Now, with the advent of SABRE-Relay there is the possibility that this molecule can be hyperpolarised a lot quicker and cheaper than current methods. The following section examines polarisation of urea, investigating both ^{13}C and ^{15}N signal enhancements with SABRE-Relay.

4.3.1 Polarisation of ^{13}C and ^{15}N in urea *via* SABRE-Relay

Urea does not dissolve in dichloromethane-d_2 (DCM-d_2) and therefore needs a small volume of water to aid dissolving. Previous work has shown that using 100% D_2O interferes with the polarisation transfer between the amine and the substrate but using 100% H_2O can be very

Expanding the range of molecular scaffolds amenable to hyperpolarisation using SABRE detrimental.[168, 169, 241, 242] In this work it was demonstrated that using a 50:50 H_2O:D_2O mixture provided better signal enhancements.[168, 169, 241, 242]

^{13}C,^{15}N-Urea (20 mM) was investigated with two amine carriers, benzylamine–d_7 (25 mM) and NH_3 (35 mM) which were dissolved in a 50:50 H_2O:D_2O mixture (10 µL) with the pre-catalyst [IrCl(COD)(IMes)] (5 mM) in DCM-d_2 (0.6 mL). NH_3 gave the best signal enhancement for both ^{13}C and ^{15}N on the basis of $^{13}C_2$,^{15}N-urea as shown in Figure 4.9 and Figure 4.10 respectively. For ^{13}C, signal enhancements of 5117 ± 536-fold and 832 ± 74-fold were observed with NH_3 and benzylamine-d_7 respectively. Given the challenge in obtaining a control ^{15}N measurement, I report that with NH_3, a ^{15}N SNR of 16 could be readily achieved in a single scan whereas for benzylamine-d_7 this was 14.

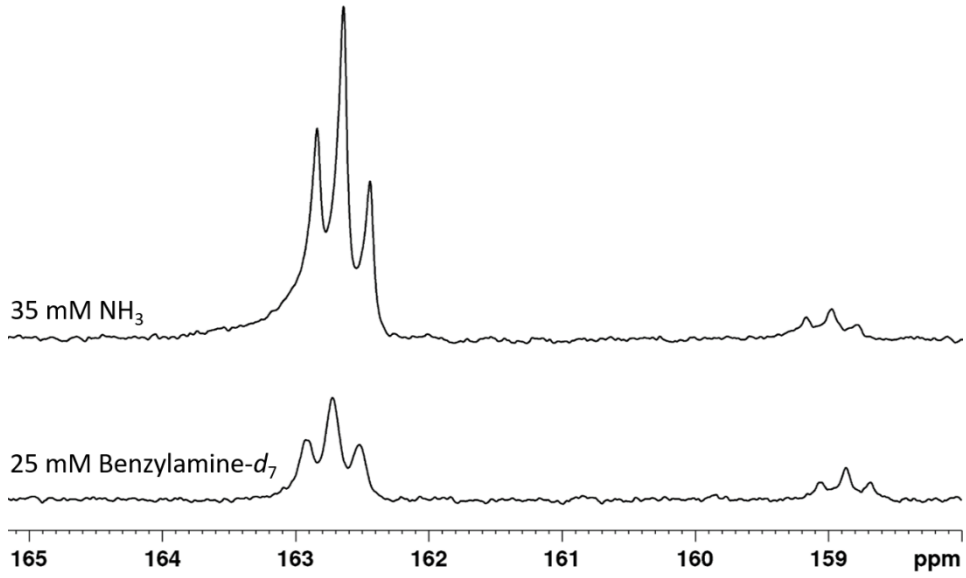

Figure 4.9 – ^{13}C NMR hyperpolarised spectra of ^{13}C,$^{15}N_2$-urea (20 mM) dissolved in 50:50 H_2O:D_2O (10 µL) using [IrCl(COD)(IMes)] (5 mM) as the SABRE pre-catalyst in DCM-d_2 (0.6 mL), 25 mM of benzylamine-d_7 gave a 832 ± 74-fold enhancement, 35 mM NH_3 gave a 5117 ± 536-fold enhancement.

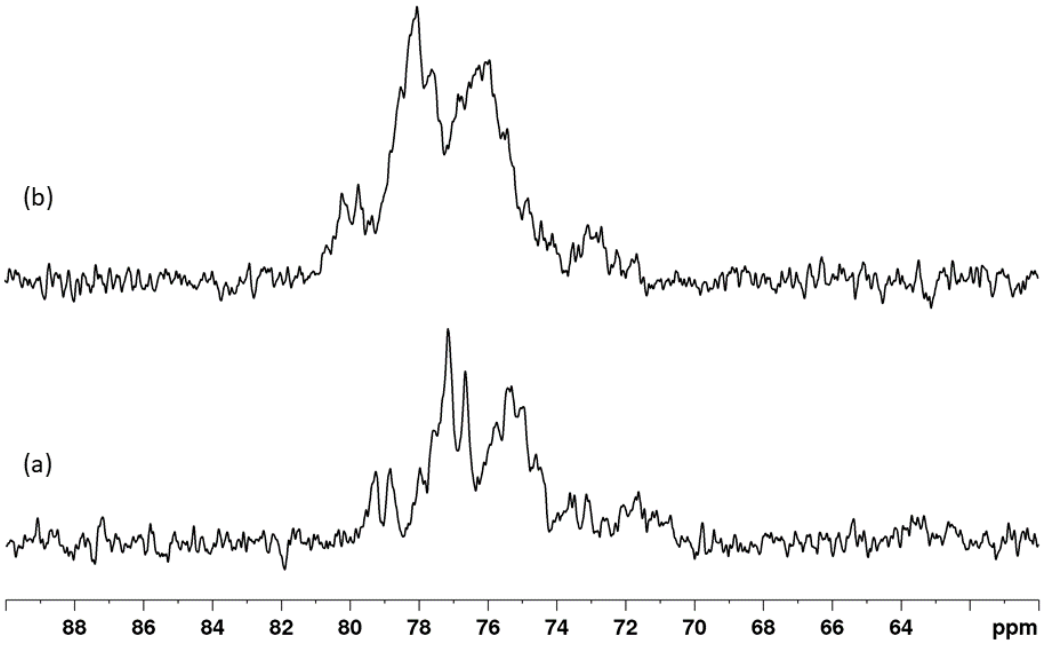

Figure 4.10 – ^{15}N NMR hyperpolarised spectra of ^{13}C,$^{15}N_2$-urea (20 mM) dissolved in 50:50 H_2O:D_2O (10 µL) using [IrCl(COD)(IMes)] (5 mM) as the SABRE pre-catalyst in DCM-d_2 (0.6 mL), (a) is when 25 mM of benzylamine-d_7 has been used as the amine carrier and produced an SNR of 14 (b) is where 35 mM NH_3 has been used as the amine carrier and produced an SNR of 16.

4.3.2 ^{13}C-Urea imaging

As a proof of concept, a sample of ^{13}C-urea (100 mM) with [IrCl(COD)(IMes)] (5 mM) and benzylamine-d_7 (25 mM) in DCM-d_2 (3 mL) was exposed to 4 bar *p*-H_2. Polarisation was transferred at 60 G and the sample in an NMR tube (phantom) was imaged with a Magnetom Prisma 3 T MRI scanner (Siemens Healthcare, Erlangen, Germany). A ^{1}H/^{13}C flex-surface coil was used for the *r. f.* transmission/reception. The Chemical Shift Imaging (CSI) parameters used were matrix size 8*8, 512 spectral points, across a ppm range of 300 ppm, FOV = 20*20*25 cm with TE = 2.3 ms, TR = 200 ms with a flip angle = 5 deg. Single scan thermal and hyperpolarised spectra of ^{13}C-urea are shown in Figure 4.11a. The associated CSI of the phantom is shown in Figure 4.11b. Results demonstrate that a ^{13}C SABRE-Relay hyperpolarised image can be obtained with a 3 T clinical MRI system.

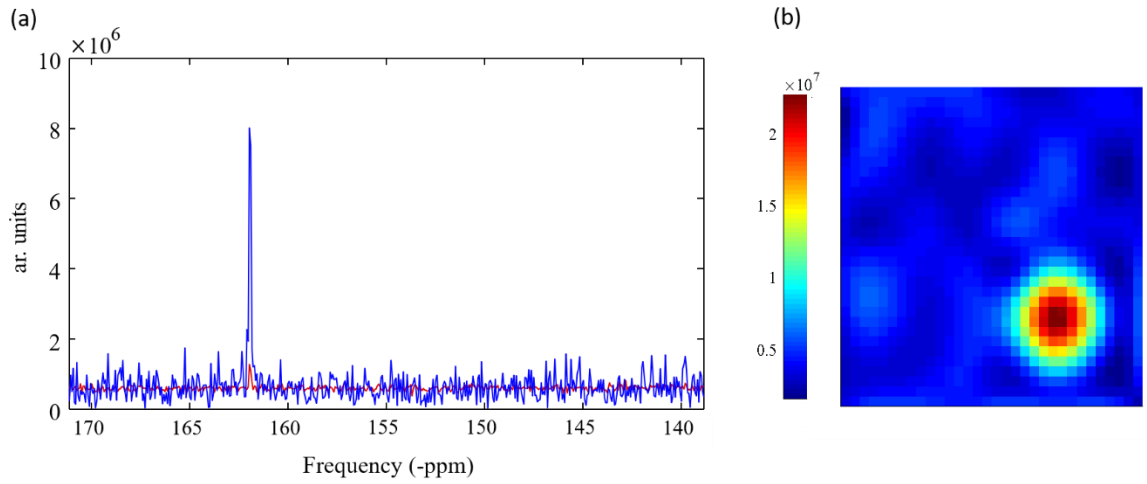

Figure 4.11 – ^{13}C phantom MRI of the 100 mM ^{13}C-urea with 5 mM [IrCl(COD)(IMes)] and 25 mM benzylamine-d_7 in methanol-d_4 exposed to 4 bar *p*-H_2. CSI image taken using a Magnetom Prisma 3 T MRI scanner (Siemens Healthcare, Erlangen, Germany). Using a flex-surface coil for the *r. f.* transmission/reception. The imaging parameters used were a matrix size 8*8, 512 spectral points, FOV = 20*20*25 cm with TE = 2.3 ms, TR = 200 ms with a flip angle = 5 deg. (a) shows the ^{13}C thermal and hyperpolarised spectra acquired. (b) shows a 1 scan ^{13}C hyperpolarised image.

Figure 4.12 demonstrates an increase in the signal to noise ratio (SNR) between the thermal and the hyperpolarised permitting imaging. With further development, including solvent biocompatibility and removal of catalyst, this could be viable for clinical based MR perfusion imaging.

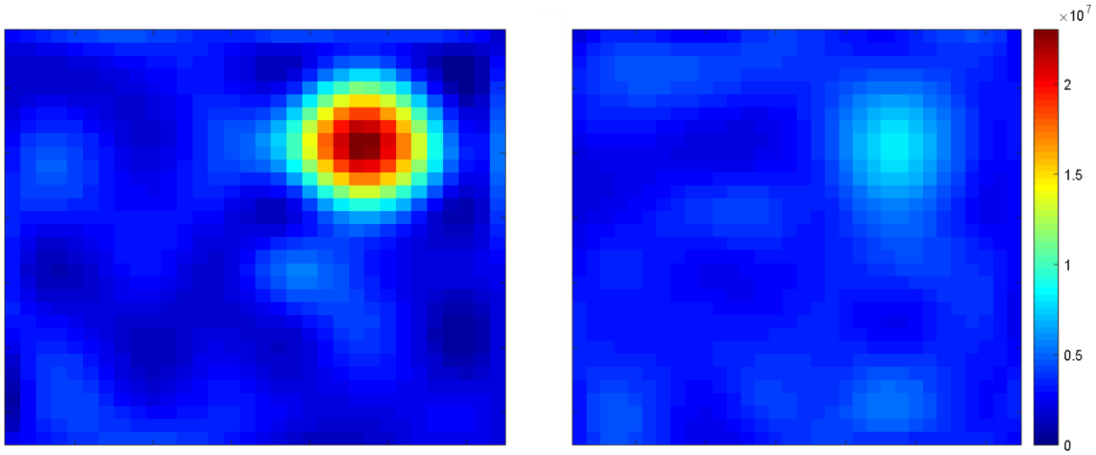

Figure 4.12 – ^{13}C phantom MRI of the 100 mM ^{13}C-urea with 5 mM [IrCl(COD)(IMes)] and 25 mM benzylamine-d_7 in methanol-d_4 exposed to 4 bar *p*-H_2. CSI image taken using a Magnetom Prisma 3 T MRI scanner (Siemens Healthcare, Erlangen, Germany). Using a flex-surface coil for the *r. f.* transmission/reception. The imaging parameters used were a matrix size 8*8, 512 spectral points, FOV = 20*20*25 cm with TE = 2.3 ms, TR = 200 ms with a flip angle = 5 deg. The image on the left shows a 1 scan ^{13}C hyperpolarised image of ^{13}C-urea. The image on the right is a 1 scan thermal recorded under Boltzmann conditions of the sample.

Unfortunately, there wasn't access to a ^{15}N coil for the clinical MRI scanner and therefore no ^{15}N images could be recorded for $^{13}C_2$,^{15}N-urea.

4.4 Exploring SABRE-Relay with monosodium phosphate, ^{31}P and ^{1}H

Phosphorous pH chemical shift changes can be used to analyse phosphorylation changes in peptide structures[276] and monitor phosphorous containing metabolites.[277] These changes have been detected with hyperpolarised ^{31}P *via* DNP for pH sensing.[63] More recently, the SABRE-Relay method has been shown to be amenable to the hyperpolarisation of phosphate and therefore it offers a cost effective alternative to DNP.[168] However, the reported signal enhancements for ^{31}P in monosodium dihydrogen orthophosphate (MSP) were just 226-fold[168] and thus need to increase in order to realise potential applications. Here I optimise the polarisation of MSP as a simple motif of ATP, providing a proof of concept route for the polarisation of ^{31}P that could potentially be examined with ATP.

A sample was prepared that contained monosodium dihydrogen phosphate (MSP, 50 mM) in H_2O (10 μL), phenethylamine (PEA, 13 mM) and [IrCl(COD)(IMes)] (5 mM), in DCM-d_2 (0.6 mL)

(referred to as sample **1**). The addition of H_2O was made to dissolve the substrate as MSP does not dissolve in DCM-d_2. It was noted that the addition of H_2O would negatively impact the overall enhancement achieved, however, no suitable aprotic alternatives could be found. This sample was subsequently exposed to 4 bar *p*-H_2 in a 65 G polarisation transfer field prior to a ^{31}P NMR spectrum being recorded at 9.4 T. The ^{31}P response of MSP showed a signal enhancement of 66 ± 3-fold (Figure 4.13).

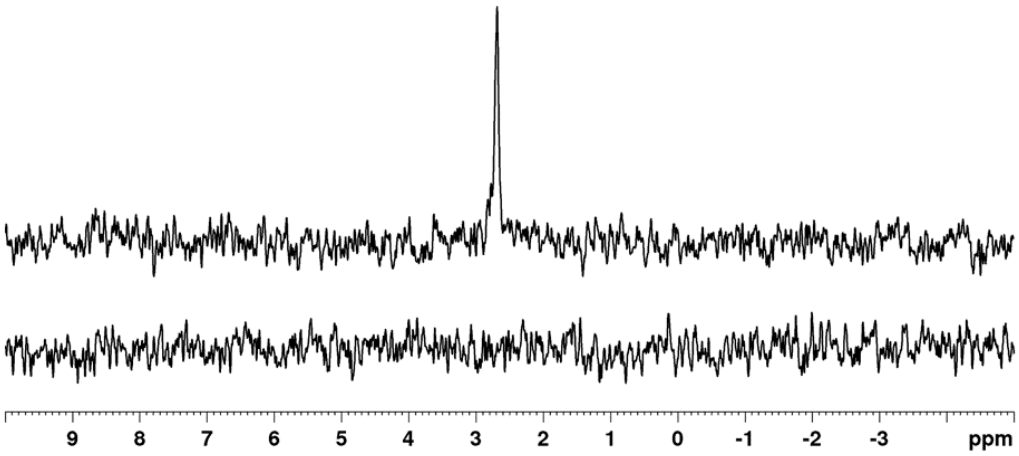

Figure 4.13 – ^{31}P NMR of MSP (50 mM) dissolved in H_2O (10 µL) with [IrCl(COD)(IMes)] (5 mM) and PEA (13 mM) in DCM-d_2 (0.6 mL) with 4 bar of *p*-H_2 at 65 G. Top is a 1 scan ^{31}P SABRE-Relay spectrum after polarisation transfer at 65 G, producing a signal enhancement of 66 ± 3-fold. Bottom is a 1 scan thermally equilibrated spectrum which was left in the NMR for 2 minutes prior to acquisition.

It is known that the concentration of the substrate effects polarisation levels.[111, 116] Therefore the concentration of MSP was varied from 20 mM to 60 mM whilst maintaining the same concentrations for the other reagents as described in sample **1**. However, in order to dissolve the higher concentrations of MSP, an increased volume of H_2O was needed. Therefore, a total 40 µL of H_2O was added to each sample. Figure 4.14 shows the effect of changing MSP concentration on the SNR of ^{31}P. As shown by this figure, a linear dependence of signal enhancement on the concentration of MSP is observed.

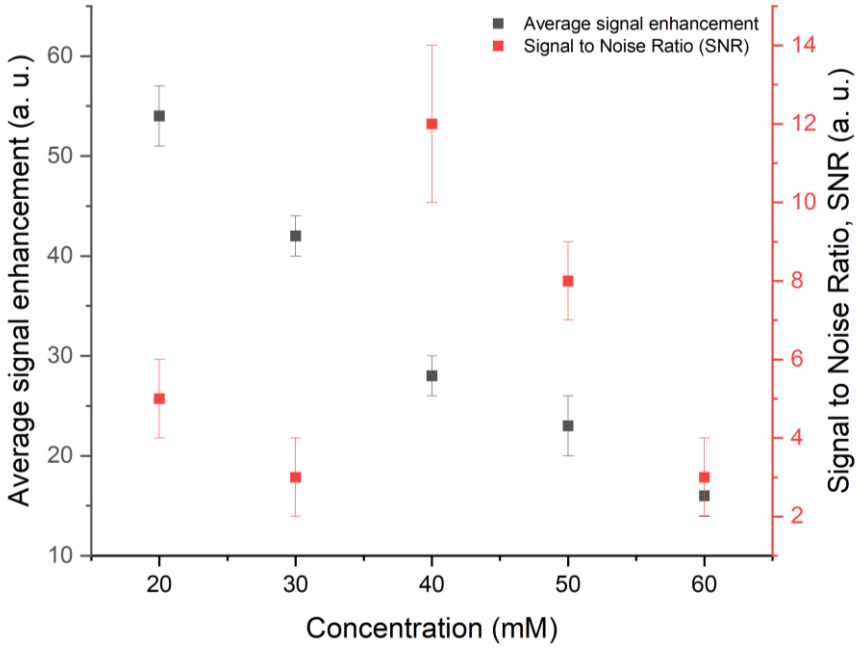

Figure 4.14 – Average signal enhancement and SNR of ^{31}P for varying concentrations of MSP dissolved in 40 µL H_2O with [IrCl(COD)(IMes)] (5 mM), PEA (13 mM) in DCM-d_2 (0.6 mL).

At 20 mM of MSP the average ^{31}P NMR signal enhancement 54 ± 3-fold was observed in the spectrum after SABRE-Relay transfer. In contrast, just a 16 ± 2-fold signal enhancement was seen at 60 mM. This is consistent with the effects of spin dilution, which acts to reduce the total polarisation level when there are an increased number of spins.[129]

However, the SNR from the NMR spectra (right axis of Figure 4.14) does not show the same linear dependence. Instead, a maximum signal is observed at 40 mM concentration of MSP. Although this was repeated several times, the same result was observed. This could be due to the balance between total available nuclei for detection and signal enhancement. Therefore, 40 mM MSP concentration was used for the following further optimisation experiments because there is more available signal for detection, which is particularly needed for 1 shot hyperpolarised MRI experiments.

Next, the effect of PEA on the signal enhancement was also investigated. A series of samples containing [IrCl(COD)(IMes)] (5 mM), MSP (40 mM) and varying concentrations of PEA (15 – 55 mM) were prepared. After polarisation transfer under the standard SABRE-Relay conditions a series of ^{31}P NMR spectra were collected. The resulting signal enhancements are displayed in

Figure 4.15. At 15 mM of PEA, the signal enhancement is 15.1 ± 1, whereas at 55 mM no ^{31}P signal enhancement was observed.

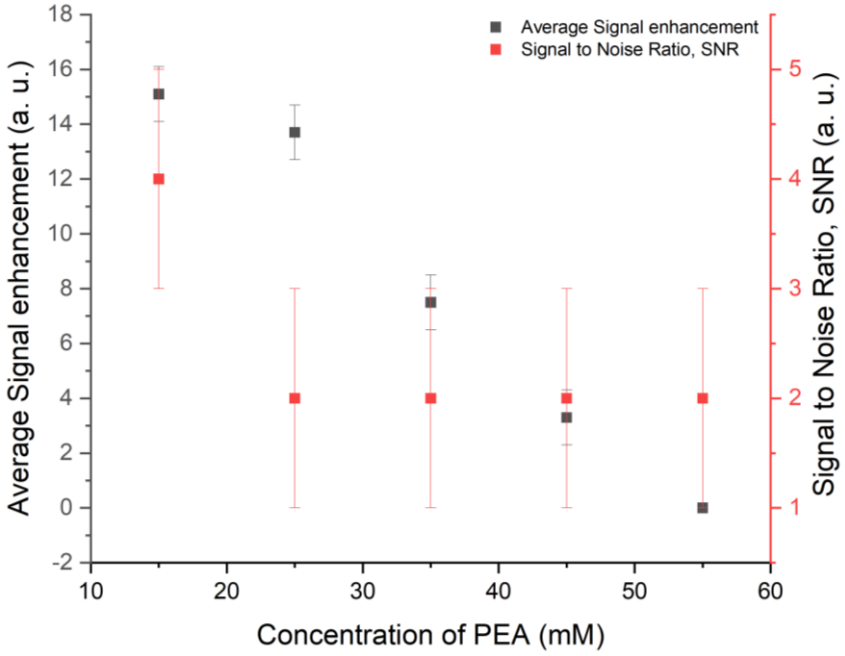

Figure 4.15 – Hyperpolarised ^{31}P NMR spectra of MSP (40 mM) dissolved in H_2O (40 µL) with [IrCl(COD)(IMes)] (5 mM) in DCM-d_2 (0.6 mL) and varying concentrations of the carrier amine, PEA. All samples were exposed to 4 bar of *p*-H_2, polarisation transfer was carried out at 60 G. All spectra were taken with a 9.4 T Bruker NMR.

As demonstrated in literature[168, 169, 241, 242] and in section 4.3.1, other carrier amines have previously been shown to offer better SABRE-Relay transfer than PEA. Therefore, PEA was changed for NH_3 and examined under these optimal conditions, MSP (40 mM), amine carrier (15 mM), water (40 µL). The resulting ^{31}P NMR spectrum is shown in Figure 4.16 with comparison to the analogous spectrum with PEA.

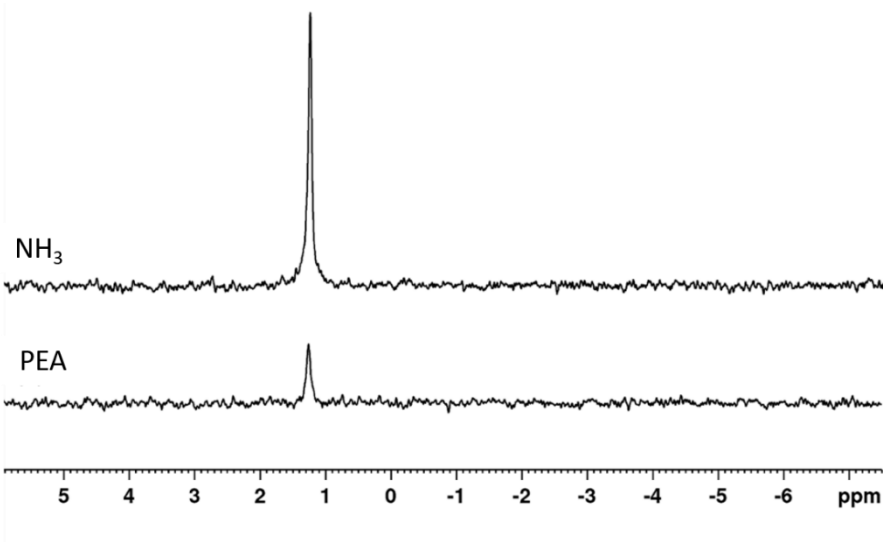

Figure 4.16 – ^{31}P spectra of MSP (40 mM) dissolved in 40 µL H_2O with [IrCl(COD)(IMes)] (5 mM) in DCM-d_2 (0.6 mL), exposed to 4 bar *p*-H_2, using different amines. Polarisation transfer occurred at 60 G. Bottom is with PEA (15 mM), producing a signal enhancement of 33 ± 2 (SNR = 14 ± 2). Top is with NH_3 (15 mM), producing a signal enhancement of 136 ± 2 (SNR = 49 ± 8).

It is clear that NH_3 performs much better than PEA. This data fits in with previous literature descriptions for other SABRE-Relay substrates and nuclei.[168, 169, 241, 242] It is hypothesised that the ^{1}H exchange rate between PEA and MSP is too rapid for efficient polarisation transfer through the H-O-P coupling. This is mitigated by using NH_3 which has a lower pK_a than PEA; 9.21 compared to 9.83 respectively.[278] However, it is also entirely plausible that rapid relaxation of the HO or ^{31}P signals for MSP is the leading mechanism for loss of polarisation.

It was postulated that using deuterium would slow this relaxation rate and hence, experiments were conducted with 100% D_2O, 50:50 of H_2O:D_2O or 100% H_2O as the co-solvent. Each sample also contained [IrCl(COD)(IMes)] (5 mM), MSP (40 mM), PEA (15 mM) in DCM-d_2 (0.6 mL). Although NH_3 produced a larger SNR than PEA, PEA was used for this investigation as it is easier to prepare accurate solutions. Figure 4.17 shows that a 50:50 mixture of H_2O and D_2O resulted in the largest, average ^{31}P signal enhancement of 94 ± 2-fold; over double that when using either solvent at 100% (28 ± 2-fold for H_2O and 45 ± 7-fold for D_2O). A more in-depth investigation is

Expanding the range of molecular scaffolds amenable to hyperpolarisation using SABRE

required into the ratio of H_2O and D_2O and the volume of that mixture. Additionally, the T_1 relaxation times for each of the nuclei should be determined.

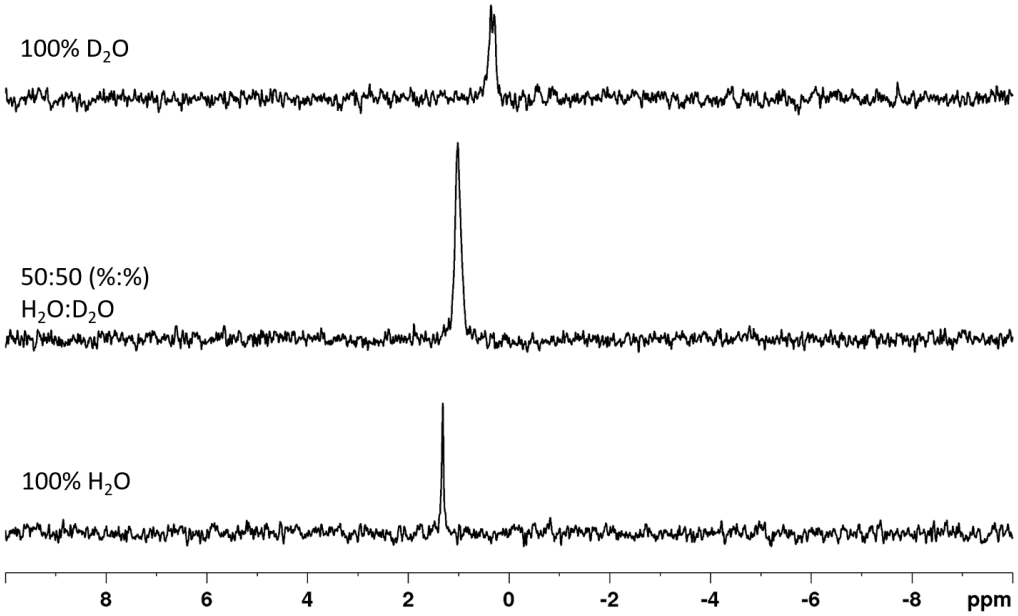

Figure 4.17 – Hyperpolarised ^{31}P NMR spectrum with MSP (40 mM) dissolved in either 100% H_2O (bottom spectrum, signal enhancement = 28 ± 2-fold), 50:50 H_2O:D_2O (middle spectrum, signal enhancement = 94 ± 2-fold) or 100 % D_2O (top spectrum, signal enhancement = 45 ± 7-fold) with [IrCl(COD)(IMes)] (5 mM) and PEA (15 mM) in DCM-d_2 (0.6 mL). All experiments were conducted in the presence of 4 bar of *p*-H_2 at 65 G and observed with a 9.4 T Bruker NMR.

4.4.1 Adenosine triphosphate

After establishing that MSP could be polarised and detected, an investigation was carried out with a more complex substrate with larger steric bulk. Due to the nitrogen on the adenosine triphosphate (ATP) molecule, hyperpolarisation *via* direct SABRE could be investigated with this substrate. However due to the steric bulk of the molecule it is unlikely to bind sufficiently, or at all, to the iridium centre of the SABRE active catalyst. Therefore, a sample containing [IrCl(COD)(IMes)] (5 mM), ATP (20 mM) in H_2O (30 µL) and PEA (15 mM) in DCM-d_2 (0.6 mL) was prepared. 30 µL of H_2O was required to completely dissolve the ATP. SABRE-Relay experiments were conducted on carbon, proton and phosphorus. To guarantee the same concentration of amine, PEA was again used instead of NH_3, as previously described in Section 4.2.1. With this system, only hyperpolarisation of the phosphorus nuclei was observed (see Figure 4.18). Examination of the ^{31}P NMR spectrum shows enhanced signals for the γ, α and β forms of

Expanding the range of molecular scaffolds amenable to hyperpolarisation using SABRE

ATP. These are reported to have chemical shifts of δ −5, −10 and −18.5 respectively in a cell culture using a bioreactor circuit.[279] Here they are observed at δ −10, −11.5 and −22, producing substantial ^{31}P signal enhancements.

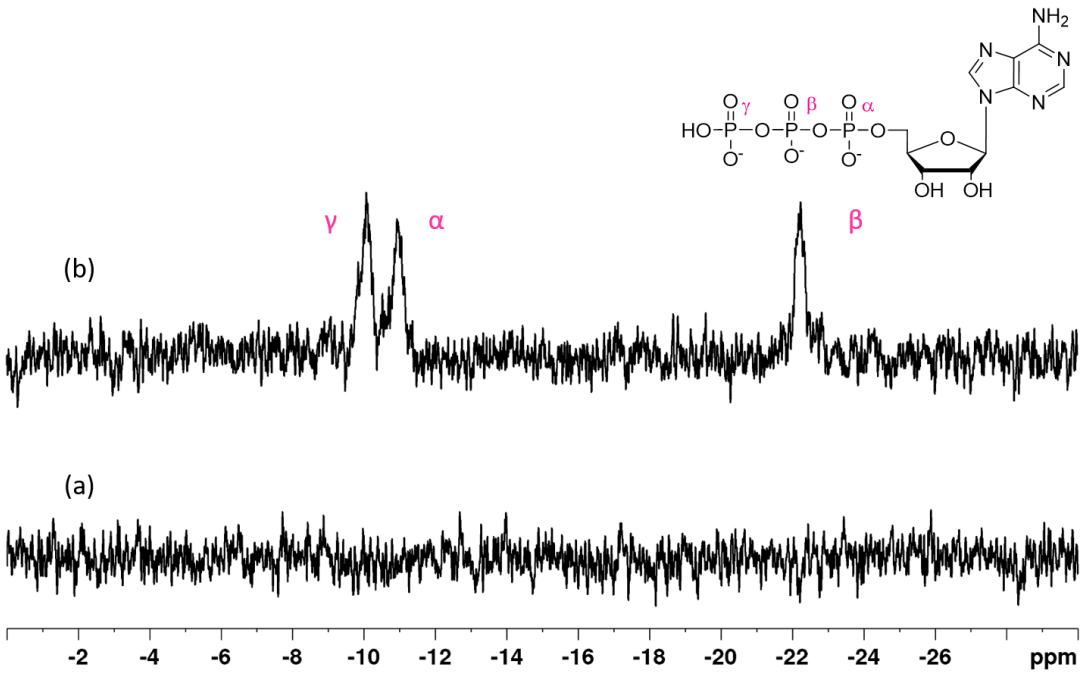

Figure 4.18 – ^{31}P NMR of ATP (20 mM) dissolved in H_2O (30 µL) with PEA (15 mM) and [IrCl(COD)(IMes)] (5 mM) in DCM-d_2 (0.6 mL). Top is a SABRE-Relay spectrum after polarisation transfer at 65 G. Bottom is a 1 scan thermally equilibrated spectrum which was left in the NMR for 2 minutes prior to acquisition.

As the volume of water can affect signal enhancement, another sample was prepared using ATP (20 mM) PEA (13 mM) dissolved in H_2O (10 µL) with [IrCl(COD)(IMes)] (5 mM) in DCM-d_2 (0.6 mL). Examining the ^{31}P signal on this sample a smaller enhanced signal (SNR = 3) was produced for the γ, α and β forms of ATP. Figure 4.19 shows a comparison of ^{31}P enhancement for both this sample and that shown in Figure 4.18. Surprisingly, using a greater volume of water produces a greater SNR due to higher solubility, which is not what has been described for other substrates.[169, 242] Further improvements in this signal could possibly be achieved by utilising a D_2O/H_2O mix as seen for MSP. Additionally, the use of NH_3 would also be expected to provide higher signal gains. Disappointingly, the ^{31}P signal gains for MSP and ATP are both still lower than the ^{31}P signal gains achieved with DNP (>11,000 in potassium dihydrogen phosphate).[63]

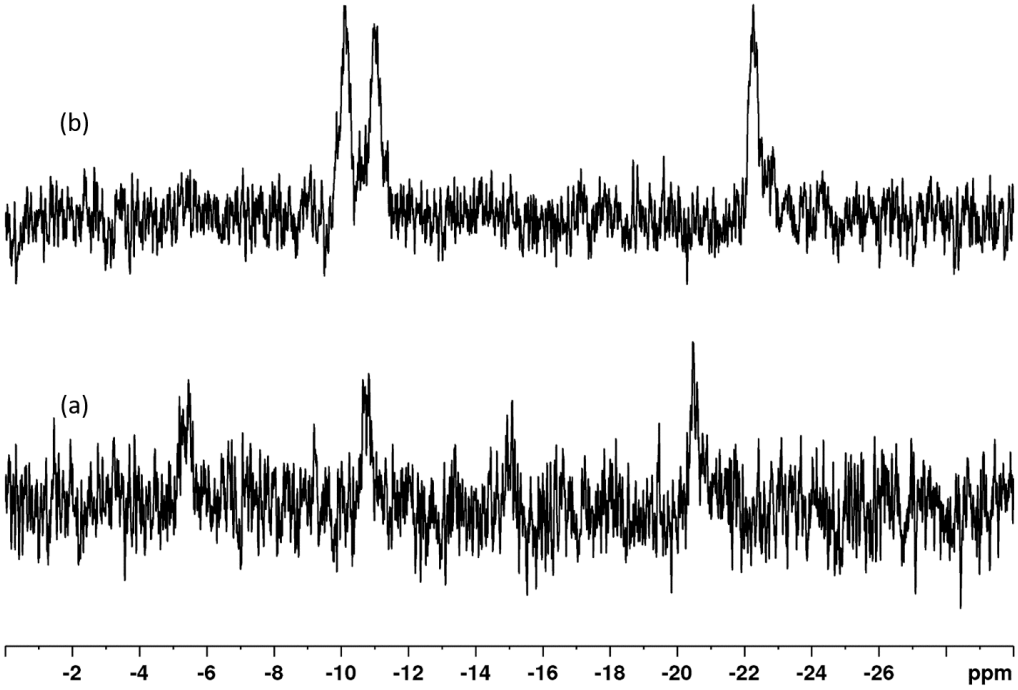

Figure 4.19 – SABRE-Relay hyperpolarised ^{31}P spectra of ATP (20 mM), [IrCl(COD)(IMes)] (5 mM), PEA (15 mM) in DCM-d_2, polarisation transfer occurred at 60 G. Top is using 30 µL H_2O to dissolve ATP, bottom is using 10 µL H_2O to dissolve ATP.

4.5 Exploring SABRE-Relay with Sodium oxalate, ^{13}C polarisation

Sodium oxalate was also examined under SABRE-Relay conditions. Although sodium oxalate does not have labile protons, it was hypothesised that the sodium ion would be replaced by the hyperpolarised amine proton within the proton exchange process in SABRE-Relay, creating an enhanced ^{13}C NMR oxalate signal.

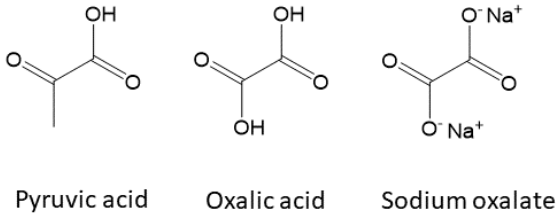

Figure 4.20 – The chemical structures of pyruvic acid, oxalic acid and sodium oxalate.

4.5.1 Polarisation of ^{1}H and ^{13}C nuclei in sodium oxalate

A sample was prepared with sodium oxalate (20 mM) dissolved in H_2O (30 µL) with [IrCl(COD)(IMes)] (5mM) and PEA (15 mM) in DCM-d_2 (0.6 mL) and was exposed to 4 bar *p*-

H_2. A SABRE-Relay experiment was conducted at 60 G. No substrate hyperpolarisation was observed.

To remove the use of water and to aid solubility of the oxalate substrate, dimethylformamide (DMF) was investigated as a solvent. DMF was added in 10 µL increments to 20 mM sodium oxalate until a colourless solution was formed, 100 µL of DMF was required to achieve this. In order for SABRE-Relay to be tested the DMF solution was then added to 0.5 mL of DCM-d_2 containing [IrCl(COD)(IMes)] (5 mM) with PEA (15 mM). SABRE-Relay was then undertaken at 60 G[106] (with 4 bar of *p*-H_2) but no ^{13}C NMR signal was observed for sodium oxalate.

To track where the polarisation was being lost/transferred a more in-depth investigation of the PEA intermediate was completed. When PEA is polarised *via* SABRE, there is a ^{1}H enhancement for the ^{1}H on the NH_2, the CH_2, the NCH_2 and for the phenyl.[241] The PEA ^{13}C SABRE response can only be observed using an INEPT NMR sequence and only for the resonances at approximately δ 139.9, 128.8 and 40.2 ppm.[241] *Via* SABRE-Relay however, an INEPT sequence was not required and all six ^{13}C resonances were detected. In the ^{1}H hyperpolarised spectrum, only the ^{1}Hs within the PEA were observed.

The efficiency of SABRE-Relay is known to be highly dependent upon the solvent/intermediate formulation.[169, 241, 242] Alongside this, finding a solvent in which to solubilise sodium oxalate that wouldn't hinder SABRE-Relay needed to be found. To find a formulation which allows a ^{13}C response in sodium oxalate to be detected, a range of samples were prepared. These all contained [IrCl(COD)(IMes)] (5 mM), sodium oxalate (20 mM) and an amine (either PEA, NH_3 or benzylamine). Different solvents, with varying volumes were used to dissolve the sodium oxalate. They were either dimethylformamide (DMF) or H_2O. For one sample dimethylsulfoxide (DMSO) was used. Sodium oxalate dissolves in DMSO but too much of this solvent and it will bind preferentially into the catalyst. Table 4.1 gives the details of the sample formulations used.

Unfortunately, no ^{13}C hyperpolarised signals were observed for sodium oxalate. Spectral peaks were observed for PEA and are shown on the right hand side of Table 4.1.

Table 4.1 – Table of sample formulations on the left. If there is a tick, then this and the volume given were used to make that sample. On the right hand side, the ^{13}C hyperpolarised signals of the solvents present, which were observed in the corresponding NMR spectra that were taken for each sample. If there is a blank, this means that the molecule was not added and therefore no signal should be seen. At G the SABRE catalyst was activated with the PEA before the substrate was added. ^{13}C chemical shifts: *DMF = 162.60, 36.43, 31.31 ppm, #PEA = 139.93, 128.8, 128.4, 126.09, 43.60, 40.19 ppm, ^$Na_2C_2O_4$ = 162.31 ppm. * = benzylamine was used, ** = NH_3 was used, # = added after sample was activated, ⋆ = 1 µL was added, ♦ = 30 µL used, ~ = 50:50 H_2O:D_2O.

	Formulation						^{13}C Hyperpolarised signal observed			
	H_2O (10 µL)	*DMF (100 µL)	DMF-d_7 (100 µL)	#PEA (45 mM)	^$Na_2C_2O_4$ (20 mM)	DMSO (20 mM)	$Na_2C_2O_4$	PEA	DMF	DMF-d_7
A	×	×	×	✓#⋆	✓	×	×	×	×	×
B	✓♦	×	×	✓⋆	✓	×	×	×	×	×
C	×#~	✓	×	✓	✓	×	×	✓	×	×
D	×	×	✓	✓	✓	×	×	✓	×	×
E	×	×	✓	✓*	✓	×	×	✓	×	×
F	×	×	✓	✓	✓	×	×	✓	×	×
G	×	×	×	✓	✓	×	×	✓	×	×
H	×	×	✓	×	✓	×	×	×	×	×
I	✓	×	×	✓⋆	✓	✓	×	×	×	×
J	✓~	×	×	✓**	✓	×	×	×	×	×

For formulations **C**-**G** the ^{13}C spectra exhibit a peak in the hydride region at δ −24.1 ppm (Figure 4.21 examples the finding for formaulation **C** – DMF (100 µL) and PEA (45 mM)). This is direct

Expanding the range of molecular scaffolds amenable to hyperpolarisation using SABRE

evidence that the amine (PEA) is bound to the Ir catalyst.[168, 242] From here polarisation should transfer from *p*-H_2 to the amine and then relay to the substrate.

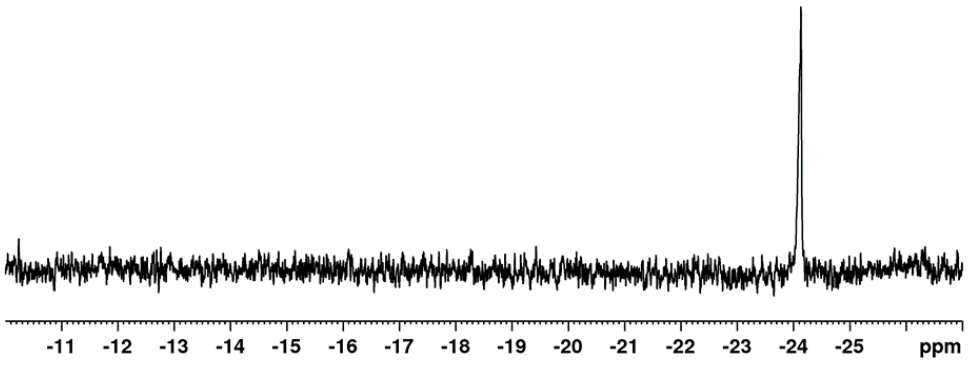

Figure 4.21 – Thermally equilibrated 1 scan, ^{1}H NMR spectrum which was left in the NMR for two minutes prior to acquisition, of the hydride region of sample C which contained [IrCl(COD)(IMes)] (5 mM), sodium oxalate (20 mM) dissolved in DMF (100 µL), PEA (45 mM), with an addition of 10 µL of H_2O in DCM-d_2 (0.5 mL) after sample activation.

Using sample **C** as an example, the only ^{13}C hyperpolarised response observed, was from PEA. This sample contained [IrCl(COD)(IMes)] (5 mM), sodium oxalate (20 mM) dissolved in DMF (100 µL) and PEA (45 mM), in 0.5 mL DCM-d_2. The sample was activated with 4 bar *p*-H_2 and a hyperpolarised ^{13}C response was detected within the amine, PEA, see Figure 4.22. No relay response to the sodium oxalate was observed.

At this point, it was still unclear whether or not water was required to drive the SABRE-Relay mechanism, therefore, an addition of 10 µL of H_2O was made. Fresh *p*-H_2 was added and a further ^{13}C experiment was undertaken, in the first experiment hyperpolarisation was detected in both the amine and the DMF, but in all other subsequent experiments, only the amine was polarised. However, when using DMF-d_7, a ^{13}C hyperpolarised response was detected for four of the carbons in PEA rather than the one detected in all other experiments and shown in Figure 4.22. None of the samples produced a ^{13}C response in sodium oxalate.

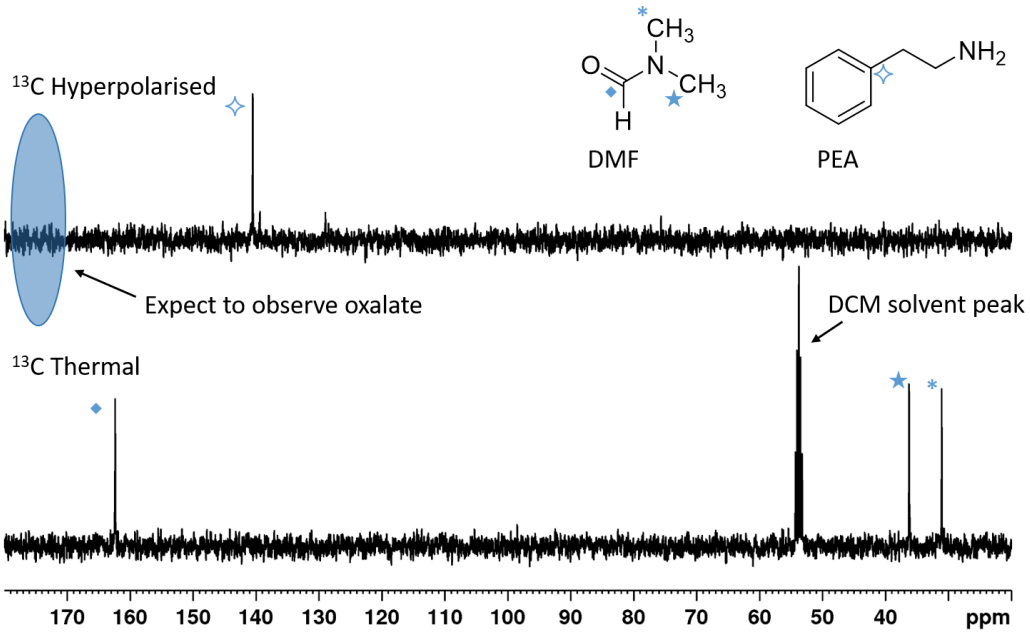

Figure 4.22 – ^{13}C NMR spectrum of sample C containing [IrCl(COD)(IMes)] (5 mM), sodium oxalate (20 mM) dissolved in DMF (100 µL), PEA (45 mM) in DCM-d_2 (0.5 mL), with an addition of H_2O (10 µL) after sample activation. Bottom is a thermally equilibrated spectrum which was left in the NMR for two minutes prior to acquisition, both DMF and DCM-d_2 are observed. Top is a 1 scan hyperpolarised spectrum after polarisation transfer at 60 G, only the PEA is observed. The smaller two peaks within this spectrum are also from the PEA.

It was hypothesised that DMF acted as a polarisation sink. If this was the case, deuteration of the solvent would prevent this. Therefore DMF-d_7 was used. Still no ^{13}C polarisation was observed with sodium oxalate. Therefore, the results suggest that this is not the main driver of polarisation loss/lack of transfer to the sodium oxalate.

It was further hypothesised that sodium oxalate did not hyperpolarise *via* SABRE-Relay due to insolubility. One solvent which does successfully dissolve sodium oxalate is DMSO. Therefore, sodium oxalate was examined, using SABRE, whereby the oxalate was dissolved in DMSO.

4.5.2 SABRE Polarisation of ^{13}C of sodium oxalate using a co-ligand

The minimum amount of DMSO required to dissolve 20 mM of sodium oxalate was found to be 100 µL. This was then added to [IrCl(COD)(IMes)] (5 mM) in methanol-d_4 (0.5 mL), and the solution subsequently exposed to 4 bar of *p*–H_2 and shaken in a mu metal shield. Again, no hyperpolarisation of sodium oxalate was observed. Indeed, even the intermediate did not polarise

Expanding the range of molecular scaffolds amenable to hyperpolarisation using SABRE

suggesting that the DMSO binds competitively to form $[IrCl(H)_2(DMSO)_2(IMes)]$ as the major species in solution.

In previous work when using DMSO to polarise pyruvic acid,[204] only 1 µL (20 mM) was used. The pyruvic acid bound to the catalyst and hyperpolarised directly when DMSO was present as a co-ligand.[204] The role of the co-ligand was to stabilise the catalyst, allowing the weakly coordinating pyruvate to bind and thereby facilitate polarisation transfer.

These conditions were replicated here for sodium oxalate. A sample containing sodium oxalate (25 mM), DMSO (20 mM), [IrCl(COD)(IMes)] (5 mM) was exposed to 4 bar *p*-H_2 and shaken in a mu metal shield at room temperature (298 K). Using these conditions, a hyperpolarised ^{13}C response resulted as shown in Figure 4.23. The ^{13}C signal enhancement for this signal was 4112 ± 484-fold, based on standard methods (see Experimental 7.2.8). It is noteworthy that these signals must come from the labelled sodium oxalate precursor and that both resonances receive similar amounts of polarisation.

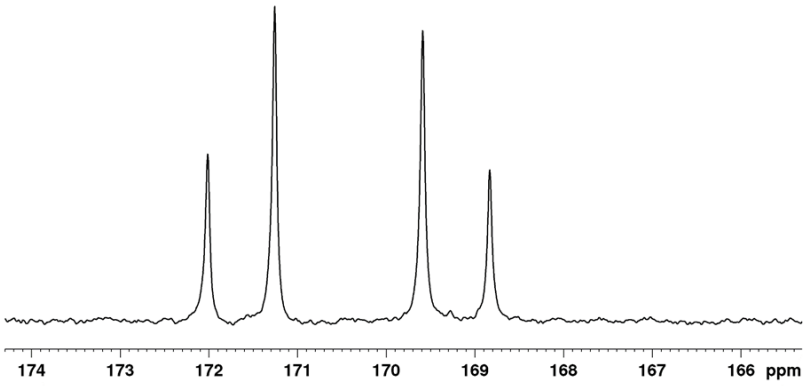

Figure 4.23 – ^{13}C NMR spectrum of hyperpolarised sodium oxalate (20 mM) using DMSO (20 mM) as a co-ligand with [IrCl(COD)(IMes)] (5 mM) in 0.6 mL methanol-d_4. Polarisation transfer was carried out in a mu metal shield and the spectrum was acquired using a 9.4 T Bruker NMR.

The splitting pattern of the ^{13}C NMR of the hyperpolarised sodium oxalate, is not as expected. For symmetry reasons, a single ^{13}C peak would have been predicted. The observed spectrum instead reveals roofing and can be explained by considering the strong coupling of ^{13}C-^{13}C nuclei (an AB spin system) within an oxalate motif. An AX system presents four possible spin states, αα, αβ, βα and ββ. In an AB system, the αβ and βα states are sufficiently close in energy to mix

Expanding the range of molecular scaffolds amenable to hyperpolarisation using SABRE and the probability of a transition is no longer simple. Rather than a doublet of doublets of the same peak intensities being observed, as seen in an AX system, the intensities are distributed in a manner as shown in Figure 4.24.[280] Therefore, with this type of splitting pattern the actual chemical shift difference must be calculated using equation 4.1.

$$Chemical\ shift\ difference = \sqrt{[(\nu_A - \nu_B)^2 + J^2]} \qquad (4.1)$$

ν_A and ν_B are specific frequencies defined as the centre of gravity for each doublet (Figure 4.24) as calculated by equation 4.2 and 4.3 respectively.

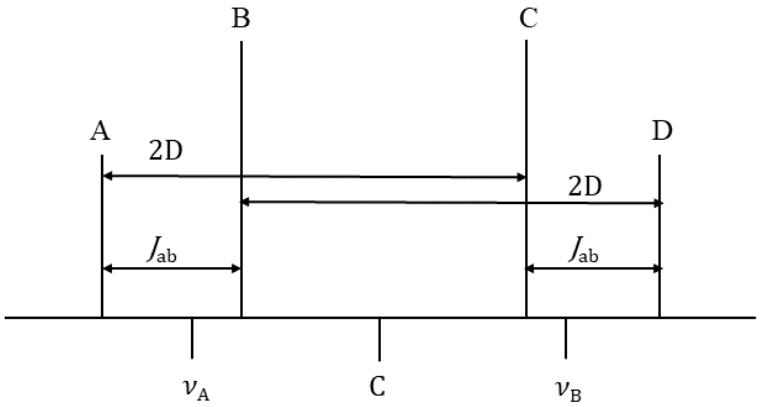

Figure 4.24 – A diagram of the splitting observed in an AB coupling system, this pattern is described as a 'roofing effect'.

$$\nu_A = C + \frac{\Delta\nu}{2} \qquad (4.2) \qquad\qquad \nu_B = C + \frac{\Delta\nu}{2} \qquad (4.3)$$

Where *C* is the centre of the two doublets and $\Delta\nu$ is calculated from equation 4.4,

$$\Delta\nu = \sqrt{[(2D)^2 - J^2]} \qquad (4.4)$$

where 2D is the frequency shift between peak A to C (B to D) and *J* is the coupling between the doublet peaks (Figure 4.24). Examining the ^{13}C hyperpolarised spectrum, 2D = 243.75 Hz and J_{ab} = 75.86 Hz, when placed into equation 4, $\Delta\nu$ = 231.645. When this is substituted into equation 4.2, where C = 17065.426 Hz, ν_A = 17181.2484 Hz and ν_B = 16949.6036 Hz. When these are substituted into equation 4.1 the chemical shift difference is 243.75 Hz, converting this to ppm is (243.75 / (100.613 x 10^6)) = 2.4226 x 10^{-6} = 2.423 ppm. This coupling of 75.9 Hz is also close to that of oxalate itself which according to Levitt is 86.9 Hz.[181] We deduce it must reflect signals

from coordinated oxalate with the binding mode leading to two inequivalent carbon centres. We note at this point that the NMR spectrum recorded in Figure 4.23 was recorded with proton decoupling. There is no evidence therefore of any hydride couplings to these signals.

4.5.3 Characterisation of the complexes in 4.5.2

The work with oxalate revealed that greater understanding of the basic reactions with DMSO was needed. It has been reported that when DMSO, pyruvate and H_2 react with [IrCl(COD)(IMes)], complexes **A**, **B** and **C** of Figure 4.25 are produced. These complexes are readily distinguished by their hydride resonance positions (Figure 4.25). This reaction mixture can be used to hyperpolarise the ^{13}C signals of 1,2 ^{13}C-pyruvate (Figure 4.26) under SABRE conditions. In this ^{13}C hyperpolarised NMR spectrum, free pyruvate displays two inequivalent multiplets with a common J_{cc} of 62.5 Hz at δ 170 and δ 203 for its C_1 and C_2 sites respectively.[165, 204] The ligated pyruvate yielded ^{13}C NMR signals at approximately δ 207 and δ 165.9 for complex **A**, and at approximately δ 197 and δ 165 for complex **B**. It is important to note that the δ 165 signals due to carboxyl site binding are very close to those of oxalate as described earlier. The hyperpolarised signals for complex **A** are 32 times stronger than those for complex **B**. These integral ratios are approximately the same under thermal Boltzmann conditions. In addition, the ratio of the bound to free pyruvate signal is 1:5. It is concluded therefore that ligand exchange is likely to be slow in accordance with the small ratio.

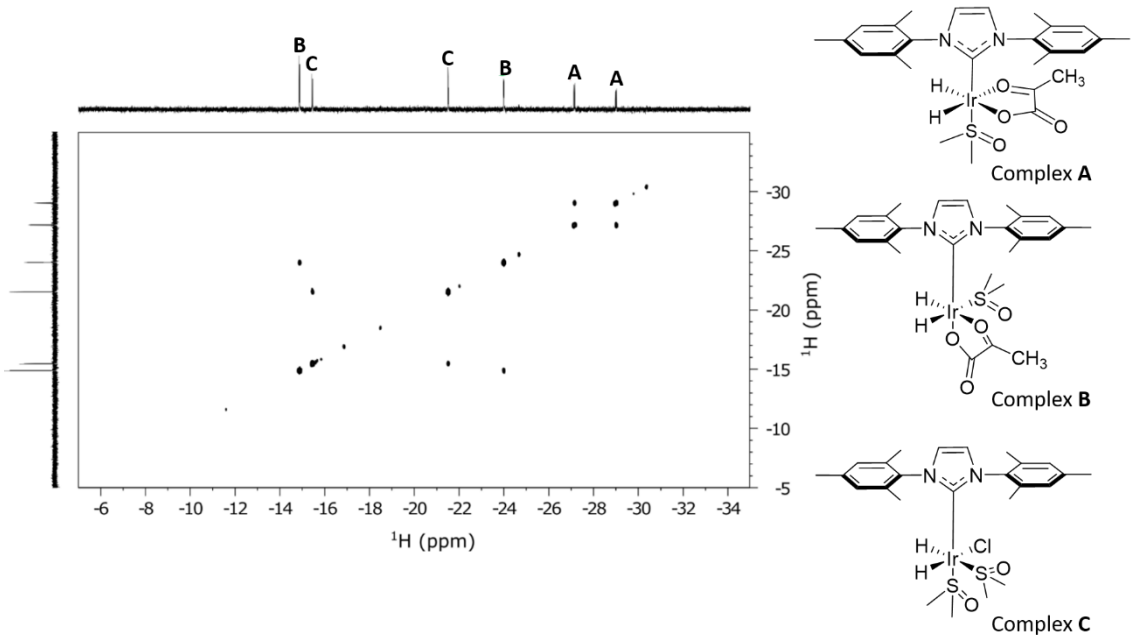

Figure 4.25 – ^{1}H-^{1}H COSY NMR spectrum used to aid hydride peak assignments for the products formed when [IrCl(COD)(IMes)], DMSO and pyruvate react with H_2.

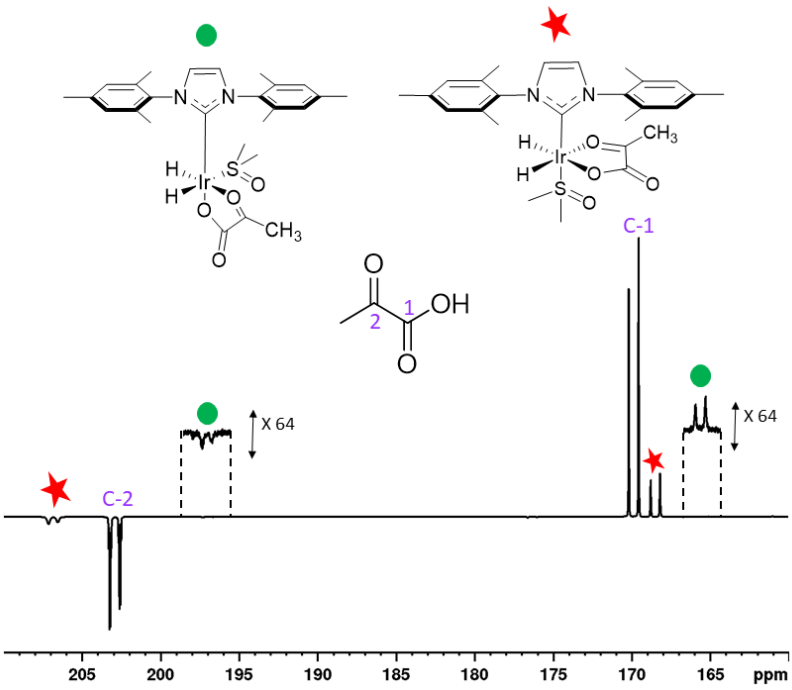

Figure 4.26 – Adapted from figure 3 from *Chem. Sci.*, 2019, 10, 7709-7717 published by The Royal Society of Chemistry showing a single scan hyperpolarised SABRE ^{13}C NMR spectrum of $^{13}C_2$-labelled sodium pyruvate taken from reference 165.[165]

It is worth noting at this point that in its acidic form, oxalic acid can behave as a mono-, bi-, tri- and in some cases a tetradentate ligand therefore leading it to form mono- and polynuclear metal

Expanding the range of molecular scaffolds amenable to hyperpolarisation using SABRE complexes.[281, 282] Figure 4.27 shows oxalate bound to metal centres and how it can form different ligands within these metal complexes, demonstrating the versatility of oxalate as a ligand.[283]

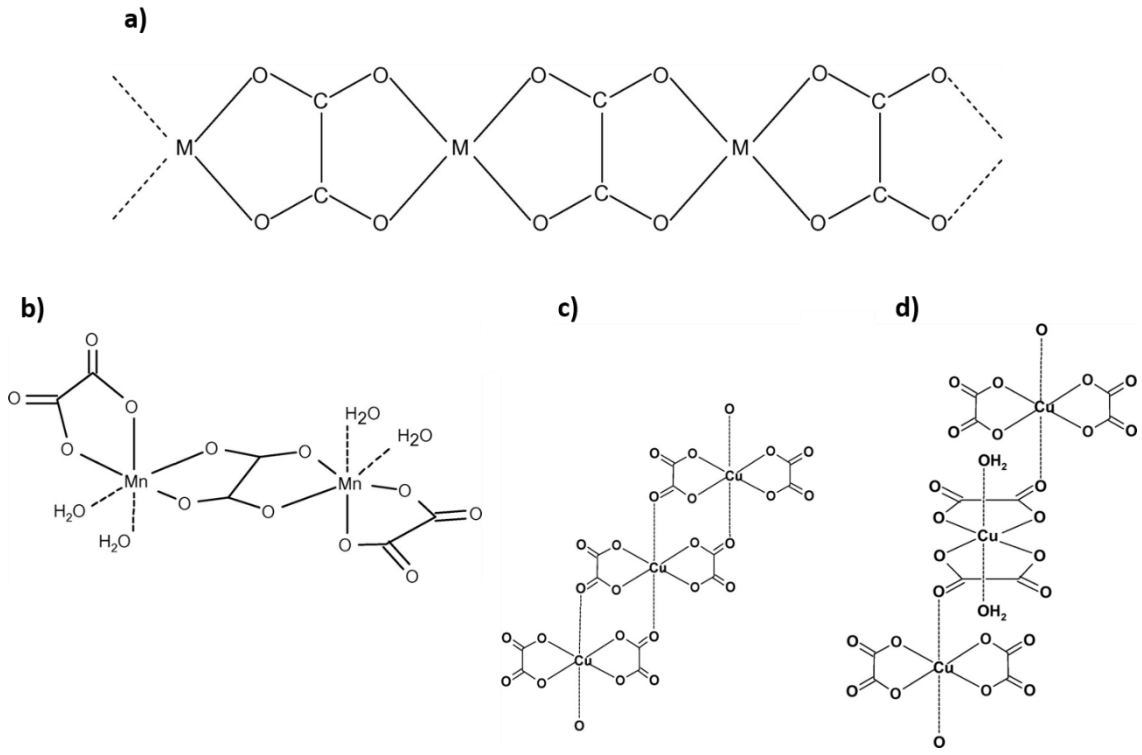

Figure 4.27 – Scheme 1 from *Chem. Sci.*, 2019, 10, 7709-7717 published by The Royal Society of Chemistry schematic drawings from reference 283 of a) metal oxalate complexes $M^{II}(C_2O_4).2H_2O$, b) oxalate ligands with Mn(II) in $[MnC_2O_4(H_2O)_2].H_2O$ and c) $Na_2Cu(C_2O_4)_2.2H_2O$ d) is $Na_2Cu(C_2O_4)_2.2H_2O$ with the respective K, Rb, Cs and NH_4 salts.

A study of sodium oxalate binding and its hyperpolarisation might therefore be expected to produce similar observations to that of pyruvate. For example, the hydride region of the corresponding ^{1}H NMR spectrum might be expected to yield signals for complex **C** alongside complexes **D** and **E** (Figure 4.28). Given the importance of the hydride ^{13}C couplings in SABRE, complex **D** would be expected to yield similar ^{13}C signal enhancements to both ^{13}C centres in oxalate while complex **E** might be expected to promote the enhancement of just one group. Furthermore, to explain the complex splitting pattern observed (Figure 4.23) for bound oxalate, the two ^{13}C signals must remain distinct.

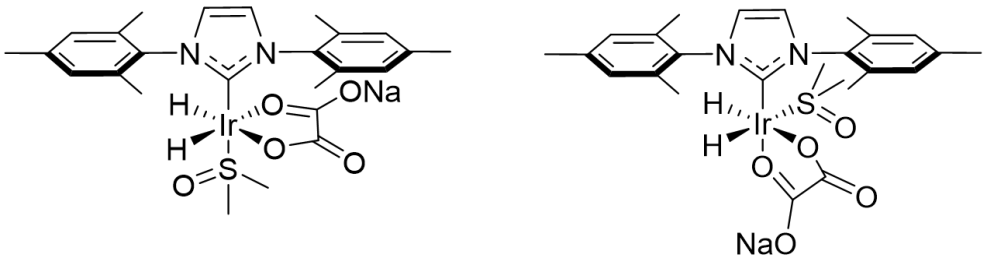

Figure 4.28 – Possible complexes of sodium oxalate bound into the iridium catalyst based upon the observations from pyruvate.

To try and understand what is happening within the ^{13}C polarised spectrum, a series of ^{1}H NMR spectra were recorded under the same sample conditions. The resulting ^{1}H NMR spectrum (Figure 4.29 (b)) resulted in strongly hyperpolarised hydride ligand signals at δ −15.50 and δ −21.12. These peaks are diagnostic of $[IrCl(H)_2(IMes)(DMSO)_2)]$.[165, 167] This complex has been shown to play a direct role in pyruvate hyperpolarisation after chloride and DMSO loss. It is conceivable that such processes also account for the bound oxalate signal described earlier. The actual product that is detected must either exhibit very limited ^{13}C-hydride couplings or reflect an Ir(I) product such as $Na[Ir(IMes)(DMSO)_2)(oxalate)]$. The hyperpolarised peak seen at δ −28.0 in these NMR spectra suggests that a complex where oxygen is bound to iridium *trans* to hydride is formed.[111]

To examine the temperature dependence of the formation of these complexes the experiment was repeated at 245 K. Figure 4.29 compares the hydride region of the spectra at 245 and 298 K. At 245 K the hydride ligand signal detected at δ −27.47 exhibits increased polarisation. This is a result of sharper/narrower peaks being observed at this temperature; the full width half maximum of this peak at 298 K is 20.9 Hz while at 245 K it is 16.4 Hz. Peak narrowing here demonstrates a slower exchange between the *p*-H_2, DMSO and sodium oxalate. This slower exchange is reflected in the improved ^{13}C polarisation transfer signal enhancement which is 151 ± 81-fold at 298 K, ~4 times less than that observed at 245 K (509 ± 106-fold).

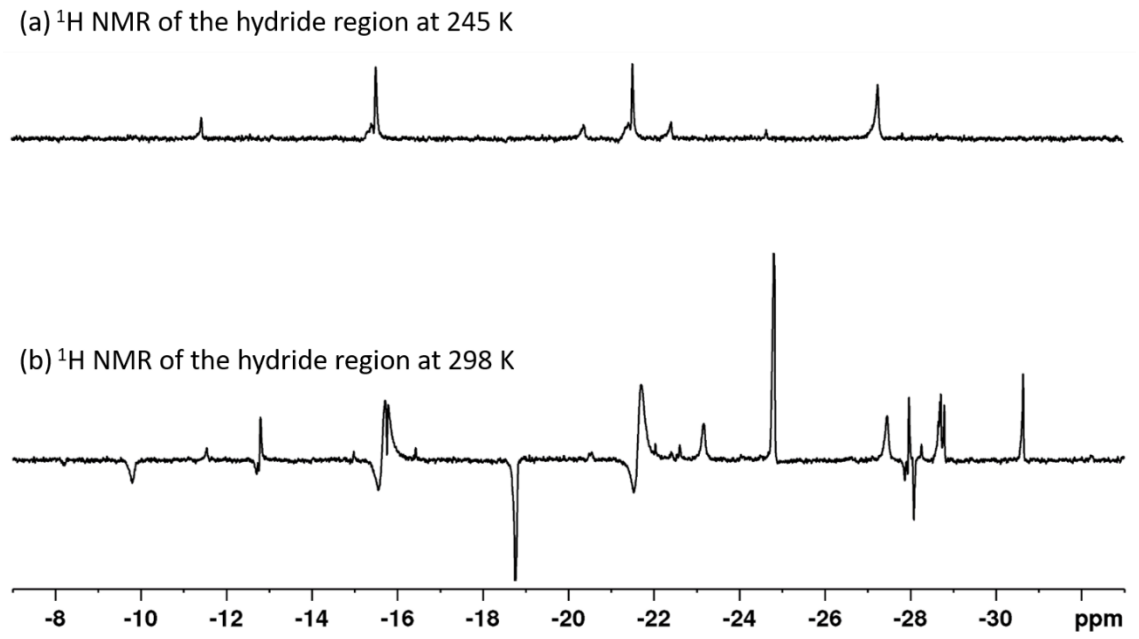

Figure 4.29 – Hyperpolarised ^{1}H NMR spectra of the hydride region of a sample of sodium oxalate (25 mM), DMSO (20 mM), [IrCl(COD)(IMes)] (5 mM) both NMR spectra were taken as a 1 scan. Top (a) was taken at 245 K, bottom (b) was taken at 298 K.

In addition, to the two previously polarised signals, a ^{13}C hyperpolarised singlet resonance at δ 165.05 was observed at 245 K (Figure 4.30). This ^{13}C resonance could reflect the singlet for free sodium oxalate, oxalic acid is expected to appear at δ 174.[284]

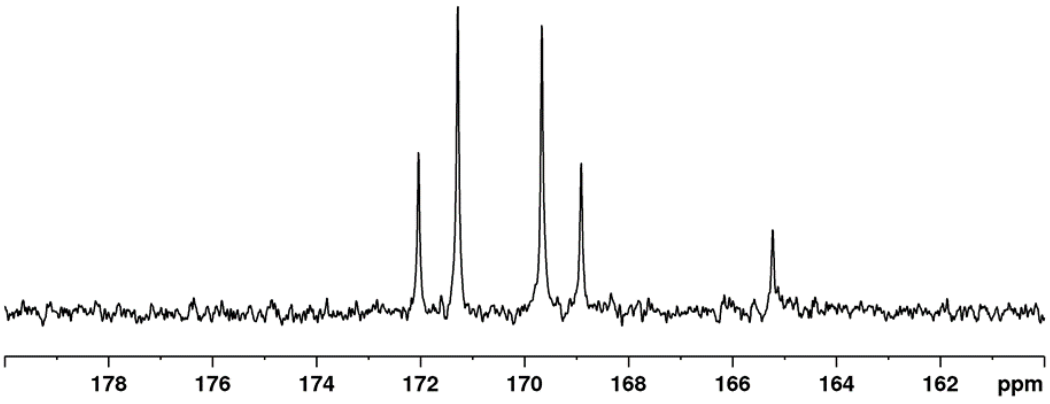

Figure 4.30 – ^{13}C hyperpolarised NMR of sodium oxalate (25 mM), DMSO (20 mM) and [IrCl(COD)(IMes)] (5 mM) exposed to 4 bar *p*-H_2 at 245 K. Polarisation transfer occurred in a mu metal shield.

A repeat of the variable temperature experiment was undertaken involving 10 mM of DMSO (0.5 µL), [IrCl(COD)(IMes)] (5 mM) and $^{13}C_2$-sodium oxalate (25 mM) in methanol-d_4 (0.6 mL)

Expanding the range of molecular scaffolds amenable to hyperpolarisation using SABRE to try and form the complex which produces hyperpolarisation. When carrying out this experiment, all of the reactants were added prior to the addition of H_2. The resulting SABRE experiments were conducted at 245 K to try and slow down exchange. During filling, the sample was placed in an acetone/$CO_{2(s)}$ bath to keep it cold. The hydride region of the resulting hyperpolarised ^{1}H NMR spectra clearly showed larger ^{1}H NMR signal enhancements than those previously described for 20 mM of DMSO (see Figure 4.31). Unfortunately, no ^{13}C polarisation for sodium oxalate was observed. The concentration of DMSO was then increased to 20 mM but still no ^{13}C polarisation was observed for sodium oxalate.

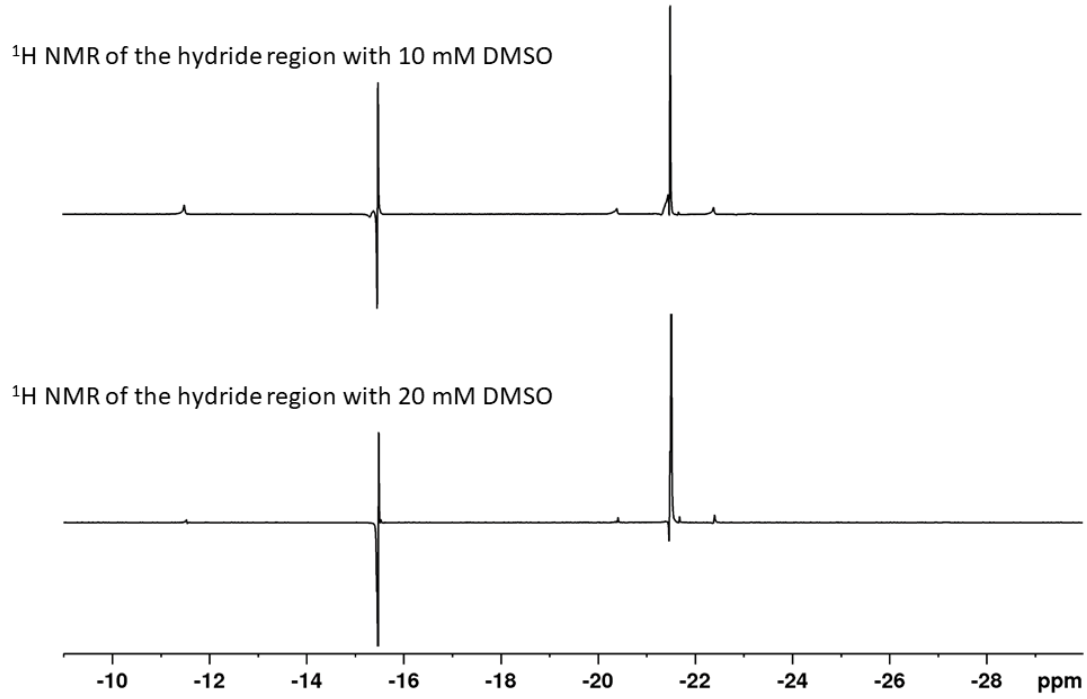

Figure 4.31 – ^{1}H NMR hyperpolarised spectra of the hydride region of a sample containing sodium oxalate (25 mM), DMSO and [IrCl(COD)(IMes)] (5 mM) in methanol-d_4 (0.6 mL) with 4 bar *p*-H_2 at 245 K. Top is with 10 mM DMSO and bottom is with 20 mM DMSO.

Figure 4.32 shows the corresponding long acquisition thermally polarised ^{1}H NMR spectrum. $[IrCl(H)_2(DMSO)_2(IMes)]$ clearly dominates. Despite this, the hyperpolarised ^{13}C signal gain is the greatest for this sample (see Figure 4.33). Here a ^{13}C signal enhancement of 4112 ± 484-fold is observed.

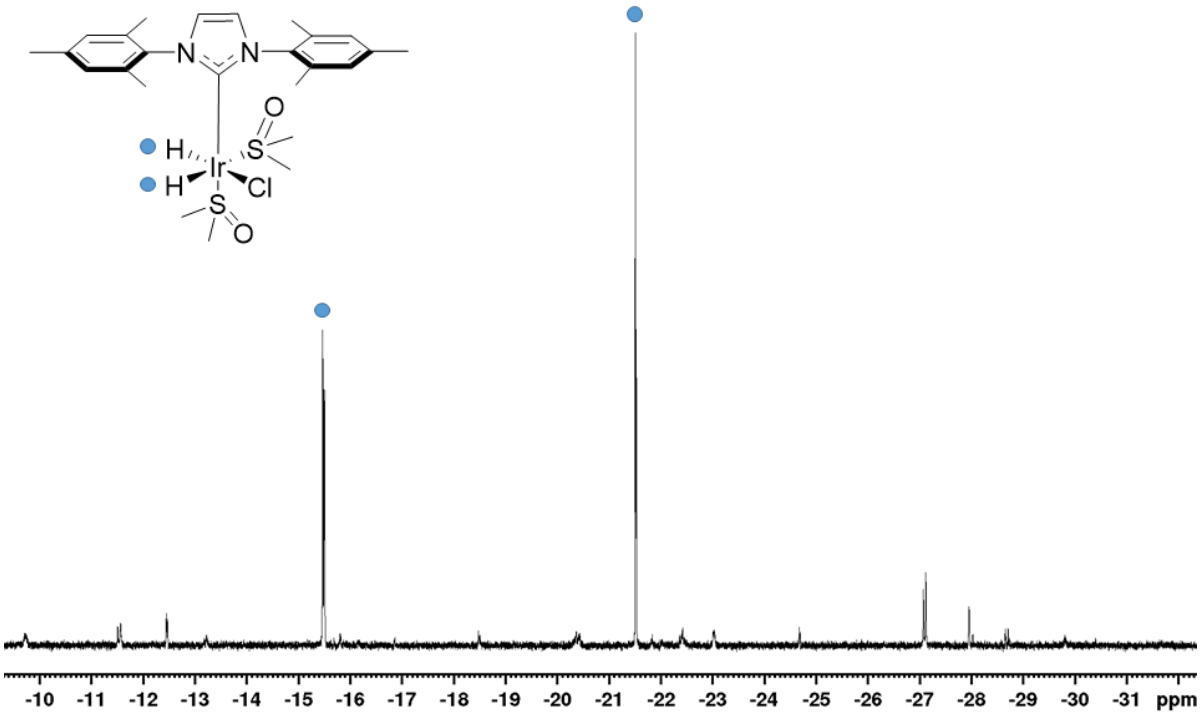

Figure 4.32 – ^{1}H NMR spectrum of the hydride region of the dominant complex formed with $^{13}C_2$-sodium oxalate (20 mM), [IrCl(COD)(IMes)] (5 mM) and DMSO-d_6 (20 mM) exposed to 4 bar of H_2. The spectrum was taken after the sample was left in the spectrometer for two minutes prior to acquisition. Inset is the structure of this complex.

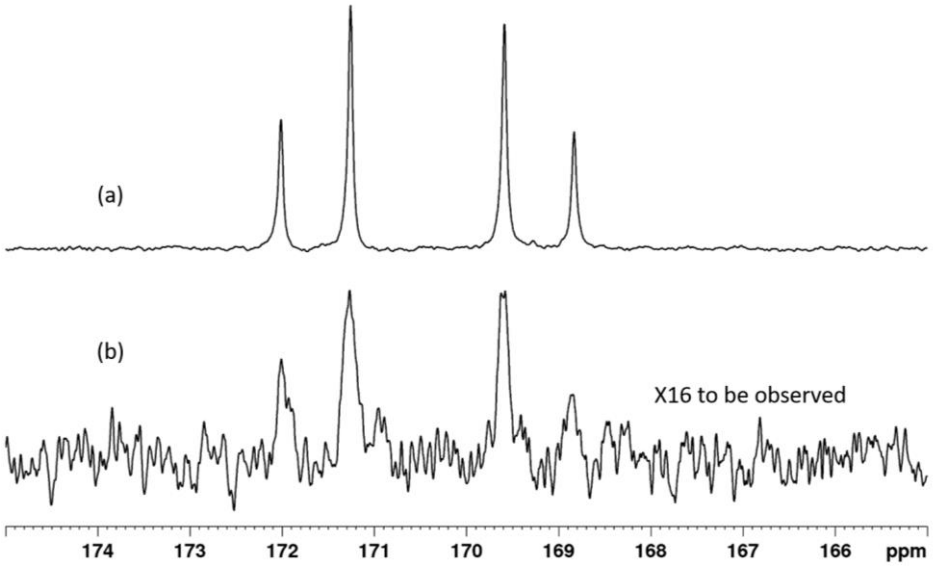

Figure 4.33 – ^{13}C NMR spectra of $^{13}C_2$-sodium oxalate (20 mM), [IrCl(COD)(IMes)] (5 mM) and DMSO (20 mM) in methanol-d_4 (0.6 mL). Top is from Figure 4.23, recorded at 298 K with a signal enhancement of 4012 ± 484-fold. Bottom was recorded after the sample had been at 245 K and then warmed to 298 K, this gave a signal enhancement of 750 ± 235-fold, the spectrum has been expanded x16.

In previous experiments the catalyst, sulfoxide and oxalate had been added together and activated with *p*-H_2. To help aid the solubility of the oxalate and therefore hopefully form more of the active species in solution, a small amount of DMSO was first added to the substrate and this was then added to the activated catalyst, $[IrCl(H)_2(IMes)(DMSO)_2]$[165] in methanol-$d_4$. The oxalate did not dissolve, and no ^{13}C hyperpolarisation was observed.

Studies were then repeated in DCM-d_2 with the aim to solubilise an oxalate product. In this work, the concentration of DMSO was started at 10 mM, and all other concentrations were kept the same with experiments run at 298 K. This sample took much longer to activate. During this process, the colour of the sample changed from yellow to pale yellow, rather than colourless as observed with methanol-d_4. $[IrCl(H)_2(IMes)(DMSO)_2]$ proved to form cleanly, yielding hydride signals of δ −15.85 and −21.21, which are similar to those in methanol-d_4. No additional hydride ligands were observed.

At 10 mM concentration of DMSO, no ^{13}C polarisation is observed for either the oxalate or DMSO. Therefore, a further 0.5 µL of DMSO was added to the sample bringing the concentration to 20 mM. The corresponding ^1H NMR spectrum again revealed a single product (Figure 4.34) and no ^{13}C signals could be seen.

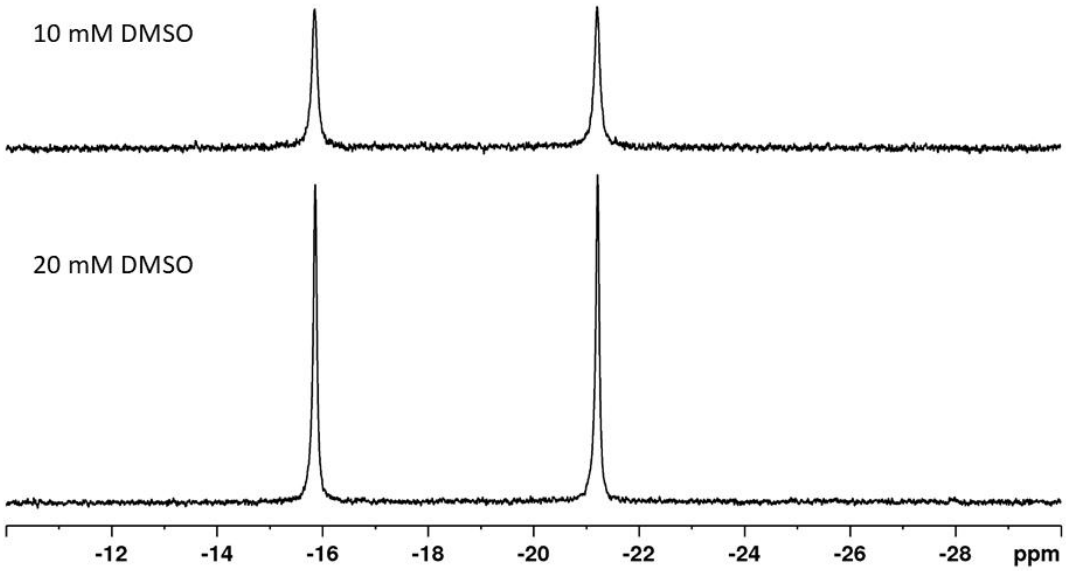

Figure 4.34 – ^{1}H NMR spectra of the hydride region of samples of [IrCl(COD)(IMes)] (5 mM), $^{13}C_2$-sodium oxalate (25 mM) and DMSO under H_2 in DCM-d_2 (0.6 mL). Top shows the hydride region when the sample contained 10 mM DMSO. Bottom shows the hydride region when the concentration of DMSO was increased to 20 mM.

A final sample was then prepared and 50 μL of D_2O added to further solubilise sodium oxalate. It therefore contained D_2O, DMSO (20 mM), [IrCl(COD)(IMes)] (5 mM) and $^{13}C_2$-sodium oxalate (25 mM). The sodium oxalate now proved to dissolve. Unfortunately, no ^{13}C polarisation was again detected. However, the resulting ^{1}H NMR spectrum showed a single product with new hydride resonances at δ −27.27 and δ −27.235. The resonances for the IMes ligand in this product appear at δ 2.07, 2.347, 7.06 and 7.106 and bound DMSO provides a signal at δ 2.94. Based on NMR integrals, this species is of the form $[Ir(H)_2(IMes)(DMSO)(L)_n]_x$ (Figure 4.35).

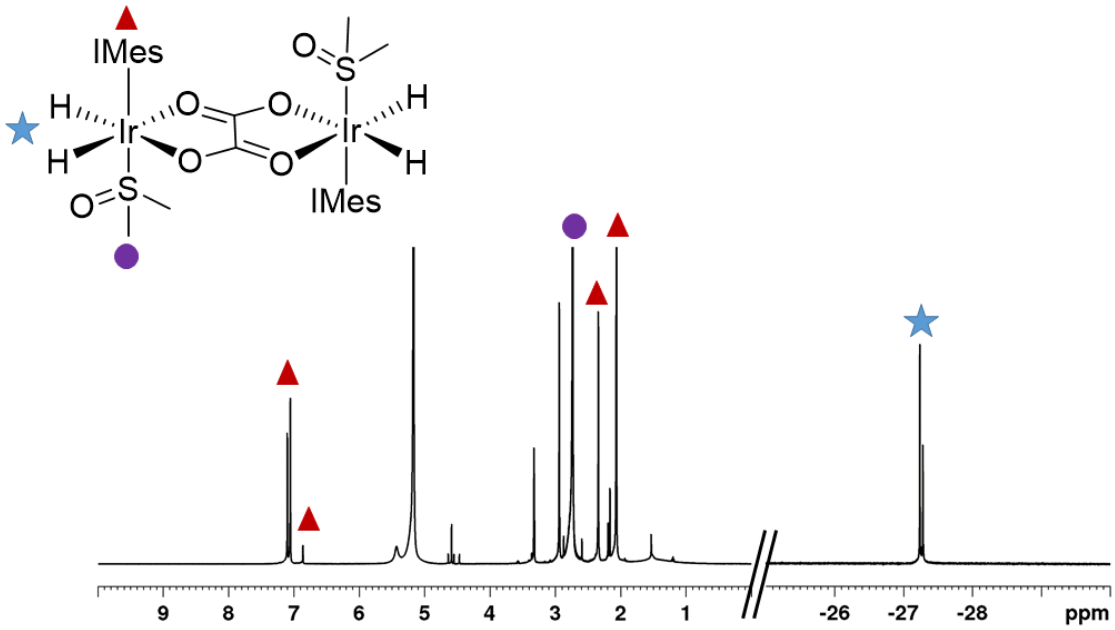

Figure 4.35 – ^{1}H NMR of the sample of [IrCl(COD)(IMes)] (5 mM), DMSO (30 mM) and $^{13}C_2$-sodium oxalate (35 mM) dissolved in D_2O (0.4 mL) and of MeOD-d_4 (0.2 mL). The hydride region has been expanded x8 to be seen here.

When the hydride region of this sample was monitored by NMR over an hour time period the hydride signal intensities change with that at δ −27.235 becoming dominant. This is indicative of H/D exchange and the conversion of a dihydride into a monohydride-deuteride. 3 mL of degassed hexane was added to the samples described, and crystals successfully grown from the resulting mixture. Upon examination with X-ray crystallography, the product was found to be the dimer of Figure 4.36. This product contains a single oxalate bridging two metal centres. Dimer formation is not uncommon with oxalate species.[285-287] It is likely that the signal at δ 165 ppm is due to this product.

Expanding the range of molecular scaffolds amenable to hyperpolarisation using SABRE

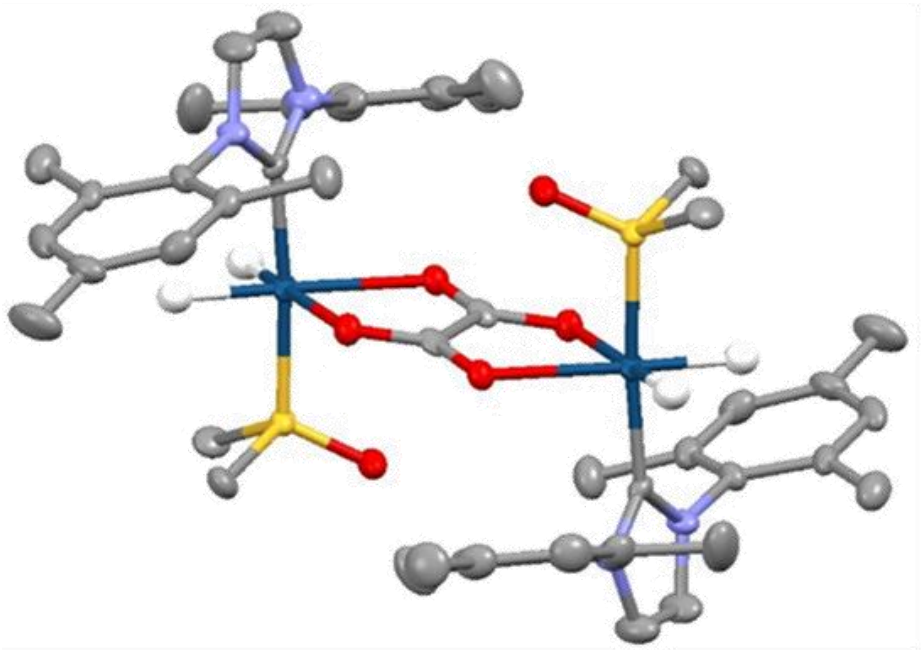

Figure 4.36 – Structure of $[Ir_2(H)_4(DMSO)_2(IMes)_2(\mu\text{-oxalate})]$ determined by X-ray crystallography. For clarity any non-hydride hydrogens and any solvents have been omitted (see Appendix A.12).

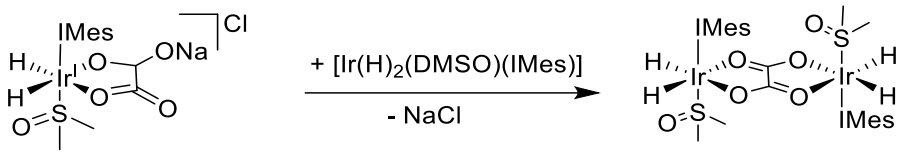

Figure 4.37 – The reaction of Complex D with $[Ir(H)_2(DMSO)(IMes)]$ to form the dimer illustrated in Figure 4.36, $[Ir(H)_2(DMSO)(IMes)]_2(\mu\text{-oxalate})$.

For all characterisation data refer to Appendix A.12

4.5.4 Rate of hydrogen and sulfoxide exchange

Ligand exchange rates are often studied in SABRE complexes. Information collected from these rate based experiments allows mechanistic conclusions to be drawn and therefore insights into why the signal enhancement observed is greater or lower than expected. Another detail that can be gathered from exchange rate data is whether or not PHIP or SABRE can occur. If the substrate ligand is not labile, then PHIP is probably occurring and if the ligand is not lost from the catalyst, then polarisation will not build up within the solution in the free ligand.

If a range of rate data is collected at varying temperatures then the Gibbs free energy, entropy and enthalpy values for activation can be calculated from the Eyring plot. The mechanism of exchange within a catalytic cycle can be further proven by looking at concentration effects.

From previous experiments[165, 167, 288] the first part of the predicted mechanism for ligand exchange in $[IrCl(H)_2(DMSO)_2(IMes)]$ is shown in Figure 4.38. H_a and H_b are different at the start due to the different ligands bound *trans* to them in the equatorial plane. If DMSO loss is dissociative, as expected, then this should be independent of DMSO concentration and the intermediate that forms would retain distinct hydrides if a square bipyramidal shape is adopted. If, however, a trigonal bipyramidal shape were to be adopted then when DMSO is lost from the complex, H_a and H_b would become equivalent, and yield a single hydride peak. A set of 1D-EXSY experiments[289-291] were carried out to examine this behaviour (see experimental, Chapter 7 section 7.2.10 for details).

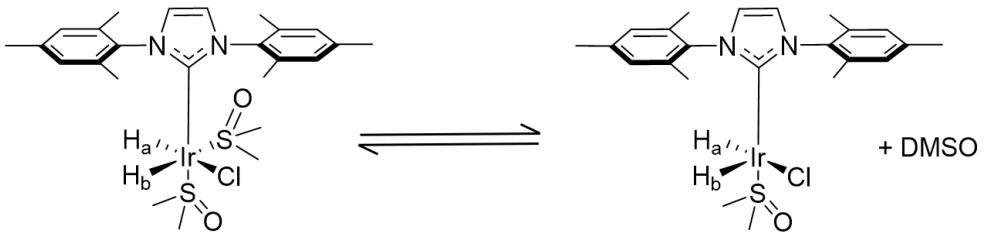

Figure 4.38 – The mechanism of both DMSO and *p*-H_2 exchange for the complex $[IrCl(H)_2(DMSO)_2(IMes)]$ follow a common first step.

Exchange of DSMO follows a simple and reversible pathway from which it should be straightforward to extract $k_{(DMSO)}$. The inequivalent methyl groups of the bound DMSO in this complex resonate at approximately δ 3.21, 3.16, 3.05 and 2.73. These resonances were separately excited and demonstrate exchange with the free DMSO peak at approximately δ 2.27 when *trans* to hydride. These experiments were conducted in both methanol-d_4 and DCM-d_2. The experimental data was simulated using a differential kinetic model in conjunction with the solver add-on in Microsoft EXCEL, which minimises the sum of the squares of the differences between real and simulated data points to produce appropriate rate constants. Errors in the extracted rate constants were calculated by the Jack knife method.

Unfortunately, the free and bound DMSO signal intensities failed to fit any sensible kinetic model even though the hydride signals fit well to the same model. The experiments were therefore repeated but at each temperature the T_1 of the free and bound DMSO (and the T_1 of the hydrogen signals) were determined. These T_1 values were then included into the differential expressions

used to model the reaction. For the hydride fitting, no improvement was seen by adding in the T_1 values. However, for the DMSO it was necessary to include the T_1 effects during the fitting of the data. Table 4.2 shows that the rate of hydrogen loss, $k_{(H2)}$ from $[IrCl(H)_2(DMSO)_2(IMes)]$ in DCM-d_2 is 1.16 ± 0.04 s^{-1} at 263 K while the rate of DMSO loss for the ligand trans to hydride, $k_{(DMSO)}$ is 1.56 ± 0.01 s^{-1}. In addition, the inequivalent DSMO signals for the axial ligand interchange at a rate of 0.8 s^{-1} as the chloride swops sides in the intermediate. These rates are fast relative to those of similar complexes[167, 292] at these temperatures. The rate of hydrogen loss is slower than that of the substrate as predicted by the reaction pathway.

Table 4.2 – Rate constants for elimination of H_2 and DMSO loss in $[IrCl(H)_2(DMSO)_2(IMes)]$ in dichloromethane-d_2 or methanol-d_4 solution with temperature, obtained *via* selective 1D-EXSY experiments using a 500 MHz Bruker NMR spectrometer.

Temperature (K)	In DCM-d_2 Rate of loss / s^{-1}		In MeOD-d_4 Rate of loss / s^{-1}	
	Hydride	DMSO	Hydride	DMSO
233	-	-	0.00	0.03 ± 0.01
238	-	-	0.06 ± 0.01	0.07 ± 0.01
243	0.04 ± 0.01	0.05 ± 0.01	0.16 ± 0.01	0.15 ± 0.01
248	0.04 ± 0.01	0.12 ± 0.01	0.35 ± 0.01	0.32 ± 0.01
253	0.26 ± 0.01	0.29 ± 0.01	0.67 ± 0.01	0.64 ± 0.01
258	0.54 ± 0.02	0.64 ± 0.01	1.51 ± 0.02	1.52 ± 0.01
263	1.16 ± 0.04	1.54 ± 0.01	3.31 ± 0.26	3.35 ± 0.01
268	2.56 ± 0.08	3.05 ± 0.01	5.04 ± 0.37	7.28 ± 0.02
273	3.93 ± 0.03	6.13 ± 0.01	-	-

The same complex dissolved in methanol-d_4 exhibited the following rates at 263 K; for hydrogen loss, $k_{(H2)}$ 3.31 ± 0.26 s^{-1}**,** for DMSO loss, $k_{(DMSO)}$ was 3.35 ± 0.01 s^{-1}. The rates of ligand loss are therefore slower in less polar DCM-d_2.

Using these rate data, the activation energy barriers were calculated using Eyring analysis. Table 4.3 shows these parameters in DCM-d_2 solvent and methanol-d_4. The $\Delta H^{\pm}_{(H2)}$ for DCM-d_2 is 83 ± 8 kJ mol^{-1} and the $\Delta S^{\pm}_{(H2)}$ is 79 ± 29 J mol^{-1} K^{-1}, for the DMSO loss $\Delta H^{\pm}_{(DMSO)}$ is 83 ± 8 kJ mol^{-1}and the $\Delta S^{\pm}_{(DMSO)}$ is 94 ± 8 J mol^{-1} K^{-1}. In methanol-d_4 the $\Delta H^{\pm}_{(H2)}$ is 78 ± 6 kJ mol^{-1} and the $\Delta S^{\pm}_{(H2)}$ is 66 ± 25 J mol^{-1} K^{-1}. For DMSO the $\Delta H^{\pm}_{(DMSO)}$ is 79 ± 4 kJ mol^{-1} and the $\Delta S^{\pm}_{(DMSO)}$ is 72 ± 16 J mol^{-1} K^{-1}. The energy barrier to hydrogen loss, in DCM-d_2 $\Delta G^{\pm 300K}$ is 60 ± 0.1 kJ mol^{-1} and for DMSO, $\Delta G^{\pm 300K}$ is 58 ± 0.1 kJ mol^{-1}, showing that it is more favourable to lose the DMSO ligand. The energy barrier to hydrogen loss, in methanol-d_4 $\Delta G^{\pm 300K}$ is 58 ± 0.3 kJ mol^{-1} and for DMSO, $\Delta G^{\pm 300K}$ is 57 ± 0.2 kJ mol^{-1}, again showing that it is more favourable to lose the DMSO ligand than hydrogen.

Table 4.3 – Activation parameters for ligand exchange in [IrCl(H)$_2$(DMSO)$_2$(IMes)] in dichloromethane-d_2 and methanol-d_4 solution.

Solvent	Ligand	ΔH kJ mol^{-1}	ΔS J mol^{-1} K^{-1}	$\Delta G^{\pm 300}$ kJ mol^{-1}
DCM-d_2	DMSO	86.5 ± 2.1	93.6 ± 8.2	58.4 ± 0.1
	Hydride	83.1 ± 7.6	78.9 ± 29.3	59.5 ± 0.1
MeOD-d_4	DMSO	78.9 ± 3.8	71.7 ± 15.7	57.4 ± 0.2
	Hydride	77.6 ± 6.2	66.1 ± 24.5	57.8 ± 0.3

To determine the effect of methanol on this behaviour, the DCM-d_2 solution was spiked with two aliquots of 15 µL of methanol. The activation parameters were calculated for both additions as shown in Table 4.4. They show that the $\Delta G^{\pm 300K}$ changes slightly but still demonstrate that ligand loss is more favourable than the hydrogen.

Table 4.4 – Activation parameters for ligand exchange in [IrCl(H)$_2$(DMSO)$_2$(IMes)] in dichloromethane-d_2 after the addition of 2 x 15 µL portions of methanol.

Total volume of methanol added (µL)	Ligand	ΔH kJ mol^{-1}	ΔS J mol^{-1} K^{-1}	ΔG$^{\pm 300}$ kJ mol^{-1}
15	DMSO	74.6 ± 10.8	52.8 ± 42.0	58.7 ± 0.3
	Hydride	71.0 ± 3.8	34.1 ± 14.9	60.7 ± 0.1
30	DMSO	78.5 ± 12.0	67.8 ± 46.7	58.1 ± 0.4
	Hydride	84.8 ± 4.5	88.9 ± 17.4	58.2 ± 0.2

Samples of [IrCl(H)$_2$(DMSO)$_2$(IMes)] in DCM-d_2 were then spiked with 30 µL methanol and 0.5 µL DMSO in steps until 3.0 µL of DMSO had been added. The rate of hydrogen and DMSO loss was then calculated as a function of DMSO and the results presented in Figure 4.39. From these data it can be seen that the addition of DMSO has little effect on the rate of both DMSO and hydrogen loss in agreement with dissociative DSMO loss preceding both.

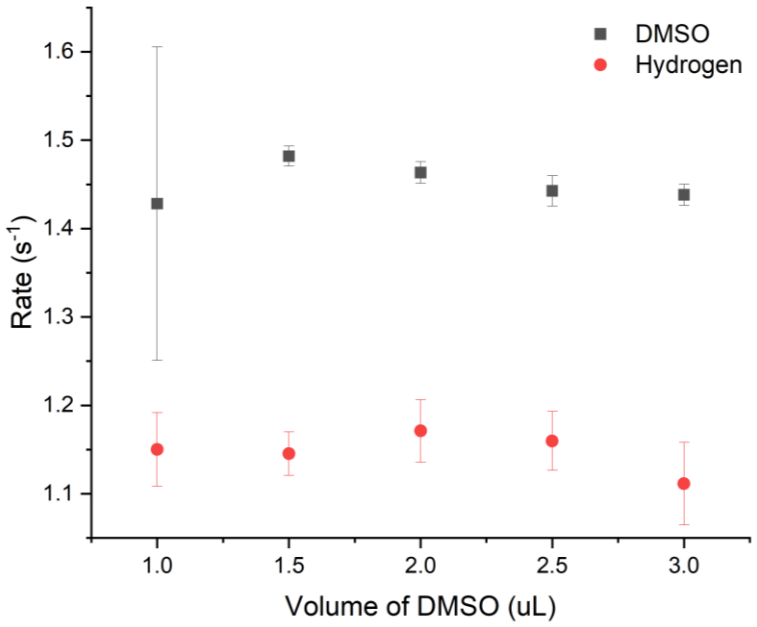

Figure 4.39 – Rates of ligand loss in [IrCl(H)$_2$(DMSO)$_2$(IMes)] in dichloromethane-d_2 when the volume of DMSO is increased from 1.0 - 3.0 µL. The grey squares represent the rate of loss of DMSO and the red circles represent the rate of loss of hydrogen.

The effect of increasing the concentration of hydrogen gas was then explored. Again, the rate of hydrogen and DMSO loss was calculated for several hydrogen pressures as shown in Figure 4.40. From these data it can be seen that there is an increase in both the rate of hydrogen and DMSO loss before they plateau.

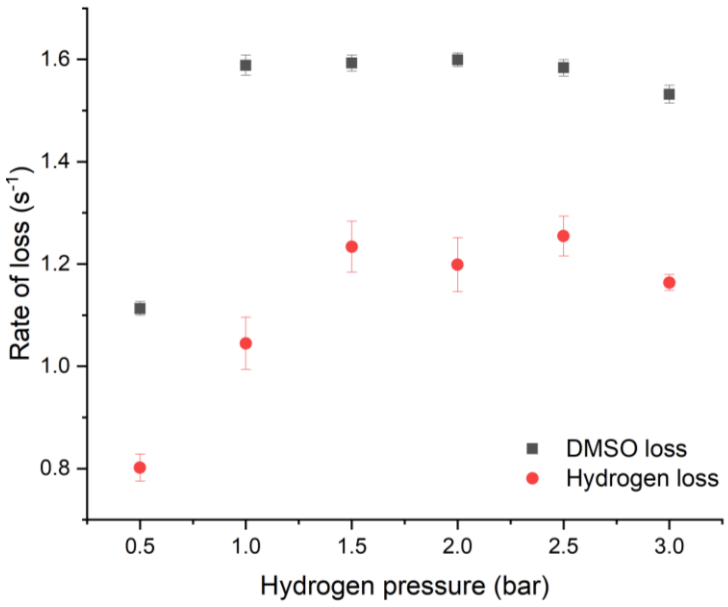

Figure 4.40 – Rate of ligand loss in [IrCl(H)$_2$(DMSO)$_2$(IMes)] in dichloromethane-d_2 as a function of pressure of hydrogen. The grey squares represent the rate of loss of DMSO while the red circles represent the rate of loss of hydrogen.

These results are fully consistent with a mechanism that features dissociative loss of DMSO in the first step.

Rate data at 263 K was also collected when methyl phenyl sulfoxide was used as a co-ligand instead of DMSO. The methyl phenyl sulfoxide loss rate was 21.48 s^{-1} in DCM-d_2 this increased to 49.02 s^{-1} when methanol was added. This demonstrates that the exchange rate is linked to the binding potential of the sulfoxide.[165]

4.6 Conclusions

$^{13}C,^{15}N_2$-Urea has been shown to successfully hyperpolarise *via* SABRE-Relay with strong ^{13}C and ^{15}N signal gains resulting and ^{13}C phantom images were successfully recorded on a 3 T clinical MRI scanner. Both benzylamine and NH_3 were screened as amine carriers for $^{13}C,^{15}N$-urea hyperpolarisation. They yielded ^{13}C signal enhancements of 832 ± 74-fold and 5117 ± 536-

Expanding the range of molecular scaffolds amenable to hyperpolarisation using SABRE

fold and with ^{15}N SNR of 14 and 16 respectively. Although NH_3 provided the greatest signal enhancement for optimisation purposes benzylamine-d_7 is needed as it is far easier to handle.

The ^{31}P signals of both monosodium dihydrogen phosphate (MSP) and adenosine triphosphate (ATP) were successfully hyperpolarised.

The polarisation levels obtained for their ^{31}P nuclei were lower than those previously achieved under traditional SABRE (3588-fold ^{31}P signal enhancement[146]) and *via* d-DNP (> 11,000-fold ^{31}P signal enhancement[63]) in related substrates. The presence of water which contains labile protons accounts for this[169] as demonstrated in the NMR spectra of Figure 4.41.

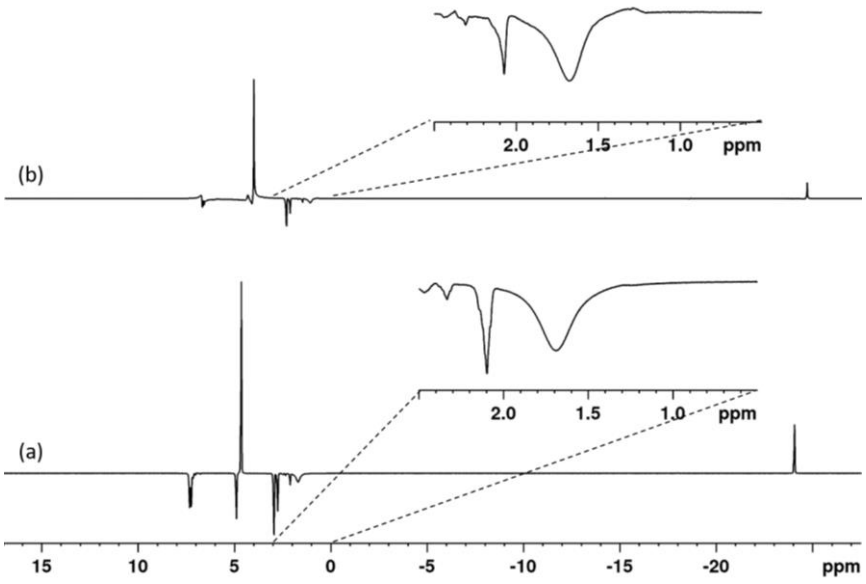

Figure 4.41 – SABRE-Relay hyperpolarised ^1H NMR of [IrCl(COD)(IMes)] (5 mM) with PEA (15 mM) in DCM-d_2 (0.6 mL). Top is of MSP (20 mM) dissolved in 40 µL H_2O. Bottom is of ATP dissolved in 40 µL H_2O. Expansion of both spectra between 0 - 2.5 ppm is of hyperpolarised H_2O.

Free sodium oxalate did not undergo polarisation *via* SABRE-Relay, but when a sulfoxide co-ligand was used it proved to polarise when bound to iridium. A crystal structure of $[Ir(H)_2(DMSO)(IMes)]_2$(µ-oxalate) confirmed oxalate can bridge two iridium centres in these systems. We interpret this to suggest that $[IrCl(H)_2(DMSO)_2(IMes)]$ (**C**) in Figure 4.25reacts first to form Na[Ir(H)$_2$(μ-oxalate)(DMSO)(IMes)] prior to the formation of $[Ir(H)_2(DMSO)(IMes)]_2$(µ-oxalate). The chemical shifts of the detected ^{13}C oxalate resonances in Na[Ir(H)$_2$(μ-oxalate)(DMSO)(IMes)] are consistent with those in complex **A** of Figure 4.25.

Studies of the ligand exchange processes undergone by **C** were undertaken to confirm whether **D** should form rapidly. The ligand exchange rates are high, and it can therefore be concluded that substrate solubility is a major impediment to this process.

Changing the pre-catalyst to [Ir(COD)(OC(CH_3)$_2$)(IMes)]PF_6 increased the ^{13}C signal enhancement in the oxalate peaks from 4112 ± 484-fold to 4907 ± 861-fold. This demonstrated that the Cl^- played a negative role in this process. The identity of the active species detected in these oxalate studies is, however, not fully confirmed.

In this chapter the viability of the molecules, ^{13}C,$^{15}N_2$-urea, MSP, ATP and sodium oxalate to undergo polarisation *via* SABRE-Relay has been discussed. Three of these molecules proved successful. These were ^{13}C,$^{15}N_2$-urea, MSP and ATP, though ATP gave a low signal enhancement. These molecules were polarised *via* the proton exchange between themselves and the amine which underwent SABRE polarisation. In the case of ^{13}C,$^{15}N_2$-urea, hyperpolarised ^{13}C MR images were obtained on a Siemens 3 T clinical scanner. These results mark significant additions to the SABRE effect.

4.7 Further work

For monosodium phosphate dihydrogen, adenosine phosphate and urea, the ratio of D_2O:H_2O and possibly the volume needs further optimising. An investigation into the rate of proton exchange could also be carried out more generally for SABRE-Relay. In view of the complexity of the underlying process the polarisation transfer field plots that have been undertaken currently reveal 60 G and transfer into the amine is controlling. This cannot however match transfer in the second stage. It is therefore likely that rapid field cycling is needed to match both conditions. Other solvent systems and metal phosphates might also be explored.

In the case of sodium oxalate, a more extensive study into the effect of the sulfoxide co-ligand is warranted. This could be undertaken alongside optimising the catalyst and substrate concentrations. To aid our understanding of the SABRE mechanism, it may also be worth examining the exchange rate specifically as a function of substrate. The isolation of

Expanding the range of molecular scaffolds amenable to hyperpolarisation using SABRE

$[Ir(H)_2(DMSO)(IMes)]_2$(μ-oxalate) offers the opportunity to see if any added ligands can displace the bound oxalate and thereby improve our ability to control this process. Just as with the SABRE method, temperature and pressure of *p*-H_2 effects could be further studied to help improve the polarisation of this substrate.

Chapter 5: SABRE-Relay with Uracil and Fluorouracil

5.1 Introduction

The hyperpolarisation of biomolecules and their detection using magnetic resonance techniques has been shown to provide metabolic and mechanistic information on a cellular level.[40, 96, 293] The utility of NMR methods for the detection of nucleic acids has also been established and conformational changes that correlate with biological events.[294, 295] However, the NMR detection and monitoring of these processes is none-trivial due to low sensitivity. Therefore, methods to improve the detectability of nucleic acids are desirable.

Ribonucleic acid (RNA) and deoxyribonucleic acid (DNA) are possibly the most crucial macromolecules in cell biology. DNA is present in the cell nucleus and stores the genetic information for an organism. RNA transfers the genetic information from the nucleus to the ribosomes where it is responsible for the synthesis of proteins.[43] There are four nucleobases that make up RNA; cytosine, guanine, adenine and uracil (Figure 5.1). Guanine forms a complimentary pair with cytosine due to their ability to form three hydrogen bonding interactions.[296] Adenine and uracil also form a pair through two hydrogen bonds.[43, 296-298] Nucleobases are the foundations of nucleotides which contain a ribose sugar and a phosphate ester as shown in Figure 5.1.[43]

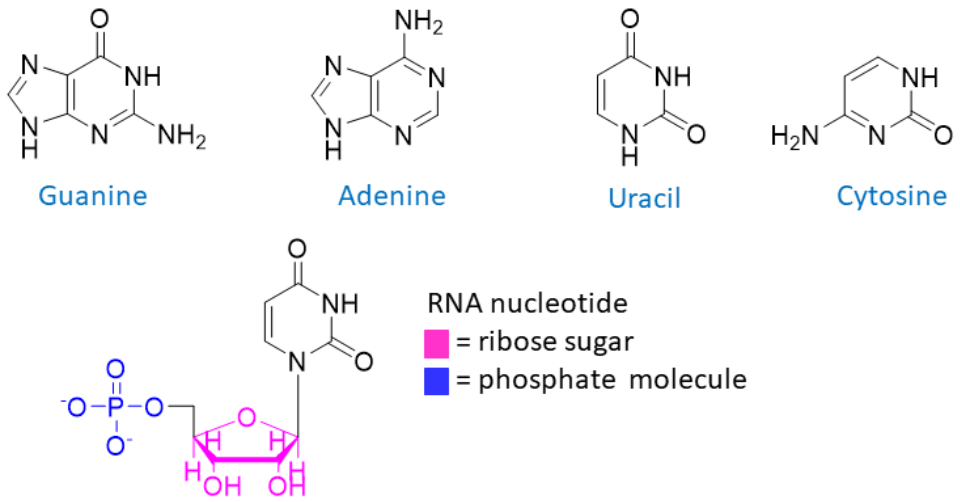

Figure 5.1 – The nucleobases guanine, adenine, uracil, and cytosine alongside an RNA nucleotide containing ribose sugar, phosphate ester and uracil.

Combinations of these nucleotides form RNA, which is usually a single stranded macromolecule, although it can form a double helix during the translation process whereby a gene is expressed.[299] During translation, messenger RNA (mRNA) is paired with the terminal amino acid of the transfer RNA (tRNA) and this is repeated until the desired protein has been formed. In contrast, DNA exists as a two stranded double helix and contains thymine rather than uracil. Thymine is structurally related to uracil, however it contains a methyl group at position 5.[43, 300, 301]

The nucleotide of uracil is known as deoxyuridylate (dUMP) and the thymine derived nucleotide is called thymidylate (TMP). Methylation of dUMP to form TMP is achieved in the cell using thymidylate synthase (TS) as shown in Figure 5.2.[43, 302, 303] This transformation helps to maintain the genetic information within DNA of the cell.

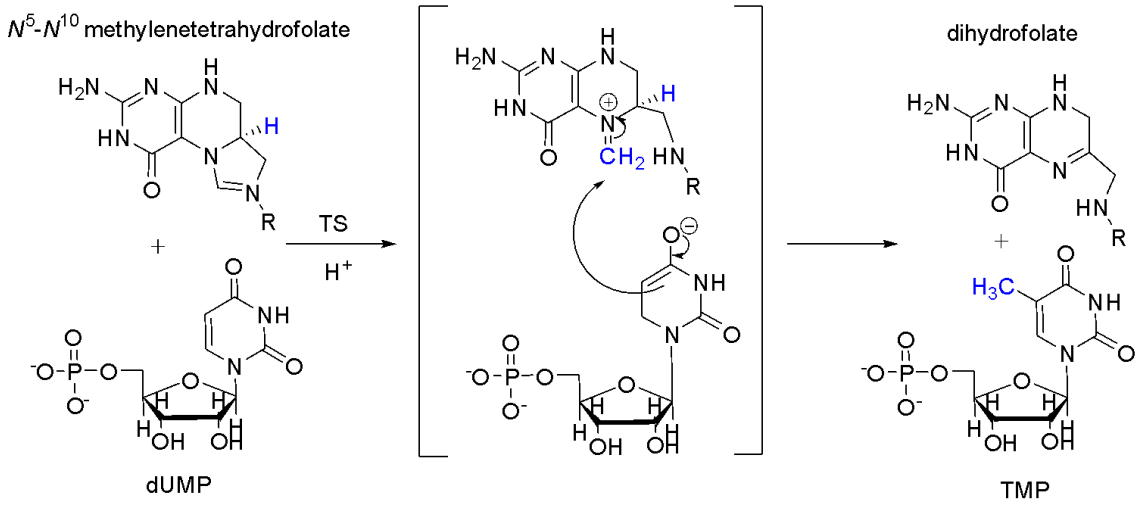

Figure 5.2 – Formation of thymidylate (TMP) and dihydrofolate from deoxyuridylate, (dUMP) and N^5-N^{10} methylenetetrahydrofolate *via* the enzyme thymidylate synthase (TS).

In a cancerous cell, TMP production is increased due to higher rates of cell proliferation.[43, 304] Disabling the production of TMP using chemotherapy agents is a major route for the treatment of a range of cancers. One blockbuster drug is 5-fluorouracil which prevents TMP production by creating fluorodeoxyuridylate (F-dUMP) which is unable to be cleaved by TS.[177, 178, 305-307] Therefore, the enzymes' catalytic turnover is prohibited in a process known as suicide inhibition.[43, 178, 305, 308] Monitoring of suicide inhibition would be advantageous in quantifying cell death in tumours and drug efficacy.

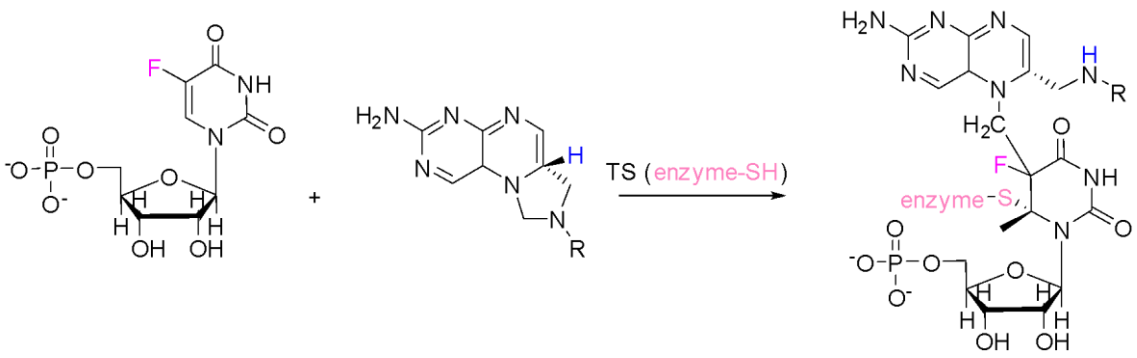

Figure 5.3 – The mechanism to blocking the methylation of TMP (thymidylate) with the incorporation of fluorouracil into the dUMP, to form F-dUMP (fluorodeoxyuridylate, suicide inhibitor).

Previously, DNP has been used to polarise 4,5-$^{13}C_2$-uracil and ^{13}C-NMR signal enhancements of 5000 times were reported at a field strength of 400 MHz.[309] These signal gains were sufficient for the observation and characterisation of the reaction product pseudouridine monophosphate during the cleavage of the C-C glycosidic bond in the metalloenzyme, psedouridine monophosphate glycosidase.[309] Additionally, adenine has been polarised using SABRE under continuous flow conditions, however, no signal enhancements were quantified.[310] It is proposed here that if uracil could be polarised using *p*-H_2 it would provide a cheap way to monitor the *in vivo* construction of biological molecules.

In Chapter 3, the hyperpolarisation of the ^{19}F nuclei of 5-fluorouracil was shown to be successful. This was achieved by using 5 mM of the pre-catalyst [IrCl(COD)(IMes)] in 0.6 mL methanol-d_4 in the presence of 10 mM of Cs_2CO_3 with 20 mM 5-fluorouracil. A ^{1}H NMR signal enhancement of 106-fold was produced and a ^{19}F MRI of a phantom was also collected. It was concluded that ligation of 5-fluorouracil to the iridium centre must occur in order for transfer of the spin order from *p*-H_2 to the substrate to be observed. Unfortunately, catalyst deactivation was also observed within 10-15 minutes of *p*-H_2 addition due to possible C-H bond activation pathways and resultant cyclometallation.[229] After this time, the substrate could no longer be hyperpolarised. In contrast, previous unreported attempts within the group to hyperpolarise uracil directly *via* SABRE were unsuccessful when using similar conditions. In these studies, no enhanced NMR signals were

observed after interaction with *p*-H_2 and no evidence for the formation of an iridium hydride complex was found.

As both uracil and 5-fluorouracil contain labile protons, it was proposed they could be hyperpolarised *via* SABRE-Relay.[168, 241] This process should remove the need for a base to remove the proton from the masked nitrogen binding site and hence prevent degradation of the catalyst. In this chapter uracil and 5-fluorouracil will be examined under SABRE and SABRE-Relay conditions and discussions as to the viability of these methods will be presented.

5.2 Polarisation of uracil *via* SABRE

The investigation into the hyperpolarisation of uracil began by utilising analogous conditions to those which were successful for 5-fluorouracil. Therefore, a sample was prepared that contained [IrCl(COD)(IMes)] (5 mM) uracil (20 mM) with Cs_2CO_3 (10 mM) in methanol-d_4 (0.6 mL). After exposure to 4 bar *p*-H_2 in a 60 G polarisation transfer field, a 9-fold ^{1}H NMR signal enhancement was observed in the δ 7.5 signal due to proton H-4 as detailed in Figure 5.4. In an attempt to increase this polarisation level, the Cs_2CO_3 was replaced by the sterically hindered base ^{i}Pr$_2$EtN. However, this reduced the polarisation level.

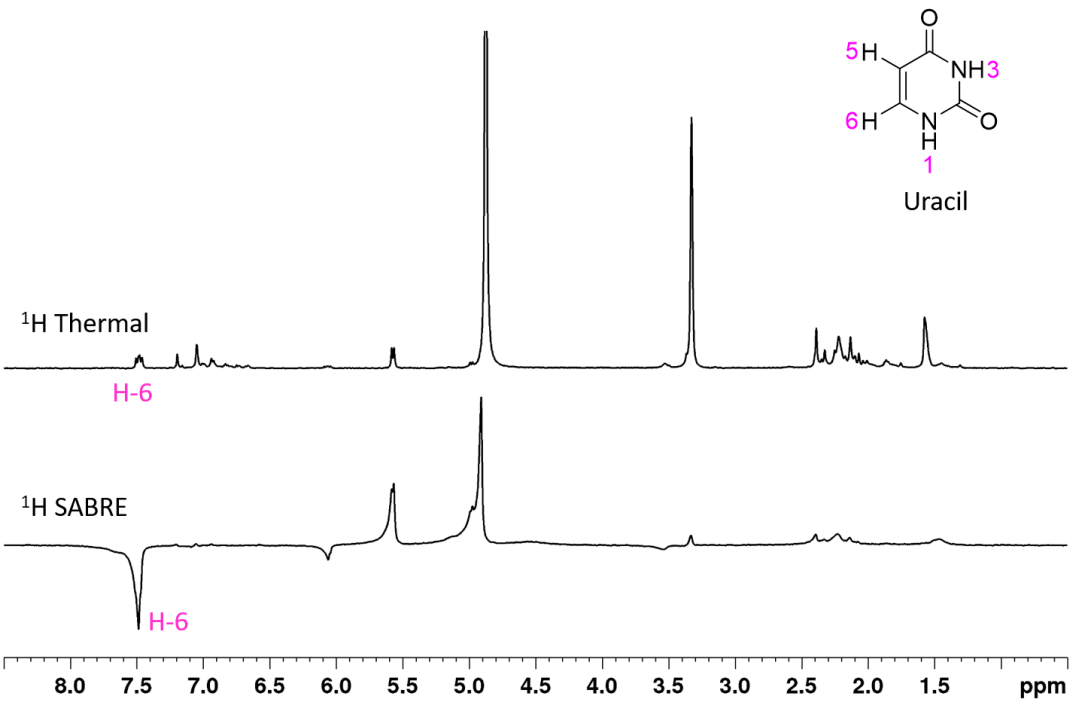

Figure 5.4 – ^{1}H NMR spectra of unlabelled uracil (20 mM) with [IrCl(COD)(IMes)] (5 mM) and Cs_2CO_3 (10 mM) in methanol-d_4 (0.6 mL). Bottom, 1 scan SABRE hyperpolarised spectrum after polarisation transfer at 60 G. The corresponding thermally equilibrated spectrum which was left in the NMR for two minutes prior to acquisition is shown above. No hydride ligand signals were observed in either NMR spectrum, consequently this region is omitted.

The use of a co-ligand to change the nature of the active SABRE catalyst has also been shown to result in an increase in polarisation transfer efficiency, into a range of materials.[168, 241, 242] This effect is most likely associated with changing the binding potential of weakly co-ordinating substrates thereby allowing the formation of the necessary catalytically active species. A sample containing [IrCl(COD)(IMes)] (5 mM), uracil (20 mM), Cs_2CO_3 (5 mM) and dimethylsulfoxide (DMSO, 20 mM) in methanol-d_4 (0.6 mL) was therefore prepared. After SABRE transfer, the observed ^{1}H NMR signal enhancement of the H-6 signal increased to 28-fold. However, when the ^{13}C nucleus was probed no polarisation was detected.

5.3 Polarisation uracil *via* SABRE-Relay using NH_3

Disappointingly, uracil gave very low ^{1}H NMR signal enhancements under SABRE conditions and, this approach would therefore be unsuitable as a method for monitoring its biological role. Therefore, SABRE-Relay was tested. As described in Chapter 4.2, SABRE-Relay utilises an

$[Ir(H)_2(IMes)(amine)_3]Cl$ type catalyst and it is the amine, rather than the substrate of interest, which is bound to the catalyst.[168, 241, 242] Polarisation from *p*-H_2 is transferred to the protons of the amine by SABRE before it disassociates from the catalyst. The now hyperpolarised protons of the amine are then able to exchange with labile protons of the target substrate. Thus, the substrate becomes polarised without binding directly to the catalyst. As uracil contains a weakly bound imide proton, we proposed SABRE-Relay might be effective in improving ^{1}H NMR signal enhancements and delivering a hyperpolarised ^{13}C NMR signal.

The solvent in which the SABRE-Relay method is performed needs to be free of exchangeable protons in order to prevent spin dilution.[168, 169, 241, 242] Thus, the most commonly used solvent for SABRE-Relay is dichloromethane-d_2 (DCM-d_2), however, it proved unable to solubilise uracil at the concentrations required. After a brief solvent screening process, 200 μL of dimethylformamide (DMF), a highly polar, aprotic solvent, was found to promote dissolution of the necessary amount of uracil in the reaction medium. Therefore, [IrCl(COD)(IMes)] (5 mM) was dissolved in 0.4 mL DCM-d_2 prior to the addition of NH_3 (25 mM). After the addition of 4 bar of hydrogen gas, NMR measurement confirmed that the active catalyst was formed. Subsequently, uracil (20 mM of total volume) was then dissolved in 0.2 mL of DMF and this mixture added to the solution that contained the active catalyst inside a glovebox.[169] The resulting sample was then degassed and exposed to 4 bar *p*-H_2 at 65 G, prior to being analysed by NMR spectroscopy. Figure 5.5 shows the resulting ^{1}H NMR spectrum. Unfortunately, no ^{1}H signal NMR enhancement was observed for uracil; however, a PHIP enhanced hydride resonance is evident in this spectrum at δ −23.8, which confirmed that a SABRE active catalyst formed.[168, 169, 241, 242]

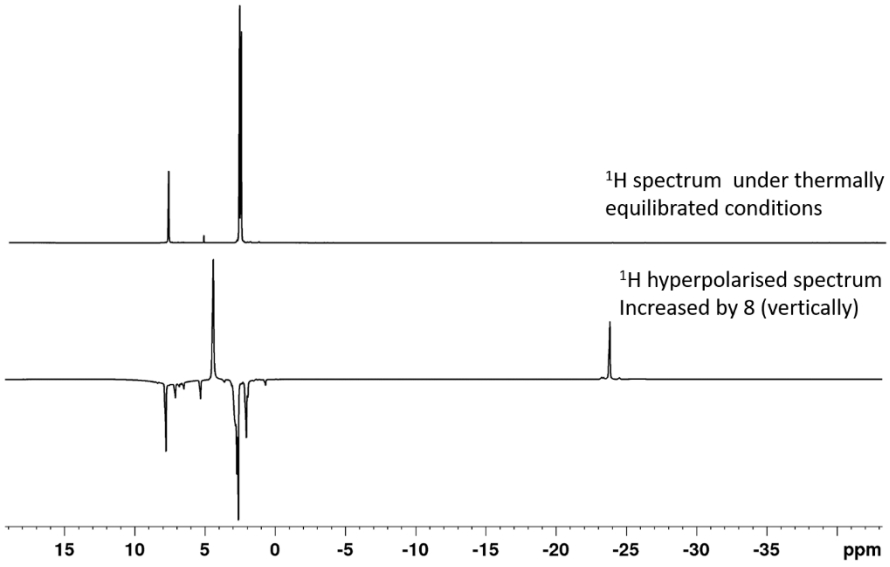

Figure 5.5 – ^{1}H spectra of uracil (20 mM) in 0.2 mL DMF with [IrCl(COD)(IMes)] (5 mM) pre-catalyst and NH_3 (25 mM) in 0.4 mL DCM-d_2. Top, a 1 scan ^{13}C thermally equilibrated NMR spectrum which was left in the NMR spectrometer for two minutes prior to acquisition. Bottom, 1 scan SABRE-Relay hyperpolarised NMR spectrum after polarisation transfer at 60 G. The hyperpolarised spectrum has been increased (vertically) by 8 times relative to the thermal spectrum.

In contrast, when a ^{13}C SABRE-Relay NMR experiment was performed on the same sample hyperpolarised signals were readily detected as shown in Figure 5.6. This result is all the more remarkable when considering that uracil is present at natural isotopic abundance. The hyperpolarised signal at δ 151.7 can be attributed to the carbon at position 2 of uracil by comparison with the literature.[311] This process could be repeated, and the resulting hyperpolarised ^{13}C NMR spectra proved to reflect an average signal enhancement of 223 ± 54-fold. Additionally, two enhanced quartets are observed at δ 35.69 and δ 30.64 in these spectra which can be attributed to the inequivalent methyl groups in DMF that result from slow C-N bond rotation. These signals appear as a consequence of the large volumes of DMF present in solution. They too show weak SABRE, indicating that DMF can itself be hyperpolarised through this process.

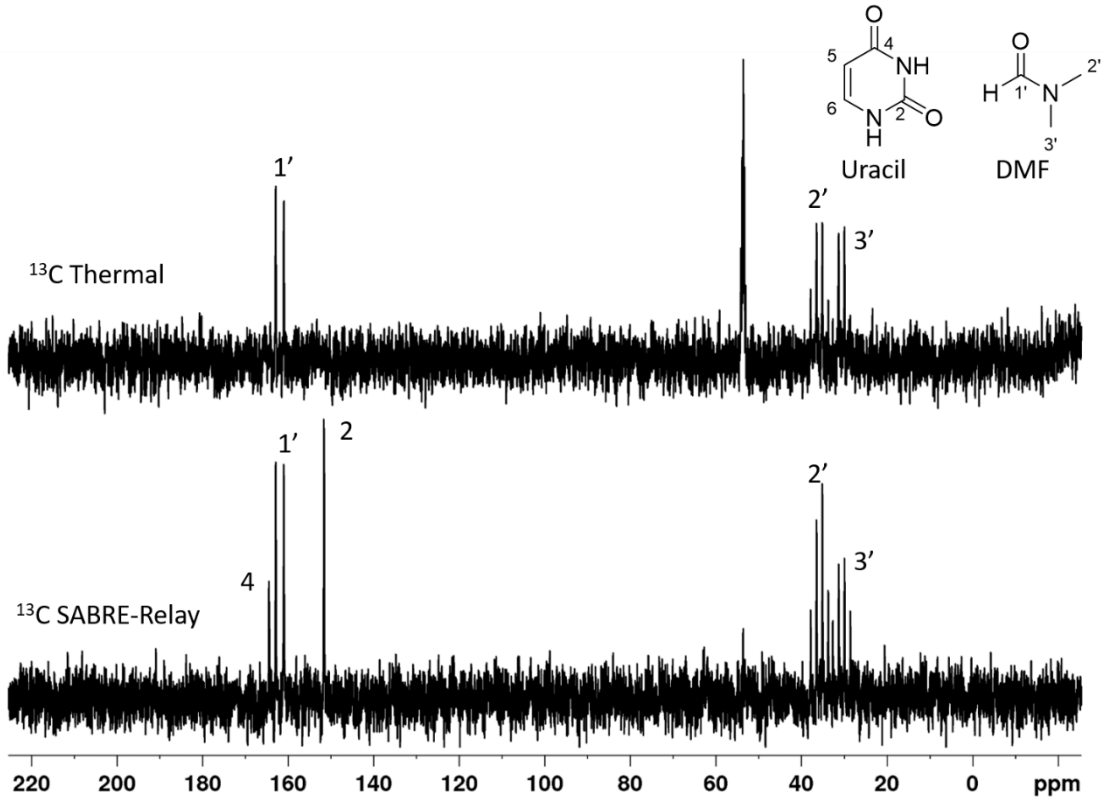

Figure 5.6 – ^{13}C NMR spectra of uracil (20 mM) in 0.2 mL DMF with [IrCl(COD)(IMes)] (5 mM) and NH_3 (25 mM) in 0.4 mL DCM-d_2. Top, 1 scan ^{13}C thermally equilibrated NMR spectrum which was left in the NMR for two minutes prior to acquisition. Bottom, 1 scan SABRE-Relay hyperpolarised NMR spectrum after polarisation transfer at 60 G. Signal assignments are as shown in the inset structures.

The ^{15}N detection of the SABRE-Relay hyperpolarisation was also observed as demonstrated in Figure 5.7, peak assignments were made by comparison to literature data.[312] There are two signals present at δ 158.3 and δ 129.9 with signal enhancements of 6.5 ± 3.3 and 12.8 ± 3.8-fold respectively when compared to a high concentration standard.[313] Whilst the NMR signal gains are low, it is important to note that no ^{15}N signal was observed in a thermally equilibrated NMR spectrum of uracil at a concentration of 20 mM under the same acquisition conditions. Additionally, these results provide a suitable starting point for further studies which will now be presented.

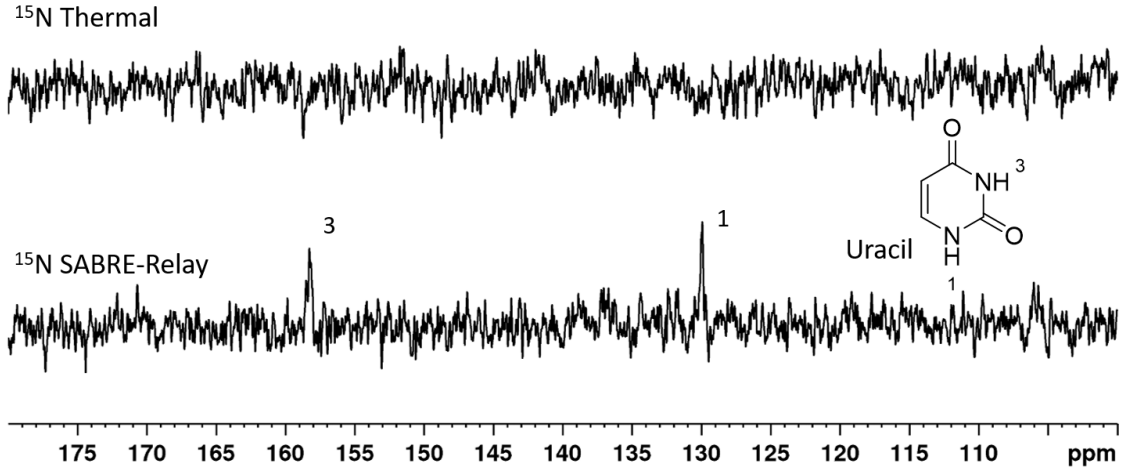

Figure 5.7 – ^{15}N NMR spectra of uracil (20 mM) in 0.2 mL DMF with [IrCl(COD)(IMes)] (5mM) and NH_3 (25 mM) in 0.4 mL DCM-d_2. Top, 1 scan ^{15}N thermally equilibrated NMR spectrum which was left in the NMR for two minutes prior to acquisition. Bottom, 1 scan SABRE-Relay hyperpolarised NMR spectrum after polarisation transfer at 60 G. Inset is the structure of uracil and corresponding peak assignments.

5.3.1 Examination of SABRE-Relay with 2-^{13}C-uracil

Based on the success of SABRE-Relay with the unlabelled substrate, 2-^{13}C-uracil was investigated under SABRE-Relay conditions with the hope that an improved ^{13}C NMR signal would now result. These samples contained different carrier amines. First, a solution of 2-^{13}C-uracil (1.36 mg, 60 mM) in 0.2 mL DMF was added to a solution containing [IrCl(COD)(IMes)] (5 mM) and NH_3 (40 mM) in 0.4 mL DCM-d_2. Second, a solution of 2-^{13}C-uracil (1.36 mg, 60 mM) in 0.2 mL DMF was added to a solution containing [Ir(Cl(COD)(IMes)] (5 mM) benzylamine-d_7 (25 mM) in 0.4 mL DCM-d_2.

After SABRE-Relay polarisation transfer at 60 G, the resulting signal enhancements were quantified (Table 5.1). Whilst there were no improvements observed in the ^{1}H NMR spectrum for either sample, significant signal gains were found in the ^{13}C NMR spectra with both samples showing over a 100-fold signal enhancement when compared to the corresponding thermal signal. It is hypothesised that the greater signal gains observed on ^{13}C compared to ^{1}H is due to the longer T_1 relaxation times of ^{13}C compared to ^{1}H.[34] Therefore, there is an increase time for the polarisation to accumulate on ^{13}C during the SABRE-Relay process. In contrast, relaxation effects dominate for ^{1}H.

Table 5.1 – Average NMR signal enhancements for ^{1}H and ^{13}C nuclei with 2-^{13}C- uracil (20 mM) dissolved in 0.3 mL DMF with [IrCl(COD)(IMes)] (5 mM) in DCM-d_2 (0.3 mL). The carrier is identified, along with its concentration.

Sample number	Carrier and amount	Average ^{13}C enhancement
1	NH_3 (35 mM)	171 ± 14
2	$BnNH_2$-d_7 (25 mM)	125 ± 13

5.3.2 Examination of SABRE-Relay with 2-^{13}C,^{15}N-uracil

A sample containing 2-^{13}C,$^{15}N_2$-uracil (20 mM) dissolved in 0.2 mL DMF-H_7 with [IrCl(COD)(IMes)] (5 mM) and benzylamine-d_7 (25 mM) in 0.4 mL DCM-d_2 was then examined. As seen for 2-^{13}C-uracil, the proton NMR spectrum is not enhanced. However, the signal enhancement for ^{13}C is now 129-fold and therefore comparable to those achieved with 2-^{13}C uracil. Thus, it is concluded that that isotopic labelling of the nitrogen does not change the ^{13}C signal enhancement. This is similar to the effect observed with ^{13}C-urea and ^{13}C,$^{15}N_2$-urea after hyperpolarisation with d-DNP.[314] In this report, ^{13}C-urea gave 19 ± 5% polarisation and ^{13}C,$^{15}N_2$-urea gave 22 ± 2% polarisation.[314]

In contrast, the ^{15}N NMR signal seen for uracil is greatly improved when an isotopically labelled substrate is used. Figure 5.8 shows the ^{15}N NMR spectra of 2-^{13}C,$^{15}N_2$-uracil after SABRE-Relay hyperpolarisation transfer at 60 G under 4 bar *p*-H_2 and the corresponding thermally equilibrated spectra. By comparison to a reference sample at high concentration,[313] the ^{15}N signal enhancement could now be calculated, and proved to be 610 ± 29 and 840 ± 35-fold for the N1 and N3 positions respectively. This signal reflects a dramatic improvement when compared to that for the sample that contained uracil with ^{15}N at natural isotopic abundance.

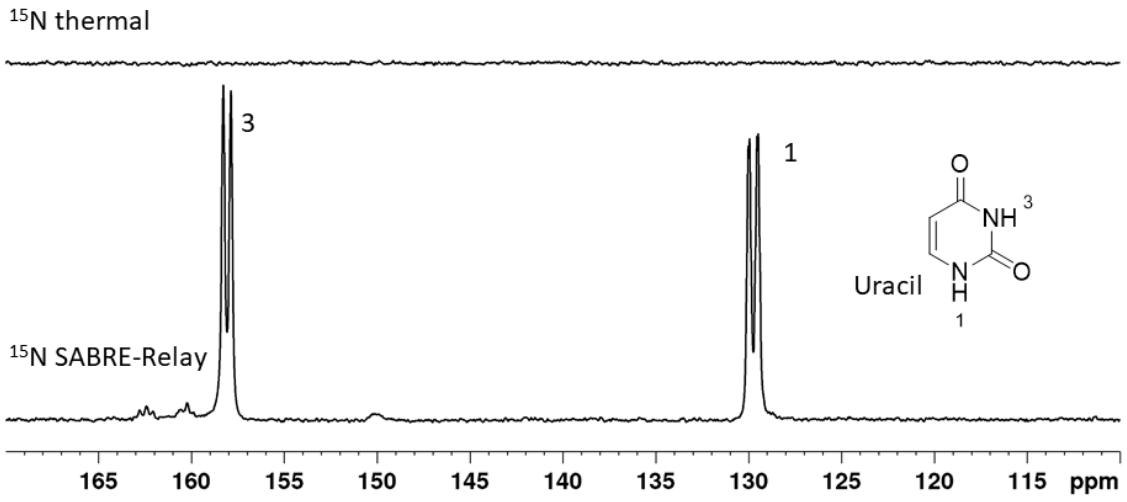

Figure 5.8 – ^{15}N NMR spectra of the signal response when 2-^{13}C,^{15}N$_2$-uracil (20 mM) in 0.2 mL of DMF with benzylamine-d_7 (25 mM) and [IrCl(COD)(IMes)] (5 mM) in 0.4 mL of DCM-d_2 is examined. Top, the thermally equilibrated ^{15}N NMR spectrum. Bottom, the SABRE-Relay hyperpolarised ^{15}N NMR spectrum after polarisation transfer at 60 G.

In summary, the SABRE-Relay hyperpolarisation of 2-^{13}C,^{15}N$_2$-uracil gave strong signal enhancements in both the ^{13}C and ^{15}N NMR spectra after polarisation transfer at 60 G. Whilst the signal gains for ^{13}C are similar to that seen for 2-^{13}C-uracil, the ^{15}N signal enhancement are significantly improved when compared to the unenriched samples. Previous studies using SABRE to achieve ^{13}C hyperpolarisation have suggested that the presence of ^{14}N leads to quadrupolar relaxation and correspondingly low ^{13}C gains.[313] There is no evidence for such an effect here.

5.3.3 Analysis of the T_1 relaxation values of ^{13}C and ^{15}N in ^{13}C-uracil and 2-^{13}C,^{15}N$_2$-uracil

Longitudinal relaxation (T_1) data was collected for the two labelled uracil molecules, ^{13}C-uracil and 2-^{13}C,^{15}N$_2$-uracil. In Chapter 2 and 3, the inversion recovery method was used to find the T_1 data of protons. However, trying to ascertain the T_1 data of carbon and nitrogen though this method is very time consuming. Despite the compounds studied here being labelled, the ^{13}C and ^{15}N signal to noise is low and therefore long time periods would be needed to acquire accurate data. Therefore, both 2-^{13}C-uracil and 2-^{13}C,^{15}N$_2$-uracil were examined by a hyperpolarised single shot T_1 method.[6] This method uses the large signals gained through hyperpolarisation and exploits them to ascertain the T_1 of the nuclei within the substrate. There are two methods to calculate the

T_1 when using a hyperpolarised T_1 sequence. First, a constant flip angle (cfa) can be employed and is often used in DNP where polarisation levels are very high[32] and T_1 times are very long.[315] More recently, Semenova *et. al.* demonstrated the use of a variable flip angle (vfa) when using SABRE to hyperpolarise the substrate and subsequently was able to calculate the T_1.[6] In the vfa method, a series of 15 experiments are conducted with increasing flip angle for each one which are calculated to excite the same fraction of available magnetisation each time. Therefore, a near complete loss of magnetisation should be achieved in the final spectrum. An FID is collected for each experiment, just like with previous methods, and the integrals are then fitted to an exponential decay to give the constant, T_1. Due to the use of *r. f.* pulses within this method, the pulse for each substrate and nuclei of interest needs to be calibrated, see experimental 7.2.11.3 for flip angle calculations.

For the measurements with uracil, we chose to use the vfa method due to lower starting polarisation levels than that which would be compatible with the cfa method. The T_1 values determined for 2-^{13}C-uracil and 2-^{13}C,$^{15}N_2$-uracil are presented in Table 5.2. These T_1 values are promising as they are comparable to the 14 seconds associated with the successful *in-vivo* detection of ^{13}C nicotinamide. This image was obtained within the group *via* DNP and is shown below in Figure 5.9.

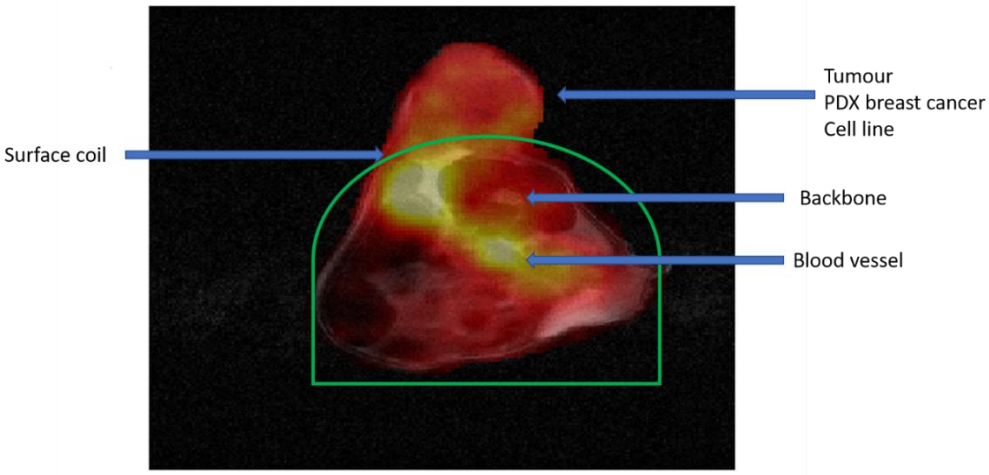

Figure 5.9 – Hyperpolarised ^{13}C-nicotinamide CSI of the abdomen of a mouse with a PDX breast cell line tumour. A 32*32 interpolated 128*128 overlaid on a ^{1}H MRI scan. White/yellow colour shows the areas with the greatest hyperpolarised signal.

Table 5.2 – ^{13}C and ^{15}N T_1 data for the carbon in the 2 position of uracil and both nitrogens using either ^{13}C-uracil (20 mM) or ^{13}C,$^{15}N_2$-uracil (20 mM) dissolved in 0.2 mL of DMF in the presence of [IrCl(COD)(IMes)] (5 mM), using NH_3 (45 mM) as the amine carrier in DCM-d_2 (0.4 mL) at 298 K with 4 bar of hydrogen. These values are determined at 9.4 T.

Compound	Average T_1 (s)		
Nuclei	2-^{13}C	1-^{15}N	3-^{15}N
2-^{13}C-uracil	15.02 ± 0.50	-	-
2-^{13}C,$^{15}N_2$-uracil	18.96 ± 0.84	10.23 ± 0.68	9.53 ± 0.57

5.4 Polarisation of fluorouracil with SABRE-Relay

With the success of uracil with SABRE-Relay, 5-fluorouracil was investigated under analogous conditions. Whilst 5-fluorouracil showed enhanced signals for both ^{1}H and ^{19}F under SABRE conditions, degradation of the catalyst meant that these signals decreased immediately after the first experiment. It was hoped that with SABRE-Relay degradation of catalyst may not occur.

A sample was prepared using 5-fluorouracil (20 mM) in 0.3 mL DMF. This was added to a prepared sample of [IrCl(COD)(IMes)] (5 mM) and benzylamine-d_7 (25 mM) in 0.4 mL DCM-d_2 which had already been exposed to 4 bar p-H_2. SABRE-Relay experiments were carried out at 60 G using a handheld shaker.[169] The resulting ^{13}C NMR spectrum is shown in Figure 5.10. The

signal for the carbon at the 2 position showed an enhancement of 47 ± 8-fold when compared to the spectrum recorded under Boltzmann equilibrium. The signal enhancement is lower than that obtained with non-labelled uracil, where a signal enhancement of 223-fold was observed with NH_3 as the carrier.

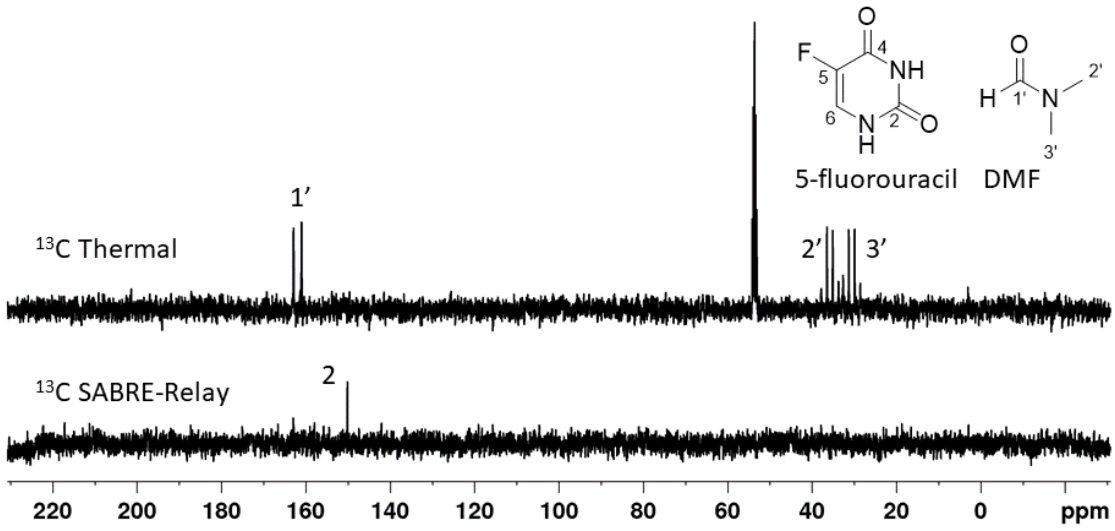

Figure 5.10 – ^{13}C NMR spectrum of the signal response when 5-fluorouracil (20 mM) in 0.2 mL of DMF with benzylamine-d_7 (25 mM) and [IrCl(COD)(IMes)] (5 mM) in 0.4 mL DCM-d_2. Top, thermally equilibrated (which was left in the NMR for two minutes prior to acquisition) ^{13}C NMR spectrum. Bottom, SABRE-Relay hyperpolarised ^{13}C NMR spectrum after polarisation transfer at 60 G.

Pleasingly, the SABRE-Relay derived ^{19}F NMR signal gains were improved when compared to that achieved by direct SABRE transfer as reported in Chapter 3. Examination of the resulting ^{19}F NMR spectrum showed a 23 ± 5-fold signal enhancements after SABRE-Relay hyperpolarisation at 60 G (Figure 5.11). This is compared to a 0.85 ± 0.53 signal gain achieved by SABRE. Additionally, there is no observable degradation of the catalyst and therefore the sample can be re-examined over a period of hours. In contrast, the SABRE experiment was unable to transfer polarisation after 10-15 minutes.

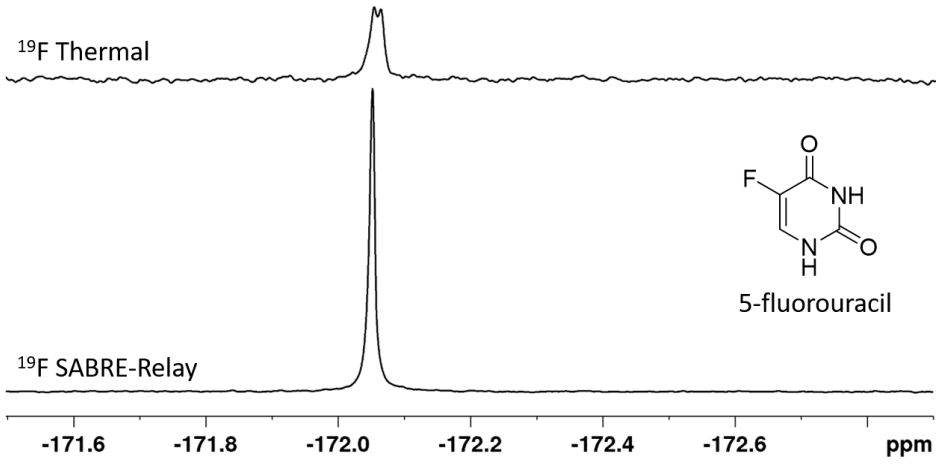

Figure 5.11 – ^{19}F NMR spectra 5-fluorouracil (20 mM) in 0.3 mL DMF-d_7 with [IrCl(COD)(IMes)] (5 mM) and benzylamine-d_7 (25 mM) in 0.4 mL DCM-d_2. Top, 1 scan thermally equilibrated spectrum which was left in the NMR for two minutes prior to acquisition. Bottom, 1 scan SABRE-Relay hyperpolarised spectrum after polarisation transfer at 60 G. Inset structure of 5-fluorouracil.

As benzylamine-d_7 had shown to give good ^{19}F signal enhancements, it was proposed that using NH_3 as the carrier amine may lead to further improvements.[168, 241, 242] Therefore, an analogous sample containing 9 equivalents (45 mM) of NH_3 was prepared using DMF-d_7 as the co-solvent and exposure to 4 bar p-H_2 under SABRE-Relay conditions. The resulting ^{19}F NMR spectrum showed an improved 84 ± 13-fold signal gain. Additionally, this sample also produced good ^{13}C signal gains and a 140 ± 13-fold signal enhancement was quantified for carbon in position 2. When applying a ^{1}H decoupled ^{13}C sequence, this signal gain improved to 241 ± 4-fold and increased further to 416 ± 68-fold when a ^{1}H-^{13}C INEPT sequence was employed. The carbon signals observed here are all greater than that observed with uracil which gave a maximum signal enhancement of 223-fold ± 54 under analogous conditions. Reducing the concentration of NH_3 from 45 mM to 35 mM did not further improve the signal enhancement which is contradictory to that previously reported in the literature.[242] This could be further investigated in future to determine the optimal carrier concentration.

Pleasingly, the SABRE-Relay conditions that have been developed here result in significant improvements to the ^{19}F signal enhancements that were observed under direct SABRE.

5.5 Conclusions

The hyperpolarisation of uracil at natural isotopic abundance was examined using SABRE and SABRE-Relay conditions. The signal gains when using SABRE were just 9-fold for ^{1}H, however, adding a DMSO co-ligand produced a hyperpolarised response of 28-fold. Neither of these methods produced a hyperpolarised response in the ^{13}C or ^{15}N NMR spectra. When moving to the SABRE-Relay method, no ^{1}H hyperpolarised signal was observed but hyperpolarised signals were obtained for both ^{13}C and ^{15}N nuclei. This is a consequence of the short ^{1}H T_1 and reflective of the challenges associated with creating hyperpolarisation outside the detection device. The longer ^{13}C T_1 values enabled signal enhancements of 223 ± 54-fold to be quantified in the ^{13}C NMR spectrum and 1.6 and 3.4 for N-1 and N-3 respectively in the ^{15}N spectrum when using NH_3 as the carrier amine. The effect of the carrier amine was examined and benzylamine-d_7 was also found to be successful for ^{13}C polarisation transfer with a 111 ± 3-fold signal enhancement now being quantified. The reduction in polarisation level observed between benzylamine-d_7 and NH_3 has been seen previously with alcohols and proposed to relate to the more efficient NH polarisation levels achieved prior to the relayed transfer step.[168, 242]

When examining the isotopically labelled 2-^{13}C-uracil under analogous SABRE-Relay conditions a similar level of signal enhancement for ^{13}C was observed at 171 ± 1-fold with NH_3 as the carrier amine. It can be seen that the error in the measurement is now much lower as a consequence of the improved SNR values achieved in the associated NMR spectra. Switching to benzylamine-d_7 caused a reduction in the level of ^{13}C NMR signal enhancements to 125 ± 13-fold. No ^{15}N NMR hyperpolarised signal could however be detected for 2-^{13}C uracil. This probably is a spin dilution effect that is a consequence of the change from ^{12}C to ^{13}C.[34, 316]

2-^{13}C,$^{15}N_2$-Uracil was also examined with NH_3. Now both ^{13}C and ^{15}N nuclei could be detected with the enhanced signals showing gains of 155 ± 9-fold for ^{13}C and 295 and 291-fold for N1 and N3 respectively. The reduced ^{13}C signal gain could be a link to increased spin dilution within the molecule. Pleasingly, a strong signal was now obtained in the corresponding ^{15}N NMR spectrum which means with further optimisation it should be possible to monitor biological processes with ^{15}N magnetic resonance techniques.

The blockbuster anti-cancer drug, 5-fluorouracil, was also examined *via* SABRE-Relay. Examination of the ^{13}C NMR spectrum after SABRE-Relay polarisation allowed a signal enhancement of 47 ± 8-fold to be quantified with benzylamine-d_7 as the carrier amine. This was further improved to 140 ± 13-fold when using NH_3 as the amine carrier. When using a ^{1}H-^{13}C INEPT sequence, this signal gain improved to 416 ± 68-fold for the ^{13}C of 5-fluorouracil. ^{19}F NMR detection of 5-fluorouracil gave an initial signal enhancement of 23 ± 5 prior to further optimisation. This level is greater than that achieved *via* SABRE where a 0.85 ± 0.53-fold enhancement is obtained (*c.f.* Chapter 3.2). When changing to NH_3, the ^{19}F signal enhancement increased to 84 ± 13-fold. Unfortunately, no signal was observed in the ^{15}N NMR spectrum after SABRE-Relay transfer, although this situation should change if a labelled precursor could be sourced. It should however be remembered that adding in ^{19}F will increase the level of spin dilation relative to uracil and provide a route to relaxation. However, the SABRE-Relay method, in contrast to the SABRE method, now leads to no observable catalyst deactivation and therefore the sample can be re-hyperpolarised multiple times over a number of hours.

Whilst the use of NH_3 as the carrier amine for the SABRE-Relay process gave higher signal enhancements, as a reactant it is problematic to work with due to it being a gas at room temperature. Consequently, it is difficult to add reproducible concentrations of it to the sample and there are additional safety implications. For optimisation purposes, benzylamine-d_7 is more favourable as it is a liquid at room temperature and consequently it is easier to add a specific concentration to a sample. Thus, using this amine carrier is advantageous for reproducibility despite the associated decrease in signal enhancement.

Due to the insolubility of uracil and 5-fluorouracil in DCM-d_2, it was necessary to add a co-solvent to dissolve it. After screening a variety of solvents, DMF was found to be able to solubilise the desired amount of substrate and also did not interfere in the SABRE-Relay process. However, it is worth noting that DMF would be unsuitable for use in biological systems and therefore, eliminating its use would be beneficial in the future. Attempts to use H_2O/D_2O as alternative co-

solvents did not yield any polarisation transfer under SABRE-Relay conditions which is due to the hyperpolarised proton carrier spin dilution this addition causes.[169, 242]

The results presented in this chapter have therefore demonstrated the viability of SABRE-Relay as a tool to hyperpolarise molecules which may not be compatible for hyperpolarisation *via* traditional SABRE. They also indicate the promise of the SABRE-Relay method with 5-fluorouracil and significantly improved signal gains were achieved compared with the SABRE method. Interestingly, uracil and 5-fluorouracil gave different signal gains under SABRE-Relay despite their similar structure. With uracil, a hyperpolarised signal was observed for both ^{13}C and ^{15}N nuclei. With 5-fluorouracil, there was no observable ^{15}N signal and the ^{13}C signals achieved were less than that on the unlabelled uracil. The electronegativity of the fluorine may play a part in this and such effects could be investigated in the future.

Chapter 6: Conclusions and further work

The work presented in this thesis has demonstrated and optimised SABRE polarisation transfer to X-nuclei within an array of biologically relevant molecules. To accomplish this, a comprehensive set of experiments were conducted that included examining the polarisation transfer field (PTF), substrate concentration, catalyst concentration and catalyst type. Alongside this, other SABRE based techniques were also employed; including SABRE-Relay *via* proton exchange and the use of a co-ligand, to stabilise the SABRE catalyst and allow the binding of weakly ligating substrates. The success of these innovations was exemplified by the acquiring of both high resolution ^{1}H and X-nuclei phantom images at 9.4 T using a Bruker vertical bore magnet and a 3 T Siemens clinical scanner.

6.1 Pyrimidine

Pyrimidine was the starting motif for this thesis as it is the basis of many successful drug therapies, for example cidofir[183] and trimethoprim[184] and nucleobases uracil, cytosine and thymine.[43] The ^{1}H signal enhancement for pyrimidine after polarisation transfer under SABRE conditions was examined and optimised. NMR characterisation of the complexes formed was carried out which revealed that two complexes were forming in solution; $[Ir(H)_2(IMes)(pyrimidine)_3]$ was the major product and $[IrCl(H)_2(IMes)(pyrimidine)_2]$ was the minor. The importance of the minor species was shown when examining the rate of hydride loss. When using a rate of exchange model where only the *tris* complex was formed, the rate data did not converge. The rate of hydride loss from these complexes was determined when the minor *bis* complex was included. It was shown that the loss of the hydride ligands from $[Ir(H)_2(IMes)(pyrimidine)_3]$ (**A**) proceeds *via* the $[IrCl(H)_2(IMes)(pyrimidine)_2]$ (**B**) intermediate. The rate of conversion of **A** to **B** at 295 K is 2.5 s^{-1} and the conversion from **B** back to **A** was found to be slower at 17.1 s^{-1}. Barskiy *et al* reported an optimal ligand loss of 4.5 s^{-1},[110] which was achieved at 300 K (4.6 s^{-1}) for hydride loss from complex **B**. Therefore, optimal enhancements would be expected at this temperature, though this may be hard to maintain when shaking the sample either in the stray field of the magnet or using the hand haeld shaker. Examining the $\Delta G^{\ddagger 300}$ for both the conversion of **A** to **B**

and **B** to **A**, 68.2 ± 1 kJ mol^{-1} and 63.7 ± 1 kJ mol^{-1} respectively, it was clear that **A** was the dominant species as $\Delta G^{\ddagger 300}$ was greater for **A** to **B**. Unfortunately, the temperature range was too small to make any clear conclusions about $\Delta S^{\ddagger}$.

The ^{1}H signal enhancement for pyrimidine was optimised to be −542 ± 16, −584 ± 15 and −506 ± 13 for H-2, H-4 and 6 and H-5 respectively. This is lower than for pyridine which gives −2397, −1472 and −1629 for the hydrogens in the *ortho*, *meta* and *para* positions respectively.[111] The optimal pyrimidine concentration was found to be 50 mM which is higher than most other substrates.[111, 129] It was hypothesised that this was due to the multivalency of pyrimidine leading to the formation of iridium trimers at lower concentrations as previously demonstrated by Olaru *et. al.* with 5-(tributylstannyl)pyrimidine and 5-(trimethylsilyl)pyrimidine.[139]

The concentration of catalyst was also investigated and although larger ^{1}H signal enhancements were obtained at the lowest concentration of 0.5 mM, 2.5 mM provided a larger signal to noise ratio. The identity of the pre-catalyst was then examined and when the pre-catalyst [IrCl(COD)(1,3-bis(2,4,6-trimethylphenyl)-4,5-dimethylimidazol-2-ylidine)] (catalyst **4**) was utilised, the largest ^{1}H signal enhancement was yielded. For MRI studies, the optimal catalyst for SNR proved to be [IrCl(COD)(1,3-bis(4-*tert*-butyl)-2,6-dimethylphenyl)imidazol-2-ylidine)] (catalyst **2**). This could be due to increasing the substrate in concentration to 500 mM for the MRI experiments in order to increase the SNR. This concentration may prove to be detrimental to catalyst **4** but better for catalyst **2**. This work demonstrates the intricacies of the polarisation transfer *via* SABRE and each change, however small, needs to be fully evaluated.

Although a thorough investigation into the rate of hydride loss was carried out, investigations into the rate of substrate loss should be conducted in the future. EXSY experiments should also be carried out with the optimal catalyst for signal enhancement (catalyst **4**) and SNR for the MRI experiments (catalyst **2**) to determine their different effects on the SABRE process. The optimisation experiments conducted in this thesis for [IrCl(COD)(IMes)] should also be conducted for these catalysts with pyrimidine to not only achieve the highest ^{1}H signal enhancement in NMR experiments but also to gain the highest SNR for MRI experiments. In

order to move towards biological applications of the SABRE technique, investigations into using a different solvent or using the CASH-SABRE method would be worthwhile.[157] This would allow the removal of the iridium catalyst and to have the hyperpolarised substrate in a bio-compatible solvent then possible *in vivo* MR experiments could be conducted.

6.2 ^{19}F hyperpolarisation *via* SABRE

Seven fluorinated *N*-heterocyclic compounds containing either pyridine or pyrimidine motif were examined for SABRE hyperpolarisation of their ^{1}H and ^{19}F nuclei. Of these molecules, 2-fluoropyridine and 4-fluoropyridine did not exhibit SABRE. It was hypothesised that the minimal signal enhancement observed with 2-fluoropyridine was due to the highly electron withdrawing group near to the binding site of the catalyst which could hinder polarisation transfer due to electronic effects. 4-Fluoropyridine is an unstable molecule and is therefore only available as a salt. The presence of this salt, however, means that the nitrogen is unable to bind to the catalyst and therefore prevents SABRE from occurring. Attempts to prepare the free base proved unsuccessful. These two molecules were not investigated further. The other five molecules gave successful SABRE enhanced signals for both ^{1}H and ^{19}F nuclei. The most successful of these molecules was 3-fluoropyridine where ^{1}H signal enhancements of −1287 ± 65-fold, −535 ± 18-fold, −924 ± 38-fold and −817 ± 26-fold for H-2, 4, 5 and 6, respectively were achieved and the ^{19}F signal enhancement was 62 ± 6-fold. Comparing the ^{1}H enhancements with pyridine, these signals are between 1.8 and 3 times smaller than those of pyridine,[111] which may reveal subtle electronic effects within the SABRE process. When 5-fluorouracil was examined, both ^{1}H and ^{19}F hyperpolarised signals were observed. Unfortunately, upon refreshing *p*-H_2 and repeating the SABRE experiments, the enhancements reduced considerably. This was due to possible cyclometallation and subsequent deactivation of the catalyst.

The identity of the complexes formed with the fluorinated *N*-heterocyclic compounds and the SABRE pre-catalyst [IrCl(COD)(IMes)] was determined by multi-dimensional NMR spectroscopy. In these cases, two complexes were shown to form of type $[Ir(H)_2(sub)_3(IMes)]$ (**A**) and $[IrCl(H)_2(sub)_2(IMes)]$ (**B**) for all substrates except 5-fluoropyridine-3-carboxylic acid in the

presence of Cs_2CO_3, where only catalyst **A** was formed. Both the loss of substrate and the loss of hydride were examined.

For the substrates 3,5-difluorpyridine, 2-fluoropyrazine and 5-fluoropyridine-3-carboxylic acid without base the data collected could not be fitted. Unfortunately, there was overlap between the ligand and free substrate resonances and as such no suitable kinetic solution could be found for ligand loss. However, for 3-fluoropyridine and 5-fluoropyridine-3-carboxylic acid in the presence of Cs_2CO_3 where 88% and 100%, respectively, of complex **A** was formed the rate of ligand loss could be fitted. At 280 K these were calculated to be 2.04 ± 0.001 s^{-1} and 0.57 ± 0.002 s^{-1} respectively, which is not the reported optimal exchange rate of 4.5 s^{-1} as reported by Barskiy *et al* and may therefore go someway to explain why the enhancements observed for these substrates are not as high as those for pyridine.[111] For pyridine at 300 K the rate of ligand loss in the presence of [IrCl(COD)(IMes)] is 23 s^{-1}.[111] Activation parameters for ligand loss for 3-fluoropyridine is found to be $\Delta H^{\ddagger}_{(Ligand)}$ 99 ± 3 kJ mol^{-1} and $\Delta S^{\ddagger}_{(Ligand)}$ is 122 ± 10 J mol^{-1} K^{-1}, for 5-fluoropyridine-3-carboxylic acid in the presence of base $\Delta H^{\ddagger}_{(Ligand)}$ for loss of is 96 ± 6 kJ mol^{-1} and $\Delta S^{\ddagger}_{(Ligand)}$ is 101 ± 22 J mol^{-1} K^{-1}. Comparing this to pyridine where $\Delta H^{\ddagger}_{(Ligand)}$ 95 ± 1 kJ mol^{-1} and $\Delta S^{\ddagger}_{(Ligand)}$ is 96 ± 2 J mol^{-1} K^{-1}. For all of these substrates $\Delta S^{\ddagger}_{(Ligand)}$ is large and positive and therefore the reaction is dissociative. The associated Gibbs free energy to ligand loss at 300 K is 63 ± 1 kJ mol^{-1} for 3-fluoropyridine and for 5-fluoropyridine-3-carboxylic acid in the presence of base this increases slightly to 66 ± 1 kJ mol^{-1} which is the same as that for pyridine (66 ± 1 kJ mol^{-1}).[111]

Examination of hydride loss could be completed with the substrates 3-fluoropyridine, 3,5-difluorpyridine and 2-fluoropyrazine. However, the mechanism of hydride exchange for complexes of type **A**, where complex **B** was present, were found to go *via* catalyst **B**. This could be modelled computationally to give strong correlation to the experimental data. Therefore, examination of the rate of hydride loss at 265 K with 3-fluoropyridine was 0.37 s^{-1} whereas with 3,5-difluoropyridine or fluoropyrazine it was 0.43 s^{-1} and 0.16 s^{-1} respectively. The analogous rate was 0.3 s^{-1}, which is between the previous substrates, when 5-fluoropyridine-3-carboxylic acid in the presence of Cs_2CO_3 was used, though the method of fitting this data did not include

catalyst **B**. Examining the rate of hydride loss for [Ir(H)$_2$(methanol)(pyridine)$_2$(IMes)] complex reported by Lloyd *et. al.* (2014), was 1.72 s^{-1} at 265 K. This reduction in catalyst lifetime when fluorinated *N*-heterocyclic compounds are present may explain why their ^{1}H signal enhancements are lower than those for pyridine (−1287 ± 65 for H-2 on 3-fluoropyridine,[219] −2397 for H-2 on pyridine[111]). When examining the exchange process for each step of the exchange mechanism, conversion of **A** to **B**, loss of H_2 from **B**, swopping of inequivalent hydrides within complex **B** and conversion of **B** to **A**. It is found that substrate loss from **B** is favoured and this happens first as the transition state barriers are lower for this step. After this hydride loss occurs from **B**. From the data obtained substrate loss from **A** is less favoursed than from **B**. Examining the activation parameters for hydride loss for substrates **2**, **4** and **5**, they were all found to be within error of each other and $\Delta S^{\ddagger}$ is large and positive, demonstrating this is still a dissociative pathway.

For 5-fluoropyridine-3-carboxylic acid without base the hydride region was not as clean as the other substrates. Several species are formed and the signals under examination are weak. This is probably due to the molecule being zwitterionic, many species are formed and make exchange data difficult to ascertain.

^{19}F phantom MR images were collected for all molecules which successfully hyperpolarised *via* SABRE, including 5-fluorouracil. However, if ^{19}F is to be used in clinic, the short T_1 needs to be overcome.

To further improve the ^{19}F signal enhancement gained here, direct SABRE experiments should be carried out using a hand-held magnet array,[106] with a field of 35 mG or mu-metal shield. This would allow for optimal polarisation to transfer from the *p*-H_2 derived hydrides to the ^{19}F nuclei. Unfortunately, two main barriers prevent this being used as an imaging agent, the short T_1 of ^{19}F and the solvent (methanol-d_4) used to demonstrate the signal enhancement here. Methods to remove the catalyst and use a different solvent system, as described in Chapter 1 section 1.3.4, could also be implemented here.

6.3 Hyperpolarisation of X-nuclei *via* SABRE-Relay

The SABRE-Relay method was used to successfully hyperpolarise ^{13}C, ^{15}N, ^{31}P and ^{19}F nuclei of urea, uracil, monosodium dihydrogen phosphate (MSP), adenosine triphosphate (ATP) or 5-fluorouracil. The greatest ^{13}C signal enhancements obtained for $^{13}C,^{15}N_2$-urea were 5117 ± 536-fold when using NH_3 as the amine carrier. This carrier also provided the greatest SNR for ^{15}N, which was 16. As a proof of concept, hyperpolarised ^{13}C phantom MR images were obtained for ^{13}C-urea using a 3 T Siemens clinical MR scanner. Thus, the potential for clinical based MR perfusion imaging using a SABRE-Relay hyperpolarised contrast agent has been demonstrated.

Uracil was one of the most successful substrates examined using the SABRE-Relay method and gave ^{13}C signal enhancements for unlabelled (223 ± 54-fold, with NH_3), ^{13}C labelled (171 ± 14, with NH_3) and ^{13}C and $^{15}N_2$ labelled uracil (129-fold). Also, the unlabelled and $^{13}C,^{15}N_2$-uracil molecules demonstrated hyperpolarised signals in the ^{15}N NMR spectra with signal gains of 6.5 ± 3.3 and 12.8 ± 3.8-fold and 610 ± 29 and 840 ± 35-fold respectively.

Hyperpolarised ^{31}P signals for both MSP and ATP were successfully recorded. MSP ^{31}P signal was optimised and with these conditions the greatest ^{31}P signal enhancement for MSP (40 mM) was recorded as 136 ± 2-fold (SNR of 49 ± 8), with NH_3 (15 mM) as the amine carrier. To increase this further, MSP should be dissolved in a 50:50 H_2O:D_2O mix which could reduce spin dilution and decrease relaxation.

Examination of the ^{13}C and ^{19}F hyperpolarised NMR response for 5-fluorouracil was also carried out by SABRE-Relay, where signal enhancements of 47 ± 8-fold and 23 ± 5-fold respectively were observed. Comparing the ^{19}F signal enhancement that was attained by using SABRE and SABRE-Relay, a 55 times improvement is seen with SABRE-Relay compared to that of SABRE. As well as this, when the SABRE-Relay samples that contained 5-fluorouracil were examined after a few hours of catalyst activation, ^{19}F signals were still observed. In contrast, the corresponding SABRE samples no longer exhibit a hyperpolarised response. It is postulated that cyclometallation of 5-fluorouracil with the iridium complex leads to deactivation of the active SABRE catalyst.

For all substrates NH_3, benzylamine-d_7 and or phenethylamine (PEA) were examined as carriers. Without exception, NH_3 provided the greatest signal enhancement for all X-nuclei examined. However, for optimisation purposes it is more straightforward to use a liquid amine as these are far easier to handle.

For substrates dissolved in H_2O or using a D_2O:H_2O mix, the ratio and volume should be optimised as water does reduce signal enhancement observed on the substrate of interest, regardless of which nuclei is being examined. An in depth study of the mechanism between the SABRE active catalyst and the amine has already been conducted.[242] It would therefore be advantageous to explore possible field cycling[317, 318] experiments as the polarisation transfer field (PTF) from the *p*-H_2 derived hydrides to the amine are unlikely to be the same as the PTF from the hyperpolarised ^{1}H nuclei to the X-nuclei of the substrate of interest. Examination of the exchange mechanism between the amine and the substrate was explored in collaboration with another group but proved too complex. Improvements in NMR exchange experiment techniques could be examined and used to investigate these exchange rates and mechanisms.

The ^{31}P substrate range could be widened to include other metal phosphates and possibly longer chain phosphate molecules. Optimisation of this and the ^{15}N signal observed in uracil should also be undertaken to improve upon the signal gains already achieved here. However, the insolubility of uracil and 5-fluorouracil meant that the co-solvent DMF was used along with DCM-d_2 which are both unsuitable for use in biological systems. However, the identification of intermediates in the drug development process could be identified using this method. Despite the similarity in structure, no ^{13}C or ^{15}N signal enhancements were seen for 5-fluorouracil. This could be due to the electronegativity of fluorine; therefore, this effect could also be investigated which may see further improvements in signal enhancement from other, similar molecules.

6.4 ^{13}C hyperpolarisation using SABRE with a co-ligand

Sodium oxalate was first examined under SABRE-Relay conditions which proved to be unsuccessful. In contrast, SABRE hyperpolarisation in the presence of a sulfoxide co-ligand led to a ^{13}C signal enhancement of 4112 ± 484-fold for sodium oxalate. This could be improved to

4907 ± 861-fold when using $[Ir(COD)(OC(CH_3)_2)(IMes)]PF_6$ as the SABRE pre-catalyst. The complex responsible for SABRE in this case could not be determined with only $[IrCl(H)_2(DMSO)_2(IMes)]$ being identified in the mixture. However, when crystals of the sample were grown and examined under X-ray crystallography this revealed an oxalate dimer, bridging two iridium centres with the structure, $[Ir_2(H)_4(DMSO)_2(IMes)_2(\mu\text{-oxalate})]$.

Examining the exchange rates of the $[IrCl(H)_2(DMSO)_2(IMes)]$ complex in both methanol-d_4 and DCM-d_2 at 263 K, it was found that the rate of hydride loss was 3.31 ± 0.26 s^{-1} and 1.16 ± 0.04 s^{-1} respectively. For the loss of DMSO, rates of 3.35 ± 0.01 s^{-1} and 1.56 ± 0.01 s^{-1} respectively were determined. These results show that the rates of loss for ligand and hydride are slower in the less polar solvent, DCM-d_2 which is likely to be due to better intermediate stabilisation in methanol-d_4

In both systems it was shown that it was more favourable to lose the DMSO ligand, than hydrogen and this is only slightly more favourable with methanol-d_4 than DCM-d_2 ($\Delta G^{\pm 300K}$ for DMSO is 57 ± 0.2 kJ mol^{-1} and 58 ± 0.1 kJ mol^{-1}, respectively). The energy barrier to hydrogen loss for the complex in methanol-d_4 is 58 ± 0.3 kJ mol^{-1} and for DCM-d_2 it is 60 ± 0.1 kJ mol^{-1}. These results show that the loss of DMSO is dissociative, as is the accepted SABRE mechanism.[119] When the identity of the sulfoxide was changed to methyl phenyl sulfoxide, the rate of sulfoxide loss increased to 21.48 s^{-1} in DCM-d_2 and 49.02 s^{-1} with the addition of methanol, demonstrating the the binding potential of the sulfoxide and the rate of exchange are linked.[165]

A more extensive study into the effect of the sulfoxide co-ligand could be carried out alongside optimising the catalyst and substrate concentrations. Further optimisation of temperature and pressure of *p*-H_2 effects should also be carried out to possibly improve the polarisation of sodium oxalate. It may also be advantageous to explore the exchange rate specifically as a function of substrate. It may also be worth investigating the addition of ligands to the SABRE catalyst to see if this displaces the bound oxalate and possibly help to control and manipulate this process.

Chapter 7: Experimental

7.1 Instrumentation

7.1.1 NMR spectrometers and solvents

All NMR data were collected on either a 400 MHz (9.4 T) or a 500 MHz (11.7 T) Bruker AVIII spectrometer. Resonant frequencies used were: ^{1}H 400.1 MHz (9.4 T) and 500.1 (11.7 T) MHz, ^{13}C 100.6 MHz (9.4 T) and 125.8 MHz (11.7 T), ^{15}N 50.7 MHz (9.4 T) and 40.56 MHz (11.7 T), ^{31}P 162.0 MHz (9.4 T) and ^{19}F 470.5 MHz (11.7 T). Bruker Topspin 3.6.2 was used for data acquisition, versions 3.6.2 and 4.0.8 were used for data processing. Chemical shifts are quoted in parts per million (ppm) with respect to the normal reference point for the residual solvent signal. The solvents used for NMR analysis were methanol-d_4 (residual signal, δ_{1H} 3.34, δ_{13C} 49.86) or dichloromethane-d_2 (residual signal, δ_{1H} 5.33, δ_{13C} 54.24) and they were purchased from Sigma. For characterisation purposes, multiplicities are described as either, singlet (s), doublet (d), triplet (t), quartet (q), multiplet (m) or broad (br). All *J*-coupling values are given in Hz.

7.1.2 Para-hydrogen Generator

The *para*-hydrogen (*p*-H_2) gas used in this research was supplied from a bespoke *p*-H_2 rig where H_2 gas was cooled to 28 K and passed over a paramagnetic catalyst (Fe_2O_3) to convert *ortho*-H_2 into *p*-H_2. The conversion of *ortho*-H_2 to *p*-H_2 has been experimentally confirmed to yield *p*-H_2 purity of > 99%.[103] For all experiments carried out in this thesis, the pressure of H_2(g) used was 4 bar absolute pressure. A pressure gauge (MKS Baratron®) indicates the pressure relative to ambient temperature and pressure, therefore 3-bar on this gauge corresponds to 4 bar absolute.

7.1.3 X-ray Crystallography

Preparation of the sodium oxalate dimer crystals involved the preparation of a sample containing sodium oxalate (25 mM), DMSO (20 mM) and [IrCl(COD)(IMes)] (5 mM) and H_2 in methanol-d_4 (0.6 mL) and 50 µL H_2O. It was left for 10 hrs to activate and the H_2 atmosphere then vented. Degassed hexane (~ 3 mL) was then layered over the methanol solution in the NMR tube. This

tube was then left under a N_2(g) atmosphere for several days. A suitable crystal was selected and mounted onto an Oxford Diffraction SuperNova X-ray diffractometer. During data collection, the crystal was kept at 110 K. "CrysAliasPro" was used for the control of the diffractometer, data collection, determination of the cell, frame integration and unit cell refinement.[319] Spherical harmonics was applied using the scale algorithm SCALE3 ABSPACK, this was to correct the face-indexed absorption. The structure was solved using the ShelXT[320] programme within the Olex2[321] package, this was refined using the ShelXL[322] programme using Least Squares minimisation. The crystal structures, presented in the thesis and Appendix, along with the crystallographic data has the solvent molecules and counterions have been omitted for clarity.

7.2 General experimental procedures

7.2.1 SABRE-Sample preparation

Unless otherwise stated, NMR SABRE samples were prepared with the pre-catalyst [IrCl(COD)(IMes)] (5 mM, where COD = *cis,cis*-1,5-cyclooctadiene and IMes = 1,3-bis(2,4,6-trimethyl-phenyl)imidazole-2-ylidene). The desired concentration of the substrate under investigation was then added, and the mixture was subsequently dissolved in 0.6 mL of a specified solvent (either methanol-d_4 or dichloromethane-d_2). Samples that were prepared for imaging or for use in the flow system used a larger 3 mL volume of solvent. For both NMR and MRI analysis, the sample was placed in a 5 mm or 10 mm NMR tube respectively, fitted with a J. Young's tap. The sample was then de-gassed using the freeze-pump-thaw method, three times. If using methanol-d_4 a dry ice / acetone bath was used, for dichloromethane-d_2 a liquid nitrogen bath was used.

7.2.2 SABRE-Relay sample preparation:

Unless otherwise stated NMR SABRE-Relay samples were prepared with the pre-catalyst [IrCl(COD)(IMes)] this was dissolved in 0.6 mL of dichloromethane-d_2. If the sample was for imaging, 3 mL of solvent was used. For both NMR and MRI analysis, the sample was placed in a 5 mm or 10 mm NMR tube respectively, fitted with a J. Young's tap. The sample was then de-gassed using the freeze-pump-thaw method, three times using a liquid nitrogen bath. The desired

concentration of the amine or ammonia gas was then added. Unless stated, the catalyst and amine were activated with 4 bar hydrogen gas. Upon complete activation, whereby the cyclooctadiene is hydrogenated to form cyclooctane (COA); observed at approximately δ 1.56 and a hydride signal between δ −20 to −30 is observed reflective of the formation of $[Ir(H)_2(IMes)(sub)_3]Cl$ (etc). The desired concentration of substrate dissolved in either DMF or a combination of H_2O and/or D_2O was then added, in a glovebox to this activated sample.

7.2.3 Catalyst preparation

The [IrCl(COD)(IMes)] was provided by Dr. V. Annis or Dr. P. Rayner.[118, 323] All other catalysts used were prepared by Dr. P. Rayner.[118]

7.2.4 Substrates

Substrates were purchased from Acros (3,5-difluoropyridine), Fluorochem (3-fluoropyridine, 5-fluoro-3-carboxylic acid, 5-fluorouracil), Fisher scientific (caesium carbonate), Chem Cruz ($^{13}C_2$-sodium oxalate), Fisons (sodium oxalate) and Sigma-Aldrich (pyrimidine, 2-fluoropyridine, 4-fluoropyridine.HCl, fluoropyrazine, ^{13}C-urea, $^{13}C,^{15}N_2$-urea, adenosine-5'-triphosphate disodium salt, uracil, 2-^{13}C-uracil, 2-$^{13}C,^{15}N_2$-uracil).

7.2.5 Handheld magnet array

A range of hand-held magnet arrays have been produced in-house.[106] These are based upon a Halbach design, using permanent magnets, and have magnetic field strengths within the range of 30 G to 140 G.

7.2.6 SABRE method

Unless otherwise stated, all samples were prepared as described in the **General experimental procedures** SABRE-Sample preparation or SABRE-Relay sample preparation sections (7.2.1 and 7.2.2 respectively). All samples were activated using 4 bar hydrogen gas. Upon addition of the substrate with the pre-catalyst in solution, the substrate replaces the chloride ion within the SABRE pre-catalyst, this is shown in Figure 7.1, step 1. Once the sample has been prepared, 4 bar (absolute) of hydrogen is added to the head space of the tube and shaken. With the addition of

hydrogen, the colour of the sample usually changes indicating that the catalyst is activated. However, this process is repeated a number of times, allowing the hydrogen in the head space of the NMR tube to dissolve in the sample; this causes the COD to be hydrogenated and removed from the catalyst, leaving the corresponding SABRE active form, as identified in this work.

For the active catalyst a hydride signal appears between δ −20 to −30 ppm, which is characteristic of the formation of the complex $[Ir(H)_2(IMes)(sub)_3]Cl$. This is checked by running a single scan NMR spectrum. If there are peaks seen around δ −10 and −17 ppm, then COD is still bound to the complex (see **C** in Figure 7.1), as this has characteristic hydrides *trans* to COD. The region between δ −22 and −30 ppm is also observed to ascertain whether or not the fully activated complex has been formed, hydrides in this region are associated with complex **D** also shown Figure 7.1. Fresh hydrogen is added until the catalyst is fully activated. Once activated the headspace was evacuated and replaced by *p*-H_2 (4 bar). The sample was then shaken for 10 seconds.

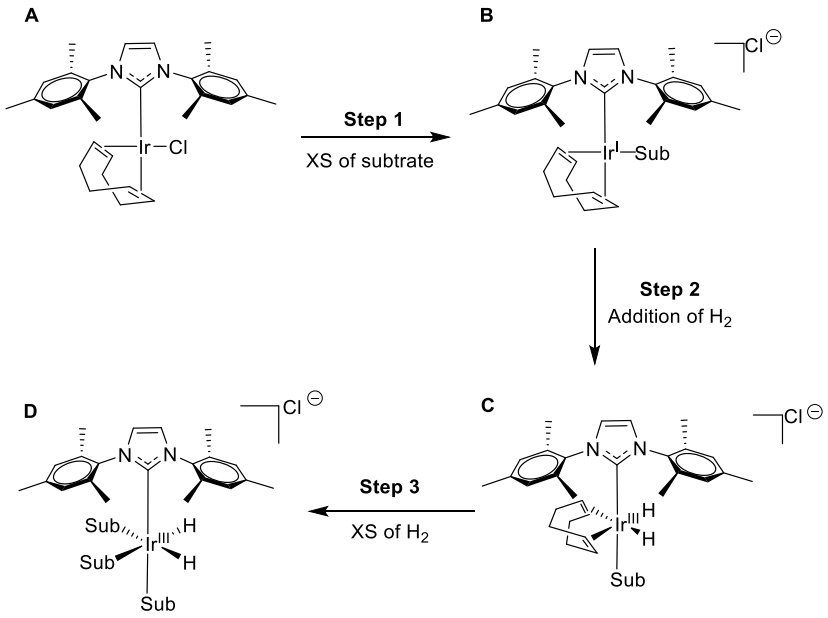

Figure 7.1 – Schematic of the activation mechanism of the SABRE pre-catalyst [IrCl(COD)(IMes)] with a substrate and excess hydrogen to form the SABRE active catalyst $[Ir(H)_2(IMes)(Sub)_3)]Cl$.

In order for the resonance conditions of the SABRE method to be met, samples were either shaken in the stray field of the Bruker 400 MHz spectrometer or in the field of a hand-held magnet array. To quantify the field a gaussmeter (GM08, Hirst Magnetic Instruments Ltd, ± 0.5%

reproducibility) was used. The shaker used here generates a magnetic field of 6.1 ± 0.3 mT (61 ± 3 G), which, for ^{1}H, is the optimal polarisation transfer field for most SABRE amenable substrates.[106] In the case of ^{15}N or ^{13}C where polarisation transfer fields of a few mG was required, a mu metal shield was employed.

The sample was then immediately placed into the NMR, where the receiver gain was set to 1, and a 90° single shot radio frequency (*r. f.*) pulse was applied and a free induction decay (FID) acquired.

In addition to hyperpolarised NMR spectra, a normal NMR spectrum is taken of the sample with hydrogen dissolved under Boltzmann conditions (thermal signal). This allows the net signal enhancement to be calculated (see section 7.2.9). This is known as the shake and drop method.

7.2.7 SABRE under automated flow

The signal enhancements achieved through the shake and drop method inherently contain sources of human error. These are due to parameter variations when shaking the sample, particularly if using the stray magnetic field, shaking time and the shake intensity of the user. The flow system circumvents the variation of all of these factors to generate more reproducible controlled results.[138]

The automated flow system was developed in collaboration with Bruker, it includes a polariser and a sample delivery system. To use the flow system, a larger 3 mL sample is prepared at the required concentration. *p*-H_2 can be bubbled through the sample at 4 bar (absolute) for a predetermined amount of time through a porous frit. This allows the sample to activate and the hyperpolarised signal to build up. The sample is subsequently transferred to the spectrometer using a pneumatic flow of nitrogen gas. Once inside the spectrometer the required pulse sequence is applied and a spectrum is obtained, the sample is then transferred back to the mixing chamber where fresh *p*-H_2 can be added to the sample, and the process can be repeated. The flow system is accurately controlled, and the triggers are incorporated into the Bruker pulse sequences directly so human error is completely removed. This allows the process to be easily repeated, a schematic of the flow system is shown in Figure 7.2.[138]

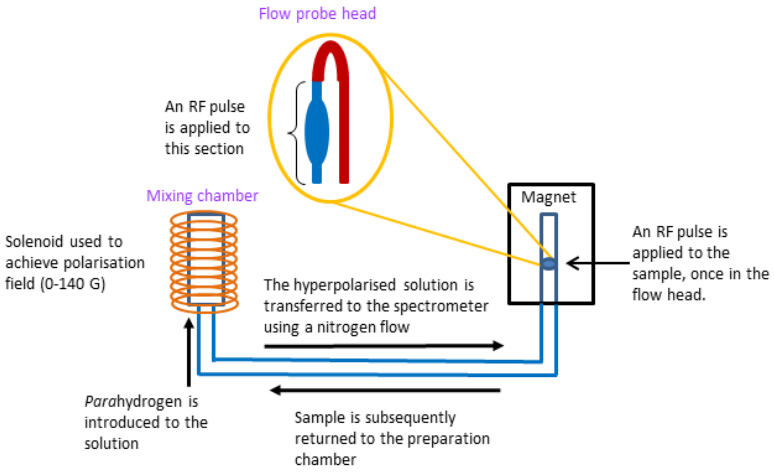

Figure 7.2 – Schematic of the flow system adapted from scheme 1 in reference 138. [138]

Although the results obtained from the flow system are more reproducible, the enhancements are consistently lower than those achieved by the corresponding shake and drop method. For example, the total ^{1}H NMR signal enhancement using the flow system for nicotinamide is 720-fold,[138] but under similar reagent conditions with manual shaking, this increases to 2167-fold,[129] over 3 times that of the flow system. This effect is most likely due to a combined effect of mixing with *p*-H_2 being less effective and longer transfer times as there is a 3 s outgassing step before transfer, allowing relaxation of the substrate before detection. However, the increased control of the flow system allows accurate measurement of the magnetic field dependency of the SABRE approach. This provides a route to ascertain the optimal polarisation transfer field to perform SABRE for any given substrate and therefore gaining the best enhancement when shaken, manually at this field. The sample chamber is placed inside a solenoid, which is used to deliver the small magnetic field required for SABRE, with a range of fields from 0 to 140 G.

For polarisation transfer field (PTF) optimisation experiments, the solenoid coil surrounding the mixing chamber can be changed, such that the magnetic field can be altered anywhere between −150 to 150 G. When using this system a sample, unless otherwise stated, was prepared with the pre-catalyst [IrCl(COD)(IMes)] (5 mM), substrate (100 mM) in methanol-d_4 (3 mL). To activate the sample, the bubble-transfer-acquire experiment was repeated, until the hydride peaks at between δ −12 and −17 disappeared and a hydride appeared for the activated species at around

δ −20 to −30. Unless otherwise stated, the bubbling time was set to 10 seconds for the hyperpolarised experiments, using a pressure of *p*-H_2 set to 4 bar.

7.2.8 Enhancement calculations

The SABRE signal enhancement (ε) is determined by dividing the hyperpolarised signal intensity (S_{hyp}) of the nuclei in question by the signal intensity of the same signal when taken under Boltzmann conditions (S_{th}) as shown in equation 7.1.

$$\varepsilon = \frac{S_{hyp}}{S_{th}} n \qquad (7.1)$$

As the SABRE experiment is conducted in one NMR transient, the integral of the Boltzmann signal must be divided by the number of scans (n), and therefore this term was added to equation 7.1. This method is viable for a nucleus where the thermal signal can be observed. However, for nuclei such as ^{13}C and ^{15}N, where a signal under Boltzmann conditions is difficult to obtain, then an NMR standard must used. This can be a concentrated sample of the substrate under investigation or the signal from the solvent, depending upon whether or not a signal under Boltzmann conditions can be obtained. When using a standard, equation 7.2 is used.

$$\varepsilon = \frac{S_{hyp} Mr_{sub} M_{ref}}{S_{ref} Mr_{ref} M_{sub}} \qquad (7.2)$$

Where Mr_{sub} is the molecular mass of the substrate, M_{ref} is the mass used of the reference compound. Mr_{ref} is the molecular mass of the reference and M_{sub} is the substrate mass. However, if the solvent is used the mass must be calculated, this is done by using equation 7.3.

$$M = vol \times \rho \qquad (7.3)$$

Where M is the mass (g), vol is the volume (mL) and ρ is the density (g mL^{-1}). From this, the concentration (c) in moles, of the solvent can be calculated as shown in equation 7.4.

$$c = \frac{M}{Mr} \qquad (7.4)$$

An accurate Boltzmann signal, per mole can now be obtained as shown in equation 7.5.

$$Solvent\ NMR\ signal = \frac{S_{ref}}{c} \qquad (7.5)$$

Another way to examine signal improvement is to use the ratio of the thermal and hyperpolarised signal to noise ratio (SNR) as shown in equation 7.6.

$$SNR\ gain = \frac{SNR_{hyp}}{SNR_{Th}} \qquad (7.6)$$

Where hyp = hyperpolarised SNR and Th = thermal SNR.

7.2.9 Error calculations

The associated error for SABRE experiments and T_1 were calculated by firstly, taking the mean ($\bar{x}$) from the repeated measurements, *n* (equation (7.7)).

$$\bar{x} = \frac{\sum x_n}{n} \qquad (7.7)$$

Then the standard deviation (S.D) for the repeated measurements (equation 7.8)

$$\mathrm{SD} = \sqrt{\frac{\sum(x_n - \bar{x})^2}{n-1}} \qquad (7.8)$$

The error was then calculated as shown in equation 7.9

$$Error = \frac{SD}{\sqrt{n}} \qquad (7.9)$$

In cases where a value was calculated based upon other values which possessed their own error, for example calculating the error in z, when both x and y have errors as shown in equation 7.10.

$$z = x + y \qquad (7.10)$$

The error was propagated using equation 7.11.

$$\Delta z^2 = \left(\frac{\delta x}{\delta z}\,.\ \Delta x\right)^2 + \left(\frac{\delta y}{\delta z}\,.\ \Delta y\right)^2 \qquad (7.11)$$

Which can be simplified to equation 7.12

$$\Delta z = \sqrt{\left(\frac{\delta x}{\delta z} . \ \Delta x\right)^2 + \left(\frac{\delta y}{\delta z} . \ \Delta y\right)^2} \qquad (7.12)$$

For rate constants the Jack-knife method was used to calculate the errors.[190, 324]

Here, the data from one time data point is removed and the rate constant is calculated, using the Microsoft Excel SOLVER package (see section A.2), without this time point. This is then inserted back into the data and the data from the next time point is removed and the data re-solved. This is repeated for each time point until a rate constant has been obtained for each removed time point and a rate constant with all time points included. The standard error was then calculated as shown by equation 7.9.

7.2.10 SABRE Exchange Kinetics – EXSY

To observe the exchange process within the complexes described in this thesis selective exchange spectroscopy (EXSY) experiments were carried out. This experiment is based on the 1D Nuclear Overhauser Effect (nOe) experiments first described by Kessler *et. al.* in 1986 and expanded upon by Stonehouse *et. al.* and Stott *et. al.*[289-291] On the Bruker system the pulse programme employed is 'selnogp' and is described graphically in Figure 7.3.

The spin magnetisation which we are interested in, is selectively excited. This is achieved by using a single pulsed-field-gradient echo, which is a 180° pulse after the initial 90° pulse. The rest of the spins in the system are left and are not observed. The following 90° pulse transfers the magnetisation onto the −z axis. There is then a delay termed the mixing time, τ_{mix}, which allows the chemical exchange to occur. This mixing time is changed to reflect the exchange time of the reaction, in the case of the complexes here, between 0.005 s and 1.0 s. A standard gradient echo is then applied to refocus the selected magnetisation, this and the exchanged resonance(s) is then detected using the usual 90° pulse.

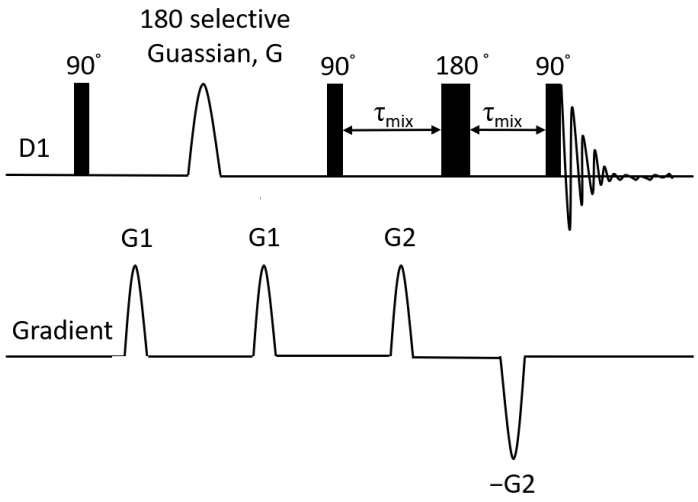

Figure 7.3 – Pulse sequence for the selective 1D NOESY experiment, otherwise known as an EXSY experiment.

7.2.11 Relaxation – T_1 experiment

T_1 is the time taken for magnetisation to return to equilibrium in the z-axis after perturbation. To understand T_1, we first need to understand the motion and collisions of molecules in liquids. In liquids, small molecules frequently undergo collisions, they also translate and rotate on a fast timescale, referred to as tumbling. Since each of the molecules in the sample are effectively small dipole magnets, the movement of these will cause local magnetic field fluctuations, which will be felt by subsequent spins. It is these fluctuating magnetic fields that causes the return to equilibrium. This type of interaction is known as dipole-dipole. For spin ½ nuclei the most dominant form of relaxation arises from dipole-dipole interactions. Another factor that dictates the value of T_1 is the local environment of the spins and is also dependent on which nucleus is being detected, as the theoretical T_1 is dependent on the gyromagnetic ratio. There are two main ways of measuring T_1, saturation recovery and inversion recovery. There is also a hyperpolarised method to measuring relaxation, known as the single shot hyperpolarised method.

7.2.11.1 Inversion recovery method

There are two main ways to measure T_1, inversion recovery and saturation recovery, both sequences start from the equilibrium position in the z-axis after being inserted into the NMR spectrometer. For the inversion recovery sequence, a 180° *r. f.* pulse is applied, inverting the magnetisation into the negative z-axis. Then a variable delay time (τ) is encoded in which the

spins will start to relax, see Figure 7.4 for the pulse sequence. The amount of relaxation will depend on the duration of this delay. Immediately after the delay a 90° *r. f.* pulse is applied which rotates the magnetisation into the xy plane for detection (see Figure 7.4), where a free induction decay (FID) is then recorded. From this a spectrum can then be obtained using a Fourier transformation.

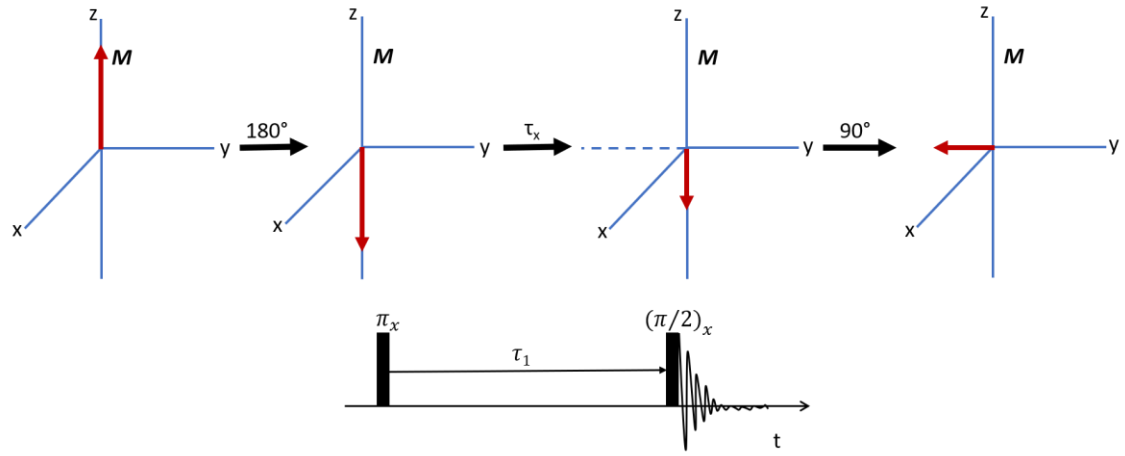

Figure 7.4 – (Top) A graphical description of the inversion recovery experiment to measure the spin-lattice relaxation times, T_1. Adapted from Nuclear magnetic resonance by P. J. Hore.[8] Bottom the pulse sequence for the inversion recovery NMR experiment to determine T_1 adapted from M. Levitt's Spin Dynamics: Basics of nuclear magnetic resonance.[9]

As depicted by the pulse sequence in Figure 7.4, this step is repeated multiple times to map out the decay and characterise the relaxation time.

Between each scan a delay equal to $5T_1$ should be left in order to fully reach equilibrium before subsequent acquisitions. Inversion recovery is described by an exponential decay of the form of equation 7.13.

$$M_{xy}(t) = M_0\left(1 - Aexp\left[\frac{-\tau}{T_1}\right]\right) \qquad (7.13)$$

Where M_{xy} is the magnetisation in the xy plane at time t, M_0 is the magnetisation at thermal equilibrium. A is a constant which ideally has a value of 2 but is left as a fitting variable to account for any imperfections in the timings of the pulse sequence, and T_1 is the spin-lattice relaxation time. The value of A is 2 due to the fact the magnetisation goes from $-M_0$ at $t=0$ to $+M_0$ at infinite

times. The intensity of magnetisation and the time delay was plotted, and the fitting of the data collected was achieved *via* the Origin software package using equation 7.13 above.

7.2.11.2 Saturation recovery

The alternative measurement, saturation recovery, is similar to inversion recovery, however, the time at the beginning of each experiment the magnetisation is saturated, so the net magnetisation is zero, and subsequently allowed to recover in the z-axis. This saturation is either achieved with spoiler gradients or applying a 90° pulse chain in quick succession effectively scrambling the magnetisation. The advantage of this sequence is not having to wait the $5T_1$ between experiments which can greatly reduce experimental time for measurements of long T_1 value samples.

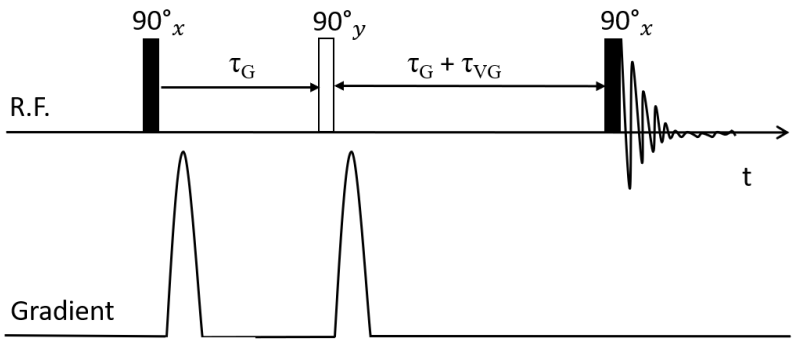

Figure 7.5 – Pulse sequence for the saturation recovery NMR experiment to determine T_1 adapted from Bruker pulse sequence files where τ is the time delay.

Within this thesis, the inversion recovery method has been used, as this is the more robust method for shorter T_1 values, however, saturation recovery may be used in future experiments in the case of very long T_1 values.

7.2.11.3 Hyperpolarised single shot T_1

A series of 15, single shot, ^{1}H NMR spectra were acquired using *r. f.* pulses of increasing flip angle for each excitation. The increasing pulse angle is calculated to ensure the same magnetisation is sampled at each measurement, with the observed decrease in signal arising from the relaxation of the hyperpolarised signal. The initial amplitude of the first flip angle will be $M_0 \sin\theta_1$ which, by the 15th spectrum, the polarisation will have decayed. Therefore, this angle

needs to be calculated for each nuclei and substrate, this was carried out using the equations from Semenova *et. al.* (2019).[6] From this the following angles were calculated: (See Table 7.1and Table 7.2)

Table 7.1 – Table of optimised pulse length for ^{13}C for both 2-^{13}C-uracil and 2-^{13}C,$^{15}N_2$-uracil.

Experiment number	flip angle, θ (°)	Pulse length (μs)	M_{xy} (%)	M_z (%)
1	15.0	2.50	25.96	96.60
2	15.5	2.58	25.80	93.10
3	16.1	2.68	25.80	89.40
4	16.8	2.80	25.80	85.60
5	17.5	2.93	25.70	81.60
6	18.4	3.08	25.80	77.50
7	19.5	3.27	25.90	73.00
8	20.7	3.47	25.80	68.30
9	22.2	3.72	25.80	63.30
10	24.1	4.03	25.80	57.70
11	26.6	4.47	25.90	51.60
12	30.0	5.05	25.80	44.70
13	35.2	5.97	25.80	36.50
14	44.9	7.68	25.80	25.90
15	86.2	15.00	25.80	1.70

Table 7.2 – Table of optimised pulse length for ^{15}N for 2-^{13}C,$^{15}N_2$-uracil.

Experiment number	flip angle, θ (°)	Pulse length (μs)	M_{xy} (%)	M_z (%)
1	15.0	4.50	25.96	96.60
2	15.5	4.64	25.80	93.10
3	16.1	4.82	25.80	89.40
4	16.8	5.04	25.80	85.60
5	17.5	5.27	25.70	81.60
6	18.4	5.54	25.80	77.50
7	19.5	5.89	25.90	73.00
8	20.7	6.25	25.80	68.30
9	22.2	6.70	25.80	63.30
10	24.1	7.25	25.80	57.70
11	26.6	8.05	25.90	51.60
12	30.0	9.09	25.80	44.70
13	35.2	10.75	25.80	36.50
14	44.9	13.82	25.80	25.90
15	86.2	27.00	25.80	1.70

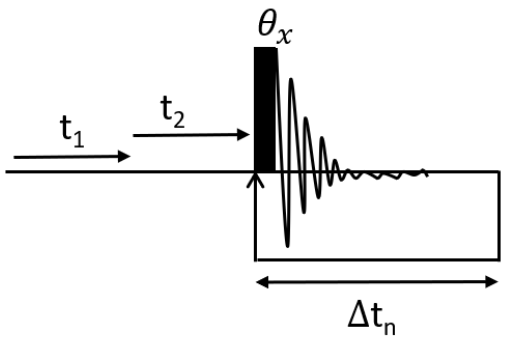

Figure 7.6 – Pulse sequence for the hyperpolarised single shot T_1 experiment, using a variable flip angle where t_1 is the SABRE polarisation transfer time, t_2 is the NMR transfer time and Δt_n is the variable time delay.

A series of 15 FIDs were recorded using the variable flip angles calculated in Table 7.1 and Table 7.2 for both ^{13}C and ^{15}N nuclei respectively in 2-^{13}C,$^{15}N_2$-uracil. The time delay between *r. f.* pulses is Δt_n, where n is the delay between θ_n and θ_{n+1} as shown in Figure 7.6.

The hyperpolarised longitudinal relaxation (T_1) times were calculated using an exponential fit of the decay of the hyperpolarised signal as shown in equation 7.14

$$M = M_0 e^{\left(\frac{-t}{T_1}\right)} + M_{Th\ equ.} \qquad (7.14)$$

Where M is magnetisation, M_0 is the initial magnetisation, T_1 is the time constant, t is the time after the first *r. f.* pulse and $M_{Th\ equ.}$ is the thermal equilibrium magnetisation.[6]

7.2.12 Imaging acquisition

Images were acquired using i) rapid acquisition with relaxation enhancement (RARE); ii) steady state free precession (SSFP); or iii) chemical shift (CSI) based approaches. All data were analysed using custom written code in MATLAB (MathWorks). Regions of interest were drawn manually where appropriate.

7.2.12.1 Rapid Acquisition with Relaxation Enhancement (RARE)

Standard spin echo sequences start with a 90° *r. f.* pulse to flip the net magnetisation of the bulk nuclei to the M_{xy} plane. Once this occurs the spins of the nuclei then start to de-phase (as shown in Figure 7.7 A-B) due to i) static inhomogeneities within the local magnetic field and ii) random spin-spin interaction. A second *r. f.* pulse (180°) is then applied, flipping the spins in this transverse plane, and spins start to rephase (as indicated in image **C** Figure 7.7). Once the spins have re-focused (**D**), an 'echo' signal is then recorded at the time point known as the echo time (TE).[325, 326] It is noted that the spin-echo approach only rephrases the effects of the static inhomogeneities in the magnetic field. The magnitude of the echo will attenuate by spin-spin interactions only (as part of a T_2 decay envelope).

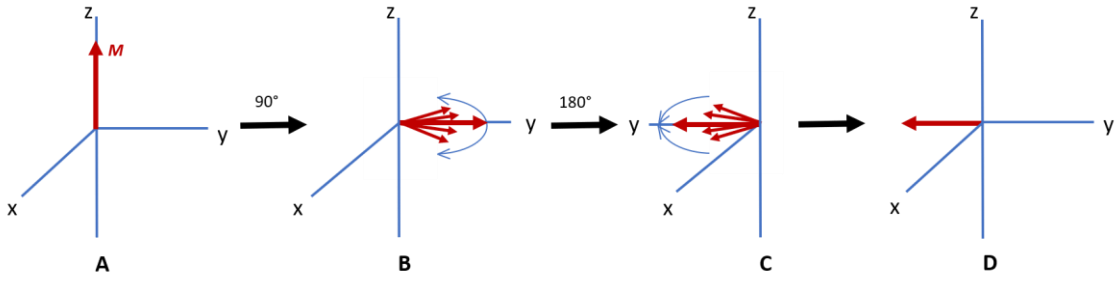

Figure 7.7 – Mapping the changes which occur in nuclear spins during a spin echo sequence.

RARE is a spin-echo variant which uses a train of 180° *r. f.* pulses, generating multiple echoes (after a single excitation pulse) with different phase encoding, in essence each echo capturing a

single line of *k*-space, within a single T_2 decay envelope.[327] This allows for shorter image acquisition times, and a 'one-shot' SABRE experiment which is advantageous (see below). Furthermore, a centric phase encoding approach where centre lines of k-space are captured first, can be implemented to ensure that low frequency (in particular the DC component) image information is captured while polarisation/signal is highest (in essence equating to a short overall image TE).

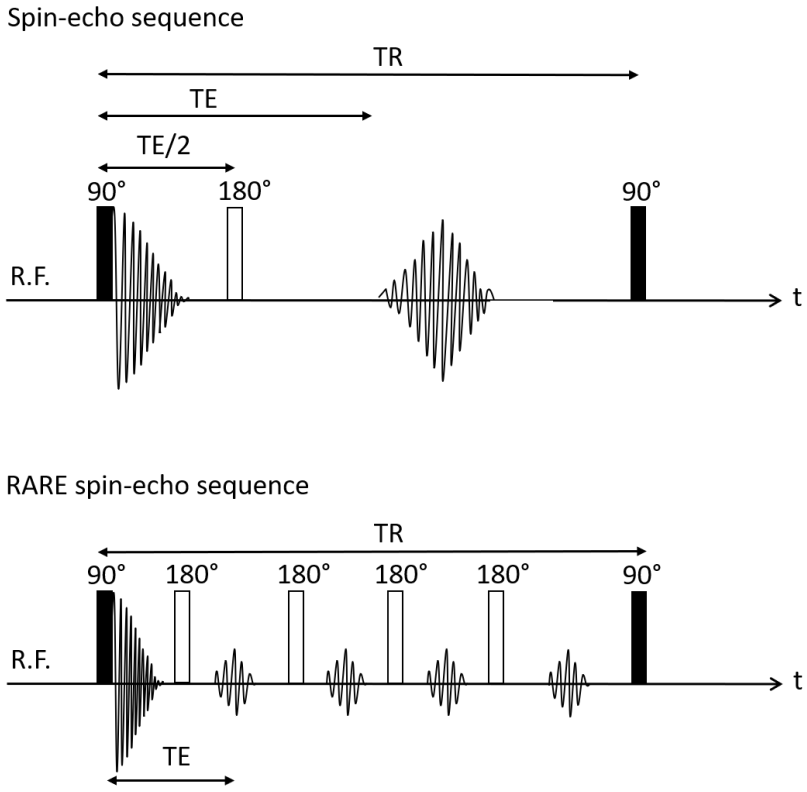

Figure 7.8 – Spin-echo and RARE pulse sequences, where R.F. is the radio frequency, TE = echo time and TR = repetition time, demonstrating the multiple echoes which can be recorded with RARE.

^{1}H and ^{19}F imaging experiments (Chapters 2 and 3) were carried out on a 400 MHz (9.4 T) Bruker spectrometer, with integrated micro 2.5 gradient set (150 mT/m), using a single shot, 2D centric encoded Rapid Acquisition with Relaxation Enhancement (RARE) image sequence. Imaging parameters were TR = 600 ms; TE = 4 ms, field of view (FOV) = 40*40 mm^2, matrix size = 64*64. Imaging used a 40 mm outer diameter dual tuned ^{1}H/^{19}F volume resonator. Hyperpolarised images were obtained after addition of 4 bar *p*-H_2 and shaken in the stray field of the MR magnet.

7.2.12.2 Steady State Free Precession (SSFP)

Application of a single 90° *r. f.* pulse on a hyperpolarised sample, will excite all the 'gained' magnetisation. From the transverse plane the magnetisation will relax back to thermal equilibrium in the longitudinal plane. In essence after this 90° *r. f.* pulse the hyperpolarised state will be 'destroyed' and no subsequent measures can be made.

Therefore, to acquire a series of images over time a steady state free precession (SSFP) was applied. Here a series of small flip angle *r. f.* pulses are applied in quick succession (repetition time, TR is extremely short ~ 4ms). In effect this keeps the magnetisation in a pseudo steady state. The free induction decays generated by each *r. f.* pulse are measured as part of *k*-space encoding generating a whole image within TR * phase lines (e.g. 4ms * 128 > 512ms) [328, 329]. The use of a small initial excitation flip angle means that some hyperpolarised magnetisation remains (cos 5° = 99.6%, signal remaining) in the longitudinal plane for later excitation to generate subsequent time resolved images (with an image repetition time ~ 512ms).

For ^{1}H and ^{19}F signal decay investigations the same 9.4 T Bruker NMR system (described above) was used. SSFP sequence parameters were TR = 4 ms, TE = 2 ms, FOV = 1.2*1.2 cm, matrix size = 64*64, 62 (NS) FISP 2D images were acquired as a function of time from the polarisation transfer step after 0.6-6.0 s, in 600 ms intervals (image repetition time). 5° flip angle *r. f* pulses were used to maintain the steady state for readout.

7.2.12.3 Chemical Shift Imaging (CSI)

Chemical Shift Imaging, CSI (an example of Magnetic Resonance Spectroscopic imaging, MRSI) uses pulsed field gradients to enable spectroscopic measures from various voxel volumes within the sample. CSI is carried out by using phase-encoding gradients as shown in Figure 7.9.[330, 331] In short spatial resolution is sacrificed to gain spectral information. As the sequence is FID based TR can be short and alongside a small flip angle CSI finds application in hyperpolarised based MRI. This is then overlaid onto a high-resolution reference ^{1}H image.

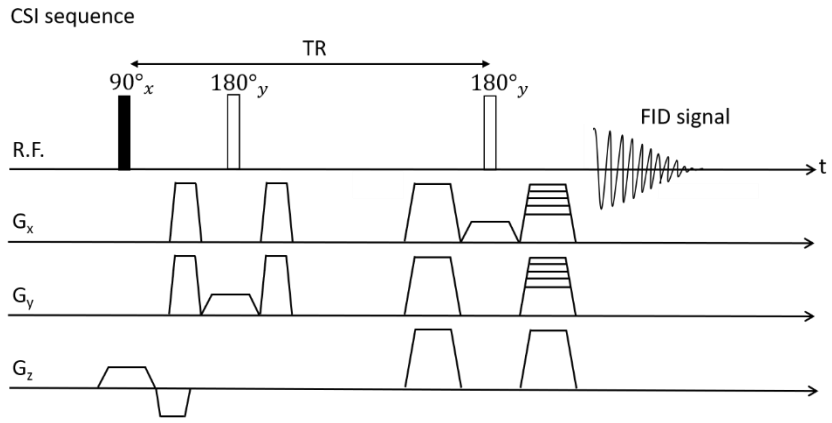

Figure 7.9 – 2D CSI pulse sequence using step gradients to allow encoding of positional information.

^{19}F CSI of 5-fluorouracil, and ^{13}C CSI of urea (Chapter 5) used a Magnetom Prisma 3 T MRI scanner (Siemens Healthcare, Erlangen, Germany). In both cases a flex-surface coil was used for the *r. f.* transmission/reception. For ^{19}F the imaging parameters used were a matrix size 8*8, 512 spectral points, across a ppm range of 172 ppm, FOV = 20*20*3 cm^3 with TE = 2.3 ms, TR = 200 ms with a flip angle = 5 deg. For ^{13}C the imaging parameters used were a matrix size 8*8, 512 spectral points, across a ppm range of 300 ppm, FOV = 20*20*3 cm^3 with TE = 2.3 ms, TR = 200 ms with a flip angle = 5 deg.

Appendix

A.1 Characterisation for Chapter 2 (pyrimidine)

[Ir(COD)(IMes)(pyrimidine)]Cl.

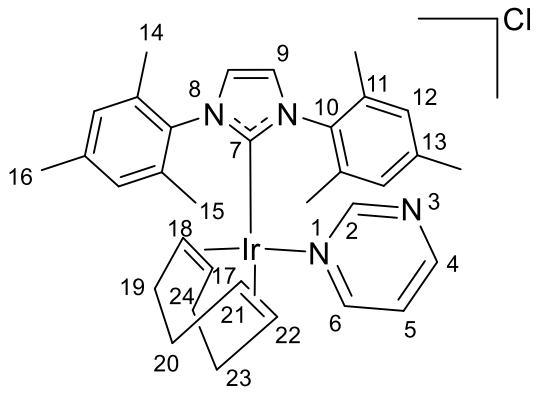

Figure A.1 – Structure of [Ir(COD)(IMes)(pyrimidine)]Cl.

[IrCl(COD)(IMes)] (5 mM) and pyrimidine (500 mM) were dissolved in methanol-d_4 (0.6 mL) at 293 K and the solution degassed using a freeze-pump-thaw method. The sample was then characterised by NMR spectroscopy at 245 K and the following data obtained for the product [Ir(COD)(IMes)(pyrimidine)]Cl which formed cleanly. Binding through nitrogen is clearly indicated by the change in ^{15}N chemical shift.

^{1}H NMR (500 MHz, methanol-d_4, 245 K) δ: 8.76 (s, 1H, H-4), 8.57 (s, 1H, H-2), 8.16 (m, 1H, H-6), 7.57 (s, 2H, H-9), 7.43 (m, 1H, H-5), 7.24 and 6.99 (m, 4H, H-12), 3.70 (m, 1H, 18 and H-17), 3.34 (m, 1H, 21 and H-22), 2.44 (s, 6H, H-16), 2.35 and 1.90 (m, 12H, H-14 and H-15), 2.05 and 1.69 (m, 4H, H-19 and H-24), 1.90 and 1.67 (m, 4H, H-20 and H-23).

^{13}C NMR (125.8 MHz, methanol,d_4, 245 K) δ: 172.0 (C-7), 158.4 (C-2), 157.5 (C-6), 157.3 (C-4), 129.2 (C-12), 125.3 (C-9), 123.1 (C-5), 81.8 (C-21 and 22), 65.9 (C17 and 18), 32.1 (C-20 and 23), 28.9 (C-19 and 24), 19.86 (C-16), 17.5 (C-14 and 15)

^{15}N NMR (50.7 MHz, 245 K) δ: 297.2 (N-1), 233.8 (N-3), 195.4 (N-8).

[Ir(H)$_2$(COD)(pyrimidine)(IMes)]Cl.

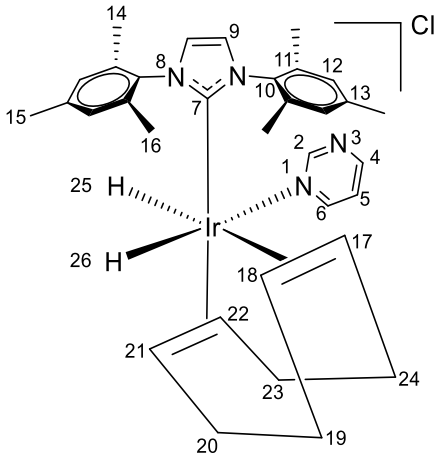

Figure A.2 – Structure of [Ir(H)$_2$(COD)(IMes)(pyrimidine)]Cl.

[IrCl(COD)(IMes)] (5 mM) and pyrimidine (500 mM) were dissolved in methanol-d_4 (0.6 mL) at 293 K and degassed with a freeze-pump-thaw method. The sample was then exposed to 4 bar of H_2 gas and the resulting reaction monitored at 245 K. A single product formed in high yield, [Ir(H)$_2$(COD)(IMes)(pyrimidine)]Cl, and this was characterised by NMR spectroscopy at 245 K.

This corresponds to the H_2 addition product of the Cl^- displacement product, [Ir(COD)(IMes)(pyrimidine)]Cl. It is notable that there are four alkene resonances thereby confirming that COD remains coordinated at this stage. ^{1}H resonances at δ 9.45, 9.05, 8.76 and 8.69 are indicative of the pyrimidine ligand and they appear alongside hydride resonances at δ −12.05 and −17.03 which have the same intensity. Ligand orientation was confirmed by nOe connections and magnetisation transfer from the hydride resonances.

^{1}H (500 MHz, methanol-d_4, 245 K) δ: 9.07 (s, 1H, H-2), 8.93 (dd, J = 4.83 and 1.99 Hz, 1H, H-4), 8.65 (dd, J = 4.94 and 2.50 Hz, 1H, H-6,), 7.46 (s, 2H, H-9), 7.38 (t, J = 4.96 Hz, 1H, H-5), 7.11 (s, 2H, H-12), 4.98 (m, 1H, H-22), 4.79 (t, 1H, J = 7.25 Hz, H-18), 4.37 (m, 1H, possible J = 7.93 and 4.98 Hz, H-17), 3.66 (m, 1H, H-21), 2.57 (m, 2H, H-19), 2.39 (m, 3H, H-15), 2.31 (m, 2H, H-20), 2.07 (s, 6H, H-14), 1.94 (s, 6H, H-16), 1.83 (m, 2H, H-23), 1.75 (m, 2H, H-24), −12.05 (s, 1H, H-25), −17.03 (s, 1H, H-26).

^{13}C (125.8 MHz, methanol-d_4, 245 K) δ: 165.9 (C-2), 156.5 (C-4), 153.5 (C-7), 139.9 (C-13), 136.7 (C-10), 134.9 (C-11), 129.25 (C-12), 124.6 (C-9), 123.4 (C-5), 91.54 (C-18), 87.80 (C-17),

84.3 (C-21), 82.12 (C-22), 35.26 (C-19), 30.30 (C-20), 30.1 (C-23), 24.8 (C-24), 19.9 (C-15), 17.05 (C-14), 16.80 (C-16).

^{15}N NMR (50.7 MHz, methanol-d_4, 245 K) δ: 298.6 (N-3), 213.8 (N-1), 196.9 (N-8).

[Ir(H)$_2$(IMes)(pyrimidine)$_3$]Cl.

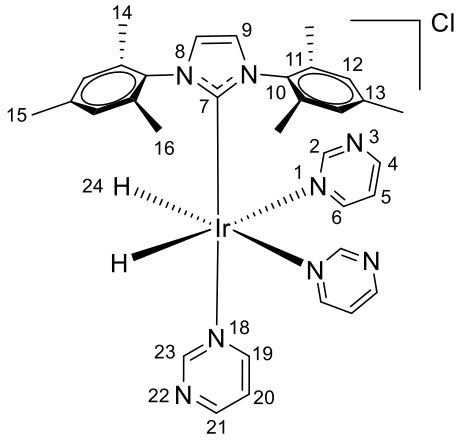

Figure A.3 – Structure of [Ir(H)$_2$(IMes)(pyrimidine)$_3$]Cl.

Upon warming solutions of [Ir(H)$_2$(COD)(IMes)(pyrimidine)]Cl in methanol-d_4 (0.6 mL) from 245 K to 293 K under 4 bar H_2 a further reaction occurs. This process yields a dominant hydride resonance at δ −22.06 and the product giving rise to it, [Ir(H)$_2$(IMes)(pyrimidine)$_3$]Cl, which was characterised by NMR spectroscopy after cooling to 245 K.

^{1}H NMR (500 MHz, methanol-d_4, 245 K) δ: 9.06 (t, J = 1.1 Hz, 1H, H-23), 8.99 (t, J = 0.8 Hz, 1H, H-2), 8.81 (dd, J = 2.2, 4.9 Hz, 1H, H-4), 8.717 (dd, J = 2.2, 4.85 Hz, 1H, H-19), 8.62 (dd, J = 2.5, 6.6 Hz, 1H, H-6), 8.34 (d, J = 4.77 Hz, 1H, H-21), 7.33 (t, J = 1.2, 5.5 Hz, 2H, H-9), 7.32 (ddd, 1.36, 5.0, 5.5 Hz, 1H, H-5), 7.17 (ddd, J = 1.3, 4.85, 6.0 Hz, 1H, H-20), 6.73 (s, 4H, H-12), 2.21 (s, 6H, H-15), 2.08 (s, 12H, H-14), −22.06 (s, 2H, H-24)

^{13}C (125.8 MHz, methanol-d_4, 245 K) δ: 168.51 (s, C-19), 165.47 (s, C-6), 163.0 (s, C-21), 162.76 (s, C-4), 162.02, (s, C-2), 161.92 (s, C-23), 150.5 (s, C-1), 137.3 (s, C-10), 137.0 (s, C-13), 135.0 (s,C-11), 128.5 (s, C-12), 123.0, (s, C-9), 20.10 (s, C-15), 17.64 (s, C-14)

^{15}N NMR (50.7 MHz, methanol-d_4, 245 K) δ: 297.9 (s, N-22), 295.4 (s, N-3), 241.4 (s, N-1), 228 (s, N-18), 194.6 (s, N-8)

A.2 Modelling hydride ligand exchange in $[Ir(H)_2(IMes)(pyrimidine)_3]Cl$

The accepted mechanism for substrate exchange during the SABRE process is summarised in Figure 7.4. This process is normally on a timescale where the 1D EXSY protocol is possible. In order to undertake this, the hydride ligand signal of $[Ir(H)_2(IMes)(pyrimidine)_3]Cl$ is selectively excited and the resulting exchange in the free hydrogen signal observed.

The mechanism of hydrogen loss, is complex and involves prior dissociation of a ligand *trans* to hydride, as put forward by Lloyd *et. al.* (2014).[111] The reversible formation of a dihydrogen-dihydride intermediate then enables H_2 cycling. Given this complexity, it is normal just to fit the loss of H_2 to a simple exponential involving A_1 and hence an experimental flux for H_2 loss is quantified.

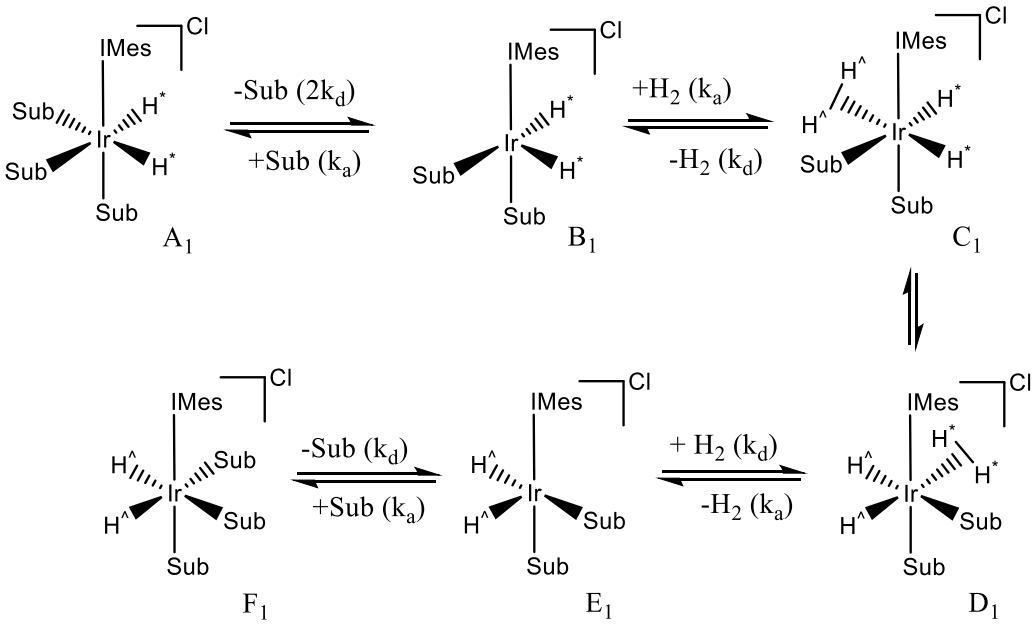

Figure A.4 – Exchange pathway for hydrogen loss during the SABRE process with pyrimidine.

Examination of the results of this process with pyrimidine revealed that this exchange is complicated as it proceeds into a further product with inequivalent hydride ligands at δ −23.43 and −24.83 alongside H_2. This product is proposed to be $[IrCl(H)_2(IMes)(pyrimidine)_2]$. Figure A.5 shows a revised scheme with rates k_1, k_{-1}, k_2, k_{-2}, k_3 and k_{-3} that are used to model the EXSY data.

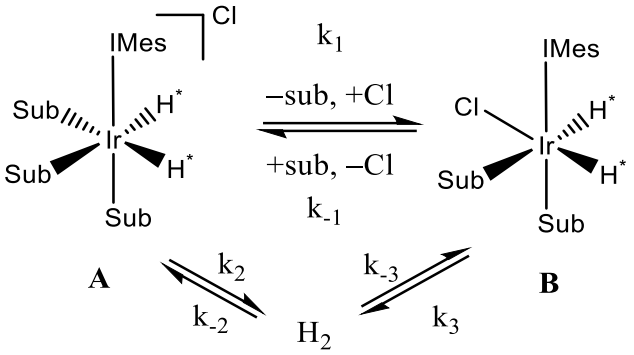

Figure A.5 – Simplified mechanism of hydrogen exchange within the SABRE process.

This modelling involves the analysis of a series of connected exponential decays that are simulated according to a differential kinetic model. Using equations A.1 and A.2, simulated rate equations could be written into Excel as shown in Table A.1 and therefore the concentrations of [A], [B] and [H_2] could be calculated where t = 0 to 0.5 s. As a rate constant is required (k_1, k_2 and k_3) estimated values had to be used. At t = 0, it was assumed that the concentration of A was 100% and that of B and H_2 was 0%.

$$[A]_t = [A]_0 - k_1[A]_0\delta t + k_{-1}[B]_0\delta t - k_2[H_2]_0\delta t + k_{-2}[H_2]_0\delta t \qquad (A.1)$$

$$[B]_t = [B]_0 - k_{-1}[B]_0\delta t + k_1[A]_0\delta t - k_3[H_2]_0\delta t + k_{-3}[H_2]_0\delta t \qquad (A.2)$$

Table A.1 – The cell inputs used for the Excel spreadsheet to calculate the simulated rate data for the conversion of A to B, B to A and the loss of H_2 from B when the substrate used is pyrimidine.

A	B	C	D
Time (s)	[A]	[B]	[H_2]
0	100	0	0
0.001	=@INDEX(MMULT($B60:$F60,$B$15:$F$19)*($A61-$A60)+B60,1)	=@INDEX(MMULT($B60:$F60,$B$15:$F$19)*($A61-$A60)+C60,2)	=@INDEX(MMULT($B60:$F60,$B$15:$F$19)*($A61-$A60)+E60,4)

The least squares regression was then calculated by subtracting the simulated values from the experimental ones. Each of these was then squared and summed to give the sum of the squared residual as shown in equation A.3

$$S = \sum_{n}^{i} r_i^2 \qquad (A.3)$$

Where *S* is the sum of the squared residuals, *n* the number of data points, *i* a specific data point and r_i, the residual of the given data point.[190] An example of the least squares regression errors for the rate constants for 290 K are given in Table A.2.

Table A.2 – Least squared regression error for the experimental data obtained at 290 K for hydrogen exchange in the complex $[Ir(H)_2(IMes)(pyrimidine)_3]Cl$ *via* the intermediate $[IrCl(H)_2(IMes)(pyrimidine)$.

Enter observed data:				Calculated least squares regression errors:			
time(s)	[A]	[B]	[C]	[A]	[B]	[C]	sum
0	100	0	0				0
0.005	99.12	0.25	0.03	0.028978	0.01114451	0.001070319	0.100282
0.05	94.12	2.93	0.04	0.016706	4.93293E-05	0.009442203	0.026826
0.075	92.34	3.76	0.13	0.381731	0.056216729	0.025001132	0.512511
0.1	89.87	4.59	0.67	0.001926	0.063765256	0.036800073	0.102774
0.125	87.93	5.57	0.73	0.092804	0.001649578	0.001142759	0.148597
0.15	86.81	5.95	1.02	0.007024	0.018504563	0.007246872	0.050923
0.175	85.73	6.72	1.15	0.00042	0.037262134	0.001990287	0.056037
0.2	84.64	7.12	1.33	0.018394	0.055516498	0.01612508	0.090764
0.25	83.13	7.59	1.83	0.008376	0.04204482	0.028575211	0.082078
0.3	81.68	7.83	2.54	0.127839	0.016593512	0.000231135	0.204168
0.35	81.25	7.79	2.99	0.01839	0.010982722	0.010441446	0.044908
0.4	80.66	8.03	3.56	0.078118	0.001060483	0.003516525	0.146582
0.45	79.70	7.90	4.30	0.003625	0.024000827	0.031077766	0.060213
0.5	79.38	8.25	4.71	0.01861	0.027046063	0.014420905	0.237285
							1.863947

Data convergence is achieved by using the SOLVER package in Microsoft Excel to minimise the sum of the squares of the differences between real and simulated points according to equations A.1 and A.2. In this case the rate constants k_1, k_2 and k_3 were changed until an optimal fit was observed as shown in Figure A.6. Typically, 10 data points were collected for any one temperature at a range of time points set to monitor the process to around 50% exchange. The results of this process for the data obtained at 295 K is presented in Figure A.6.

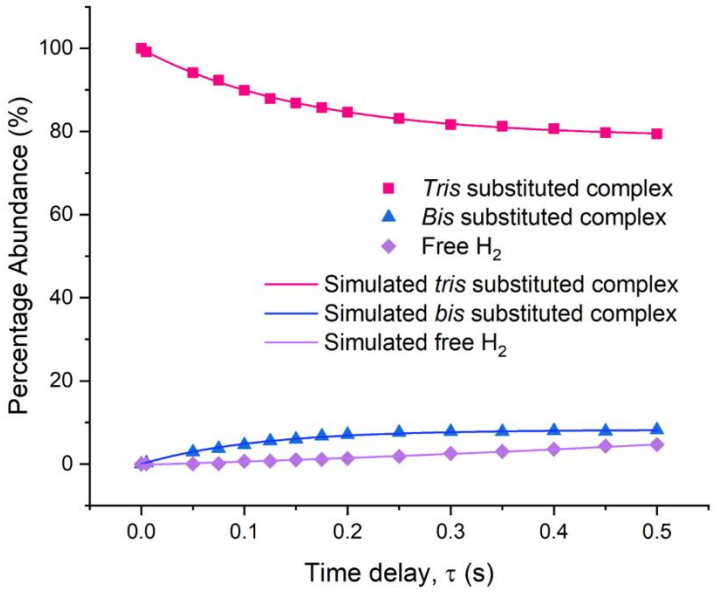

Figure A.6 – Experimental and simulated hydrogen exchange data for $[Ir(H)_2(IMes)(pyrimidine)_3]Cl$ at 290 K.

The error for the rate constants was calculated using the Jack knife method as described in Chapter 7, section 7.2.9, the Jack-knife errors for 290 K are given in Table A.3.

Table A.3 - Jack-knife error for the experimental data of the hydride exchange obtained at 290 K for $[Ir(H)_2(IMes)(pyrimidine)_3]Cl$ *via* the intermediate $[IrCl(H)_2(IMes)(pyrimidine)_2]$.

	A to B	**B to A**	**H_2 from B**
All	1.35	10.51	0.80
0.005	1.37	10.63	0.83
0.05	1.33	10.20	0.87
0.075	1.34	10.33	0.80
0.1	1.37	10.62	0.82
0.125	1.36	10.62	0.78
0.15	1.34	10.48	0.80
0.175	1.35	10.30	0.91
0.2	1.36	10.64	0.82
0.25	1.36	10.59	0.76
0.3	1.35	10.37	0.83
0.35	1.35	10.51	0.80
0.4	1.37	10.63	0.83
0.45	1.33	10.20	0.87
0.5	1.34	10.33	0.80
Error	0.004	0.047	0.012

It is usual to use this rate data as a function of temperature to determine activation parameters for the process *via* Eyring analysis as shown below in Figure A.7. In this case these correspond to the activation barriers for complex **A** ($[Ir(H)_2(IMes)(pyrimidine)_3]Cl$) to form complex **B** ($[IrCl(H)_2(IMes)(pyrimidine)_2]$), the formation of H_2 from **B** and the conversion of **B** into **A**.

Fitting suggested that **A** itself does not lose H_2 directly. The results of this process are presented in Chapter 2 section 2.1.3.

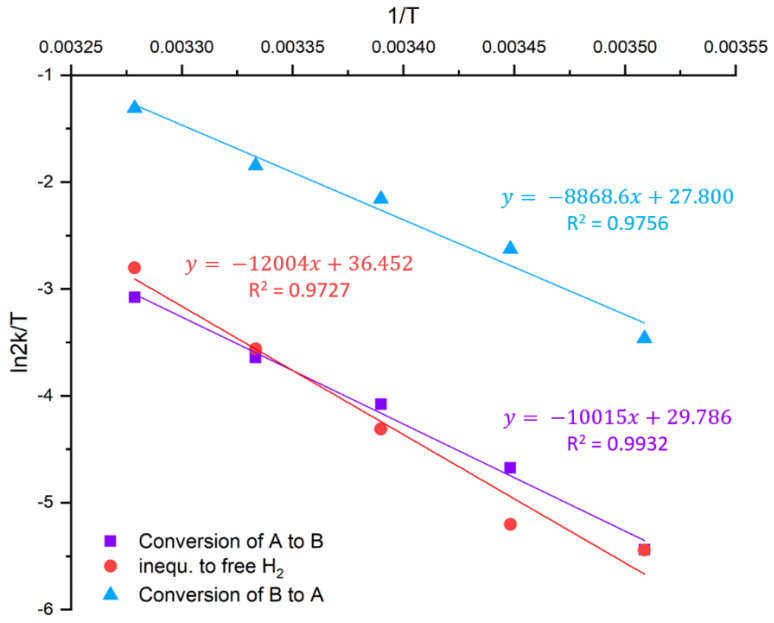

Figure A.7 – Eyring plot of the conversion of complex A to B, the conversion of B to free hydrogen and the conversion of B back to A. The results of a linear regression analysis on each set of data is given in the plot in the same presentation colour.

A.3 Effect of changing pyrimidine concentration (from Chapter 2.2.1)

Samples of [IrCl(COD)(IMes)] (5 mM) with varying concentrations of pyrimidine (20 mM to 500 mM) in methanol-d_4 (0.6 mL), were prepared and exposed to 4 bar *para*-hydrogen (*p*-H_2). SABRE experiments were then performed, and the resulting ^{1}H NMR signal enhancements recorded as described in experimental 7.2.8. The results of these experiments are presented in Table A.4 and displayed graphically in Figure 2.7 (Chapter 2.2.1).

Table A.4 – ^{1}H-NMR signal enhancements for the indicated resonances of pyrimidine achieved through [Ir(H)$_2$(IMes)(pyrimidine)$_3$]Cl (5 mM) in methanol-d_4 (0.6 mL) under 4 bar of *p*-H$_2$ as a function of substrate concentration at 298 K.

Concentration of substrate (mM)	Average enhancement of each proton on pyrimidine		
	H-2	Normalised H-4, H-6 for one proton	H-5
20	−489 ± 15	−439 ± 13	−381 ± 9
30	−412 ± 8	−381 ± 8	308 ± 6
40	−381 ± 109	−419 ± 117	−348 ± 98
50	−542 ± 16	−584 ± 15	−506 ± 13
60	−526 ± 23	−531 ± 13	−445 ± 17
80	−486 ± 15	−411 ± 19	−369 ± 19
100	−502 ± 8	−330 ± 21	−301 ± 16
150	−214 ± 10	−206 ± 11	162 ± 12
200	−162 ± 7	−145 ± 5	−114 ± 4
250	−162 ± 7	−125 ± 6	−104 ± 4
300	−169 ± 6	−142 ± 4	−114 ± 4
400	−62 ± 1	−54 ± 1	−45 ± 1
500	−32 ± 1	−32 ± 1	−28 ± 1

A.4 Effect of changing catalyst concentration (from Chapter 2.2.2)

Samples with varying concentrations of [IrCl(COD)(IMes)] (0.5 to 20 mM) with the optimal concentration of pyrimidine (50 mM) in methanol-d_4 (0.6 mL), were prepared and exposed to 4 bar *p*-H$_2$. SABRE experiments were then performed and ^{1}H NMR signal enhancements calculated as described in experimental 7.2.8. The results are shown in Table A.5 and are graphically represented in Figure 2.8 of Chapter 2, section 2.2.2.

Table A.5 – Signal enhancements for the ^{1}H-NMR resonnces of pyrimidine as a function of [Ir(H)$_2$(IMes)(pyrimidine)$_3$]Cl concentration whilst maintaining a 1:40 catalyst :pyrimidine ratio in methanol-d_4 (0.6 mL) at 298 K.

Concentration [IrCl(COD)(IMes)] (mM)	Average enhancement of each proton on pyrimidine		
	H-2	Normalised H-4, H-6 for one proton	H-5
20	−82 ± 3	54 ± 4	−74 ± 3
15	−57 ± 2	−49 ± 1	−38 ± 1
10	−117 ± 3	34 ± 3	−100 ± 2
7.5	−150 ± 3	−124 ± 3	−103 ± 1
5	−169 ± 6	−154 ± 6	−128 ± 4
2.5	−266 ± 6	−269 ± 6	−236 ± 7
0.5	−329 ± 6	−280 ± 4	−197 ± 1

A.5 The effect of changing the SABRE pre-catalyst (from Chapter 2.2.3)

The effect of the SABRE pre-catalyst was investigated for agents 1-7, for a 2.5 mM concentration with a concentration of pyrimidine (25 mM), in methanol-d_4 (0.6 mL). These samples were exposed to 4 bar *p*-H_2 for SABRE. The resulting ^{1}H NMR signal enhancements are presented in Table A.6. A graph of this data is presented in Figure 2.10, Chapter 2 section 2.2.3.

Table A.6 – Average ^{1}H NMR signal enhancement factor for the indicated pyrimidine resonance as a function of catalyst. All samples contained 2.5 mM of catalyst and pyrimidine (25 mM) in methanol-d_4 (0.6 mL) with 4 bar *p*-H_2. Polarisation transfer was conducted at 65 G. Five experiments were conducted for statistical analysis.

Catalyst number	Average enhancement of each proton on pyrimidine		
	H-2	H-4,6	H-5
1	−258 ± 15	−232 ± 6	−196 ± 8
2	−280 ± 15	−316 ± 13	−237 ± 9
3	−287 ± 8	−279 ± 3	−217 ± 4
4	−382 ± 14	−385 ± 19	−313 ± 19
5	−349 ± 11	−274 ± 12	−231 ± 10
6	−184 ± 3	−169 ± 4	−152 ± 2
7	−284 ± 22	−176 ± 10	−120 ± 7

A.6 Temperature study

A series of SABRE experiments were conducted on a range of samples at varying temperatures. A sample was prepared at 293 K containing [IrCl(COD)(IMes)] (2.5 mM) and pyrimidine (25 mM) in methanol-d_4 (0.6 mL). SABRE polarisation transfer was then conducted within the temperature range of 280-315 K. For values below 298 K, varying amounts of dry ice in acetone was used to achieve the required temperature whereas for temperatures above 298 K a thermostatically controlled water bath was used. The sample was submerged into the relevant bath for approximately 15 minutes to allow the sample to equilibrate to the desired temperature. The NMR spectrometer was also set to the desired temperature. Addition of *p*-H_2 was carried out whilst the sample was at the required temperature in order to keep the temperature of the sample from fluctuating. The NMR sample was then removed, dried and the SABRE experiment was then carried out. Five SABRE experiments were carried out at each temperature and an average was obtained. The error was calculated as described in the experimental section 7.2.9.

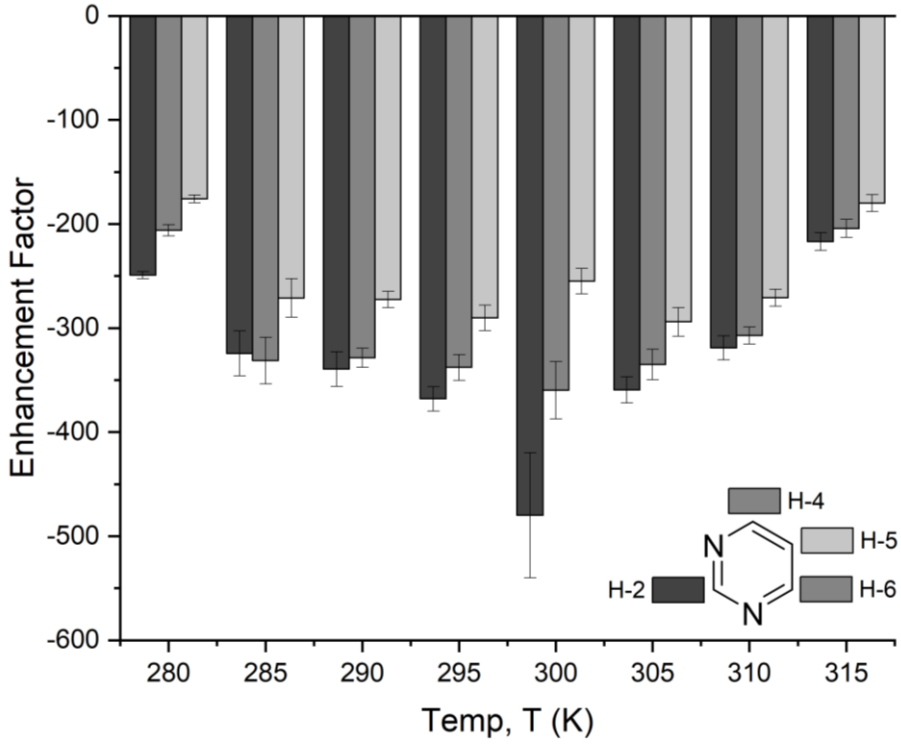

Figure A.8 – A plot of the individual signal enhancement of the ^{1}H resonances of the free substrate pyrimidine as a function of temperature.

Two other temperature studies were conducting using different samples and varying the temperatures at random to minimise the error within these experiments. The results for all three

temperature studies for each proton on free pyrimidine are shown in Figure A.9 to Figure A.11. Again, five SABRE experiments were conducted on each sample, at each temperature and an average was taken. The error was again calculated as described in the experimental section 7.2.9.

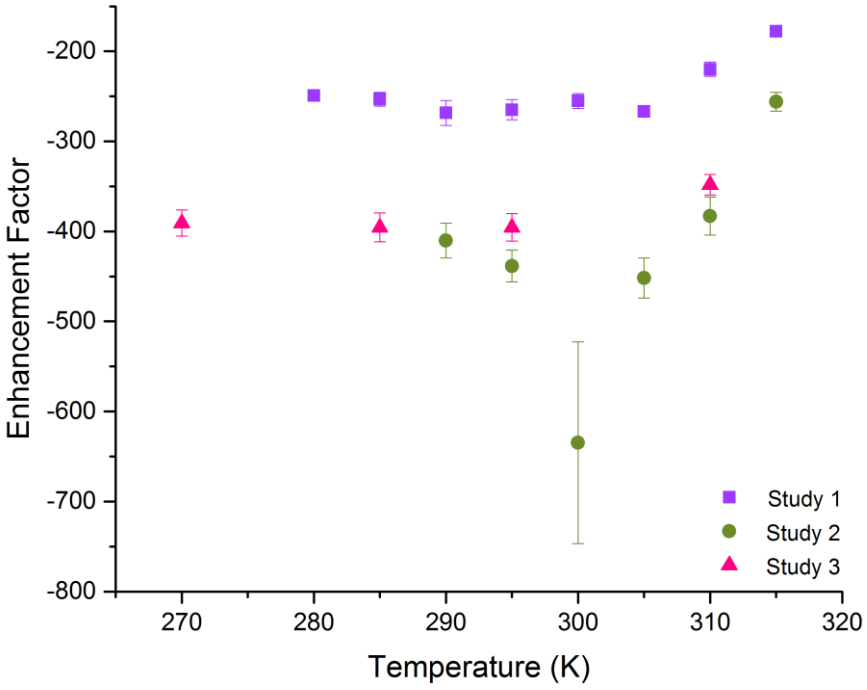

Figure A.9 – ^{1}H NMR signal enhancement for H-2 of pyrimidine from as a function of temperature.

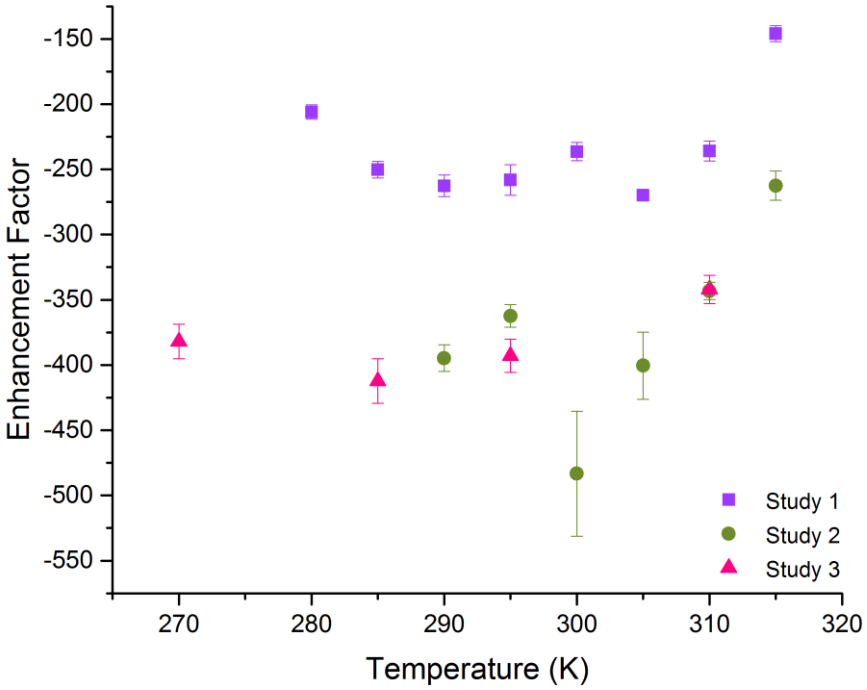

Figure A.10 – ^{1}H NMR signal enhancement for H-4, 6 of pyrimidine as a function of temperature.

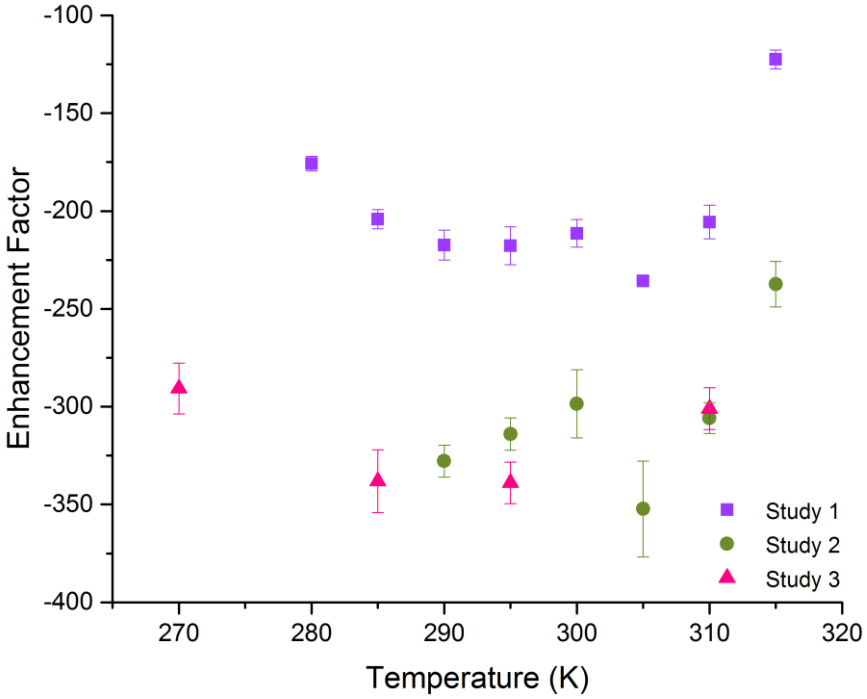

Figure A.11 – ^{1}H NMR signal enhancement for H-5 of pyrimidine as a function of temperature.

The first study did not produce the same enhancements as the second and third ones. This is probably due to human error within the technique as these were some of the first measurements taken. Studies 2 and 3 were carried out after the shake and drop method had been repeated for several months. From each of the figures, it is clear that temperature studies 2 and 3 are more reproducible but the method itself is not particularly robust. There will be a lot of heat loss between taking the sample out of the water bath, shaking it at 65 G and then transferring it to the NMR. At the colder temperatures, it is also difficult to maintain the temperature of the water bath. As well as this, the time spent with the sample out of the bath and subsequently transferring to the spectrometer, the sample quickly starts to warm up. The method itself does give a good indication of the optimal temperature but it is not definitive

The large error obtained makes this data difficult to compare. Therefore, this has been omitted from the main thesis.

A.7 Calculation of ^{1}H T_1 data for pyrimidine and fluorinated *N*-heterocyclic compounds

T_1 data was obtained using the inversion recovery method as described the Experimental section, Chapter 7 section 7.2.11. The free ^{1}H signals on the pyrimidine were examined. Using the data

obtained this was placed into the Origin software package and using equation A.4, where M_{xy} is the magnetisation in the xy plane at time t, M_0 is the magnetisation at thermal equilibrium, A is a constant which ideally has a value of 2 but is left free to account for any imperfections in the pulse sequence and T_1 is the spin-lattice relaxation time.

$$M_{xy}(t) = M_0\left(1 - Aexp\left[\frac{-t}{T_1}\right]\right) \qquad (A.4)$$

The resulting T_1 values are shown in Figure A.12 below.

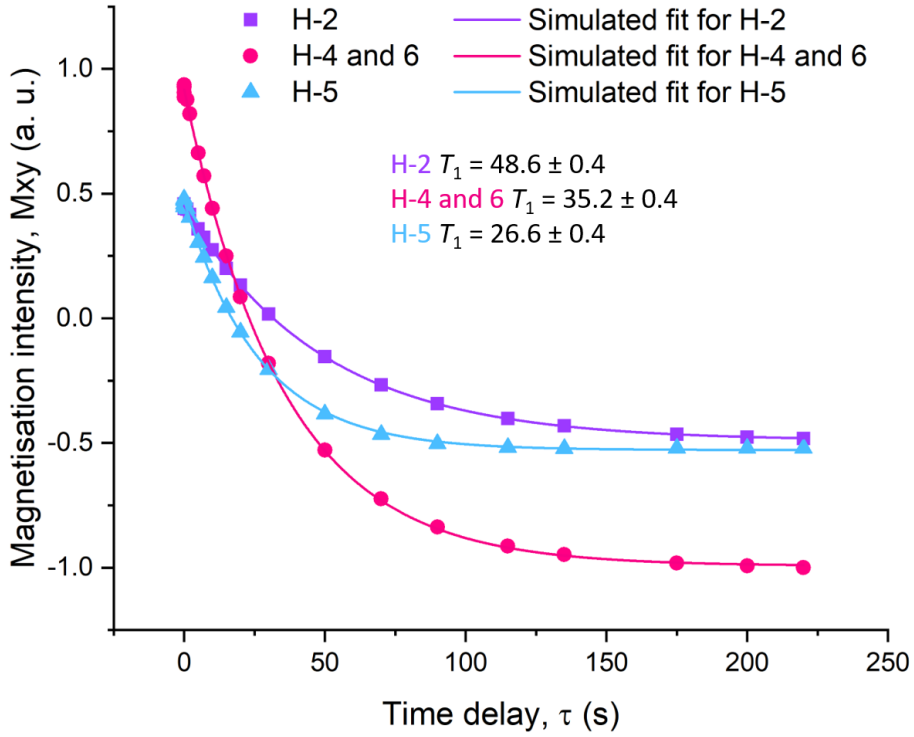

Figure A.12 – Plot of magnetisation intensity at different delay times (τ) during an inversion recovery experiment in which the T_1 relaxation has been calculated for free pyrimidine (25 mM) in the presence of pre-catalyst [IrCl(COD)(1,3-bis(2,4,6-trimethylphenyl)-4,5-dichloroimidazol-2-ylidine)] (2.5 mM) and H_2 (4 bar) in methanol-d_4 (0.6 mL). From this the T_1 relaxation time was calculated using equation A.4.

A.8 Calculation and plots of ^{19}F T_1 data for fluorinated *N*-heterocyclic compounds

T_1 data for ^{19}F was also obtained using the inversion recovery method as described in the Experimental section, Chapter 7.2.11 and above (Appendix section A.7). The free ^{19}F signals on the fluorinated *N*-heterocyclic compounds were examined. Using the data obtained this was placed into the Origin software package and using equation A.4. The T_1 values were found using

this data and simulating fit as shown in Figure A.13 below. The data was collected in collaboration with Dr. A. Olaru.

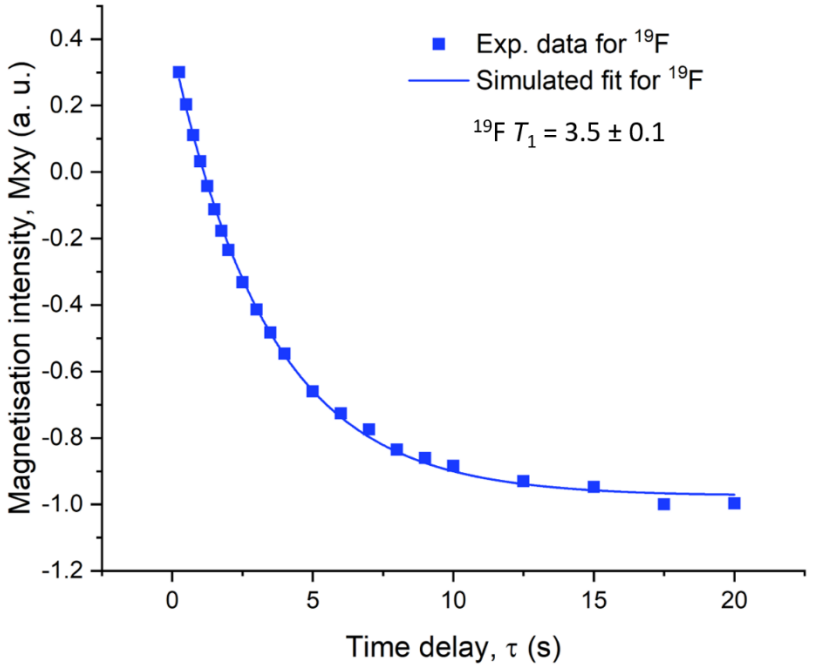

Figure A.13 – A plot of the magnetisation decay at varying time delays, τ for ^{19}F of free 5-fluoropyridine-3-carboxylic acid in the presence of Cs_2CO_3 and the SABRE pre-catalyst [IrCl(COD)(IMes)]. From this the T_1 relaxation time was calculated using equation A.4.

A.9 Characterisation (fluorinated *N*-heterocyclic compounds)

Characterisation of [Ir(H)$_2$(3-fluoropyryridine)$_3$(IMes)]Cl.

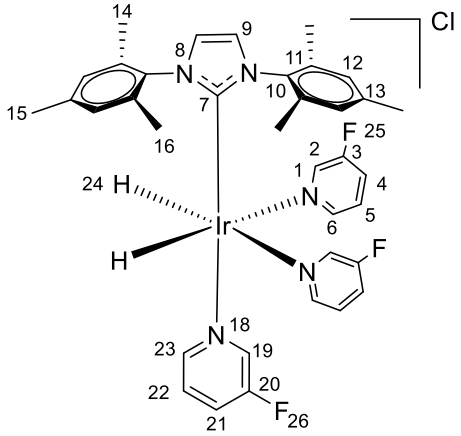

Figure A.14 – Structure of [Ir(H)$_2$(IMes)(3-fluoropyridine)$_3$]Cl complex.

[IrCl(COD)(IMes)] (5 mM) and 3-fluoropyridine (500 mM) were dissolved in methanol-d_4 (0.6 mL) at 293 K and degassed using a freeze-pump-thaw method. The sample was then exposed

to 4 bar (absolute) H_2. The sample was then repeatedly exposed to 4 bar H_2 until a hydride appeared at δ −22.85. This was then characterised by NMR at 245 K.

^{1}H (500 MHz, methanol-d_4, 245 K) δ: 8.42 (d, *J* = 4.92 Hz, 1H, H-2), 8.25 (d, *J* = 4.83 Hz, 1H, H-23,), 8.00 (q, *J* = 7.87, 1H, H-6,), 7.94 (q, *J* = 7.86 Hz, 1H, H-19,), 7.72 (m, *J* = 8.63 Hz, 1H, H-5), 7.64 (q, *J* = 7.22 Hz, 1H, H-22), 7.38 (d, *J* = 7.07 Hz, 1H, H-4), 7.23 (s, 2H, H-9), 7.08 (d, *J* = 5.72 Hz, 1H, H-21), 6.72 (s, 4H, H-12), 2.22 (s, 6H, H-15), 2.07 (s, 12H, H-14), − 22.85 (s, 2H, H-24).

^{13}C (125.8 MHz, methanol-d_4, 245 K) δ: 151.38 (C-19), 149.13 (C-12), 144.51 (C-23), 144.22 (C-6), 138.45 (C-13), 137.00 (C-10), 135.00 (C-11), 128.32 (C-12), 126.67 (C-21), 126.23 (C-4), 123.93 (C-22), 123.74 (C-5), 122.71 (C-9), 19.90 (C-15), 17.62 (C-14 and C-16).

^{15}N (50.7 MHz, methanol-d_4, 245 K) δ: 260.18 (N-1), 242.73 (N-18), 194.69 (N-8).

^{19}F (470.6 MHz, methanol-d_4, 245 K) δ: −124.5 (F-26), −124.20 (F-25).

Characterisation of [Ir(H)$_2$(3,5-difluoropyridine)$_3$(IMes)]Cl.

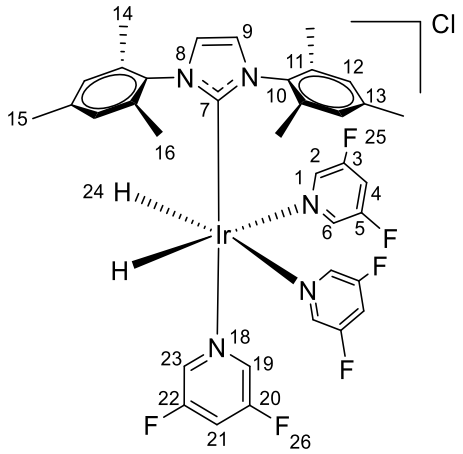

Figure A.15 – Structure of [Ir(H)$_2$(3,5-difluoropyridine)$_3$(IMes)]Cl complex.

[IrCl(COD)(IMes)] (5 mM) and 3,5-difluoropyridine (500 mM) were dissolved in methanol-d_4 (0.6 mL) at 293 K and degassed using a freeze-pump-thaw method. The sample was then exposed to 4 bar (absolute) H_2. The sample was then repeatedly exposed to 4 bar H_2 until a single hydride appeared at δ −23.22. This was then characterised by NMR at 245 K.

^{1}H (500 MHz, methanol-d_4, 245 K) δ: 8.21 (s, 2H, H-19 and H-23), 8.19 (s, 2H, H-2 and H-6), 7.88 (tt, J = 8.49, 2.10 Hz, 1H, H-4), 7.77 (tt, J = 9.15, 2.40 Hz, 1H, H-21), 7.27 (s, H-9), 6.78 (s, 4H, H-12), 2.25 (s, 6H, H-15), 2.09 (s, 12H, H-14 and H-16), − 23.22 (s, 2H, H-24).

^{13}C (125.8 MHz, methanol-d_4, 245 K) δ: 159.6 (C-3 and C-5), 148.3 (C-7), 141.48 (C-19 and C-23), 136.8 (C-10), 135.1 (C-5), 122.94 (C-9), 112.72 (C-4), 112.02 (C-21), 19.67 (C-15), 17.59 (C-14).

^{15}N (50.7 MHz, methanol-d_4, 245 K) δ: 261.6 (N-1), 243.8 (N-18), 194.97 (N-7).

^{19}F (470.6 MHz, methanol-d_4, 245 K) δ: −124.77 (F-26), −124.35 (F-25).

Characterisation of [Ir(H)$_2$(fluoropyrazine)$_3$(IMes)]Cl.

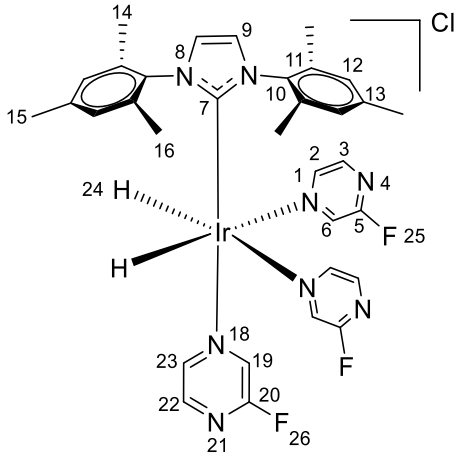

Figure A.16 – Structure of [Ir(H)$_2$(fluoropyrazine)$_3$(IMes)]Cl complex.

[IrCl(COD)(IMes)] (5 mM) and fluoropyrazine (500 mM) were dissolved in methanol-d_4 (0.6 mL) at 293 K and degassed using a freeze-pump-thaw method. The sample was then exposed to 4 bar (absolute) H_2. The sample was then repeatedly exposed to 4 bar H_2 until a hydride appeared at δ −22.20. This was then characterised by NMR at 245 K.

^{1}H (500 MHz, methanol-d_4, 245 K) δ: 8.52 (t, J = 2.70 Hz, 1H, H-2) 8.39 (dd, J = 1.13 and 5.89 Hz, 1H, H-19), 8.25 (d, J = 2.77, 1H, H-3), 8.15 (d, J = 6.10 Hz, 1H, H-6), 8.10 (s, 1H, H-23), 7.97 (d, J = 3.33 Hz, 1H, H-22), 7.33 (s, 2H, H-9), 6.73 (s, 4H, H-12), 2.26 (s, 6H, H-15), 2.09 (s, 12H, H-14 and H-16), − 22.20 (s, 2H, H-24).

^{13}C (125.8 MHz, methanol-d_4, 245 K) δ: 161.25 (C-5), 148.00 (C-7), 147.28 (C-23), 147.20 (C-20), 145.54 (C-2), 144.24 (C-22), 143.72 (C-13), 140.40 (C-19), 139.70 (C-16), 139.20 (C-11), 136.53 (C-10), 135.25 (C-13), 128.40 (C-12), 123.23 (C-9), 19.54 (C-15), 17.60 (C-14 and C-16).

^{15}N (50.7 MHz, methanol-d_4, 245 K) δ: 291.4 (N-21), 290.90 (N-4), 283.70 (N-1), 266.25 (N-18), 194.83 (N-8).

^{19}F (470.6 MHz, methanol-d_4, 245 K) δ: −78.35 (F-26), −77.91 (F-25).

Characterisation of [Ir(H)$_2$(5-fluoropyridine-3-carboxylic acid)$_3$(IMes)]Cl.

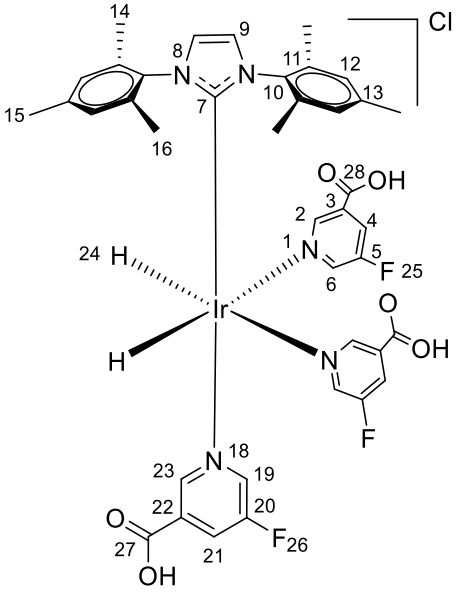

Figure A.17 – Structure of [Ir(H)$_2$(5-fluoro-3-carboxylic acid)$_3$(IMes)]Cl complex.

[IrCl(COD)(IMes)] (5 mM) and 5-fluoropyridine-3-carboxylic acid (500 mM) were dissolved in methanol-d_4 (0.6 mL) at 293 K and degassed using a freeze-pump-thaw method. The sample was then exposed to 4 bar (absolute) H_2. The sample was then repeatedly exposed to 4 bar H_2 until a hydride appeared at δ −22.58. This was then characterised by NMR at 245 K.

^{1}H (500 MHz, methanol-*d*4, 245 K) δ: 8.88 (s, 1H, H-2), 8.73 (s, 1H, H-20), 8.51 (s, 1H, H-21), 8.40 (s, 1H, H-6), 8.28 (s, 1H, H-4), 8.22 (s, 1H, H-23), 7.29 (s, 2H, H-9), 6.73 (s, 4H, H-12), 2.21 (s, 6H, H-15), 2.09 (s, 12H, H-14 and H-16), − 22.58 (s, 2H, H-24).

^{13}C (125.8 MHz, methanol-d_4, 245 K) δ: 153.99 (C-19), 151.04 (C-2), 149.58 (C-7), 146.23 (d, *J* = 33 Hz, C-6), 146.2 (C-21), 139.66 (C-13), 136.88 and 137.62 (C-11), 134.95 (C-10), 128.53 (C-12), 124.35 (C-3), 122.97 (C-9), 19.62 (C-15), 17.63 (C-14 and C-16).

^{15}N (50.7 MH, z methanol-d_4, 245 K) δ: 259.8 (N-1)

^{19}F (470.6 MHz, methanol-d_4, 245 K) δ: −126.67 (F-26), −123.59 (F-25).

Characterisation of [Ir(H)$_2$(5-fluoropyridine-3-carboxylic acid)$_3$(IMes)]Cl in the presence of Cs_2CO_3.

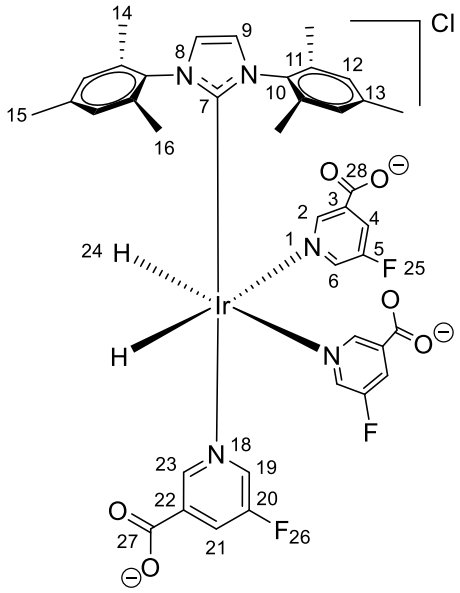

Figure A.18 – Structure of [Ir(H)$_2$(5-fluoro-3-carboxylic acid)$_3$(IMes)]Cl, in the presence of Cs_2CO_3.

[IrCl(COD)(IMes)] (5 mM), 5-fluoropyridine-3-carboxylic acid (500 mM) and Cs_2CO_3 (100 mM) were dissolved in methanol-d_4 (0.6 mL) at 293 K and degassed using a freeze-pump-thaw method. The sample was then exposed to 4 bar (absolute) H_2. The sample was then repeatedly exposed to 4 bar H_2 until a hydride appeared at δ −22.66. This was then characterised by NMR at 245 K.

^{1}H (500 MHz and 400 MHz, methanol-d_4, 245 K) δ: 8.87 (s, 1H, H-2), 8.79 (s, 1H, H-19), 8.15 (s, 1H, H-6), 8.05 (s, 1H, H-23), 7.98 (s, 1H, H-4), 7.93 (s, 1H, H-21), 7.22 (s, 2H, H-9), 6.69 (s, 4H, H-12), 2.20 (s, 6H, H-15), 2.08 (s, 12H, H-14 and H-16), − 22.66 (s, 2H, H-24).

^{13}C (125.8 MHz and 100.6 MHz, methanol-d_4, 245 K) δ: 154.15 (C-19), 151.00 (C-2), 144.3 (C-6), 144.00 (C-23), 136.72 (C-11), 128.35 (C-12), 123.15 (C-4), 122.61 (C-9), 19.72 (C-15^s), 17.76 (C-14 and C-16).

^{15}N (50.7 MHz and 40.6 MHz, methanol-d_4, 245 K) δ: 241.0 (N-18), 258.0 (N-1), 194.6 (N-8).

^{19}F (470.6 MHz and 376.5 MHz, methanol-d_4, 245 K) δ: −125.67 (F-26), −125.99 (F-25).

Characterisation of [IrCl(H)$_2$(3,5-difluoropyryridine)$_2$(IMes)].

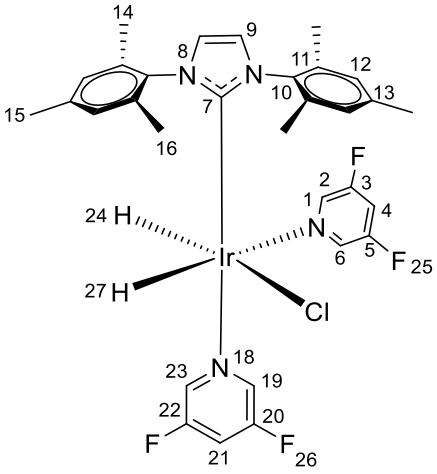

Figure A.19 – Structure of [IrCl(H)$_2$(3,5-difluoropyridine)$_2$(IMes)] complex.

[IrCl(COD)(IMes)] (5 mM) and 3,5-difluoropyridine (500 mM) were dissolved in methanol-d_4 (0.6 mL) at 293 K and degassed using a freeze-pump-thaw method. The sample was then exposed to 4 bar (absolute) H_2. The sample was then repeatedly exposed to 4 bar H_2 until two hydrides appeared at δ −23.94 and −24.69. This was then characterised by NMR at 245 K.

^{1}H (500 MHz, methanol-d_4, 245 K) δ: 8.66 (d, J = 2.16 Hz, 2H, H-19 and H-23), 8.18 (s, br, 2H, H-2 and H-6), 7.60 (m, 1H, H-4), 7.06 (s, 2H, H-9), 6.86 and 6.77 (s, 4H, H-12), 2.25 (s, 12H, H-14 and H-16), 2.22 and 2.20 (s, 6H, H-15), − 23.94 (d, 1H, J = 7.82 Hz, H-27), − 24.69 (d, 1H, J = 8.3 Hz, H-24).

^{13}C (125.8 MHz, methanol-d_4, 245 K) δ: 159.3 (C-5), 159.0 (C-3), 150.05 (C-7), 140.53 (C-19 and C-23), 139.65 (C-2 and C-6), 138.33 (C-10), 135.9 and 135.5 (C-11), 128.25 and 128.18 (C-6), 121.92 (C-7), 111.8 (C-21), 110.20 (C-4), 17.84 (C-14 and C-15), 17.68 and 17.50 (C-15).

^{15}N (50.7 MHz, methanol-d_4, 245 K) δ: 269.0 (N-1), 247.4 (N-18), 193.4 (N-8).

^{19}F (470.6 MHz, methanol-d_4, 245 K) δ: −124.9 (F-26), −124.16 (F-25).

Characterisation of [IrCl(H)$_2$(fluoropyrazine)$_2$(IMes)].

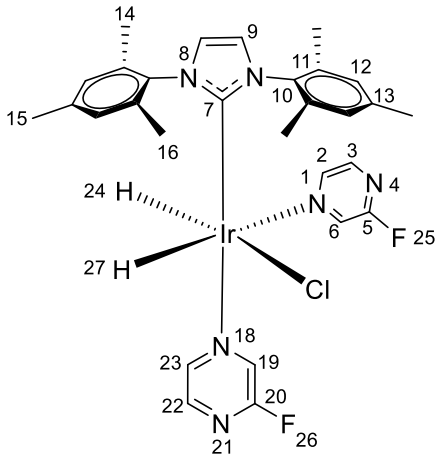

Figure A.20 – Structure of [IrCl(H)$_2$(fluoropyrazine)$_3$(IMes)] complex.

[IrCl(COD)(IMes)] (5 mM) and fluoropyrazine (500 mM) were dissolved in methanol-d_4 (0.6 mL) at 293 K and degassed using a freeze-pump-thaw method. The sample was then exposed to 4 bar (absolute) H_2. The sample was then repeatedly exposed to 4 bar H_2 until a single hydride appeared at δ −22.73 and −24.35. This was then characterised by NMR at 245 K.

^{1}H (500 MHz, methanol-d_4, 245 K) δ: 8.78 (s, 1H, H-6), 8.69 (m, 1H, H-3), 7.88 (d, J = 3.2 Hz, 1H, H-2), 7.11 (s, 2H, H-9), 6.87 and 6.71 (s, br, 4H, H-12), 2.25 (s, 6H, H-15), 2.22 and 2.18 (s, 12H, H-14 and H-15), − 22.73 (s, br, 1H, H-24), − 24.35 (s, br, 1H, H-27).

^{13}C (125.8 MHz, methanol-d_4, 245 K) δ: 161.10 (C-5), 150.72 (C-7), 147.96 (C-3), 142.57 (C-2), 138.5 (C-6), 138.43 and 138.22 (C-11), 136.07 (C-10), 135.59 (C-13), 127.98 (C-12), 122.09 (C-9), 19.71 (C-15), 17.60 and 17.37 (C-14 and C-16).

^{15}N (50.7 MHz, methanol-d_4, 245 K) δ: 292.401 (N-21), 290.00 (N-4), 272.97 (N-18), 272.26 (N-1), 193.47 (N-8).

^{19}F (470.6 MHz, methanol-d_4, 245 K) δ: −80.85 (F-26), −79.7 (F-25).

A.10 Exchange mechanism for substrate and hydride exchange (Chapter 3)

Modelling substrate exchange for a *tris* substituted complex, $[Ir(H)_2(IMes)(sub)_3]Cl$

The accepted method of substrate exchange within the SABRE mechanism is outlined in Figure A.21, where the substrates are now 3-fluoropyridine or 5-fluoropyridine-3-carboxylic acid in the presence of Cs_2CO_3.

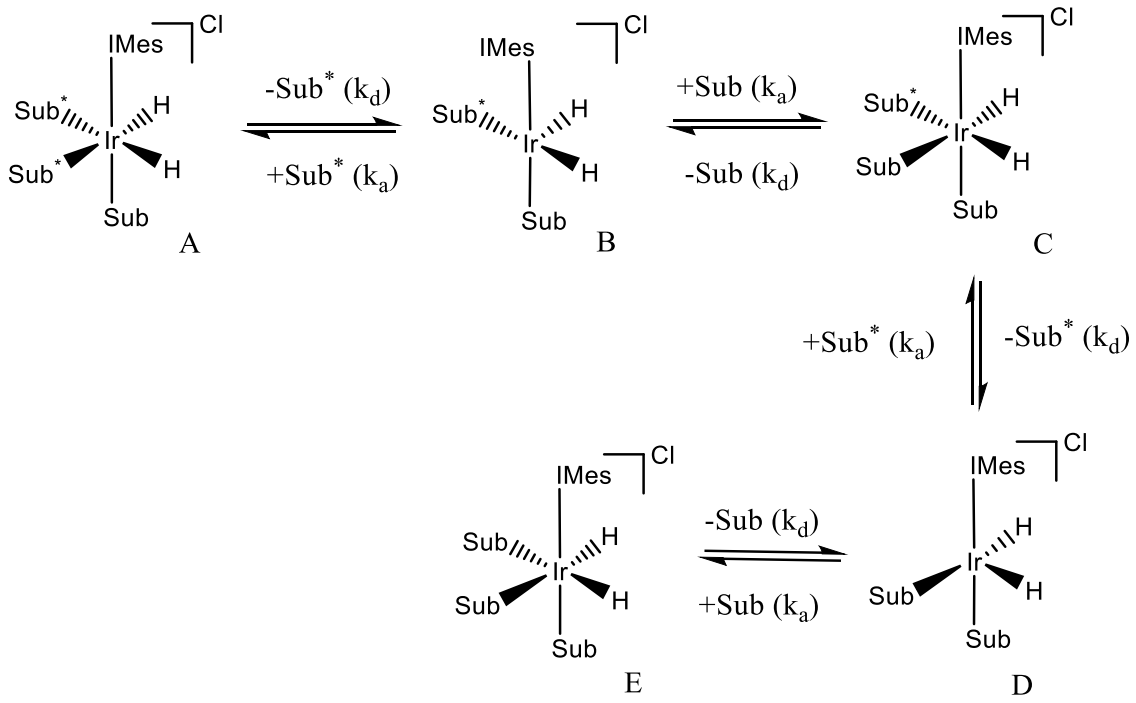

Figure A.21 – Exchange pathway for substrate loss for $[Ir(H)_2(sub)(IMes)]Cl$ during the SABRE process where the substrate is 3-fluoropyridine or 5-fluoropyridine-3-carboxylic acid in the presence of base.

EXSY data was collected to investigate this behaviour. The rate equations used to fit the resulting data are based on the mechanism shown in Figure A.21 (above) and described using equations A.5 and A.11.

$$[A]_t = [A]_0 - 2k_d[A]_0\delta t + k_a[B]_0\delta t \qquad (A.5)$$

$$[B]_t = [B]_0 + 2k_d[A]_0\delta t + 2k_d[C]_0\delta t \; - k_a[B]_0\,[Sub^*]\delta t - k_a[B]_0\,[Sub^*]\delta t \qquad (A.6)$$

$$[C]_t = [C]_0 + k_a[B]_0[Sub]\delta t + k_a[D]_0\,[Sub^*]\delta t - 2k_d[C]_0\,\delta t \qquad (A.7)$$

$$[D]_t = [D]_0 + 2k_d[C]_0\delta t + 2k_d[E]_0\,\delta t - k_a[D]_0[Sub]\delta t - k_a[D]_0[Sub^*]\delta t \qquad (A.8)$$

$$[E]_t = [E]_0 + k_a[B]_0[Sub]\delta t - 2k_d[E]_0\delta t \qquad (A.9)$$

$$[Sub^*]_t = [Sub^*]_0 + 2k_d[A]_0\delta t - k_a[B]_0[Sub^*]\delta t + k_d[C]_0\,\delta t - k_a[D]_0[Sub]\delta t \quad (A.10)$$

$$[Sub]_t = [Sub]_0 - k_a[B]_0[Sub]\delta t + k_d[C]_0\delta t - k_a[D]_0[Sub]\delta t + 2k_d[E]_0\delta t \qquad (A.11)$$

Using equations A.5 and A.11, simulated rate equations was written into Excel as shown in Table A.7 and therefore the concentrations of bound substrate, [A] and free substrate, [B] could be calculated where t = 0 to 0.5 s. As a rate constant is required (k_d) estimated values had to be used. At t = 0, it was assumed that the concentration of A was 100% and that of B was 0%.

Table A.7 – The cell inputs used for the Excel spreadsheet to calculate the simulated rate data for substrate exchange for the *tris* complex when the substrate is either 3-fluoropyridine or 5-fluoropyridine-3-carboxylic acid.

A	B	C
Time (s)	[A]	[B]
0	100	0
0.001	=@INDEX(MMULT($W60:$AA60,$B$15:$F$19)*($A61-$A60)+W60,1)	=@INDEX(MMULT($W60:$AA60,$B$15:$F$19)*($A61-$A60)+X60,2)

From these equations, a plot of simulated rate data can be obtained as shown in Figure A.22. This is achieved in conjunction with the Microsoft Excel SOLVER package. The least squares regression was calculated as described in Appendix section A.2. An example of the least squares regression is given for the substrate exchange for 3-fluoropyridine at 280 K in Table A.8.

Table A.8 – Least squared regression error for data obtained at 280 K for the substrate exchange for the complex $[Ir(H)_2(IMes)(sub)_3]Cl$ when the substrate is 3-fluoropyridine.

time(s)	[A]	[B]	[A]	[B]	sum
0	100	0			0
0.005	98.89	0.14	0.03	0.65	0.69
0.05	88.00	9.40	6.44	0.01	6.52
0.075	82.92	15.12	8.78	1.49	10.28
0.1	78.86	17.14	6.23	1.37	7.71
0.125	74.48	21.81	6.31	0.53	6.87
0.15	70.90	26.02	3.77	0.31	4.08
0.175	68.19	28.31	0.52	4.28	4.80
0.2	63.76	32.34	2.18	2.58	4.76
0.225	61.74	35.34	0.01	3.72	3.84
0.25	58.61	39.52	0.01	0.65	1.04
0.275	56.43	41.15	0.43	3.95	4.71
0.3	52.75	44.19	0.15	2.28	2.63
0.35	48.95	49.48	0.12	0.39	1.35
0.4	44.08	53.75	0.75	0.01	1.41
0.45	41.35	58.04	0.51	2.50	4.69
0.5	38.21	60.53	2.66	3.56	7.51
					72.90

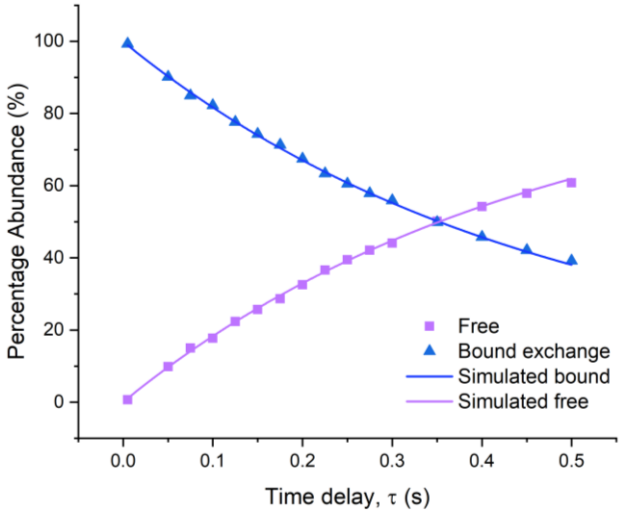

Figure A.22 – Showing the experimental and simulated change in percentage abundance of the free and bound substrate 3-fluoropyridine at 280 K. Simulated data was achieved using the formula given in equations A.5 to A.11.

The error for the rate constants was calculated using the Jack knife method as described in Chapter 7, section 7.2.9, the Jack-knife errors for the substrate exchange at 280 K for 3-fluoropyridine are given in Table A.9Table A.3.

Table A.9 - Jack-knife error for the experimental data obtained for substrate exchange of the complex $[Ir(H)_2(IMes)(sub)_3]Cl$ at 280 K where sub = 3-fluoropyridine.

	A
All	1.883
0.005	1.869
0.05	1.862
0.075	1.853
0.1	1.862
0.125	1.859
0.15	1.860
0.175	1.877
0.2	1.870
0.225	1.879
0.25	1.873
0.275	1.880
0.3	1.873
0.35	1.869
0.4	1.869
0.45	1.871
0.5	1.883
Error	0.002

From these rate data activation parameters could be obtained from the corresponding Eyring plots which are shown in Figure A.23. The resulting activation parameters are presented in Chapter 3 section 3.4.

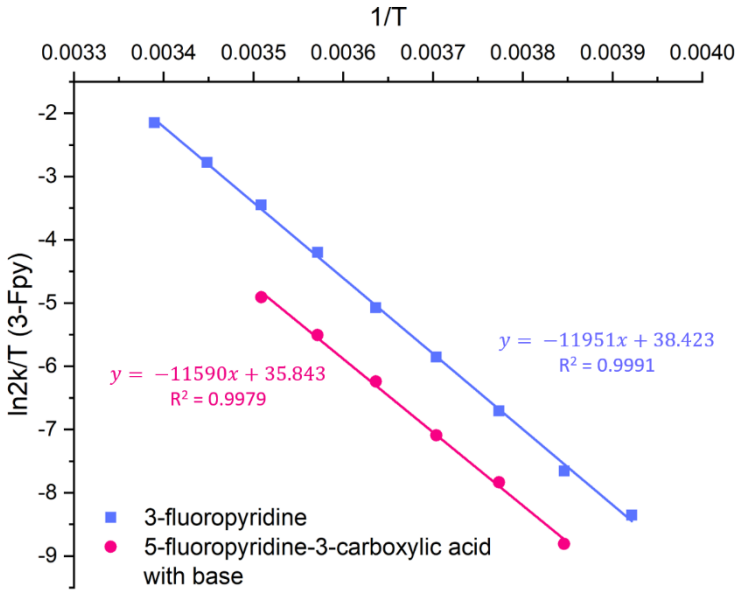

Figure A.23 – Eyring plots for the loss of 3-fluoropyridine or 5-fluoropyridine-3-carboxylic acid in the presence of base, from $[Ir(H)_2(IMes)(sub)_3]Cl$. These data were then used to calculate the activation parameters for ligand exchange. The linear regression analysis results are also presented.

Modelling substrate exchange in $[Ir(H)_2(IMes)(sub)_3]Cl$ in the presence of complex $[IrCl(H)_2(IMes)(sub)_2]$

As demonstrated with pyrimidine, there can be other exchange pathways present. Within the substrate exchange for the complex $[IrCl(H)_2(IMes)(sub)_2]$, where sub is the substrate 3-fluoropyridine, 3,5-difluoropyridine, fluoropyrazine or 5-fluoropyridine-3-carboxylic acid. Unfortunately, due to peak overlap it was not possible to reliably fit the collective data to any exchange mechanism. However, when only one species is present then this can be modelled by the scheme above (Figure A.21).

Modelling hydride exchange for $[Ir(H)_2(IMes)(sub)_3]Cl$

A series of 1D-EXSY experiments were used to examine H_2 loss from $[Ir(H)_2$(5-fluoropyridine-3-carboxylic acid$)_3$(IMes)]Cl in the presence of Cs_2CO_3. The hydride ligand exchange was modelled in a similar way to that previously described for $[Ir(H)_2(IMes)(sub)_3]Cl$, as illustrated in Figure A.4 and Figure A.5. As only complex **A** forms with $[Ir(H)_2$(5-fluoropyridine-3-carboxylic acid$)_3$(IMes)]Cl in the presence of Cs_2CO_3, this mechanism can be simplified further as shown in Figure A.24 and using the equations A.12 to A.14.

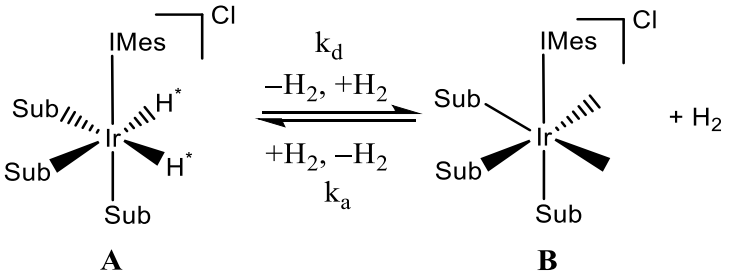

Figure A.24 - Hydride ligand exchange mechanism for $[Ir(H)_2(DMSO)_3(IMes)]$. To examine this mechanism, the loss of both hydride and DMSO was investigated *via* the 1D EXSY protocol.

$$[A]_t = [A]_0 - k_a[A]_0\delta t + k_a[B]_0[H_2]_0\delta t \quad (A.12)$$

$$[B]_t = [B]_0 + k_a[A]_0\delta t + k_a[B]_0[H_2]_0\delta t \quad (A.13)$$

$$[H_2]_t = [H_2]_0 + k_a[A]_0\delta t - k_a[B]_0[H_2]_0\delta t \quad (A.14)$$

A simple connection to H_2 was evident in the resulting spectra. Using equations A.12 to A.14, simulated rate equations were written into Excel as shown in Table A.10 and therefore the concentrations of bound hydrogen, [A] and free hydrogen, [B] could be calculated where t = 0 to

1.0 s. As with previous rate models, a rate constant is required (k_d) and again estimated values had to be used. At t = 0, it was assumed that the concentration of A was 100% and that of B was 0%.

Table A.10 - The cell inputs used for the Excel spreadsheet to calculate the simulated rate data for hydrogen exchange for the *tris* complex [Ir(H)$_2$(5-fluoropyridine-3-carboxylic acid)$_3$(IMes)]Cl in the presence of Cs_2CO_3.

A	B	C
Time (s)	[A]	[B]
0	100	0
0.001	=((+($B$5*C22)-($B$6*B22))*(A23-A22))+B22	=((+($B$6*B22)-($B$5*C22))*(A23-A22))+C22

These data fit a simple exponential growth and decay as detailed in Figure A.25 using the Microsoft Excel SOLVER package.

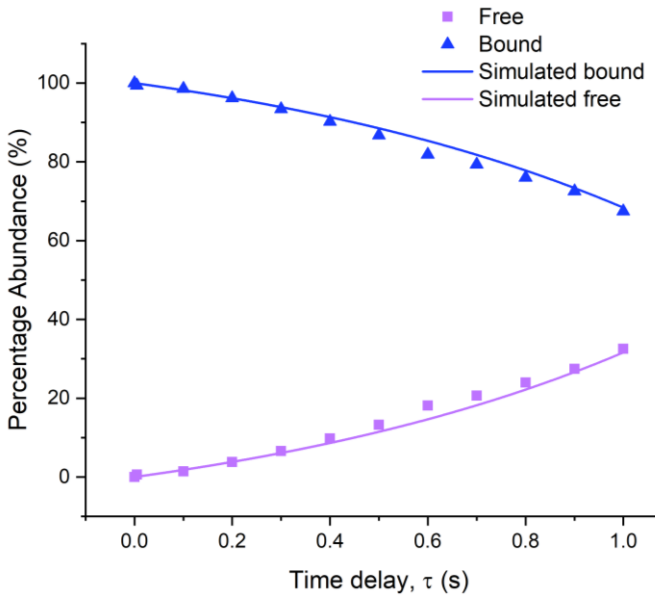

Figure A.25 – The experimental and simulated change in percentage abundance of free hydrogen and bound hydride in the complex [Ir(H)$_2$(5-fluoropyridine-3-carboxylic acid)$_3$(IMes)] in the presence of Cs_2CO_3 in methanol-d_4 (0.6 mL) at 280 K. Simulated data was achieved using the formula given in equations A.12 to A.14.

The least squares regression was calculated as described in Appendix section A.2. An example of the least squares regression is given for the substrate exchange for 5-fluoropyridine-3-carboxylic acid in the presence of $CsCO_3$ at 280 K in Table A.11.

Table A.11 - Least squared regression error for data obtained at 280 K for the hydride exchange for the complex $[Ir(H)_2(IMes)(sub)_3]Cl$ when the substrate is 5-fluoropyridine-3-carboxylic acid in the presence of $CsCO_3$.

time(s)	[A]	[B]	[A]	[B]	sum
0	100	0			0
0.005	99.37	0.63	0.29	0.01	0.30
0.1	98.55	1.45	0.13	1.40	1.53
0.2	96.21	3.79	0.01	5.69	5.69
0.3	93.38	6.62	0.26	5.34	5.61
0.4	90.25	9.75	1.24	4.09	5.33
0.5	86.78	13.22	3.04	2.98	6.02
0.6	81.89	18.11	11.95	2.04	13.99
0.7	79.34	20.66	6.04	0.01	6.05
0.8	76.04	23.96	3.20	2.29	5.48
0.9	72.54	27.46	0.71	7.04	7.75
1.0	67.49	32.51	17.01	17.01	34.01
					57.75

The error for the rate constants was calculated using the Jack knife method as described in Chapter 7, section 7.2.9, the Jack-knife errors for the substrate exchange at 280 K for 5-fluoropyridine-3-carboxylic acid in the presence of $CsCO_3$ are given in Table A.12Table A.3.

Table A.12 - Jack-knife error for the experimental data obtained for hydride exchange for the complex $[Ir(H)_2(IMes)(sub)_3]Cl$ at 280 K where sub = 5-fluoropyridine-3-carboxylic acid in the presence of $CsCO_3$.

	A
All	0.171
0.005	0.171
0.1	0.173
0.2	0.178
0.3	0.178
0.4	0.175
0.5	0.171
0.6	0.164
0.7	0.166
0.8	0.171
0.9	0.155
1.0	0.171
Error	0.007

From the resulting rate data activation parameters could be obtained from the Eyring plot as shown in Figure A.26. These are presented in Chapter 3 section 3.4.

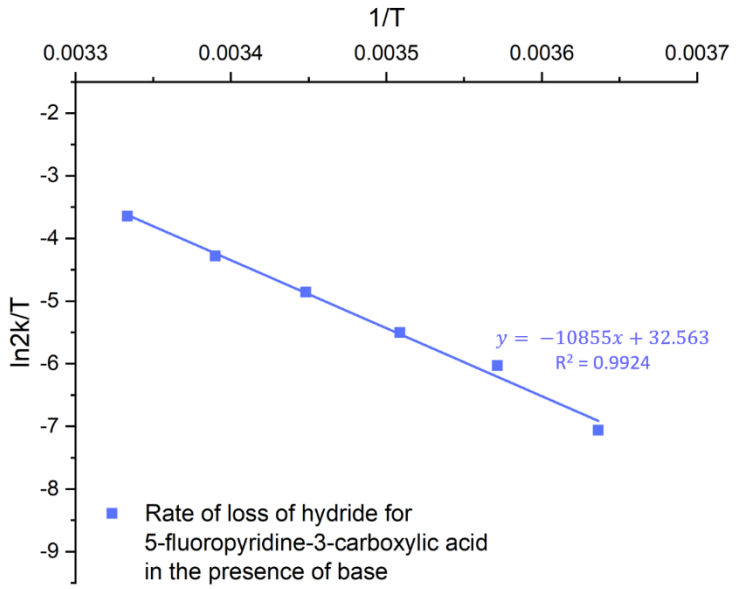

Figure A.26 – Eyring plot for the loss of H_2 from[Ir(H)$_2$(5-fluoropyridine-3-carboxylic acid)$_3$(IMes)]Cl in the presence of Cs_2CO_3. These data were used to calculate the activation parameters for H_2 loss.

Modelling hydride exchange for [Ir(H)$_2$(IMes)(sub)$_3$]Cl *via* the intermediate [Ir(H)$_2$(H$_2$)(IMes)(sub)$_2$]Cl

Hydride exchange was also investigated for the other fluorinated *N*-heterocycles, through the mechanism now was altered to allow for [IrCl(H)$_2$(IMes)(sub)$_2$] as described earlier. The full scheme is shown in Figure A.27, but the simplified version of Figure A.5 was used for this purpose as here complex **A** and complex **B** could interconvert and lose hydrogen. Figure A.28 shows a typical result for 3-fluropyrazine.

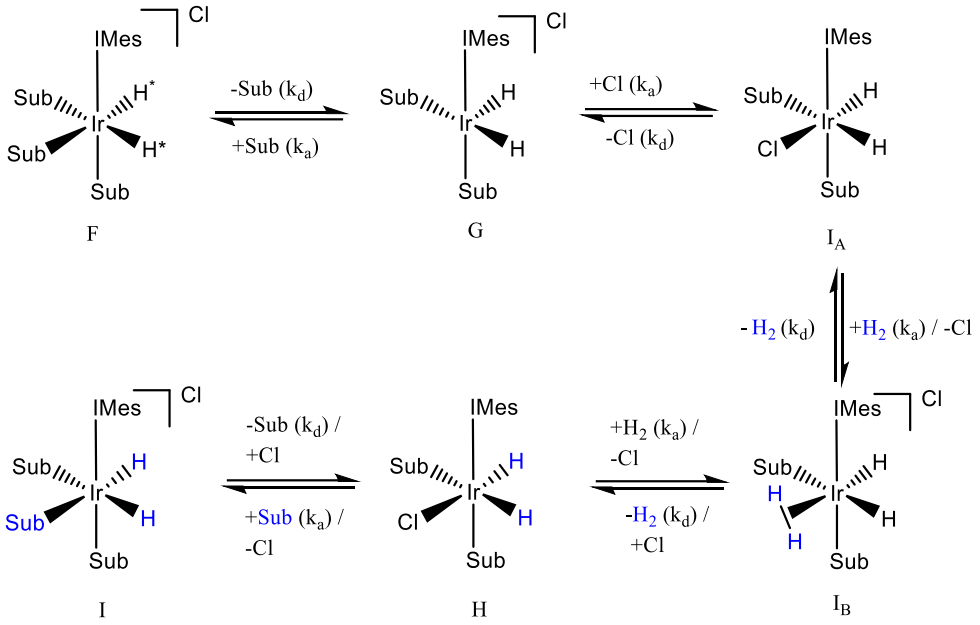

Figure A.27 – Proposed hydride exchange mechanism of the SABRE experiment with substrates 2 to 6, including the complex [IrCl(H)$_2$(IMes)(sub)$_2$].

Using equations A.1 and A.2, from Appendix section A.2, simulated rate equations were written into Excel as shown in Table A.13 to calculate the concentrations of [A] interchange to [B], the interchange of hydrides and [H_2] could be calculated where t = 0 to 0.5 s. Rate constants were again estimated to allow the data to be fitted. At t = 0, it was assumed that the concentration of [A_1] was 100% and that of the intermediates and [H_2] was 0%.

Table A.13 – The cell inputs used for the Excel spreadsheet to calculate the simulated rate data for hydride exchange for the *tris* complex, [Ir(H)$_2$(IMes)(sub)$_3$]Cl *via* the intermediate [Ir(H)$_2$(H$_2$)(IMes)(sub)$_2$], where the substrate is fluoropyrazine.

A	B	C	D	E
Time (s)	[A_1] interchange to [B_1]	[B_1] interchange to [A_1]	Interchange of hydrides	[H_2]
0	100	0	0	0
0.005	=@INDEX(MMULT($B64:$F64,$B$15:$F$19)*($A65-$A64)+B64,1)	=@INDEX(MMULT($B64:$F64,$B$15:$F$19)*($A65-$A64)+C64,2)	=@INDEX(MMB64:$F64,$B$15:$19)*($A65-A64)+D64,3)	=@INDEX(MMULT($B64:$F64,$B$15:$F$19)*($A65-$A64)+E64,4)

Both hydrides were used to simulate the data. However, for the intermediate hydride [B] was set to 100, rather than [A].

Table A.14 - The cell inputs used for the Excel spreadsheet to calculate the simulated rate data for hydride exchange for the intermediate complex $[Ir(H)_2(H_2)(IMes)(sub)_2]$ to the *tris* complex, $[Ir(H)_2(IMes)(sub)_3]Cl$ when the substrate is fluoropyrazine.

A	B	C	D	E
Time (s)	$[A_1]$ interchange to $[B_1]$	$[B_1]$ interchange to $[A_1]$	Interchange of hydrides	$[H_2]$
0	0	100	0	0
0.005	=@INDEX(MMULT($W76:$AA76,$B$15:$F$19)*($A77-$A76)+W76,1)	=@INDEX(MMULT($W76:$AA76,$B$15:$F$19)*($A77-$A76)+X76,2))	=INDEX(MMULT($W76:$AA76,$B$15:$F$19)*($A77-$A76)+Y76,3)	=INDEX(MMULT($W76:$AA76,$B$15:$F$19)*($A77-$A76)+Z76,4)

The experimaental and simulated data were then fitted to a simple exponential growth and decay as detailed in Figure A.28 using the Microsoft Excel SOLVER package

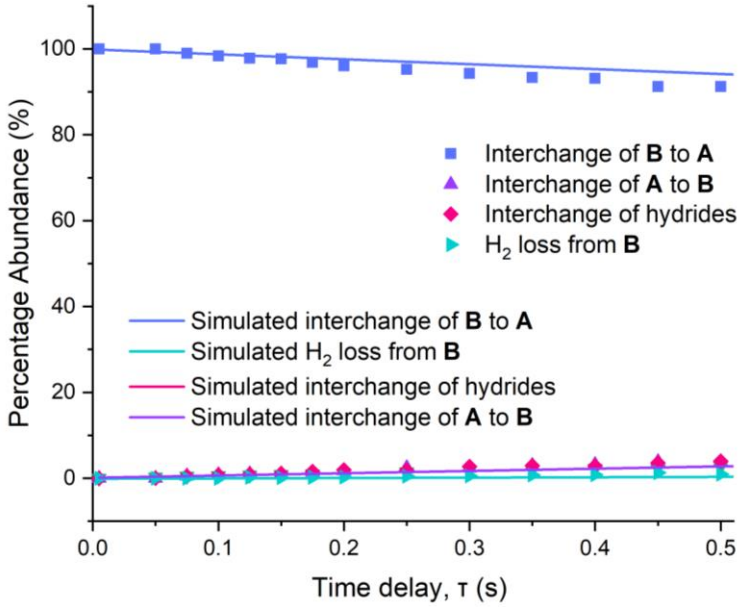

Figure A.28 – Showing the experimental and simulated change in percentage abundance of the free and bound hydride resonances of fluoropyrazine at 265 K. Simulated data was achieved using the formula given in equations A.1 and A.2.

Simulated interchange for both the hydrides and that of **A** to **B** are very similar and therefore only the interchange of hydride can be seen on the graph.

The least squares regression was calculated as described in Appendix section A.2. An example of the least squares regression is given for hydride exchange *via* interchange of **A** and **B** and the interchange of hydrides for fluoropyrazine at 265 K in Table A.15.

Table A.15 - Least squared regression error for data obtained at 265 K for the hydride exchange for the complex [Ir(H)$_2$(IMes)(sub)$_3$]Cl *via* interchange of A **and** B **and the interchange of hydrides when the substrate is fluoropyrazine.**

time(s)	[A]	[B]	[C]	[D]	[A]	[B]	[C]	[D]	sum
0	100	0	0	0			-	-	0
0.005	100	0	0	0	0.003	0.0009	0.0009	3.2E^{-10}	0.006
0.05	100	0	0	0	0.37	0.09	0.09	5.8E^{-06}	0.56
0.075	98.98	0.52	0.50	0	0.01	0.01	0.002	3.0E^{-05}	0.018
0.1	98.38	0.82	0.81	0	0.16	0.05	0.04	9.5E^{-05}	0.25
0.125	97.82	0.10	0.95	0.24	0.45	0.062	0.04	0.05	0.59
0.15	97.70	1.03	1.14	0.13	0.24	0.02	0.06	0.014	0.33
0.175	96.85	1.41	1.54	0.21	1.07	0.134	0.244	0.034	1.48
0.2	96.08	1.75	1.91	0.26	2.26	0.314	0.514	0.054	3.14
0.25	95.25	2.45	1.85	0.45	3.04	0.96	0.14	0.154	4.29
0.3	94.31	2.41	2.74	0.53	4.36	0.43	0.98	0.20	5.97
0.35	93.32	2.96	2.95	0.77	6.22	0.86	0.84	0.43	8.35
0.4	93.12	3.20	2.88	0.80	4.46	0.79	0.33	0.42	6.00
0.45	93.23	3.90	3.57	1.30	11.74	1.76	0.98	1.22	15.71
0.5	91.24	3.88	3.95	0.94	8.10	1.08	1.23	0.49	10.89
									57.57

The error for the rate constants was calculated using the Jack knife method as described in Chapter 7, section 7.2.9, the Jack-knife errors for the hydride exchange at 265 K for fluoropyrazine *via* interchange of **A** and **B** and the interchange of hydrides are given in Table A.16Table A.3.

Table A.16 - Jack-knife error for the experimental data obtained for hydride exchange *via* interchange of A **and** B **and the interchange of hydrides for the complex [Ir(H)$_2$(IMes)(sub)$_3$]Cl at 265 K where sub = fluoropyrazine.**

	[A_1] interchange to [B_1]	[B_1] interchange to [A_1]	Interchange of hydrides	[H_2]
All	0.6401	0.0612	0.0133	0.1623
0.005	0.6389	0.5960	0.0154	0.1623
0.05	0.6394	0.9506	0.0172	0.1625
0.075	0.6373	1.5580	0.0200	0.1630
0.10	0.6368	1.4907	0.0198	0.1629
0.125	0.6385	0.6050	0.0156	0.1618
0.15	0.6412	0.3421	0.0136	0.1638
0.175	0.6341	1.5072	0.0207	0.1630
0.2	0.6399	0.0000	0.0116	0.1624
0.225	0.6383	0.0000	0.0104	0.1633
0.25	0.6428	0.2356	0.0136	0.1594
0.275	0.6388	0.7152	0.0180	0.1634
0.30	0.6376	0.5464	0.0162	0.1615
0.35	0.6365	0.0000	0.0158	0.1617
0.40	0.6392	2.2110	0.0208	0.1603
0.45	0.6389	0.6318	0.0156	0.1623
0.50	0.6389	0.6318	0.0156	0.1623
Error	0.0005	0.1623	0.0007	0.0003

From the rate data collected activation parameters could be obtained from the Eyring plots shown below in Figure A.29. These were used to find the activation parameters for complex **A** ($[Ir(H)_2(IMes)(sub)_3]Cl$) converting to complex **B** ($[IrCl(H)_2(IMes)(sub)_2]$), the formation of H_2 from **B** and the conversion of **B** back to **A**. Activation parameters are presented in Chapter 3 section 3.4.3.

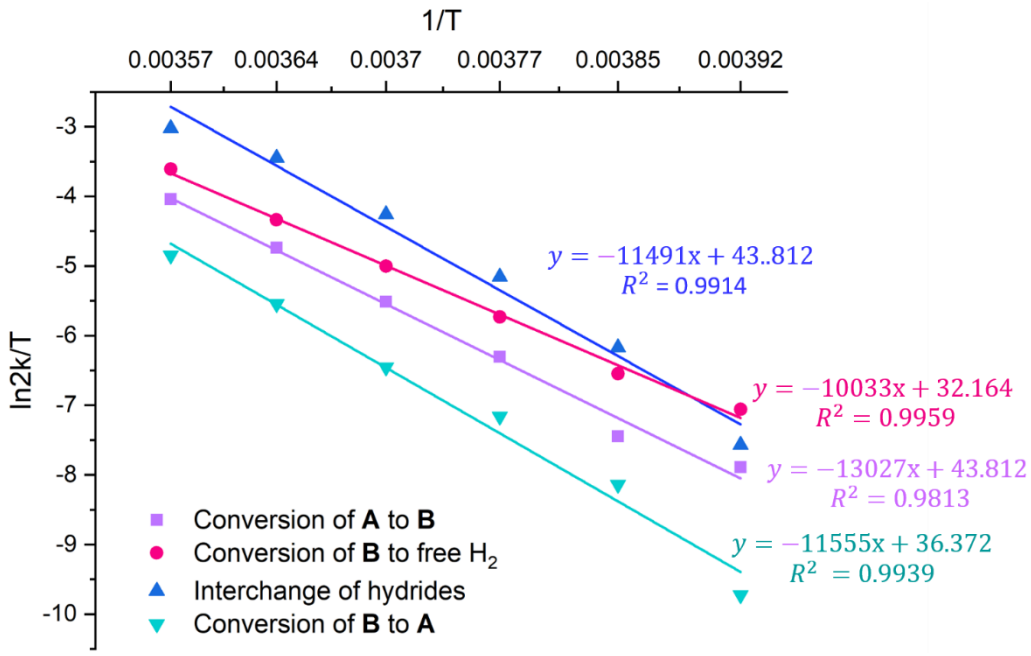

Figure A.29 – Eyring plot of the conversion of complex A to B, the conversion of B to free hydrogen and the conversion of B back to A for the substrate 3,5-difluoropyridine. This plot was then used to calculate the activation parameters for each of these pathways. The linear regression analysis for each process is given in the same colour as that shown in the plot.

Rate data for hydride exchange for the interconversion of the *tris* and *bis* complexes

Table A.17 and Table A.18 show the rate constants for the interconversion complex **A** and complex **B** for the substrates 3-fluoropyridine and fluoropyrazine respectively, as described in the Appendix section above.

Table A.17 – Rate constants for the ligand exchange processes for 3-fluoropyridine (2), in methanol-d_4 as a function of temperature, results *via* selective 1D-EXSY experiments at 500 MHz.

Temp T (K)	Experimental rate constants for the indicated process (s^{-1})			
	$[Ir(H)_2(\mathbf{2})_3(IMes)]Cl$ (rate **A** goes to **B**)	$[IrCl(H)_2(\mathbf{2})_2(IMes)]$ (**B**) (rate H_2 loss)	$[IrCl(H)_2(\mathbf{2})_2(IMes)]$ (**B**) (rate interchange of hydrides)	$[IrCl(H)_2(\mathbf{2})_2(IMes)]$ rate **B** goes to **A**
260	0.037	0.122	0.154	0.199
265	0.112	0.374	0.688	1.231
270	0.275	0.730	1.113	2.345
275	0.652	1.572	2.124	4.816
280	1.538	3.409	4.483	10.157
285	2.837	6.103	8.483	15.439
290	5.703	10.724	9.600	27.832

Table A.18 – Rate constants for the ligand exchange processes for fluoropyrazine (5), in methanol-d_4 as a function of temperature, results *via* selective 1D-EXSY experiments at 500 MHz.

Temp T (K)	Experimental rate constants for the indicated process (s^{-1})			
	$[Ir(H)_2(\mathbf{5})_3(IMes)]Cl$ (rate **A** goes to **B**)	$[IrCl(H)_2(\mathbf{5})_2(IMes)]$ (**B**) (rate H_2 loss)	$[IrCl(H)_2(\mathbf{5})_2(IMes)]$ (**B**) (rate interchange of hydrides)	$[IrCl(H)_2(\mathbf{5})_2(IMes)]$ rate **B** goes to **A**
255	0.000	0.034	0.028	0.006
260	0.000	0.088	0.247	0.000
265	0.061	0.162	0.640	0.013
270	-	-	-	-
275	0.263	0.834	4.135	0.055
280	0.765	1.930	10.213	0.132
285	1.396	3.187	19.591	0.298
290	3.687	5.086	30.459	0.635

A.11 Polarisation transfer field plots for ^{19}F

As described in Chapter 3.6 the flow system was used to collect ^{1}H signal enhancements at varying magnetic fields. These samples were also used, with the flow system to collect polarisation transfer field (PTF) data for ^{19}F on all the fluorinated *N*-heterocycles. Unfortunately, due to fast relaxation times the data is not very accurate. Of the samples tested 3-fluoropyridine, 3,5-difluoropyridine and 5-fluoro-3-carboxylic acid, have been recorded here as their data is as expected, these are presented in Figure A.30 to Figure A.32.

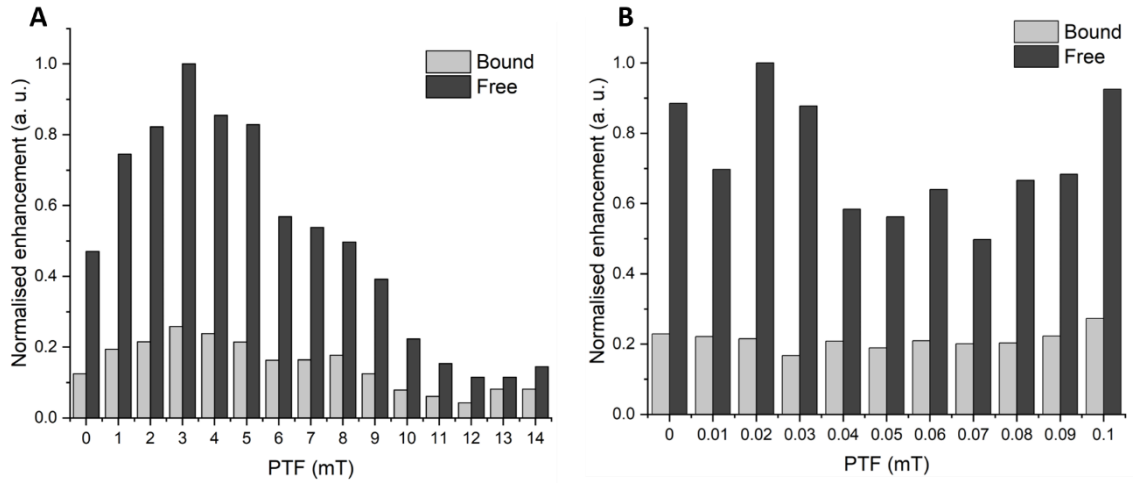

Figure A.30 – PTF plots of 3-fluorpyridine (500 mM) and [IrCl(COD)(IMes)] (25 mM) in methanol-d_4. A) is examining magnetic fields 1-14 mT (0-140 G) and B) is examining magnetic fields 0-1 mT (0-1 G).

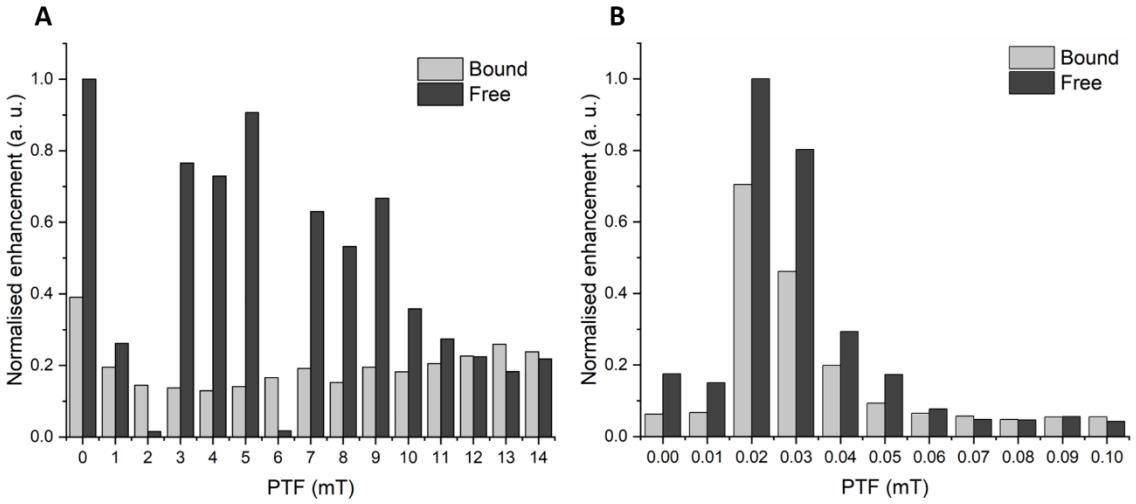

Figure A.31 – PTF plots of 3,5-difluorpyridine (500 mM) and [IrCl(COD)(IMes)] (25 mM) in methanol-d_4. A) is examining magnetic fields 1-14 mT (0-140 G) and B) is examining magnetic fields 0-1 mT (0-1 G).

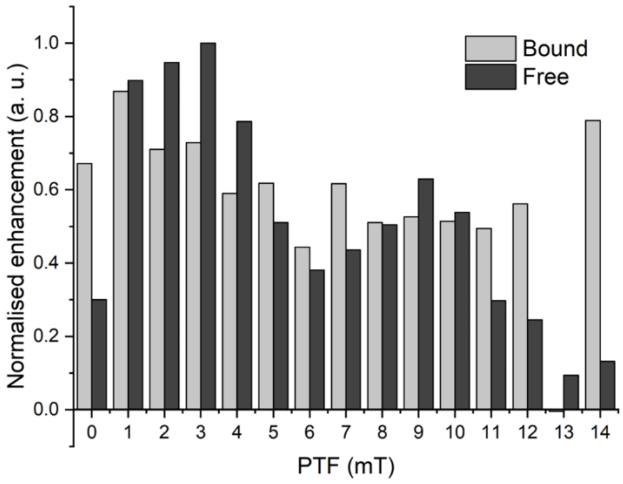

Figure A.32 – PTF plots of fluoropyrazine (500 mM) and [IrCl(COD)(IMes)] (25 mM) in methanol-d_4 examining magnetic fields 1-14 mT (0-140 G).

The optimal PTF for ^{19}F cannot be determined from the PTF plots shown, although theoretically the transfer field was calculated to be 32 mG (0.0032 mT) (see Chapter 3.6). However, what can be confirmed is that the polarisation detected for ^{19}F is going *via* ^{1}H.

A.12 Characterisation of [IrCl(H)$_2$(DMSO)$_2$(IMes)]

Characterisation of all sulfoxide complexes are given below. H_2O addition did not change this data.

Characterisation of [IrCl(H)$_2$(DMSO)$_2$(IMes)] in methanol-d_4

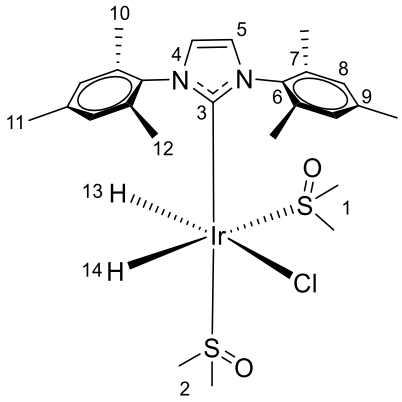

Figure A.33 – Structure of [IrCl(H)$_2$(DMSO)$_2$(IMes)] complex.

[IrCl(COD)(IMes)] (5 mM), sodium oxalate (25 mM) and DMSO (20 mM) were dissolved in methanol-d_4 (0.6 mL) at 293 K and degassed using a freeze-pump-thaw method. The sample was

then exposed to 4 bar (absolute) H_2. The sample was then repeatedly exposed to 4 bar H_2 until hydrides appeared at δ −15.53 and −21.53. This was then characterised by NMR at 245 K.

^{1}H (500 MHz, methanol-d_4, 245 K) δ: 7.24 (s, 2H, H-5), 7.02 (m, 4H, H-8), 3.27 (d, 6H, H-2), 2.83 (s, 6H, H-1), 2.37 (s, 6H, H-11), 2.20 (s, 12H, H-10 and H-12), −15.53 (d, J = 6 Hz, 1H, H-14), −21.53 (d, J = 6 Hz, 1H, H-13).

^{13}C (125.8 MHz, methanol-d_4, 245 K) δ: 152.49 (C-3), 138.43 (C-9), 137.99/136.49 (C-7), 135.22 (C-6), 128.56 (C-8), 123.42 (C-5), 57.26 (C-2), 48.77 (C-1), 19.95 (C-11), 18.34/17.55 (C-10 and C-12).

Characterisation of [IrCl(H)$_2$(DMSO)$_2$(IMes)] in dichloromethane-d_2

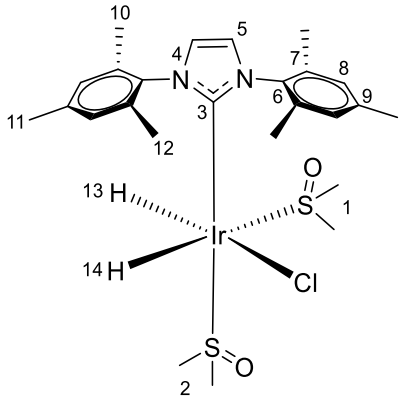

Figure A.34 – Structure of [IrCl(H)$_2$(DMSO)$_2$(IMes)].

[IrCl(COD)(IMes)] (5 mM), sodium oxalate (25 mM) and DMSO (20 mM) were dissolved in dichloromethane-d_2 (0.6 mL) at 293 K and degassed using a freeze-pump-thaw method. The sample was then exposed to 4 bar (absolute) H_2. The sample was then repeatedly exposed to 4 bar H_2 until hydrides appeared at δ −15.73 and −21.27. This was then characterised by NMR at 245 K.

^{1}H (500 MHz, methanol-d_4, 245 K) δ: 6.93 (s, 2H, H-5), 6.97 (m, 4H, H-8), 3.20 and 3.15 (d, 6H, H-2), 3.05 and 2.73 (s, 6H, H-1), 2.37 (s, 6H, H-11), 2.17 and 2.15 (s, 12H, H-10 and H-12), −15.73 (d, J = 6 Hz, 1H, H-14), −21.27 (d, J = 6 Hz, 1H, H-13).

^{13}C (125.8 MHz, methanol-d_4, 245 K) δ: 153.7 (C-3), 138.43 (C-9), 137.99/136.49 (C-7), 135.22 (C-6), 128.44 (C-8), 123.28 (C-5), 58.93 (C-2), 49.9 (C-1), 21.07 (C-11), 18.36 and 18.95 (C-10 and C-12).

Characterisation of [IrCl(H)$_2$(IMes)(PhMeSO)$_2$] in methanol-d_4

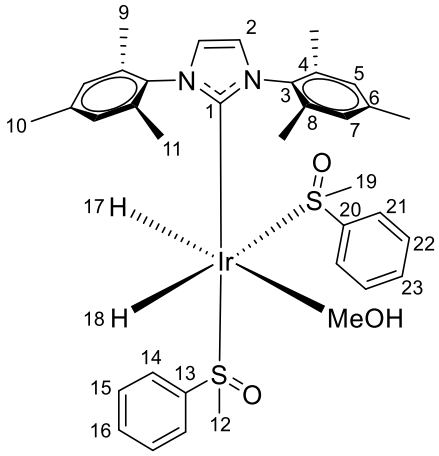

Figure A.35 – Structure of [IrCl(H)$_2$(IMes)(PhMeSO)$_2$)] complex.

[IrCl(COD)(IMes)] (5 mM), sodium oxalate (25 mM) and methyl phenyl sulfoxide (20 mM) were dissolved in dichloromethane-d_2 (0.6 mL) at 293 K and degassed using a freeze-pump-thaw method. The sample was then exposed to 4 bar (absolute) H_2. The sample was then repeatedly exposed to 4 bar H_2 until hydrides appeared at δ −23.42 and −29.52. This was then characterised by NMR at 245 K.

^{1}H (500 MHz, methanol-d_4, 245 K) δ: 7.765 (s, 1H, H-23), 7.648 (s, 2H,H-22), 7.37 (s, 2H, H-2), 7.21 (s, 2H, H-21), 7.20 (s, 1H, H-5), 7.11 (s, 2H, H-16), 6.99 (s, 4H, H-5 and H-7), 6.715 (d, J = 7.60, 2H, H-14), 3.44 (s, 3H, H-19), 3.00 (s, 3H, H-12), 2.418 (s, 6H, H-10), 2.18 (m, 6H, H-9), 2.082 (m, 6H, H-11), −23.42 (d, J = 9.42 Hz, 1H, H-17), −29.52 (t, J =9.81 Hz, 1H, H-18).

^{13}C (125.8 MHz, methanol-d_4, 245 K) δ: 160.9 (C-1), 144.32 (C-20), 142.07 (C-13), 138.27 (C-6), 136.95 (C-3), 135.97 (C-4 and C-8), 131.42 (C-23), 131.23 (C-16), 129.54 (C-22), 128.47 (C-5), 128.32 (C-21), 128.25 (C-7), 127.89 (C-15), 124.44 (C-14), 123.14 (C-2), 50.5 (C-19), 56.69 (C-12), 19.97 (C-10), 17.68 and 17.47 (C-11 and C-9).

Characterisation of $[IrCl(H)_2(IMes)(PhMeSO)_2]$ in dichloromethane-d_2

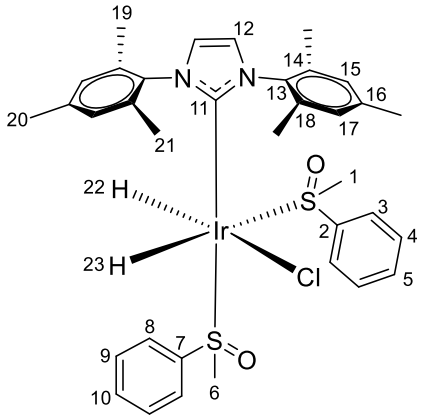

Figure A.36 – Structure of $[IrCl(H)_2(IMes)(PhMeSO)_2]$ complex.

[IrCl(COD)(IMes)] (5 mM), sodium oxalate (25 mM) and methyl phenyl sulfoxide (20 mM) were dissolved in dichloromethane-d_2 (0.6 mL) at 293 K and degassed using a freeze-pump-thaw method. The sample was then exposed to 4 bar (absolute) H_2. The sample was then repeatedly exposed to 4 bar H_2 until hydrides appeared at δ −14.81 and −21.20. This was then characterised by NMR at 245 K.

^{1}H (500 MHz, DCM-d_2, 245 K) δ: 7.70 (s, 2H, H-8), 7.54 (s, 1H, H-10), 7.53 (s, 2H, H-9), 7.34 (s, 1H, H-5), 7.20 (s, 2H, H-3), 7.04 (s, 2H, H-4), 6.89 (s, 2H, H-12), 6.83 (m, 2H, H-17), 6.44 (m, 2H, H-15), 3.43 (s, 3H, H-6), 3.26 (s, 3H, H-1), 2.20 (m, 6H, H-20), 2.19 (m, 6H, H-21), 1.93 (m, 6H, H-19), −14.81 (d, J = 6.21 Hz, 1H, H-22), −21.20 (d, J = 6.21 Hz, 1H, H-23).

^{13}C (125.8 MHz, DCM-d_2, 245 K) δ: 152.6 (C-11), 141.8 (C-7), 137.92 (C-16), 137.57 (C-18), 136.28 (C-13), 134.678 (C-14), 131.02 (C-5), 130.94 (C-9), 128.16 (C-17), 128.14 (C-15), 128.07 (C-4), 127.94 (C-10), 125.30 (C-3), 125.23 (C-8), 122.99 (C-12), 51.21 (C-6), 44.56 (C-1), 20.8 (C-20), 18.81 (C-21), 18.30 (C-19).

Characterisation of $[Ir_2(H)_4(DMSO)_2(IMes)_2(\mu\text{-oxalate})]$ in methanol-d_4 and 50 µL of D_2O

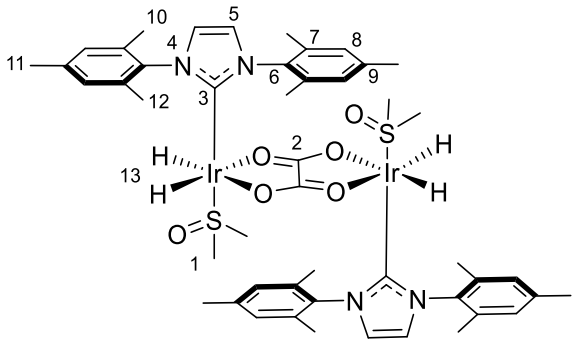

Figure A.37 – Structure of $[Ir_2(H)_4(DMSO)_2(IMes)_2(\mu\text{-oxalate})]$.

[IrCl(COD)(IMes)] (5 mM) and sodium oxalate (25 mM) were dissolved in methanol-d_4 (0.6 mL) with 50 µL of D_2O at 293 K and degassed using a freeze-pump-thaw method. The sample was then exposed to 4 bar (absolute) H_2. The sample was then repeatedly exposed to 4 bar H_2 until a single hydride appeared at δ −27.09. This was then characterised by NMR at 245 K.

^{1}H (500 MHz, methanol-d_4, 245 K) δ: 7.15 (s, 2H, H-5), 6.99 (m, 4H, H-8), 2.92 (d, 6H, H-2), 2.34 (s, 6H, H-11), 2.37 (s, 6H, H-11), 2.10 (s, 12H, H-10 and H-12), −27.09 (s, 2H, H-13).

^{13}C (125.8 MHz, methanol-d_4, 245 K) δ: 168.15 (C-2), 155-150 (C-3), 137.94 (C-9), 137.04 (C-7), 135.25 (C-6), 128.52 (C-8), 122.63 (C-5), 47.04 (C-1), 17.92 (C-11), 17.17 (C-10 and C-12).

X- ray diffraction of $[Ir_2(H)_4(DMSO)_2(IMes)_2(\mu\text{-oxalate})]$

Preparation of the sodium oxalate dimer crystals were prepared by removing the hydrogen atmosphere from a sample of activated sodium oxalate (25 mM) with DMSO (20 mM) and [IrCl(COD)(IMes)] (5 mM) in methanol-d_4 (0.6 mL) and 50 µL H_2O. Degassed hexane (~ 3 mL) was slowly layered over the top of the sample solution in the NMR tube.

The hydrides were located by difference map with one of the Ir-H bond lengths subsequently restrained to be 1.6 angstroms. The dichloromethane of crystallisation was disordered and modelled in two positions with refined occupancies of 0.771:0.229(3). The ADP of pairs of disordered atoms were constrained to be equal (C25 & C25a, Cl1 & Cl1a, Cl2 & Cl2a). The C-Cl bond lengths were restrained to be equal. The occupancy of the partial water of crystallisation refined to 0.634(13). Single crystal X ray diffraction data were collected and solved by Dr. Adrian

C. Whitwood. The chemical structure is shown in Figure A.37. Selected crystal data and structure refinement is shown in Table A.19. The structures were deposited with the Cambridge Crystallographic Database (no. 1941589).[165]

Table A.19 – Crystal data and structure refinement details for $[Ir_2(H)_4(DMSO)_2(IMes)_2(\mu\text{-oxalate})]$.

Parameter	Value
Compound	6
Empirical formula	$C_{50}H_{70.54}Cl_4Ir_2N_4O_{7.27}S_2$
Formula weight	1434.28
Temperature/K	110.00(10)
Crystal system	triclinic
Space group	P-1
a /Å	9.7187(5)
b /Å	12.0086(7)
c /Å	13.3295(11)
α /°	85.912(6)
β /°	69.210(6)
γ /°	76.361(5)
Volume /Å^3	1413.21(17)
Z	1
ρ_{calc} g/cm^3	1.685
μ /mm^{-1}	11.827
F(000)	710.7
Crystal size /mm^3	0.163 × 0.052 × 0.018
Radiation	CuK_α (λ = 1.54184)
2Θ range for data collection /°	7.094 to 134.126
Index ranges	−11 ≤ h ≤ 11, −9 ≤ k ≤ 14, −15 ≤ l ≤ 15
Reflections collected	9141
Independent reflections	5051 [R_{int} = 0.0319, R_{sigma} = 0.0472]
Data/restraints/parameters	5051/7/346
Goodness-of-fit on F^2	1.019
Final R indexes [I>=2σ (I)]	R_1 = 0.0303, wR_2 = 0.0730
Final R indexes [all data]	R_1 = 0.0354, wR_2 = 0.0768
Largest diff. peak/hole / e Å^{-3}	1.51/-1.45

A.13 Ligand exchange mechanism for $[IrCl(H)_2(DMSO)_2(IMes)]$

Modelling ligand exchange for sulfoxide complexes

The exchange of DMSO in $[IrCl(H)_2(DMSO)_2(IMes)]$ (**G**) was modelled in a similar way to that previously described for $[Ir(H)_2(IMes)(sub)_3]Cl$ by examining the concentration of the complex and free DMSO (Figure A.38).

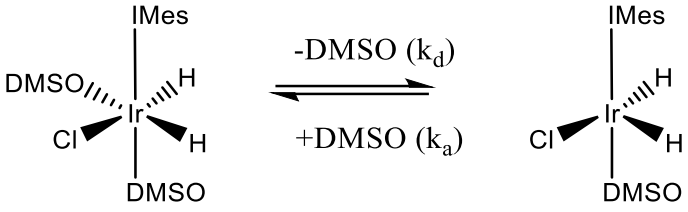

G **H**

Figure A.38 – Loss and gain of DMSO from [IrCl(H)$_2$(DMSO)$_2$(IMes)] (G).

However, the T_1 relaxation times had to be included in the fit as the simple model produced poor data. This is included as detailed in equations A.15 and A.16.

$$[DMSO]_t = [DMSO]_{t-\delta t} + \left(k_{DMSO}[\boldsymbol{C}]_t - k_{-DMSO}[DMSO]_t[Sub^*]\delta t - \frac{[DMSO]_t}{T_{1\,(DMSO)}}\right)\delta t \quad (A.15)$$

$$[\boldsymbol{C}]_t = [\boldsymbol{C}]_{t-\delta t} + \left(-k_{DMSO}[\boldsymbol{C}]_t + k_{-DMSO}[DMSO]_t[Sub^*]\delta t - \frac{[\boldsymbol{C}]_t}{T_{1\,(\boldsymbol{C})}}\right)\delta t \quad (A.16)$$

The simulated data for the Excel spreadsheet is given in Table A.20 using equations A.15 and A.16. The concentrations of bound substrate, [A] and free substrate, [B] could be calculated where t = 0 to 0.5 s. As a rate constant is required (k_d) estimated values had to be used. At t = 0, it was assumed that the concentration of A was 100% and that of B was 0%. The rate constant was then divided by the T_1 relaxation time. This allowed the excel SOLVER to fit the data. Rates were found using this model, an example is shown when complex **G** was in DCM-d_2 in Figure A.39.

Table A.20 - The cell inputs used for the Excel spreadsheet to calculate the simulated rate data for the exchange of DMSO in complex G.

A	B	C
Time (s)	[A]	[B]
0	100	0
0.00025	=@INDEX(MMULT($B59:$F59,$B$15:$F$19)*($A60-$A59)+B59,1)	=@INDEX(MMULT($B59:$F59,$B$15:$F$19)*($A60-$A59)+C59,2)

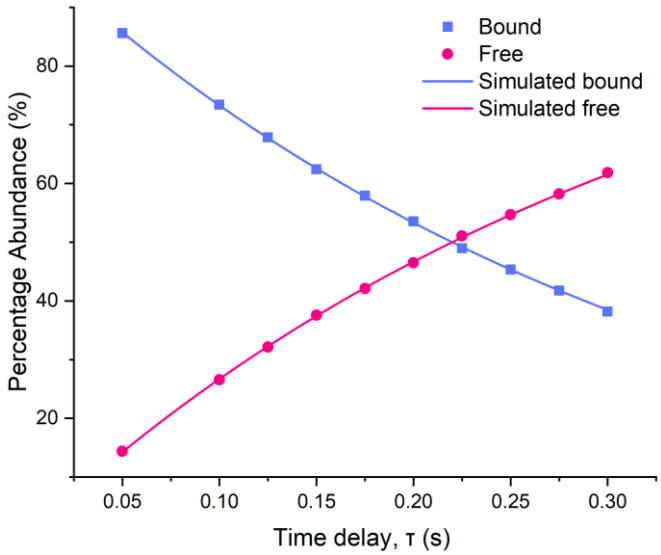

Figure A.39 – Showing the experimental and simulated change in percentage abundance of free and bound DMSO in complex G at 268 K in DCM-d_2. Simulated data was achieved using the formula given in equations A.15 and A.16.

Without the division of T_1 the fit was not a good one, as shown in Figure A. 40.

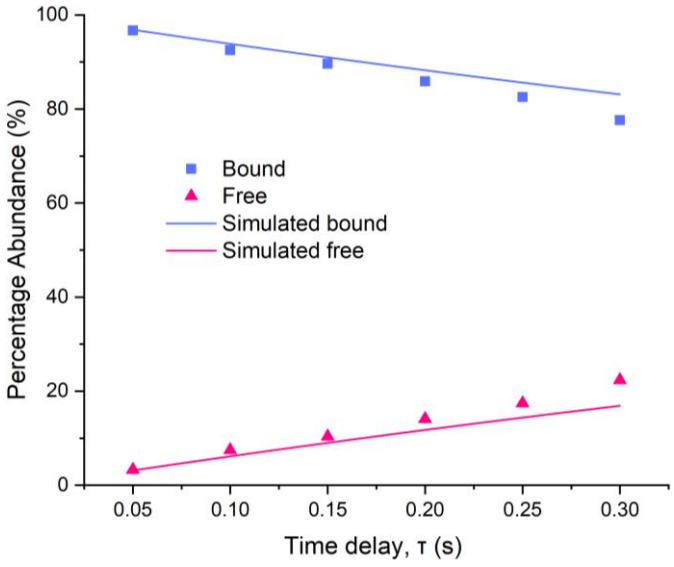

Figure A. 40 - Showing the experimental and simulated change in percentage abundance of free and bound DMSO in complex G at 258 K in DCM-d_2. Simulated data was achieved using the formula given in equations A.15 and A.16, without T_1.

The least squares regression was calculated as described in Appendix section A.2. An example of the least squares regression is given for ligand exchange for $[IrCl(H)_2(DMSO)_2(IMes)]$ at 268 K in DCM-d_2 (0.6 mL) in Table A.21.

Table A.21 - Least squared regression error for data obtained at 268 K for the ligand exchange for the complex [IrCl(H)$_2$(DMSO)$_2$(IMes)] in DCM-d_2 (0.6 mL).

time(s)	[A]	[B]	[A]	[B]	sum
0	100	0			0
0.05	85.61	14.39	85.75	14.25	16.60
0.1	73.43	26.57	73.34	26.66	54.69
0.125	67.87	32.13	67.77	32.23	76.94
0.15	62.43	37.57	62.60	37.40	99.74
0.175	57.92	42.08	57.78	42.22	126.31
0.2	53.51	46.49	53.32	46.68	153.15
0.225	48.96	51.04	49.18	50.82	181.37
0.25	45.32	54.68	45.35	54.66	211.12
0.275	41.78	58.22	41.79	58.21	244.92
0.3	38.17	61.83	38.51	61.49	330.02
					1164.86

From the rate data collected for the loss of DMSO and hydride, activation parameters could be obtained from the Eyring plots shown below in Figure A.42 below. These were used to find the activation parameters for loss of DMSO and hydride which are presented in Chapter 4 section 4.5.4.

The error for the rate constants was calculated using the Jack knife method as described in Chapter 7, section 7.2.9. The Jack-knife errors for the ligand exchange at 268 K for the complex [IrCl(H)$_2$(DMSO)$_2$(IMes)] in DCM-d_2 (0.6 mL) are given in Table A.22Table A.3.

Table A.22 - Jack-knife error for the experimental data obtained for ligand for the complex [IrCl(H)$_2$(DMSO)$_2$(IMes)] in DCM-d_2 (0.6 mL) at 268 K.

	A
All	3.056
0.005	3.045
0.05	3.046
0.075	3.046
0.1	3.044
0.2	3.047
0.25	3.047
0.3	3.044
0.35	3.045
0.4	3.169
0.45	3.169
0.5	3.046
Error	0.129

Modelling hydride exchange for sulfoxide complexes

The exchange of the hydride ligands in $[IrCl(H)_2(DMSO)_2(IMes)]$ was modelled as illustrated in Figure A.24 and using the equations A.12 to A.14, simulated data could be obtained. The Excel spreadsheet for the simulated data is given in Table A.10. Using this model rate constants were found; an example is shown when complex **G** was in DCM-d_2 (Figure A.41).

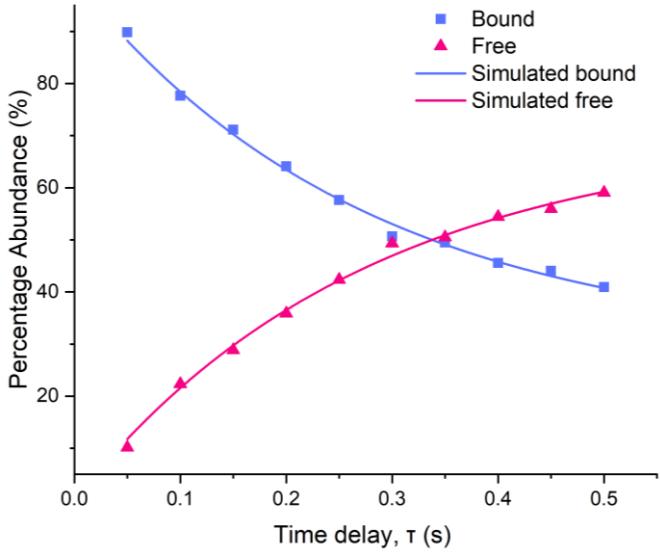

Figure A.41 – Showing the experimental and simulated change in percentage abundance of free and bound hydrogen in complex G at 268 K in DCM-d_2. Simulated data was achieved using the formula given in equations A.12 to A.14.

The least squares regression was calculated as described in Appendix section A.2. An example of the least squares regression is given for hydride exchange for $[IrCl(H)_2(DMSO)_2(IMes)]$ at 268 K in DCM-d_2 (0.6 mL) in Table A.23

Table A.23 - Least squared regression error for data obtained at 268 K for hydride exchange for the complex [IrCl(H)$_2$(DMSO)$_2$(IMes)] in DCM-d_2 (0.6 mL).

time(s)	[A]	[B]	[A]	[B]	sum
0	100	0			0
0.05	85.86	10.14	2.58	2.58	5.15
0.1	77.65	22.35	0.64	0.64	1.29
0.15	71.16	28.84	0.77	0.77	1.53
0.2	64.12	35.88	0.42	0.42	0.85
0.25	57.62	42.38	0.03	0.03	0.06
0.3	50.66	49.34	5.76	5.76	11.52
0.35	49.47	50.53	0.13	0.13	0.26
0.4	45.59	54.41	0.05	0.05	0.10
0.45	44.03	55.97	0.93	0.93	1.86
0.5	40.91	59.09	0.02	0.02	0.03
					22.64

The error for the rate constants was calculated using the Jack knife method as described in Chapter 7, section 7.2.9, the Jack-knife errors for the hydride exchange at 268 K for the complex [IrCl(H)$_2$(DMSO)$_2$(IMes)] in DCM-d_2 (0.6 mL) are given in Table A.24Table A.3.

Table A.24 - Jack-knife error for the experimental data obtained for hydride exchange for the complex [IrCl(H)$_2$(DMSO)$_2$(IMes)] in DCM-d_2 (0.6 mL) at 268 K.

	A
All	2.57
0.005	2.60
0.05	2.54
0.075	2.61
0.1	2.59
0.2	2.56
0.25	2.52
0.3	2.57
0.35	2.57
0.4	2.55
0.45	2.56
0.5	2.57
Error	0.08

From the rate data collected for the loss of DMSO and hydride in [IrCl(H)$_2$(DMSO)$_2$(IMes)] was used to determine the corresponding activation parameters as shown below in Figure A.42 and Chapter 4 section 4.5.4.

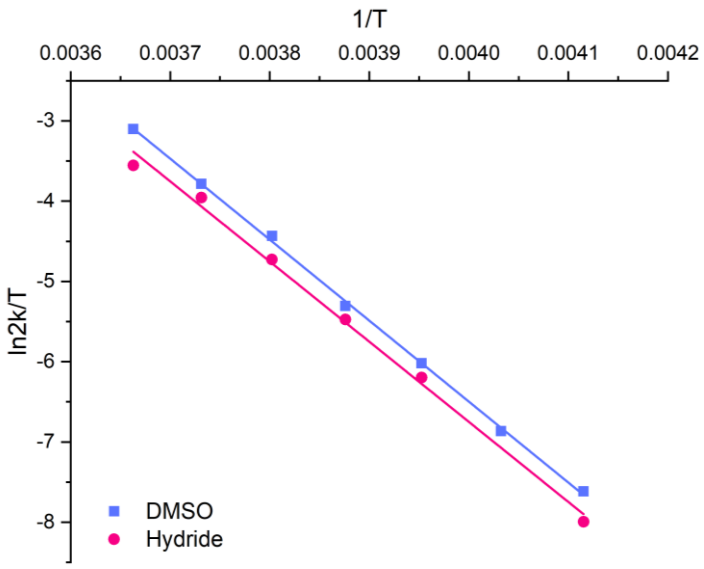

Figure A.42 – Eyring plot for the loss of either DMSO or hydride in complex [IrCl(H)$_2$(DMSO)$_2$(IMes)]. This plot was then used to calculate the activation parameters for each of these ligands. The linear regression analysis for each ligand is given in the same colour as that shown in the plot.

Table A.25 - Rate constants for elimination of H_2 and DMSO loss in [IrCl(H)$_2$(DMSO)$_2$(IMes)] in dichloromethane-d_2 or methanol-d_4 solution with temperature, obtained *via* selective 1D-EXSY experiments using a 500 MHz Bruker NMR spectrometer.

Temperature (K)	In DCM-d_2 Rate of loss / s^{-1}		In MeOD-d_4 Rate of loss / s^{-1}	
	Hydride	DMSO	Hydride	DMSO
233	-	-	0.00	0.03 ± 0.01
238	-	-	0.06 ± 0.01	0.07 ± 0.01
243	0.04 ± 0.01	0.05 ± 0.01	0.16 ± 0.01	0.15 ± 0.01
248	0.04 ± 0.01	0.12 ± 0.01	0.35 ± 0.01	0.32 ± 0.01
253	0.26 ± 0.01	0.29 ± 0.01	0.67 ± 0.01	0.64 ± 0.01
258	0.54 ± 0.02	0.64 ± 0.01	1.51 ± 0.02	1.52 ± 0.01
263	1.16 ± 0.04	1.54 ± 0.01	3.31 ± 0.26	3.35 ± 0.01
268	2.56 ± 0.08	3.05 ± 0.01	5.04 ± 0.37	7.28 ± 0.02
273	3.93 ± 0.03	6.13 ± 0.01	-	-

Table A.26 - Activation parameters for ligand exchange in [IrCl(H)$_2$(DMSO)$_2$(IMes)] in dichloromethane-d_2 and methanol-d_4 solution.

Solvent	Ligand	ΔH kJ mol^{-1}	ΔS J mol^{-1} K^{-1}	ΔG$^{\pm 300}$ kJ mol^{-1}
DCM-d_2	DMSO	86.5 ± 2.1	93.6 ± 8.2	58.4 ± 0.1
	Hydride	83.1 ± 7.6	78.9 ± 29.3	59.5 ± 0.1
MeOD-d_4	DMSO	78.9 ± 3.8	71.7 ± 15.7	57.4 ± 0.2
	Hydride	77.6 ± 6.2	66.1 ± 24.5	7.8 ± 0.3

A.14 Plot of T_1 hyperpolarised measurements

A series of 15 FIDs were recorded using the variable flip angles calculated in Chapter 7 (experimental) section 7.2.11.3, Table 7.1 and Table 7.2 for both ^{13}C and ^{15}N nuclei respectively in ^{13}C-uracil and 2-^{13}C,^{15}N$_2$-uracil. The time delay between *r. f.* pulses is Δt_n, where n is the delay between θ_n and θ_{n+1} as shown in Figure 7.6 in Chapter 7 section 7.2.11.3.

The hyperpolarised longitudinal relaxation (T_1) times were calculated using an exponential fit of the decay of the hyperpolarised signal as shown in equation A.17

$$M = M_0 e^{\left(\frac{-t}{T_1}\right)} + M_{The\ equ} \qquad (A.17)$$

Where M is magnetisation, M_0 is the initial magnetisation, T_1 is the time constant, t is the time after the first *r. f.* pulse and $M_{Th\ equ.}$ is the thermal equilibrium magnetisation.[6] An example of ^{13}C T_1 is given in Figure A.43 and in an example of ^{15}N T_1 is shown in Figure A.44, both for the substrate 2-^{13}C,^{15}N$_2$-uracil.

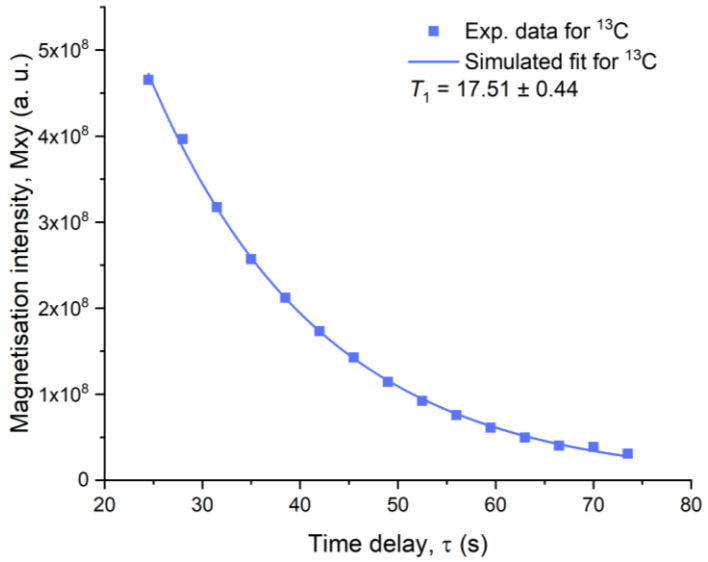

Figure A.43 – A plot of the magnetisation decay at varying time delays, τ based on the variable flip angles calculated, for ^{13}C of free ^{13}C-uracil when in the presence of the SABRE pre-catalyst [IrCl(COD)(IMes)]. From this the T_1 relaxation time was calculated using equation A.17.

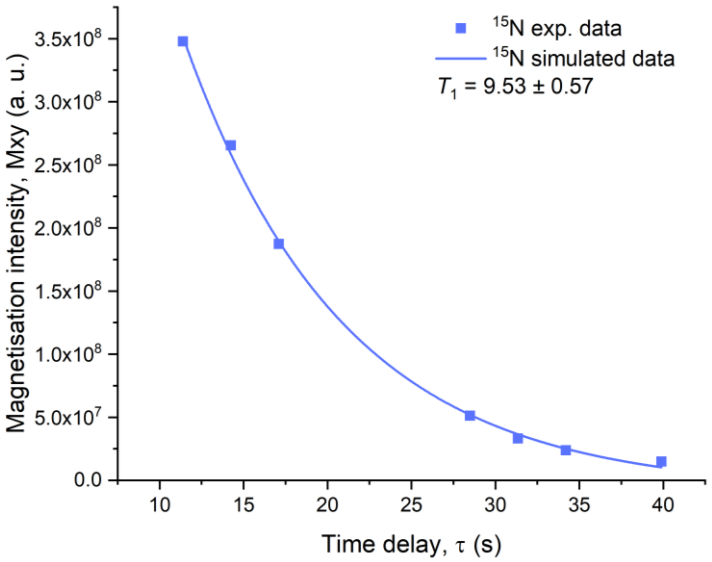

Figure A.44 - A plot of the magnetisation decay at varying time delays, τ based on the variable flip angles calculated, for ^{15}N of free ^{13}C,^{15}N$_2$-uracil when in the presence of the SABRE pre-catalyst [IrCl(COD)(IMes)]. From this the T_1 relaxation time was calculated using equation A.17.

Abbreviations

$\%V_{bur}$ - percent buried volume
h - Planck's constant
$\Delta G^{\ddagger 300}$ - Gibbs' free energy at 300 K
$\overrightarrow{\mu}$ - magnetic moment
µM - micromole per dm^3
µs - microsecond
^{18}F-FDG - ^{18}F-Fluorodeoxyglucose
1D - One-Dimensional
2D - Two-Dimensional
AHA - American Heart Association
ALTADENA - Adiabiatic Longitudinal Transport After Dissociation Engenders Net Alignment
ASL - Arterial Spin Labelling
ATP - Adenosine-Triphosphate
B **-** Boltzmann distribution
B_0 **-** magnetic field
BPS - bathophenanthrolinedisulfonic acid disodium salt
B_{PTF} - optimal polarisation transfer field
br - broad
c – concentration
ca – circa
CASH-SABRE - CAtalsyt Separated Hyperpolarisation *via* Signal Amplification By Reversible Exchange
cm - centimetre
CNR - Contrast to Noise
COA - cyclooctane
COD - 1,5-cyclooctadiene
COE - cyclooctene
COESY - Correlation Spectroscopy
COPD - Chronic Obstructive Pulmonary Disease
cf – confer/conferatur
CSI - Chemical Shift Imaging
Cy - cyclohexyl
d - deuterated
d - doublet
d1 - relaxation delay
d8 - mixing time
DC – Direct Current
DCM-d_2 - Dichloromethane-d_2
dd - doublet of doublet
d-DNP - dissolution-DNP
DEPT - Distortionless Enhancement by Polarisation Transfer
DFT - Density Functional Theory
dm - decimetre
DMF – dimethylformamide
DMSO - dimethylsulfoxide
DNA - deoxyribonucleic Acid
DNP - dynamic Nuclear Polarisation
DOSY - Diffusion Ordered SpectroscopY
dUMP - deoxyuridylate
E - energy state
E_M - energy values
exp - exponential
EXSY / Selective NOESY - Exchange SpectroscopY / Nuclear Overhauser Effect Spectroscopy
f - frequency
f - leakage factor
FDG - fluorodeoxyglucose
F-dUMP - fluorodeoxyuridylate
FID - Free Induction Decay
FISP - Free Induction with Steady-state free Procession
FLASH - Fast Low Angle Shot
FOV - Field of View
G - Gauss
g - gram
HMBC - Heteronuclear Multiple Bond Correlation Spectroscopy
HMQC - Heteronuclear Multiple Quantum Coherence
hyp -hyperpolarised
Hz -hertz
I - spin quantum number
I-integral
I_0 - Boltzmann equilibrium value
IDEG - 1,3-bis(3,4,5-tri(diethyleneglycol)benzyl)imidazole-2-ylidene
IMe - 1,3-bis(methyl)-imidazol-2-ylidene
IMes - 1,3-Bis(2,4,6-trimethylphenyl)-imidazol-2-ylidene
IMesBn - 1-mesityl-3-benzylimidazole
INEPT - Insensitive Nuclei Enhanced by Polarisation Transfer
^{i}Pr$_2$EtN - *N*,*N*-Diisopropylethylamine
IVIM - Intra Voxel Incoherent Motion
I_z - nuclear polarisation
J - scalar coupling
J - joule
k - rate constant
K - Kelvin
k_a - rate constant for association
k_B - Boltzmann constant
k_d - rate constant for dissociation
KHz - Kilohertz
kJ - kilojoule
k_{obs}- observed rate constant
L – ligand
L_1 - 3-(2-methylene-4-nitrophenolate)-1-(2,4,6-trimethylphenyl)imidazolylidene

LLS - Long Lived State
ln - natural log (base *e*)
M – moles per dm^3
m - multiplet
m - quantum number
M - mass
MCT - Monocarboxylate Transporter
MeCN - Acetonitrile
MeOD - deuterated methanol
MeOH - methanol
MHz - megahertz
min - minute
mL - mililitre
mM - milimoles per dm^3
mm – millimetre
$\boldsymbol{M_0}$ - magnetisation at thermal equilibrium
$\boldsymbol{M_{offset}}$ - offset magnetisation
mol -mole
MR - Magnetic Resonance
Mr - molecular mass
MRI - Magnetic Resonance Imaging
mRNA - messenger Ribonucleic Acid
MRS - Magentic Resonance Spectroscopy
MRSI – Magnetic Resonance Spectroscopy Imaging
ms - milisecond
MSP - Monosodium dihydrogen phosphate
mT - militesla
mtz - 1-methyl-1,2,3-triazole
Mx - Magnetisation in the x direction
Mxy - Magnetisation in the xy plane
My - Magnetisation in the y direction
Mz - Magnetisation in the z direction
N - isotope natural abundance
n - number
$\boldsymbol{n_\alpha}$ - ratio of populations in α
NADH - Reduced form of Nicotinamide Adenine Dinuleotide
NADPH - Reduced form of Nicotinamide Adenine Dinuleotide Phosphate
NH - amine protons
NH_2R - amine ligand
NHC - *N*-heterocylic Carbene
NMR - Nuclear Magnetic Resonance
nOe - Nuclear Overhauser Effect Spectroscopy
NOESY - Nuclear Overhauser Effect Spectroscopy
NS – Number of scans
NSF - Nephrogenic System Fibrosis
$\boldsymbol{n_\beta}$ - ratio of populations in β
O-DNP - Overhauser-DNP
OPSY - Only *para*-hydrogen Spectroscopy
OXO63 - tris[8-carboxy2,2,6,6-tetrakis(2-hydroxymethyl)benzo[1,2-d:4,5-d]bis(1,3)dithio-4-yl]methyl radical, trisodium salt
$\boldsymbol{P_0}$ - Polarisation
PASADENA - *Para*-hydrogen And Synthesis Allow Dramatically Enhanced Nuclear Alignment
PCy_2Ph - dicyclohexylphenylphosphine
PCy_3 - Tricyclohexylphosphine
PEA - phenethylamine
PEG - polyethylene glycol
PET - Positron Emission Tomography
***p*-H_2** - *para*-hydrogen
PHIP - *Para*-Hydrogen Induced Polarisation
ppm - parts per million
PTF - Polarisation Transfer Field
py - pyridine
pyr - pyrimidine
q - quartet
R - gas constant
R - receptivity
r. f. - Radio Frequency
rad - radian
RARE - Rapid Acquisition with Refocused Echoes
ref - reference
RNA - Ribonucleic Acid
ρ - density
ROI - region of interest
s - second
s - saturation factor
s - singlet
S - signal intensity
S.D - standard deviation
SABRE - Signal Amplification By Reversible Exchange
SABRE-SHEATH - Signal Amplification By Reversible Exchange in SHield Enables Alignment Transfer to Heteronuclei
SE - Spin Echo
SEOP - Spin-Exchange Optical Pumping
SIMes - 1,3-bis(2,4,6-trimethylphenyl)-4,5-dihydroimidazolium
sin - sine
SiPr - 1,3-bis(2,6-diisopropyl)-4,5-dihyroimidazol-2-ylidene
SNR - Signal to noise
SSFP - Steady State Free Precession
Sub - Substrate
T - temperature
T – Tesla
t - triplet
t - time
$\boldsymbol{T_1}$ - spin lattice or longitudinal relaxation time
$\boldsymbol{T_2}$ – spin-spin or transverse relaxation time

TCA - Tricarboxylic Cycle or Citric Acid Cycle or Krebs cycle
TE - Echo Time
TEP - Tolman Electronic Parameter
Th - Thermal
θ - flip angle
T_{LLS} - Long Lived State relaxation time
t_{mix} - mixing time
TMP - Thymidylate
TR - Repetition Time
TRAMP - Transgenic Adenocarcinoma Mouse Prostate
tRNA - transfer Ribonucelic Acid
TS - Thymidylate synthase
uL - microlitre
vd - variable delay or gradient list
vol - volume
w - weight
$\bar{x}$- mean
XRD - X-Ray Diffraction
α - spins aligned with the field
β - spins aligned against the field
γ - gyromagnetic moment
ΔE - energy difference
$\Delta H^{\ddagger}$ - change in enthalpy
$\Delta S^{\ddagger}$ - change in entropy
Δt - change in time
ε' - overall enhancement
ξ - coupling factor
τ - time delay
τ_G - gradient recovery delay
τ_{VG} - variable dely
ħ - reduced Planck's constant
ω_0 - angular frequency
ε - enhancement
$\Delta\delta$ - chemical shift difference

References

1. A. Cavalli, X. Salvatella, C. M. Dobson and M. Vendruscolo, *Proc. Natl. Acad. Sci. U. S. A.*, 2007, **104**, 9615-9620.
2. A. D. Bain, *Prog. Nucl. Magn. Reson. Sepc.*, 2003, **43**, 63-103.
3. H. M. Parsons, C. Ludwig, U. L. Gunther and M. R. Viant, *BMC Bioinform.*, 2007, **8**.
4. M. Gal, M. Mishkovsky and L. Frydman, *J. Am. Chem. Soc.*, 2006, **128**, 951-956.
5. I. R. Kleckner and M. P. Foster, *Biochim. Biophys. Acta. Proteins Proteom.*, 2011, **1814**, 942-968.
6. O. Semenova, P. M. Richardson, A. J. Parrott, A. Nordon, M. E. Halse and S. B. Duckett, *Anal. Chem.*, 2019, **91**, 6695-6701.
7. W. Hollingworth, C. J. Todd, M. I. Bell, Q. Arafat, S. Girling, K. R. Karia and A. K. Dixon, *Clin. Radiol.*, 2000, **55**, 825-831.
8. P. J. Hore, *Nuclear Magnetic Resonance*, Oxford University Press, USA, 1998.
9. M. H. Levitt, *Spin dynamics: basics of nuclear magnetic resonance.*, John Wiley & Sons, 2001.
10. J. Keeler, *Understanding NMR Spectroscopy*, Wiley, 2nd Edition edn., 2010.
11. P. J. Hore, J. A. Jones and S. Wimperis, *NMR: The toolkit How pulse sequences work*, Oxford University Press, Second edn., 2000.
12. S. B. Duckett and N. J. Wood, *Coord. Chem. Rev.*, 2008, **252**, 2278-2291.
13. R. W. Adams, J. A. Aguilar, K. D. Atkinson, M. J. Cowley, P. I. P. Elliott, S. B. Duckett, G. G. R. Green, I. G. Khazal, J. Lopez-Serrano and D. C. Williamson, *Science*, 2009, **323**, 1708-1711.
14. S. B. Duckett and R. E. Mewis, *Acc. Chem. Res.*, 2012, **45**, 1247-1257.
15. L. C. Balling, *Adv. Quantum. Electron.*, 1975, **3**, 1-167.
16. T. G. Walker and W. Happer, *Rev. Mod. Phys.*, 1997, **69**, 629-642.
17. C. J. Gorter, *Phys. Z.*, 1934, **35**, 923.
18. G. Kaindl, F. Bacon and D. A. Shirley, *Phys. Rev. C*, 1973, **8**, 315-319.
19. W. Brewer and M. Kopp, *Hyperfine Interact.*, 1976, 299-305.
20. M. E. Halse, *Trac-Trend Anal. Chem.*, 2016, **83**, 76-83.
21. M. L. Hirsch, N. Kalechofsky, A. Belzer, M. Rosay and J. G. Kempf, *J. Am. Chem. Soc.*, 2015, **137**, 8428-8434.
22. A. Kastler, *J. Phys. Radium*, 1950, **11**, 255-265.
23. W. Happer, *Rev. Mod. Phys.*, 1972, **44**, 169-249.
24. M. S. Albert, G. D. Cates, B. Driehuys, W. Happer, B. Saam, C. S. Springer and A. Wishnia, *Nature*, 1994, **370**, 199-201.
25. H. Middleton, R. D. Black, B. Saam, G. D. Cates, G. P. Cofer, R. Guenther, W. Happer, L. W. Hedlund, G. A. Johnson, K. Juvan and J. Swartz, *Magn. Reson. Med.*, 1995, **33**, 271-275.
26. S. Patz, F. W. Hersman, I. Muradian, M. I. Hrovat, I. C. Ruset, S. Ketel, F. Jacobson, G. P. Topulos, H. Hatabu and J. P. Butler, *Eur. J. Radiol.*, 2007, **64**, 335-344.
27. J. E. Roos, H. P. McAdams, S. S. Kaushik and B. Driehuys, *Magn. Reson. Imaging Clin. N. Am.*, 2015, **23**, 217-229.
28. A. W. Overhauser, *Phys. Rev.*, 1953, **92**, 411-415.
29. U. L. Gunther, in *Modern NMR Methodology*, eds. H. Heise and S. Matthews, 2013, vol. 335, pp. 23-69.

30. J. H. Lee, Y. Okuno and S. Cavagnero, *J. Magn. Reson.*, 2014, **241**, 18-31.
31. T. R. Carver and C. P. Slichter, *Phys. Rev.*, 1953, **92**, 212-213.
32. J. H. Ardenkjaer-Larsen, B. Fridlund, A. Gram, G. Hansson, L. Hansson, M. H. Lerche, R. Servin, M. Thaning and K. Golman, *Proc. Natl. Acad. Sci. U. S. A.*, 2003, **100**, 10158-10163.
33. Y. Lee, *Appl. Spectrosc. Rev.*, 2016, **51**, 190-206.
34. K. R. Keshari and D. M. Wilson, *Chem. Soc. Rev.*, 2014, **43**, 1627-1659.
35. T. B. Rodrigues, E. M. Serrao, B. W. C. Kennedy, D. E. Hu, M. I. Kettunen and K. M. Brindle, *Nat. Med.*, 2014, **20**, 93-97.
36. K. Golman, R. in't Zandt, M. Lerche, R. Pehrson and J. H. Ardenkjaer-Larsen, *Cancer Res.*, 2006, **66**, 10855-10860.
37. R. E. Hurd, Y. F. Yen, A. Chen and J. H. Ardenkjaer-Larsen, *J. Magn. Reson. Imaging*, 2012, **36**, 1314-1328.
38. S. J. Nelson, J. Kurhanewicz, D. B. Vigneron, P. E. Z. Larson, A. L. Harzstark, M. Ferrone, M. van Criekinge, J. W. Chang, R. Bok, I. Park, G. Reed, L. Carvajal, E. J. Small, P. Munster, V. K. Weinberg, J. H. Ardenkjaer-Larsen, A. P. Chen, R. E. Hurd, L. I. Odegardstuen, F. J. Robb, J. Tropp and J. A. Murray, *Sci. Transl. Med.*, 2013, **5**, 1-12.
39. H. A. E. Gutte H., Johannesen H. H., Clemmensen A. E., Ardenkjaer-Larsen J. H., Neilsen C. H., Kjaer A., *Am. J. Nucl. Med. Mol. Imaging*, 2015, **5**, 548-560.
40. J. Kurhanewicz, D. B. Vigneron, J. H. Ardenkjaer-Larsen, J. A. Bankson, K. Brindle, C. H. Cunningham, F. A. Gallagher, K. R. Keshari, A. Kjaer, C. Laustsen, D. A. Mankoff, M. E. Merritt, S. J. Nelson, J. M. Pauly, P. Lee, S. Ronen, D. J. Tyler, S. S. Rajan, D. M. Spielman, L. Wald, X. L. Zhang, C. R. Malloy and R. Rizi, *Neoplasia*, 2019, **21**, 1-16.
41. S. Kishimoto, J. R. Brendert, D. R. Crooks, S. Matsumoto, T. Seki, N. Oshima, H. Merkle, P. H. Lin, G. Reed, A. P. Chen, J. H. Ardenkjaer-Larsen, J. Munasinghe, K. Saito, K. Yamamoto, P. L. Choyke, J. Mitchell, A. N. Lane, T. W. M. Fan, W. M. Linehan and M. C. Krishna, *eLife*, 2019, **8**, 46312-46332.
42. E. M. Serrao and K. M. Brindle, *Front. Oncol.*, 2016, **6**, 1-6.
43. L. Stryer, *Biochemistry*, W. H. Freeman and Company, New York, Third edn., 1975.
44. P. Felig, *Metab., Clin. Exp.*, 1973, **22**, 179-207.
45. O. Warburg, F. Wind and E. Negelein, *J. Gen. Physiol.*, 1927, **8**, 519-530.
46. M. A. Schroeder, H. J. Atherton, D. R. Ball, M. A. Cole, L. C. Heather, J. L. Griffin, K. Clarke, G. K. Radda and D. J. Tyler, *FASEB J.*, 2009, **23**, 2529-2538.
47. R. E. Hurd, Y.-F. Yen, D. Mayer, A. Chen, D. Wilson, S. Kohler, R. Bok, D. Vigneron, J. Kurhanewicz, J. Tropp, D. Spielman and A. Pfefferbaum, *Magn. Reson. Med.*, 2010, **63**, 1137-1143.
48. M. J. Albers, R. Bok, A. P. Chen, C. H. Cunningham, M. L. Zierhut, V. Y. Zhang, S. J. Kohler, J. Tropp, R. E. Hurd, Y. F. Yen, S. J. Nelson, D. B. Vigneron and J. Kurhanewicz, *Cancer Res.*, 2008, **68**, 8607-8615.
49. K. R. Keshari, R. Sriram, B. L. Koelsch, M. Van Criekinge, D. M. Wilson, J. Kurhanewicz and Z. J. Wang, *Cancer Res.*, 2013, **73**, 529-538.
50. B. Sumegi, B. Podany, P. Forgo and K. E. Kover, *Biochem. J.*, 1995, **312**, 75-81.
51. O. Warburg, *Science*, 1956, **123**, 309-314.
52. L. Hertz and G. A. Dienel, *J. Neurosci. Res.*, 2005, **79**, 11-18.

53. J. E. M. Fox, D. Meredith and A. P. Halestrap, *J Physiol.-London*, 2000, **529**, 285-293.
54. V. Ganapathy, M. Thangaraju and P. D. Prasad, *Pharmacol. Ther.*, 2009, **121**, 29-40.
55. S. J. Nelson, D. Vigneron, J. Kurhanewicz, A. Chen, R. Bok and R. Hurd, *Appl. Magn. Reson.*, 2008, **34**, 533-544.
56. S. E. Bohndiek, M. I. Kettunen, D. E. Hu, B. W. C. Kennedy, J. Boren, F. A. Gallagher and K. M. Brindle, *J. Am. Chem. Soc.*, 2011, **133**, 11795-11801.
57. K. R. Keshari, V. Sai, Z. J. Wang, H. F. VanBrocklin, J. Kurhanewicz and D. M. Wilson, *J. Nucl. Med.*, 2013, **54**, 922-928.
58. K. R. Keshari, J. Kurhanewicz, R. Bok, P. E. Z. Larson, D. B. Vigneron and D. M. Wilson, *Proc. Natl. Acad. Sci. U. S. A.*, 2011, **108**, 18606-18611.
59. B. C. Dickinson, J. Peltier, D. Stone, D. V. Schaffer and C. J. Chang, *Nat. Chem. Biol.*, 2011, **7**, 106-112.
60. M. Ushio-Fukai and Y. Nakamura, *Cancer Lett.*, 2008, **266**, 37-52.
61. G. K. Balendiran, R. Dabur and D. Fraser, *Cell Biochem. Funct.*, 2004, **22**, 343-352.
62. B. Morgan, D. Ezerina, T. N. E. Amoako, J. Riemer, M. Seedorf and T. P. Dick, *Nat. Chem. Biol.*, 2013, **9**, 119-125.
63. A. Nardi-Schreiber, A. Gamliel, T. Harris, G. Sapir, J. Sosna, J. M. Gomori and R. Katz-Brull, *Nat. Commun.*, 2017, **8**, 341-348.
64. M. M. Chaumeil, T. Ozawa, I. Park, K. Scott, C. D. James, S. J. Nelson and S. M. Ronen, *Neuroimage*, 2012, **59**, 193-201.
65. D. R. Ball, R. Cruickshank, C. A. Carr, D. J. Stuckey, P. Lee, K. Clarke and D. J. Tyler, *NMR Biomed.*, 2013, **26**, 1441-1450.
66. F. A. Gallagher, M. I. Kettunen, S. E. Day, D. E. Hu, J. H. Ardenkjaer-Larsen, R. in't Zandt, P. R. Jensen, M. Karlsson, K. Golman, M. H. Lerche and K. M. Brindle, *Nature*, 2008, **453**, 940-U973.
67. M. A. Schroeder, P. Swietach, H. J. Atherton, F. A. Gallagher, P. Lee, G. K. Radda, K. Clarke and D. J. Tyler, *Cardiovasc. Res.*, 2010, **86**, 82-91.
68. S. J. Kohler, Y. Yen, J. Wolber, A. P. Chen, M. J. Albers, R. Bok, V. Zhang, J. Tropp, S. Nelson, D. B. Vigneron, J. Kurhanewicz and R. E. Hurd, *Magn. Reson. Med.*, 2007, **58**, 65-69.
69. D. M. Wilson, K. R. Keshari, P. E. Z. Larson, A. P. Chen, S. Hu, M. Van Criekinge, R. Bok, S. J. Nelson, J. M. Macdonald, D. B. Vigneron and J. Kurhanewicz, *J. Magn. Reson.*, 2010, **205**, 141-147.
70. S. C. Serra, M. Karlsson, G. B. Giovenzana, C. Cavallotti, F. Tedoldi and S. Aime, *Contrast Media Mol. Imaging*, 2012, **7**, 469-477.
71. I. Goldberga, R. Li, W. Y. Chow, D. G. Reid, U. Bashtanova, R. Rajan, A. Puszkarska, H. Oschkinat and M. J. Duer, *RSC Adv.*, 2019, **9**, 26686-26690.
72. F. A. Gallagher, R. Woitek, M. A. McLean, A. B. Gill, R. M. Garcia, E. Provenzano, F. Riemer, J. Kaggie, A. Chhabra, S. Ursprung, J. T. Grist, C. J. Daniels, F. Zaccagna, M. C. Laurent, M. Locke, S. Hilborne, A. Frary, T. Torheim, C. Boursnell, A. Schiller, I. Patterson, R. Slough, B. Carmo, J. Kane, H. Biggs, E. Harrison, S. S. Deen, A. Patterson, T. Lanz, Z. Kingsbury, M. Ross, B. Basu, R. Baird, D. J. Lomas, E. Sala, J. Wason, O. M. Rueda, S. F. Chin, I. B. Wilkinson, M. J. Graves, J. E. Abraham, F. J. Gilbert, C. Caldas and K. M. Brindle, *Proc. Natl. Acad. Sci. U. S. A.*, 2020, **117**, 2092-2098.

73. H. Stodkilde-Jorgensen, C. Laustsen, E. S. S. Hansen, R. Schulte, J. H. Ardenkjaer-Larsen, A. Comment, J. Frokiaer, S. Ringgaard, L. B. Bertelsen, M. Ladekarl and B. Weber, *J. Magn. Reson. Imaging*, **51**, 961-963.
74. A. Leavesley, C. B. Wilson, M. Sherwin and S. Han, *Phys. Chem. Chem. Phys.*, 2018, **20**, 9897-9903.
75. M. Filibian, E. Elisei, S. C. Serra, A. Rosso, F. Tedoldi, A. Cesaro and P. Carretta, *Phys. Chem. Chem. Phys.*, 2016, **18**, 16912-16920.
76. F. Kurdzesau, B. van den Brandt, A. Comment, P. Hautle, S. Jannin, J. J. van der Klink and J. A. Konter, *J. Phys. D-Appl. Phys.*, 2008, **41**, 10.
77. A. Bornet, J. Milani, B. Vuichoud, A. J. P. Linde, G. Bodenhausen and S. Jannin, *Chem. Phys. Lett.*, 2014, **602**, 63-67.
78. K. Kouril, H. Kourilova, S. Bartram, M. H. Levitt and B. Meier, *Nat. Commun.*, 2019, **10**.
79. L. Lumata, M. E. Merritt, C. R. Malloy, A. D. Sherry and Z. Kovacs, *J. Phys. Chem. A*, 2012, **116**, 5129-5138.
80. J. W. Gordon, S. B. Fain and I. J. Rowland, *Magn. Reson. Med.*, 2012, **68**, 1949-1954.
81. P. Mieville, P. Ahuja, R. Sarkar, S. Jannin, P. R. Vasos, S. Gerber-Lemaire, M. Mishkovsky, A. Comment, R. Gruetter, O. Ouari, P. Tordo and G. Bodenhausen, *Angew. Chem., Int. Ed.*, 2010, **49**, 6182-6185.
82. A. Comment, J. Rentsch, F. Kurdzesau, S. Jannin, K. Uffmann, R. B. van Heeswijk, P. Hautle, J. A. Konter, B. van den Brandt and J. J. van der Klink, *J. Magn. Reson.*, 2008, **194**, 152-155.
83. Y. P. Liu, F. A. Villamena, Y. G. Song, J. A. Sun, A. Rockenbauer and J. L. Zweier, *J. Org. Chem.*, 2010, **75**, 7796-7802.
84. J. H. Ardenkjaer-Larsen, A. M. Leach, N. Clarke, J. Urbahn, D. Anderson and T. W. Skloss, *NMR Biomed.*, 2011, **24**, 927-932.
85. C. Ludwig, I. Marin-Montesinos, M. G. Saunders and U. L. Gunther, *J. Am. Chem. Soc.*, 2010, **132**, 2508-+.
86. J. Leggett, R. Hunter, J. Granwehr, R. Panek, A. J. Perez-Linde, A. J. Horsewill, J. McMaster, G. Smith and W. Kockenberger, *Phys. Chem. Chem. Phys.*, 2010, **12**, 5883-5892.
87. C. R. Bowers and D. P. Weitekamp, *Phys. Rev. Lett.*, 1986, **57**, 2645-2648.
88. T. C. Eisenschmid, R. U. Kirss, P. P. Deutsch, S. I. Hommeltoft, R. Eisenberg, J. Bargon, R. G. Lawler and A. L. Balch, *J. Am. Chem. Soc.*, 1987, **109**, 8089-8091.
89. S. Duckett, https://www.york.ac.uk/res/sbd/parahydrogen/outline.html).
90. J. W. Leachman, R. T. Jacobsen, S. G. Penoncello and E. W. Lemmon, *J. Phys. Chem. Ref. Data*, 2009, **38**.
91. C. R. Bowers and D. P. Weitekamp, *J. Am. Chem. Soc.*, 1987, **109**, 5541-5542.
92. M. G. Pravica and D. P. Weitekamp, *Chem. Phys. Lett.*, 1988, **145**, 255-258.
93. K. D. Atkinson, M. J. Cowley, P. I. P. Elliott, S. B. Duckett, G. G. R. Green, J. Lopez-Serrano and A. C. Whitwood, *J. Am. Chem. Soc.*, 2009, **131**, 13362-13368.
94. K. D. Atkinson, M. J. Cowley, S. B. Duckett, P. I. P. Elliott, G. G. R. Green, J. Lopez-Serrano, I. G. Khazal and A. C. Whitwood, *Inorg. Chem.*, 2009, **48**, 663-670.
95. M. Goldman, H. Johannesson, O. Axelsson and M. Karlsson, *C. R. Chim.*, 2006, **9**, 357-363.
96. E. Cavallari, C. Carrera, M. Sorge, G. Bonne, A. Muchir, S. Aime and F. Reineri, *Sci. Rep.*, 2018, **8**, 8366-8374.

97. J. Natterer and J. Bargon, *Prog. Nucl. Magn. Reson. Sepc.*, 1997, **31**, 293-315.
98. T. Theis, M. Truong, A. M. Coffey, E. Y. Chekmenev and W. S. Warren, *J. Magn. Reson.*, 2014, **248**, 23-26.
99. D. A. Barskiy, K. V. Kovtunov, I. V. Koptyug, P. He, K. A. Groome, Q. A. Best, F. Shi, B. M. Goodson, R. V. Shchepin, A. M. Coffey, K. W. Waddell and E. Y. Chekmenev, *J. Am. Chem. Soc.*, 2014, **136**, 3322-3325.
100. A. N. Pravdivtsev, A. V. Yurkovskaya, H. M. Vieth and K. L. Ivanov, *Phys. Chem. Chem. Phys.*, 2014, **16**, 24672-24675.
101. R. W. Adams, S. B. Duckett, R. A. Green, D. C. Williamson and G. G. R. Green, *J. Chem. Phys.*, 2009, **131**.
102. R. A. Green, R. W. Adams, S. B. Duckett, R. E. Mewis, D. C. Williamson and G. G. R. Green, *Prog. Nucl. Magn. Reson. Sepc.*, 2012, **67**, 1-48.
103. P. M. Richardson, R. O. John, A. J. Parrott, P. J. Rayner, W. Iali, A. Nordon, M. E. Halse and S. B. Duckett, *Phys. Chem. Chem. Phys.*, 2018, **20**, 26362-26371.
104. K. L. Ivanov, A. N. Pravdivtsev, A. V. Yurkovskaya, H. M. Vieth and R. Kaptein, *Prog. Nucl. Magn. Reson. Sepc.*, 2014, **81**, 1-36.
105. A. N. I. Pravdivtsev, K. L.; Yukovskaya, A.; Petrov, P. A.; Limbach, H-H.; Kaptein, R.; Vieth, H-M., *J. Magn. Reson.*, 2015, **261**, 73-82.
106. P. M. Richardson, S. Jackson, A. J. Parrott, A. Nordon, S. B. Duckett and M. E. Halse, *Magn. Reson. Chem.*, 2018, **56**, 641-650.
107. T. Theis, M. L. Truong, A. M. Coffey, R. V. Shchepin, K. W. Waddell, F. Shi, B. M. Goodson, W. S. Warren and E. Y. Chekmenev, *J. Am. Chem. Soc.*, 2015, **137**, 1404-1407.
108. T. Theis, M. L. Truong, A. M. Coffey, R. V. Shchepin, K. W. Waddell, F. Shi, B. M. Goodson, W. S. Warren and E. Y. Chekmenev, *Journal of the American Chemical Society*, 2015, **137**, 1404-1407.
109. C. Karunakaran, M. Balamurugan and D. K. Marimuthu, in *Spin Resonacne Spectroscopy: Principles and Applications*, ed. C. Karunakaran, Elsevier, 2018, ch. 3, pp. 111-168.
110. D. A. Barskiy, A. N. Pravdivtsev, K. L. Ivanov, K. V. Kovtunov and I. V. Koptyug, *Phys. Chem. Chem. Phys.*, 2016, **18**, 89-93.
111. L. S. Lloyd, A. Asghar, M. J. Burns, A. Charlton, S. Coombes, M. J. Cowley, G. J. Dear, S. B. Duckett, G. R. Genov, G. G. R. Green, L. A. R. Highton, A. J. J. Hooper, M. Khan, I. G. Khazal, R. J. Lewis, R. E. Mewis, A. D. Roberts and A. J. Ruddlesden, *Catal. Sci. Technol.*, 2014, **4**, 3544-3554.
112. M. Fekete, P. J. Rayner, G. G. R. Green and S. B. Duckett, *Magn. Reson. Chem.*, 2017, **55**, 944-957.
113. E. B. Ducker, L. T. Kuhn, K. Munnemann and C. Griesinger, *J. Magn. Reson.*, 2012, **214**, 159-165.
114. B. J. A. van Weerdenburg, S. Gloggler, N. Eshuis, A. H. J. Engwerda, J. M. M. Smits, R. de Gelder, S. Appelt, S. S. Wymenga, M. Tessari, M. C. Feiters, B. Blumich and F. Rutjes, *Chem. Commun.*, 2013, **49**, 7388-7390.
115. H. F. Zeng, J. D. Xu, J. Gillen, M. T. McMahon, D. Artemov, J. M. Tyburn, J. A. B. Lohman, R. E. Mewis, K. D. Atkinson, G. G. R. Green, S. B. Duckett and P. C. M. van Zijl, *J. Magn. Reson.*, 2013, **237**, 73-78.
116. R. E. Mewis, *Magn. Reson. Chem.*, 2015, **53**, 789-800.
117. P. J. Rayner, Duckett, S. B., *Angew. Chem.*, 2018, **57**, 6742-6753.

118. P. J. Rayner, P. Norcott, K. M. Appleby, W. Iali, R. O. John, S. J. Hart, A. C. Whitwood and S. B. Duckett, *Nat. Commun.*, 2018, **9**.
119. M. J. Cowley, R. W. Adams, K. D. Atkinson, M. C. R. Cockett, S. B. Duckett, G. G. R. Green, J. A. B. Lohman, R. Kerssebaum, D. Kilgour and R. E. Mewis, *J. Am. Chem. Soc.*, 2011, **133**, 6134-6137.
120. B. J. A. van Weerdenburg, N. Eshuis, M. Tessari, F. Rutjes and M. C. Feiters, *Dalton Trans.*, 2015, **44**, 15387-15390.
121. W. Iali, G. G. R. Green, S. J. Hart, A. C. Whitwood and S. B. Duckett, *Inorg. Chem.*, 2016, **55**, 11639-11643.
122. C. M. Wong, M. Fekete, R. Nelson-Forde, M. R. D. Gatus, P. J. Rayner, A. C. Whitwood, S. B. Duckett and B. A. Messerle, *Catal. Sci. Technol.*, 2018, **8**, 4925-4933.
123. A. J. Ruddlesden, R. E. Mewis, G. G. R. Green, A. C. Whitwood and S. B. Duckett, *Organometallics*, 2015, **34**, 2997-3006.
124. A. J. Ruddlesden and S. B. Duckett, *Chem. Commun.*, 2016, **52**, 8467-8470.
125. D. J. Fox, S. B. Duckett, C. Flaschenriem, W. W. Brennessel, J. Schneider, A. Gunay and R. Eisenberg, *Inorg. Chem.*, 2006, **45**, 7197-7209.
126. N. Bloembergen, E. M. Purcell and R. V. Pound, *Phys. Rev.*, 1948, **73**, 679-712.
127. F. Bloch, *Phys. Rev.*, 1946, **70**, 460-474.
128. M. Carravetta, O. G. Johannessen and M. H. Levitt, *Phys. Rev. Lett.*, 2004, **92**.
129. P. J. Rayner, M. J. Burns, A. M. Olaru, P. Norcott, M. Fekete, G. G. R. Green, L. A. R. Highton, R. E. Mewis and S. B. Duckett, *Proc. Natl. Acad. Sci. U. S. A.*, 2017, **114**, E3188-E3194.
130. J. A. Iggo, *NMR spectroscopy in inorganic chemistry*, Oxford University Press New York, 1999.
131. E. Fukushima and S. B. W. Roeder, *Experimental pulse NMR : a nuts and bolts approach*, Addison-Wesley Advanced Book Program, Reading, Mass. , 1981.
132. M. Fekete, O. Bayfield, S. B. Duckett, S. Hart, R. E. Mewis, N. Pridmore, P. J. Rayner and A. Whitwood, *Inorg. Chem.*, 2013, **52**, 13453-13461.
133. P. Norcott, P. J. Rayner, G. G. R. Green and S. B. Duckett, *Chem.-Eur. J.*, 2017, **23**, 16990-16997.
134. M. Carravetta and M. H. Levitt, *J. Am. Chem. Soc.*, 2004, **126**, 6228-6229.
135. S. S. Roy, P. J. Rayner, P. Norcott, G. G. R. Green and S. B. Duckett, *Phys. Chem. Chem. Phys.*, 2016, **18**, 24905-24911.
136. S. S. Roy, P. Norcott, P. J. Rayner, G. G. R. Green and S. B. Duckett, *Angew. Chem., Int. Ed.*, 2016, **55**, 15642-15645.
137. A. M. Olaru, S. S. Roy, L. S. Lloyd, S. Coombes, G. G. R. Green and S. B. Duckett, *Chem. Commun.*, 2016, **52**, 7842-7845.
138. R. E. Mewis, K. D. Atkinson, M. J. Cowley, S. B. Duckett, G. G. R. Green, R. A. Green, L. A. R. Highton, D. Kilgour, L. S. Lloyd, J. A. B. Lohman and D. C. Williamson, *Magn. Reson. Chem.*, 2014, **52**, 358-369.
139. A. M. Olaru, A. Burt, P. J. Rayner, S. J. Hart, A. C. Whitwood, G. G. R. Green and S. B. Duckett, *Chem. Commun.*, 2016, **52**, 14482-14485.
140. D. A. Barskiy, R. V. Shchepin, C. P. N. Tanner, J. F. P. Colell, B. M. Goodson, T. Theis, W. S. Warren and E. Y. Chekmenev, *Chemphyschem*, 2017, **18**, 1493-1498.
141. M. L. Truong, T. Theis, A. M. Coffey, R. V. Shchepin, K. W. Waddell, F. Shi, B. M. Goodson, W. S. Warren and E. Y. Chekmenev, *J. Phys. Chem. C*, 2015, **119**, 8786-8797.

142. K. Shen, A. W. J. Logan, J. F. P. Colell, J. Bae, G. X. Ortiz, T. Theis, W. S. Warren, S. J. Malcolmson and Q. Wang, *Angew. Chem., Int. Ed.*, 2017, **56**, 12112-12116.
143. M. Fekete, F. Ahwal and S. B. Duckett, *J. Phys. Chem. B*, 2020, **124**, 4573-4580.
144. S. R. V., G. B. M., T. T., W. W. and C. E. Y., *Chemphyschem*, 2017, DOI: 10.1002/cphc.201700594, 1961-1966.
145. V. V. Zhivonitko, I. V. Skovpin and I. V. Koptyug, *Chem. Commun.*, 2015, **51**, 2506-2509.
146. M. J. Burns, P. J. Rayner, G. G. R. Green, L. A. R. Highton, R. E. Mewis and S. B. Duckett, *J. Phys. Chem. B*, 2015, **119**, 5020-5027.
147. R. E. Mewis, R. A. Green, M. C. R. Cockett, M. J. Cowley, S. B. Duckett, G. G. R. Green, R. O. John, P. J. Rayner and D. C. Williamson, *J. Phys. Chem. B*, 2015, **119**, 1416-1424.
148. J. B. Hovener, N. Schwaderlapp, R. Borowiak, T. Lickert, S. B. Duckett, R. E. Mewis, R. W. Adams, M. J. Burns, L. A. R. Highton, G. G. R. Green, A. Olaru, J. Hennig and D. von Elverfeldtt, *Anal. Chem.*, 2014, **86**, 1767-1774.
149. H. F. Zeng, J. D. Xu, M. T. McMahon, J. A. B. Lohman and P. C. M. van Zijl, *J. Magn. Reson.*, 2014, **246**, 119-121.
150. M. L. Truong, F. Shi, P. He, B. X. Yuan, K. N. Plunkett, A. M. Coffey, R. V. Shchepin, D. A. Barskiy, K. V. Kovtunov, I. V. Koptyug, K. W. Waddell, B. M. Goodson and E. Y. Chekmenev, *J. Phys. Chem. B*, 2014, **118**, 13882-13889.
151. M. Fekete, C. Gibard, G. J. Dear, G. G. R. Green, A. J. J. Hooper, A. D. Roberts, F. Cisnetti and S. B. Duckett, *Dalton Trans.*, 2015, **44**, 7870-7880.
152. F. Shi, P. He, Q. A. Best, K. Groome, M. L. Truong, A. M. Coffey, G. Zimay, R. V. Shchepin, K. W. Waddell, E. Y. Chekmenev and B. M. Goodson, *J. Phys. Chem. C*, 2016, **120**, 12149-12156.
153. P. Spannring, I. Reile, M. Emondts, P. P. M. Schleker, N. K. J. Hermkens, N. G. J. van der Zwaluw, B. J. A. van Weerdenburg, P. Tinnemans, M. Tessari, B. Blumich, F. Rutjes and M. C. Feiters, *Chem.-Eur. J.*, 2016, **22**, 9277-9282.
154. F. Shi, A. M. Coffey, K. W. Waddell, E. Y. Chekmenev and B. M. Goodson, *Angew. Chem., Int. Ed.*, 2014, **53**, 7495-7498.
155. K. V. Kovtunov, L. M. Kovtunova, M. E. Gemeinhardt, A. V. Bukhtiyarov, J. Gesiorski, V. I. Bukhtiyarov, E. Y. Chekmenev, I. V. Koptyug and B. M. Goodson, *Angew. Chem., Int. Ed.*, 2017, **56**, 10433-10437.
156. B. E. Kidd, J. L. Gesiorski, M. E. Gemeinhardt, R. V. Shchepin, K. V. Kovtunov, I. V. Koptyug, E. Y. Chekmenev and B. M. Goodson, *J. Phys. Chem. C*, 2018, **122**, 16848-16852.
157. W. Iali, A. M. Olaru, G. G. R. Green and S. B. Duckett, *Chem.-Eur. J.*, 2017, **23**, 10491-10495.
158. A. Manoharan, P. J. Rayner, W. Iali, M. J. Burns, V. H. Perry and S. B. Duckett, *ChemMedChem*, 2018, **13**, 352-359.
159. N. Eshuis, N. Hermkens, B. J. A. van Weerdenburg, M. C. Feiters, F. Rutjes, S. S. Wijmenga and M. Tessari, *J. Am. Chem. Soc.*, 2014, **136**, 2695-2698.
160. N. Eshuis, R. Aspers, B. J. A. van Weerdenburg, M. C. Feiters, F. Rutjes, S. S. Wijmenga and M. Tessari, *Angew. Chem., Int. Ed.*, 2015, **54**, 14527-14530.
161. I. Reile, R. Aspers, J. M. Tyburn, J. G. Kempf, M. C. Feiters, F. Rutjes and M. Tessari, *Angew. Chem., Int. Ed.*, 2017, **56**, 9174-9177.

162. L. S. Lloyd, R. W. Adams, M. Bernstein, S. Coombes, S. B. Duckett, G. G. R. Green, R. J. Lewis, R. E. Mewis and C. J. Sleigh, *J. Am. Chem. Soc.*, 2012, **134**, 12904-12907.
163. N. K. J. Hermkens, M. C. Feiters, F. Rutjes, S. S. Wijmenga and M. Tessari, *J. Magn. Reson.*, 2017, **276**, 122-127.
164. L. Sellies, I. Reile, R. Aspers, M. C. Feiters, F. Rutjes and M. Tessari, *Chem. Commun.*, 2019, **55**, 7235-7238.
165. B. J. Tickner, J. S. Lewis, R. O. John, A. C. Whitwood and S. B. Duckett, *Dalton Trans.*, 2019, **48**, 15198-15206.
166. B. J. Tickner, O. Semenova, W. Iali, P. J. Rayner, A. C. Whitwood and S. B. Duckett, *Catal. Sci. Technol.*, 2020, **10**, 1343-1355.
167. B. J. Tickner, R. O. John, S. S. Roy, S. J. Hart, A. C. Whitwood and S. B. Duckett, *Chem. Sci.*, 2019, **10**, 5235-5245.
168. W. Iali, P. J. Rayner and S. B. Duckett, *Sci Adv*, 2018, **4**, eaao6250.
169. P. M. Richardson, W. Iali, S. S. Roy, P. J. Rayner, M. E. Halse and S. B. Duckett, *Chem. Sci.*, 2019, **10**, 10607-10619.
170. P. J. Rayner, P. M. Richardson and S. B. Duckett, *Angew. Chem., Int. Ed.*, 2020, **59**, 2710-2714.
171. L. S. Bouchard, S. R. Burt, M. S. Anwar, K. V. Kovtunov, I. V. Koptyug and A. Pines, *Science*, 2008, **319**, 442-445.
172. J. L. Koenig, *Spectroscopy of Polymers*, Elsevier Science Inc, 2nd Edition edn., 1999.
173. A. Viale and S. Aime, *Curr. Opin. Chem. Biol.*, 2010, **14**, 90-96.
174. Z. J. Wang, M. A. Ohliger, P. E. Z. Larson, J. W. Gordon, R. A. Bok, J. Slater, J. E. Villanueva-Meyer, C. P. Hess, J. Kurhanewicz and D. B. Vigneron, *Radiology*, 2019, **291**, 273-284.
175. N. Bahrami, Swisher, C. L., Von Morze, C., Vigneron, D. B., Larson, P. E. Z., *Quant. Imaging Med. Surg.*, 2014, **4**, 24-32.
176. Y. C. Liu, Y. N. Gu and X. Yu, *Quant. Imaging Med. Surg.*, 2017, **7**, 707-726.
177. R. B. Diasio and B. E. Harris, *Clin. Pharmacokinet.*, 1989, **16**, 215-237.
178. H. A. Ingraham, B. Y. Tseng and M. Goulian, *Mol. Pharmacol.*, 1982, **21**, 211-216.
179. J. Wang, M. Sanchez-Rosello, J. L. Acena, C. del Pozo, A. E. Sorochinsky, S. Fustero, V. A. Soloshonok and H. Liu, *Chem. Rev.*, 2014, **114**, 2432-2506.
180. N. A. E. Meanwell, K. J. and Gillis, E. P., in *Fluorine in Heterocyclic Chemistry Volume 1: Heterocycles and Macrocycles*, ed. V. Nenajdenko, Springer, First edn., 2014, vol. 1, ch. 1, pp. 1-54.
181. M. C. D. Tayler and M. H. Levitt, *J. Am. Chem. Soc.*, 2013, **135**, 2120-2123.
182. L. J. Brown, G. Pileio, M. H. Levitt and R. C. D. Brown, *J. Labelled Compd. Radiopharm.*, 2017, **60**, 135-139.
183. I. M. Lagoja, *Chem. Biodiversity*, 2005, **2**, 1-50.
184. B. M. Association, ed., *BMA New Guide to Medicine and Drugs: The Complete Home Reference to over 2,500 Medicines*, Dorling Kindersley Ltd, 2018.
185. V. Sharma, N. Chitranshi and A. K. Agarwal, *Int J Med Chem*, 2014, **2014**, 202784.
186. K. S. Jain, T. S. Chitre, P. B. Miniyar, M. K. Kathiravan, V. S. Bendre, V. S. Veer, S. R. Shahane and C. J. Shishoo, *Curr. Sci.*, 2006, **90**, 793-803.
187. K. M. Appleby, R. E. Mewis, A. M. Olaru, G. G. R. Green, I. J. S. Fairlamb and S. B. Duckett, *Chem. Sci.*, 2015, **6**, 3981-3993.

188. A. N. Pravdivtsev, A. V. Yurkovskaya, H. M. Vieth, K. L. Ivanov and R. Kaptein, *Chemphyschem*, 2013, **14**, 3327-3331.
189. S. Knecht and K. L. Ivanov, *J. Chem. Phys.*, 2019, **150**, 11.
190. D. C. Harris, *J. Chem. Educ.*, 1998, **75**, 119-121.
191. A. M. Olaru, M. J. Burns, G. G. R. Green and S. B. Duckett, *Chem. Sci.*, 2017, **8**, 2257-2266.
192. M. Fuetterer, J. Busch, S. M. Peereboom, C. von Deuster, L. Wissmann, M. Lipiski, T. Fleischmann, N. Cesarovic, C. T. Stoeck and S. Kozerke, *J. Cardio. Magn. Reson.*, 2017, **19**, 46-57.
193. J. R. Brender, S. Kishimoto, H. Merkle, G. Reed, R. E. Hurd, A. P. Chen, J. H. Ardenkjaer-Larsen, J. Munasinghe, K. Saito, T. Seki, N. Oshima, K. Yamamoto, P. L. Choyke, J. Mitchell and M. C. Krishna, *Sci. Rep.*, 2019, **9**, 3410-3424.
194. L. T. Kuhn and J. Bargon, in *In Situ Nmr Methods in Catalysis*, eds. J. Bargon and L. T. Kuhn, Springer-Verlag Berlin, Berlin, 2007, vol. 276, pp. 25-68.
195. L. T. Kuhn, U. Bommerich and J. Bargon, *J. Phys. Chem. A*, 2006, **110**, 3521-3526.
196. L. Lumata, M. Merritt, C. Malloy, A. D. Sherry and Z. Kovacs, *Appl. Magn. Reson.*, 2012, **43**, 69-79.
197. R. V. Shchepin, D. A. Barskiy, A. M. Coffey, B. M. Goodson and E. Y. Chekmenev, *ChemistrySelect*, 2016, **1**, 2552-2555.
198. K. Golman, O. Axelsson, H. Johannesson, S. Mansson, C. Olofsson and J. S. Petersson, *Magn. Reson. Med.*, 2001, **46**, 1-5.
199. L. E. Olsson, C. M. Chai, O. Axelsson, M. Karlsson, K. Golman and J. S. Petersson, *Magn. Reson. Med.*, 2006, **55**, 731-737.
200. J. Svensson, S. Mansson, E. Johansson, J. S. Petersson and L. E. Olsson, *Magn. Reson. Med.*, 2003, **50**, 256-262.
201. K. Golman, J. H. Ardenaer-Larsen, J. S. Petersson, S. Mansson and I. Leunbach, *Proc. Natl. Acad. Sci. U. S. A.*, 2003, **100**, 10435-10439.
202. W. N. Jiang, L. Lumata, W. Chen, S. R. Zhang, Z. Kovacs, A. D. Sherry and C. Khemtong, *Sci. Rep.*, 2015, **5**.
203. A. Svyatova, I. V. Skovpin, N. V. Chukanov, K. V. Kovtunov, E. Y. Chekmenev, A. N. Pravdivtsev, J. B. Hovener and I. V. Koptyug, *Chem.-Eur. J.*, 2019, **25**, 8465-8470.
204. W. Iali, S. Roy, B. J. Tickner, F. Ahwal, A. Kennerley and S. B. Duckett, *Angew. Chem.*, 2019, **58**, 10271-10275.
205. J. Ruiz-Cabello, B. P. Barnett, P. A. Bottomley and J. W. M. Bulte, *NMR Biomed.*, 2011, **24**, 114-129.
206. E. A. Tanifum, C. Patel, M. E. Liaw, R. G. Pautler and A. V. Annapragada, *Sci. Rep.*, 2018, **8**.
207. W. Wolf, Present, C.A. and Waluch, V., *Adv. Drug Delivery Rev.*, 2000, **41**, 55-74.
208. A. N. Stevens, P. G. Morris, R. A. Iles, P. W. Sheldon and J. R. Griffiths, *Br. J. Cancer*, 1984, **50**, 113-117.
209. W. Wolf, Albright, M. J., Silver, M. S., Weber, H., Reichardt, U. and Sauer, R., *Magn. Reson. Imaging*, 1987, **5**, 165-169.
210. P. M. J. a. G. McSheehy, J. R., *NMR Biomed.*, 1989, **2**, 133-141.
211. W. Semmler, P. Bachertbaumann, F. Guckel, F. Ermark, P. Schlag, W. J. Lorenz and G. Vankaick, *Radiology*, 1990, **174**, 141-145.
212. D. J. O. McIntyre, F. A. Howe, C. Ladroue, F. Lofts, M. Stubbs and J. R. Griffiths, *Cancer Chemother. Pharmacol.*, 2011, **68**, 29-36.

213. T. Ido, C. N. Wan, V. Casella, J. S. Fowler, A. P. Wolf, M. Reivich and D. E. Kuhl, *J. Labelled Compd. Radiopharm.*, 1978, **14**, 175-183.
214. M. M. Alauddin, *Am. J. Nucl. Med. Mol. Imaging*, 2012, **2**, 55-76.
215. W. C. Dickinson, *Phys. Rev.*, 1950, **77**, 736-737.
216. M. Plaumann, U. Bommerich, T. Trantzschel, D. Lego, S. Dillenberger, G. Sauer, J. Bargon, G. Buntkowsky and J. Bernarding, *Chem.-Eur. J.*, 2013, **19**, 6334-6339.
217. U. Bommerich, T. Trantzschel, S. Mulla-Osman, G. Buntkowsky, J. Bargon and J. Bernarding, *Phys. Chem. Chem. Phys.*, 2010, **12**, 10309-10312.
218. A. Peksoz, *Magn. Reson. Chem.*, 2016, **54**, 748-752.
219. A. M. Olaru, T. B. R. Robertson, J. S. Lewis, A. Antony, W. Iali, R. E. Mewis and S. B. Duckett, *Chemistryopen*, 2018, **7**, 97-105.
220. Z. A. Bober, D.; Ożóg, Ł.; Tabarkiewicz, J.; Tutka, P. and Bartusik-Aebisher, D., *Eur. J. Clin. Exp. Med.*, 2017, **15**, 109-119.
221. A. O. Mattes, D. Russell, E. Tishchenko, Y. Z. Liu, R. H. Cichewicz and S. J. Robinson, *Concepts Magn. Reson. Part A*, 2016, **45A**.
222. D. Canet, in *Cross-Relaxation and Cross-Correlation Parameters in NMR: Molecular Approaches (New developments in NMR)*, ed. D. Canet, Royal Society of Chemistry, First edn., 2017, ch. 1: Introduction to Nuclear Spin Cross-relaxation and Cross-correlation Phenomena in Liquids, pp. 1-60.
223. S. S. Roy, K. M. Appleby, E. J. Fear and S. B. Duckett, *J. Phys. Chem. Lett.*, 2018, **9**, 1112-1117.
224. D. B. Longley, D. P. Harkin and P. G. Johnston, *Nat. Rev. Cancer*, 2003, **3**, 330-338.
225. S. Purser, P. R. Moore, S. Swallow and V. Gouverneur, *Chem. Soc. Rev.*, 2008, **37**, 320-330.
226. N. Phillips, R. Tirfoin and S. Aldridge, *Chem.-Eur. J.*, 2014, **20**, 3825-3830.
227. N. Phillips, J. Rowles, M. J. Kelly, I. Riddlestone, N. H. Rees, A. Dervisi, I. A. Fallis and S. Aldridge, *Organometallics*, 2012, **31**, 8075-8078.
228. H. J. Chen, R. H. X. Teo, J. Wong, Y. X. Li, S. A. Pullarkat and P. H. Leung, *Dalton Trans.*, 2018, **47**, 13046-13051.
229. J. R. Lusty, J. Peeling and A.-A. M. A., *Inorg. Chim. Acta*, 1981, **56**, 21-26.
230. A. Bondi, *J. Phys. Chem.*, 1964, **68**, 441-451.
231. D. O'Hagan, *Chem. Soc. Rev.*, 2008, **37**, 308-319.
232. D. Blazina, S. B. Duckett, J. P. Dunne and C. Godard, *Dalton Trans.*, 2004, 2601-2609.
233. G. A. Morris and R. Freeman, *J. Am. Chem. Soc.*, 1979, **101**, 760-762.
234. D. M. P. Doddrell, D. T. and Bendall, M. R., *J. Magn. Reson.*, 1982, **48**, 323-327.
235. J. W. Emsley, L. Philips and V. Waray, *Progress in NMR Spectroscopy*, 1976.
236. J. Z. Wang, F. Kreis, A. J. Wright, R. L. Hesketh, M. H. Levitt and K. M. Brindle, *Magn. Reson. Med.*, 2018, **79**, 741-747.
237. I. Marco-Rius, J. W. Gordon, A. N. Mattis, R. Bok, R. Delos Santos, S. Sukumar, P. E. Z. Larson, D. B. Vigneron and M. A. Ohliger, *J. Magn. Reson. Imaging*, 2018, **47**, 141-151.
238. R. J. Watts, J. S. Harrington and J. Vanhouten, *J. Am. Chem. Soc.*, 1977, **99**, 2179-2187.
239. M. S. Chan and A. C. Wahl, *J. Phys. Chem.*, 1978, **82**, 2542-2549.
240. F. F. Diaz-Rullo, F. Zamberlan, R. E. Mewis, M. Fekete, L. Broche, L. A. Cheyne, S. Dall'Angelo, S. B. Duckett, D. Dawson and M. Zanda, *Bioorg. Med. Chem.*, 2017, **25**, 2730-2742.

241. W. Iali, P. J. Rayner, A. Alshehri, A. J. Holmes, A. J. Ruddlesden and S. B. Duckett, *Chem. Sci.*, 2018, **9**, 3677-3684.
242. P. J. Rayner, B. Tickner, W. Iali, M. Fekete, A. D. Robinson and S. B. Duckett, *Chem. Sci.*, 2019, **10**, 7709-7717.
243. Y. D. Xiao, R. Paudel, J. Liu, C. Ma, Z. S. Zhang and S. K. Zhou, *Int. J. Mol. Med.*, 2016, **38**, 1319-1326.
244. FDA, FDA Drug Safety Communication: FDA warns that gadolinium-based contrast agents (GBCAs) are retained in the body; requires new class warnings, https://www.fda.gov/media/107506/download).
245. J. D. Schlaudecker and C. R. Bernheisel, *Am. Fam. Physician*, 2009, **80**, 711-714.
246. S. E. Cowper, H. S. Robin, S. M. Steinberg, L. D. Su, S. Gupta and P. E. LeBoit, *Lancet*, 2000, **356**, 1000-1001.
247. J. Garcia, S. Z. Liu and A. Y. Louie, *Philos. Trans. R. Soc. A*, 2017, **375**.
248. H. S. Thomsen, *Radiol. Clin. North Am.*, 2009, **47**, 827-+.
249. B. Wagner, V. Drel and Y. Gorin, *Am. J. Physiol. Renal Physiol*, 2016, **311**, F1-F11.
250. E. T. Petersen, I. Zimine, Y. C. L. Ho and X. Golay, *Br. J. Radiol.*, 2006, **79**, 688-701.
251. T. Yoshiura, A. Hiwatashi, T. Noguchi, K. Yamashita, Y. Ohyagi, A. Monji, E. Nagao, H. Kamano, O. Togao and H. Honda, *Eur. Radiol.*, 2009, **19**, 2819-2825.
252. F. Kober, T. Jao, T. Troalen and K. S. Nayak, *J. Cardio. Magn. Reson.*, 2016, **18**.
253. C. Federau, *NMR Biomed.*, 2017, **30**.
254. A. Cieszanowski, K. Pasicz, J. Podgorska, E. Fabiszewska, W. Skrzynski, J. Jasieniak, A. Anysz-Grodzicka, I. Grabska, J. Palucki, M. Naduk-Ostrowska, B. Jagielska and P. Kukolowicz, *Pol. J. Pharmacol.*, 2018, **83**, E437-E445.
255. E. R. McCarney, B. D. Armstrong, M. D. Lingwood and S. Han, *Proc. Natl. Acad. Sci. U. S. A.*, 2007, **104**, 1754-1759.
256. C. von Morze, P. E. Z. Larson, S. Hu, K. Keshari, D. M. Wilson, J. H. Ardenkjaer-Larsen, A. Goga, R. Bok, J. Kurhanewicz and D. B. Vigneron, *J. Magn. Reson. Imaging*, 2011, **33**, 692-697.
257. M. D. Lingwood, T. A. Siaw, N. Sailasuta, O. A. Abulseoud, H. R. Chan, B. D. Ross, P. Bhattacharya and S. Han, *Radiology*, 2012, **265**, 418-425.
258. K. W. Lipso, S. Bowen, O. Rybalko and J. H. Ardenkjaer-Larsen, *J. Magn. Reson.*, 2017, **274**, 65-72.
259. G. D. Reed, C. von Morze, A. S. Verkman, B. L. Koelsch, M. M. Chaumeil, M. Lustig, S. M. Ronen, R. A. Bok, J. M. Sands, P. E. Z. Larson, Z. J. Wang, J. H. A. Larsen, J. Kurhanewicz and D. B. Vigneron, *Tomography*, 2016, **2**, 125-137.
260. C. L. S. Naeim Bahrami, Cornelius Von Morze, Daniel B. Vigneron, Peder E. Z. Larson, *Quant. Imaging Med. Surg.*, 2014, **4**, 24-32.
261. B. Davies and T. Morris, *Pharm. Res.*, 1993, **10**, 1093-1095.
262. J. H. Ardenkjær-Larsen, C. Lausten, B. Pullinger, S. Kadlecek, K. Emami and R. Rizi, *Proc. Int. Soc. Magn. Reson. Med.*, 2011, **19**.
263. K. M. Brindle, S. E. Bohndiek, F. A. Gallagher and M. I. Kettunen, *Magn. Reson. Med.*, 2011, **66**, 505-519.
264. D. S. Robertson, *Clin. Chem. Lab. Med.*, 2011, **49**, 1405-1412.
265. P. A. Bottomley, H. C. Charles, P. B. Roemer, D. Flamig, H. Engeseth, W. A. Edelstein and O. M. Mueller, *Magn. Reson. Med.*, 1988, **7**, 319-336.
266. P. A. Bottomley, C. J. Hardy and P. B. Roemer, *Magn. Reson. Med.*, 1990, **14**, 425-434.
267. T. Ernst, J. H. Lee and B. D. Ross, *J. Comput. Assist. Tomogr.*, 1993, **17**, 673-680.

268. J. Friedrich, C. S. Apstein and J. S. Ingwall, *Circulation*, 1995, **92**, 3527-3538.
269. O. Speck, K. Scheffler and J. Hennig, *Magn. Reson. Med.*, 2002, **48**, 633-639.
270. L. Valkovic, M. Chmelik and M. Krssak, *Anal. Biochem.*, 2017, **529**, 193-215.
271. S. C. Noonan and G. P. Savage, *Asia Pac. J. Clin. Nut.*, 1999, **8**, 64-74.
272. G. Pileio and M. H. Levitt, *J. Chem. Phys.*, 2009, **130**.
273. M. Carravetta and M. H. Levitt, *J. Chem. Phys.*, 2005, **122**, 14.
274. M. H. Levitt, *J. Magn. Reson.*, 2019, **306**, 69-74.
275. G. Pileio, S. Bowen, C. Laustsen, M. C. D. Tayler, J. T. Hill-Cousins, L. J. Brown, R. C. D. Brown, J. H. Ardenkjaer-Larsen and M. H. Levitt, *J. Am. Chem. Soc.*, 2013, **135**, 5084-5088.
276. E. A. Bienkiewicz and K. J. Lumb, *J. Biomol. NMR*, 1999, **15**, 203-206.
277. P. M. L. Robitaille, P. A. Robitaille, G. G. Brown and G. G. Brown, *J. Magn. Reson.*, 1991, **92**, 73-84.
278. H. K. Hall, *J. Am. Chem. Soc.*, 1957, **79**, 5441-5444.
279. R. J. Gillies, J. P. Galons, K. A. McGovern, P. G. Scherer, Y. H. Lien, C. Job, R. Ratcliff, F. Chapa, S. Cerdan and B. E. Dale, *NMR Biomed.*, 1993, **6**, 95-104.
280. J. W. Akitt, *NMR and Chemistry: An introduction to the Fourier transform - multinuclear era*, Chapman and Hall Ltd, Second Edition edn.
281. V. N. Serezhkin, M. Y. Artem'eva, L. B. Serezhkina and Y. N. Mikhailov, *Russ. J. Inorg. Chem.*, 2005, **50**, 1019-1030.
282. M. Y. Artem'eva, V. N. Serezhkin and Y. N. Mikhailov, *Acta Crystallogr. A*, 2006, **62**, S272-S272.
283. E. J. Baran, *J. Coord. Chem.*, 2014, **67**, 3734-3768.
284. I. Bertini, C. Luchinat, L. Messori, A. Scozzafava, G. Pellacani and M. Sola, *Inorg. Chem.*, 1986, **25**, 1782-1786.
285. B. Modec and J. V. Brencic, *Eur. J. Inorg. Chem.*, 2005, 1698-1709.
286. B. Modec, J. V. Brencic, D. Dolenc and J. Zubieta, *J. Chem. Soc., Dalton Trans.*, 2002, 4582-4586.
287. M. E. Robinson, J. E. Mizzi, R. J. Staples and R. L. LaDuca, *Cryst. Growth Des.*, 2015, **15**, 2260-2271.
288. B. J. Tickner, Parker, R. R., Whitwood, A. C. and Duckett, S. B., *Organometallics*, 2019, **38**, 4377-4382.
289. H. Kessler, H. Oschkinat and C. Griesinger, *J. Magn. Reson.*, 1986, **70**, 106-133.
290. K. Stott, J. Stonehouse, J. Keeler, T. L. Hwang and A. J. Shaka, *J. Am. Chem. Soc.*, 1995, **117**, 4199-4200.
291. J. Stonehouse, P. Adell, J. Keeler and A. J. Shaka, *J. Am. Chem. Soc.*, 1994, **116**, 6037-6038.
292. T. Hascall, D. Rabinovich, V. J. Murphy, M. D. Beachy, R. A. Friesner and G. Parkin, *J. Am. Chem. Soc.*, 1999, **121**, 11402-11417.
293. A. Apps, J. Lau, M. Peterzan, S. Neubauer, D. Tyler and O. Rider, *Heart*, 2018, **104**, 1484-1491.
294. S. Nakamura, H. Yang, C. Hirata, F. Kersaudy and K. Fujimoto, *Org. Biomol. Chem.*, 2017, **15**, 5109-5111.
295. S. Nakamura, Y. Takashima and K. Fujimoto, *Org. Biomol. Chem.*, 2018, **16**, 891-894.
296. J. D. Watson and F. H. C. Crick, *Cold Spring Harbor Symp. Quant. Biol.*, 1953, **18**, 123-131.
297. R. E. Franklin and R. G. Gosling, *Acta Crystallogr.*, 1953, **6**, 673-677.

298. R. E. Franklin and R. G. Gosling, *Acta Crystallogr.*, 1953, **6**, 678-685.
299. M. Ibba and D. Soll, *Science*, 1999, **286**, 1893-1897.
300. M. Goulian, L. Z. J. and A. Kornberg, *J. Biol. Chem.*, 1967, **243**, 627-638.
301. D. Brutlag and A. Kornberg, *J. Biol. Chem.*, 1972, **247**, 241-248.
302. C. C. Richardson, C. L. Schildkraut and A. Kornberg, *Cold Spring Harbor Symp. Quant. Biol.*, 1963, **28**, 9-19.
303. T. Lindahl, *Proc. Natl. Acad. Sci. U. S. A.*, 1974, **71**, 3649-3653.
304. M. G. Rose, M. P. Farrell and J. C. Schmitz, *Clin. Colorectal Cancer*, 2002, **1**, 220-229.
305. J. L. Grem, R. T. Mucay, E. M. Miller, C. J. Allegra and P. H. Fischer, *Biochem. Pharmacol.*, 1989, **38**, 51-59.
306. T. Shirasaka, *Jap. J. Clin. Oncol.*, 2009, **39**, 2-15.
307. R. Duschinsky, E. Pleven and C. Heidelberger, *J. Am. Chem. Soc.*, 1957, **79**, 4559-4560.
308. A. Yoshioka, S. Tanaka, O. Hiraoka, Y. Koyama, Y. Hirota, D. Ayusawa, T. Seno, C. Garrett and Y. Wataya, *J. Biol. Chem.*, 1987, **262**, 8235-8241.
309. M. X. Liu, G. N. Zhang, N. Mahanta, Y. Lee and C. Hilty, *J. Phys. Chem. Lett.*, 2018, **9**, 2218-2221.
310. J. B. Hovener, N. Schwaderlapp, T. Lickert, S. B. Duckett, R. E. Mewis, L. A. R. Highton, S. M. Kenny, G. G. R. Green, D. Leibfritz, J. G. Korvink, J. Hennig and D. von Elverfeldt, *Nat. Commun.*, 2013, **4**.
311. R. L. Benoit and M. Frechette, *Can. J. Chem./Rev. Can. Chim.*, 1986, **64**, 2348-2352.
312. R. L. Lipnick and J. D. Fissekis, *J. Labelled Compd. Radiopharm.*, 1980, **17**, 247-254.
313. R. V. Shchepin, L. Jaigirdar, T. Theis, W. S. Warren, B. M. Goodson and E. Y. Chekmenev, *J. Phys. Chem. C.*, 2017, **121**, 28425-28434.
314. G. D. Reed, C. von Morze, R. Bok, B. L. Koelsch, M. Van Criekinge, K. J. Smith, H. Shang, P. E. Z. Larson, J. Kurhanewicz and D. B. Vigneron, *IEEE Trans. Med. Imgaing*, 2014, **33**, 362-371.
315. I. J. Day, J. C. Mitchell, M. J. Snowden and A. L. Davis, *Appl. Magn. Reson.*, 2008, **34**, 453-460.
316. E. Chiavazza, E. Kubala, C. V. Gringeri, S. Duwel, M. Durst, R. F. Schulte and M. I. Menzel, *J. Magn. Reson.*, 2013, **227**, 35-38.
317. A. S. Kiryutin, A. N. Pravdivtsev, K. L. Ivanov, Y. A. Grishin, H. M. Vieth and A. V. Yurkovskaya, *J. Magn. Reson.*, 2016, **263**, 79-91.
318. E. Anoardo, G. Galli and G. Ferrante, *Appl. Magn. Reson.*, 2001, **20**, 365-404.
319. Crystalis-Pro, *Oxford Diffraction Ltd.*, Version 1.71.34.41.
320. G. M. Sheldrick, *Acta Crystallogr. A*, 2015, **71**, 3-8.
321. O. V. Dolomanov, L. J. Bourhis, R. J. Gildea, J. A. K. Howard and H. Puschmann, *J. Appl. Crystallogr.*, 2009, **42**, 339-341.
322. G. M. Sheldrick, *Acta Crystallogr., Sect C: Struct. Chem.*, 2015, **71**, 3-8.
323. O. Torres, M. Martin and E. Sola, *Organometallics*, 2009, **28**, 863-870.
324. B. Efron and C. Stein, *Annals of statistics*, 1981, **9**, 586-596.
325. S. Meiboom and D. Gill, *Rev. Sci. Instrum.*, 1958, **29**, 688-691.
326. M. H. Levitt and R. Freeman, *J. Magn. Reson.*, 1981, **43**, 65-80.
327. J. Hennig, A. Nauerth and H. Friedburg, *Magn. Reson. Med.*, 1986, **3**, 823-833.
328. H. Y. Carr, *Phys. Rev.*, 1958, **112**, 1693-1701.

329. G. B. Chavhan, P. S. Babyn, B. G. Jankharia, H. L. M. Cheng and M. M. Shroff, *Radiographics*, 2008, **28**, 1147-1160.
330. T. R. Brown, B. M. Kincaid and K. Ugurbil, *Proc. Natil. Acad. Sci. USA-Biol. Sci.*, 1982, **79**, 3523-3526.
331. A. Huda, R. Nagarajan, J. Furuyama and M. A. Thomas, *Comprehensive Biomedical Physics*, 1st Edition edn., 2014.